CIVIL ENGINEERING JOURNAL

číslo 2/2024

Obsah:

11	**POSITIONAL ACCURACY OF CADASTRAL MAPS DIGITIZED FROM THE STABLE CADASTRE SYSTEM** *Martin Tauchman, Tomáš Janata*
12	**CONSTRUCTION TECHNOLOGY AND APPLICATION OF TBM IN SHENGLI TUNNEL OF TIANSHAN MOUNTAIN UNDER POOR GEOLOGICAL CONDITIONS** *Zhenping Zhao, Chen Jianxun, Geng Qi, Li Dong, Huang Dengxia, Luo Yanbin, Liu Weiwei, Mu Shaoping, Peter Anesu Kanhenga, Wu Teligen*
13	**RESEARCH ON CONSTRUCTION TECHNOLOGY OF LARGE-DIAMETER SHIELD TUNNEL IN SHALLOW COVER SECTION OF RED STRATA GEOLOGY** *Kexin Zhang, Jian Ouyang, Haijun Wang, Xin Dong, Dawei Hu, Xingwei Xue*
14	**A COMPARATIVE ANALYSIS BETWEEN PERSONAL AND TERRESTRIAL LASER SCANNING FOR THE DOCUMENTATION OF HERITAGE SITES** *Arli Llabani, Freskida Abazaj*
15	**RESEARCH ON OPTIMIZATION OF MOTORWAY ROUTE DESIGN SCHEME IN MOUNTAIN AREAS BASED ON ENTROPY WEIGHT-TOPSIS MODEL** *Yunwei Meng, zhenyu quan, Kang Chen, Binbin Li, Guangyan Qing, Zhongshuai Liu*
16	**EVALUATING FISH PASSAGE EFFICIENCY IN VERTICAL SLOT FISHWAYS USING THE ANALYTIC HIERARCHY PROCESS** *Yuheng zhai, Li jiang*
17	**ST. VITUS CATHEDRAL AT PRAGUE CASTLE DURING THE PERIOD OF NORMALIZATION** *Martin Šnorbert*
18	**FINITE ELEMENT SIMULATION ANALYSIS OF CURVILINEAR CONTINUOUS BEAM BRIDGE JACKING AND TRANSLATION CONSTRUCTION** *Xilong Zheng, Jinshuo Yan, Peng Li; Wei Li; Qiong Wang*
19	**OPTIONS SELECTION AND IMPACT STUDY OF INTERCITY RAILWAY TUNNEL CONSTRUCTION UNDER AIRPORT INTERZONE** *Ming Zhang*
20	**DIGITALIZATION OF IRRIGATION SYSTEMS FROM WATER MANAGEMENT MAPS** *Adam Tejkl, Petr Kavka*

CIVIL ENGINEERING JOURNAL

Article no. 11

THE CIVIL ENGINEERING JOURNAL 2-2024

POSITIONAL ACCURACY OF CADASTRAL MAPS DIGITISED FROM THE STABLE CADASTRE SYSTEM

Martin Tauchman and Tomáš Janata

Czech Technical University, Faculty of Civil Engineering, Department of Geomatics, Praha, Thakurova 7, Czech Republic; martin.tauchman@fsv.cvut.cz, tomas.janata@fsv.cvut.cz

ABSTRACT

The accuracy of positional data in cadastral mapping is crucial for various technical activities within the cadastre and related decision-making processes. With digital maps becoming ubiquitous in cadastral operations, assessing the positional accuracy of cadastral maps digitised from stable cadastre systems has become essential. These maps, categorised as DKM and KMD, present different challenges in determining their overall positional accuracy. While DKM maps offer high accuracy, KMD maps, derived from stable cadastre systems, pose challenges due to their varied origins, including potential positional errors inherited from historical data.

This study proposes a methodology for assessing the positional accuracy of KMD maps by comparing digitised boundaries with actual field measurements. The evaluation considers factors such as cadastral area characteristics, available survey data, and the timing of digitisation efforts. The study aims to categorise objects based on their positional accuracy by analysing shifts in boundary points and building positions.

Results from testing in selected cadastral areas reveal varying degrees of accuracy in KMD maps. While some areas demonstrate high accuracy, others exhibit significant positional inaccuracies, particularly in peripheral regions or linear parcels. The study suggests that areas outside built-up areas may require immediate remapping to ensure accuracy.

Overall, the findings highlight the importance of assessing and improving the positional accuracy of cadastral maps to enhance their utility in land management and decision-making processes. Further research could focus on developing automated methods for detecting and correcting positional errors in digital cadastral maps.

KEYWORDS

Cadastral mapping, Positional accuracy, Digital maps, Stable cadastre system, Land parcel, Boundary refinement, Geographic information systems

POSITIONAL ACCURACY OF CADASTRAL MAPS DIGITISED FROM THE STABLE CADASTRE SYSTEM

The quality of the positional data is essential for using the existing cadastral mapping work in all technical activities within the cadastre [1] and in cadastre-related activities where cadastral data are used as support for further decision-making. At present, it is possible to encounter maps in digital form in virtually all cases in the cadastre [2]. These can be divided into maps of high positional accuracy, marked DKM, which have undergone either a new mapping or a redrawing based on the cadastral map in S-JTSK on a previous numerical measurement basis. These maps constitute approximately half of the mapping operation and need not be considered further regarding their positional accuracy. In the second case, these are KMD maps created by reworking from the stable cadastre system [3]. The very principle of creating KMDs makes it impossible to determine the overall positional accuracy of such a map in any simple way. This map is partly made up of detailed points

obtained from previous measurements and partly of vectorisation of the original map data converted into raster form. The origin of the stable cadastral map dates back to the first half of the 19th century so that numerous positional errors may be preserved in these maps. The situation is complicated because each location with a digitised cadastral map may be of varying quality.

Its influence may be the structure and shape of the cadastral area, the amount of available data from previous surveying works or even the scattered or coherent nature of the intravillans in the course of refining transformations of map data. Another quality factor may be the time when the restoration took place, whether at the beginning of the ongoing digitisation or rather towards the end of it when the processor has already gained some experience. The last and most important influence on the quality of the resulting digitised map has always been the processor of the renewal, its diligence and expertise [4].

The stable cadastre system was introduced in all the crown lands of the Habsburg monarchy by the relevant patent as a means of maintaining the land tenure agenda. In most of them, the cadastres of the countries divided after the First World War underwent different developments. However, they retain some common features from the first hundred years of their joint administration.

In Austria, the home country of these cadastral inventories, there have also been efforts in recent years to establish the quality of the cadastral maps, and further steps in the refinement and development of the entire register may follow. There are conferences on this topic, e.g., in Austria, Croatia, Hungary, and Czechia. As can be seen from selected papers, also in Austria [5] or Slovakia [6], attempts to quantify the residual errors of cadastral maps are being made by comparing identical points with reality or attempts to assess the overall quality and usability of the graphical part of the cadastral maps. Polish colleagues [7], among others, attempt to compare the state of cadastres in post-Habsburg countries and show common and different elements of the related cadastral systems.

METHODOLOGY FOR DETERMINING THE POSITIONAL ACCURACY OF A KMD MAP

The positional accuracy of the map can be obtained, for example, by comparing the position of individual breakpoints of land boundaries before mapping with their actual position in the field. As each digitised cadastral map may be of different quality, it was decided to conduct testing in several territories and then evaluate the conclusions considering several factors.

Coordinates determined by mapping have significantly higher accuracy. Therefore, the coordinate differences can be used as true coordinate errors according to the statistical principle. The distance of the identical point in the digitised map (i.e. the image of reality) with its position in the digital map after the mapping, i.e. with its actual position in the field, was chosen as the tested element. In other words, the offset of the position of the refractive point of the parcel shown on the map before mapping with its position in reality shown on the map after the new mapping. This has always been consistently done within each test site for as many points as possible that can be declared identical. Thus, apparently corrected boundaries were not chosen for comparison, where a seemingly straight section of the boundary was drawn with several new breakpoints after mapping and the boundary did not correspond in shape to its course before mapping. Such cases are possible in a new mapping. However, in addition to the new mapping, they can also be dealt with by a procedure where the situation is surveyed and entered in the cadastre using a geometric plan and related deed. As far as buildings are concerned, the methodology is similar, and all buildings that have been rebuilt in any way have been ignored in the assessment of displacement. If a building showed only curvature or displacement in any direction but its perimeter shape was consistent with the condition before the mapping was carried out, such a building was surveyed, all its fracture points were examined, and its displacement monitored. In the case of linear parcels, which may include roads, paths and other communications, as well as watercourses, rivers or streams, the displacement of the line position was measured as a test feature where specific fracture points could not be identified (for instance, see Figure 1).

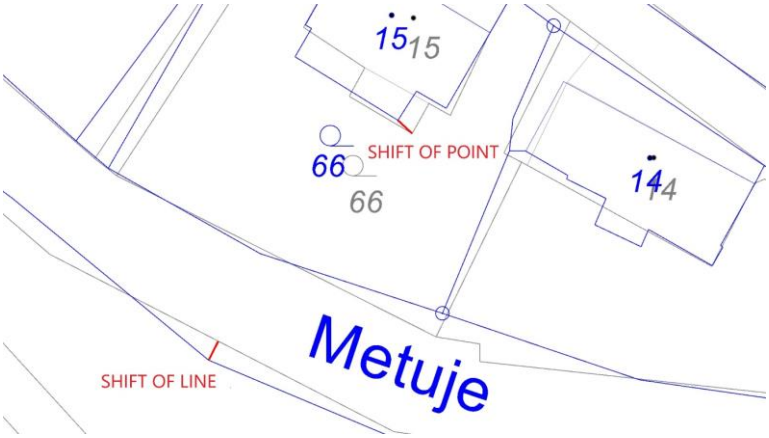

Fig. 1 – Example of a measured displacement of the rebuilt building (No. 15) and the watercourse (the Metuje River):

The individual displacements were then evaluated according to different types of objects, namely:

1. buildings,
2. plots,
3. line plots,
4. detailed points.

Furthermore, three intervals were selected, defining the range where the tracked object was evaluated either as positionally sufficient accuracy or as intended to be refined or corrected. The evaluation was therefore carried out considering the current possibilities of cadastral management and boundary refinement [8]. Only an object was selected as an object of sufficient positional accuracy if the displacement of all refractive points of the object under study lies in the interval zero to 0.28 m, where the boundary limit was chosen as the size given by the coordinate error limit of the detailed point with quality code (QC) 3. Such an object, be it a building, a parcel or a linear parcel, can be evaluated as an object whose position remained unchanged after the new mapping. The object to be refined has been determined by moving at least one refractive point of the surveyed object to the distance given by the refinement parameter for the boundary shown by quality code 8, i.e. to a distance of 2.82 m. All objects with a displacement of at least one of their breakpoints beyond 2.83 m were then identified as objects to be repaired.

Building, parcel and linear parcel objects were divided into intervals according to whether at least one point on their perimeter was already in the "worse" interval of the assessed accuracy. In order to avoid some distortion of the overall accuracy of the study area if most of the displacements on the surveyed object lay in an interval close to zero, and continually one inaccurate breakpoint would significantly worsen the resulting number of surveyed parcel or building objects, a variant of the single detailed point as such was added as a separate category.

To better visualize the displacements and conclude, it was decided to sort the displacement data for the selected object category "detailed point" even more according to their frequency in intervals of 0.40 m, which is close to multiples of the size of the limiting positional error according to the cadastral decree. The results clearly showed the quantity and size of displacements of identical points in individual territories. It is thus evident at a glance which cadastre units show the highest inaccuracies in the originally examined digitised cadastral map.

In addition, in determining the displacement of individual points, the interval of positionally sufficient accuracy has been extended by the category of so-called "technically perfect points" in the interval 0 to 10 cm since 10 cm is the distance from which broken boundaries and protrusions on buildings are displayed on the cadastral map.

The critical value has been set to establish a limit from which shifts of identical points on the map before and after mapping will be regarded as gross errors in position that cannot be refined

even with the consent of the owners. A more apparent numerical limit would be to set a specific integer figure that is easy to represent, such as 3.00 m, which is what the distance of 2.82 tends to be in practice. Similarly, the limit was set by looking for an interval of still recognisable points that did not need to be re-surveyed as part of the new cadastral survey. This is also why a specific interval of 0.00 to 0.10 m was set for monitoring the displacement of technically perfect points, completely unrelated to the values of the quality characteristic codes 3 or 8. Another evaluation interval bounded by a limit value of 0.28 m, identical to the value of the coordinate error limit, is already on the edge of perceiving points as identical. In this situation, it can be argued that identical points beyond this distance should already be redetermined in the detailed measurement of the new mapping. A position error limit of 0.40 m is literally no longer appropriate because a significant number of insulated corners of buildings would fit behind the positionally accurate points.

Priority was given to the survey to reach conclusions on the technical necessity of the new cadastral mapping. For these reasons, in further research, it would be advisable to adjust the intervals completely without reference to the values of mean errors according to the currently valid cadastral decree but rather with regard to the current measurement possibilities. Thus, the intervals should be adjusted with the limit criteria of 0.10 m as technically perfect, 0.25 m as sufficiently accurate and greater than 1 m as inaccurate. In such a case, information on the possibility of the owners' refinement of these boundaries would then drop out.

Tab. 1 - The overall table for the methodology of determining the positional accuracy of the map according to the surveyed objects

Object	Technically perfect	Of sufficient accuracy	Intended for refinement	Intended for repair
Building		0.00–0.28 m	0.29– 2.83 m	more than 2.83 m
Plot		0.00–0.28 m	0.29– 2.83 m	more than 2.83 m
Line plot		0.00–0.28 m	0.29– 2.83 m	more than 2.83 m
Point	0.00–0.09 m	0.10–0.28 m	0.29– 2.83 m	more than 2.83 m

The quality of the digitised cadastral map before mapping was determined by the percentage frequency of individual objects compared to the total number in the mapped area.

This procedure gives a very illustrative overview of the positional accuracy of the digitised cadastral map of the area. It is, of course, possible to arrive at one particular figure, either the average displacement or the maximum displacement of a control point. However, given that the quality factors described above affect each cadastral area separately, this is not essential. The methodology is based on the fact that we are using the map after the new mapping, i.e. after the boundary survey, as a comparison file. We obtain the actual difference in the boundary position agreed by the owners and the boundary registered in the cadastre before the mapping. Thus, it can be expected that, in the case of a sufficiently large number of identical points, we approach a specific and realistic result of estimating the positional accuracy of a particular territory.

Tab. 2 - Analysis of detailed point shifts in individual cadastral areas

Cadastre unit	Renewal by reworking	Renewal by mapping	Description of the territory	Cadastral office
Maršov nad Metují	28.04.2009	16.07.2020	built-up part of the village and part of the extravilan	Náchod
Levín nad Cidlinou	23.11.2009	09.07.2018	built-up part of the village *	Hradec Králové
Bělý	19.04.2010	01.12.2021	built-up part of the village	Náchod
Vinice v Podkrkonoší	14.04.2016	12.10.2021	built-up part of the village *	Jičín
Vlásenice u Makova	18.12.2013	15.12.2021	built-up part of the village *	Tábor
Skoranov	21.12.2009	18.11.2020	built-up part of the village	Chrudim
Sedlatice	27.11.2013	10.11.2023	built-up part of the village *	Jihlava
Divnice	12.01.2009	29.11.2023	built-up part of the village *	Valašské Klobouky

* the area was solved after comprehensive land development

Table 2 lists the cadastral areas selected for testing positional accuracy. The areas were chosen because they were different sites, fell under the jurisdiction of different cadastral authorities, were developed at different times, and at least some area covered the extravillage.

The initial assumption was that KMD-type maps produced during early digitisation might have some inaccuracies, for example, because of the initial experience gained in the production of KMDs through reworking. In the mapped area, including part of the extravillage, it was assumed that the inaccuracies of the KMD map type would be significantly more extensive and more frequent outside the municipality's intravillage due to the insufficient number of identical points for refining transformations in the KMD production.

For testing, freely available cadastral maps [9] in the cadastral exchange format were used on the website https://services.cuzk.cz/. The survey of the positional accuracy of the digitised cadastral maps was carried out only on maps originating from the stable cadastre at a scale of 1:2880.

Tab. 3 - Objects analysed in each location

Cadastre unit	Buildings	Plots	Line plots	Total number of points
Maršov nad Metují	50	90	14	657
Levín nad Cidlinou	41	62		302
Bělý	123	154	7	995
Vinice v Podkrkonoší	42	46		292
Vlásenice u Makova	98	122	11	792
Skoranov	77	113	6	551
Sedlatice	47	60		305
Divnice	265	358		1768
Total objects	743	1005	38	5662

RESULTS

The following graphs show the frequency of shifts of detailed points sorted in intervals of 0.4 m. They may represent a clue indicating significant shifts and large positional inaccuracies of the original map within the particular areas.

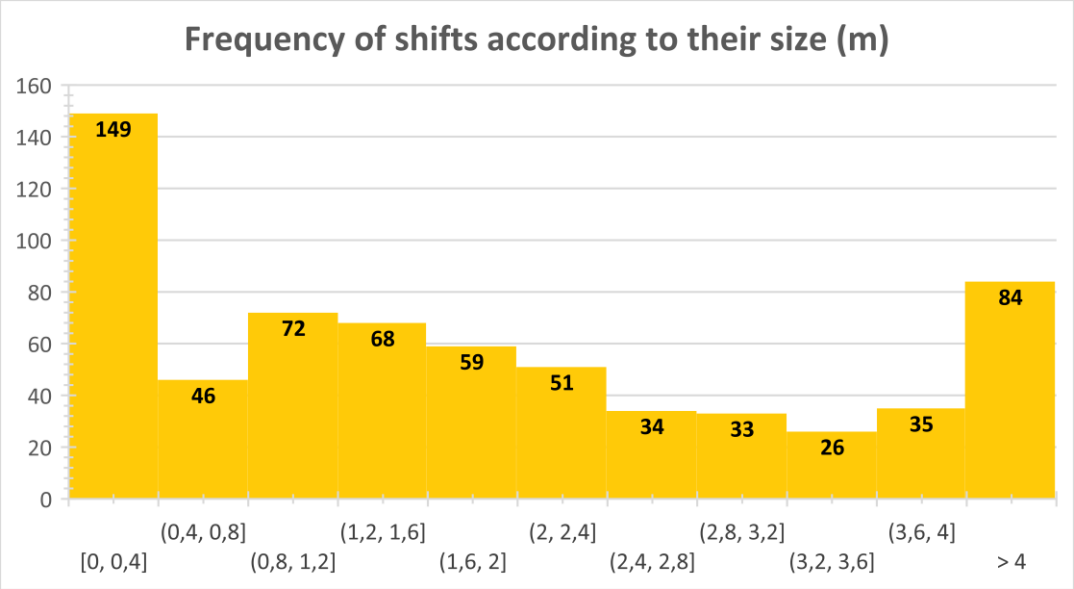

Fig. 2 – Maršov nad Metují (Cadastral Office for Hradec Králové Region)

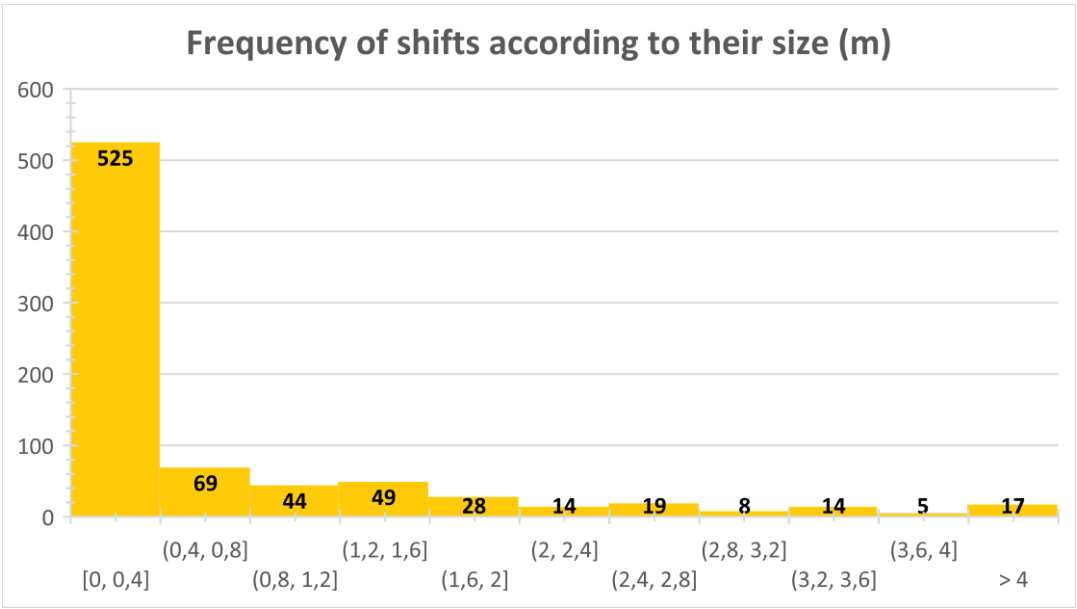

Fig. 3 – Vlásenice u Makova (Cadastral Office for the South Bohemian Region)

The graphs of the frequency of displacements in Figure 3 show that most of the points lie in the first interval up to 0.40 m. In these cases, the positional accuracy of the digitised cadastral map is relatively high.

By testing eight selected areas, many of the KMD-type maps proved to be surprisingly positionally accurate. Most of the detailed points meet the parameters for QC 3 points, and the remaining points could be refined with the owners' consent if they were interested.

Tab. 4 - Summary of the analysis of shifts in the test areas

Cadastre unit	Average shift (m)	Maximum shift (m)	Points of sufficient accuracy (%)	Points to be refined (%)	Points to be corrected (%)
Maršov nad Metují	2.00	11.09	20.4	52.5	27.1
Levín nad Cidlinou	1.12	6.39	27.8	65.2	7.0
Bělý	1.09	7.63	39.0	51.5	9.5
Vinice v Podkrkonoší	0.36	2.63	65.4	34.6	0.0
Vlásenice u Makova	0.65	9.4	62.5	32.1	5.4
Skoranov	0.56	7.45	69.0	26.1	4.9
Sedlatice	0.37	3.29	70.8	28.2	1.0
Divnice	0.52	7.74	61.1	36.2	2.7

At first glance, the grey-shaded cadastre units have an unexpectedly high positional accuracy. Almost two-thirds of the surveyed points show only a slight shift of an identical point, between 0 and 28 cm from its recorded position in the KMD. Even the size of the average shift confirms the unexpectedly high positional accuracy of most of the surveyed areas. The maximum shift's magnitude indicates the gross error that may occur in a given area. The very high maximum displacement at Maršov nad Metují is clearly also due to the mapping of the extravilane and linear parcels. The lower positional accuracy of the areas digitised in the early years is also confirmed. In all the grey-shaded areas, we can speak of relatively good-quality KMD maps. However, some parts of peripheral locations or blocks of parcels may show rough shifts of up to several metres (as in the case of the cadastral area of Skoranov and Vlásenice u Makova).

The best-quality maps (Vinice v Podkrkonoší and Sedlatice) of the surveyed areas show a tiny average shift (0.36 and 0.37 m), a maximum shift ideally within the limiting deviation for boundary refinement, and a high frequency of sufficient-accuracy points (65% and 70% of the total number of surveyed points).

Comparative charts of all cadastre units (c. u.) follows.

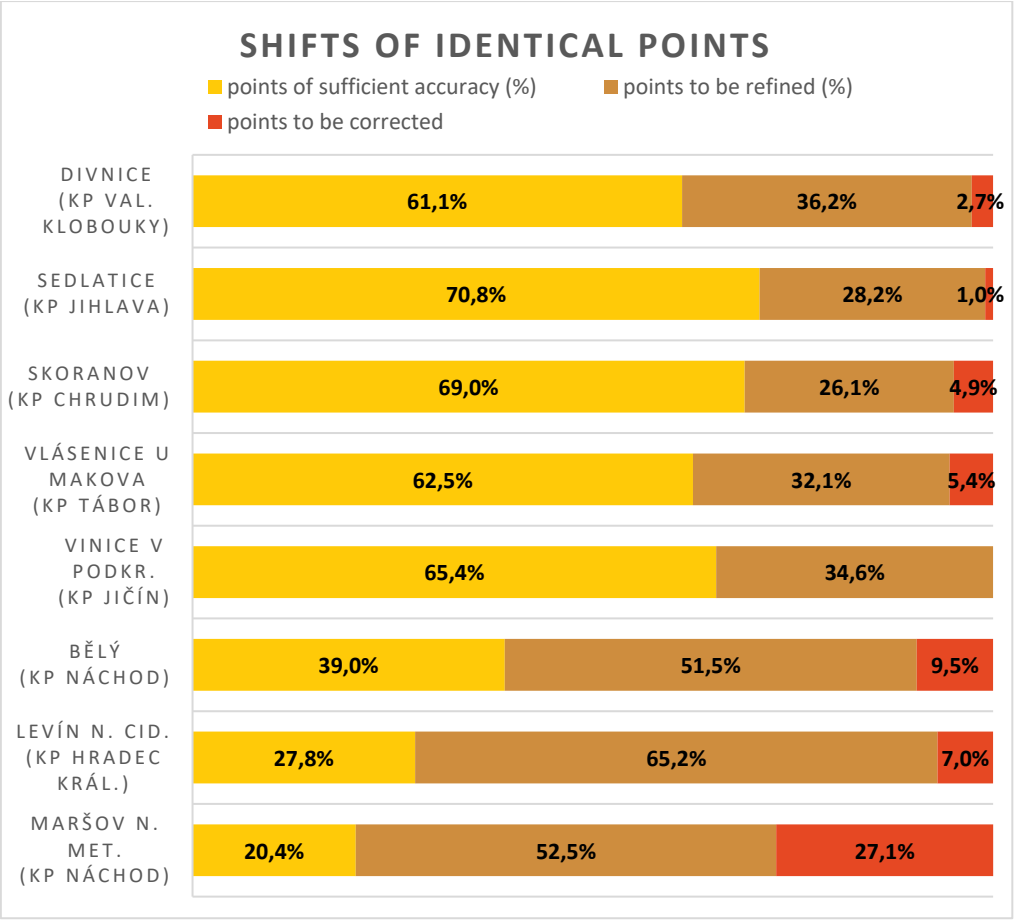

Fig. 4A – Comparative charts of the subject cadastral units

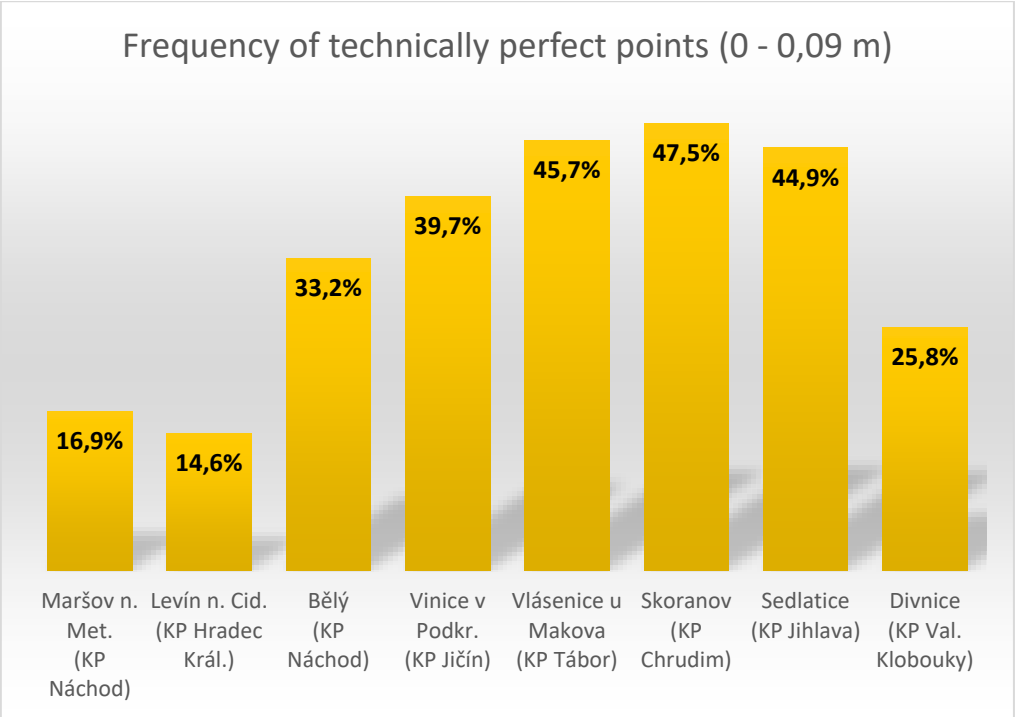

Fig. 4B – Comparative charts of the subject cadastral units

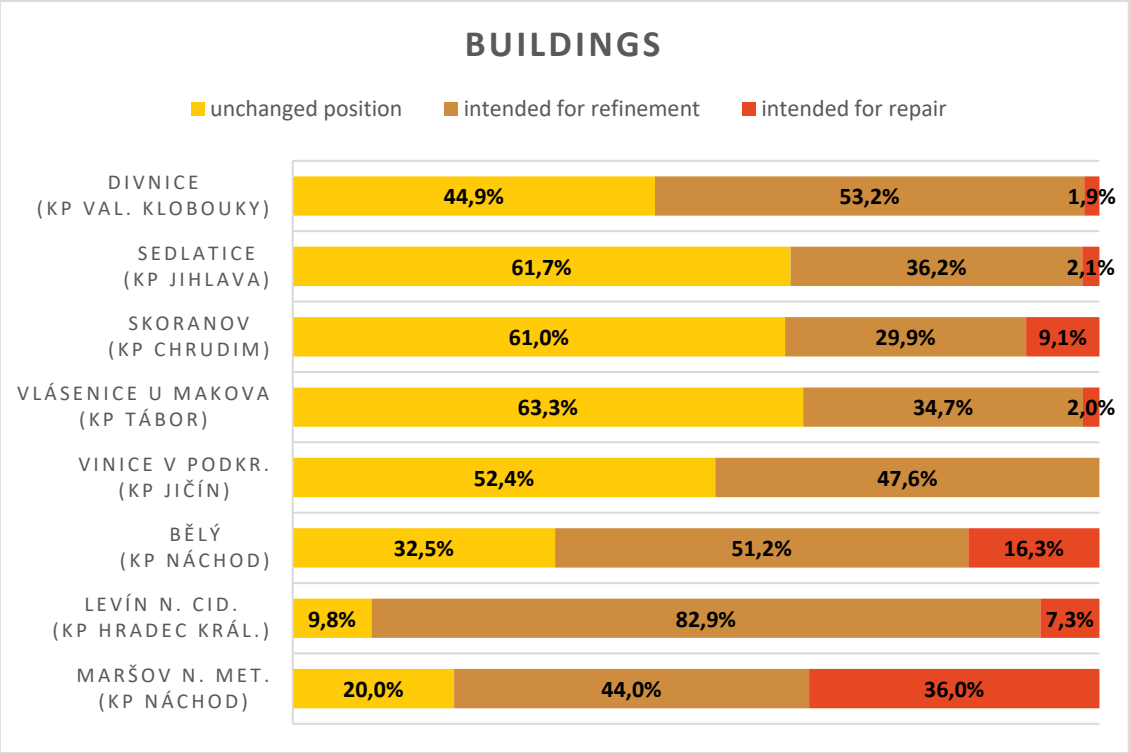

Fig. 4C – Comparative charts of the subject cadastral units

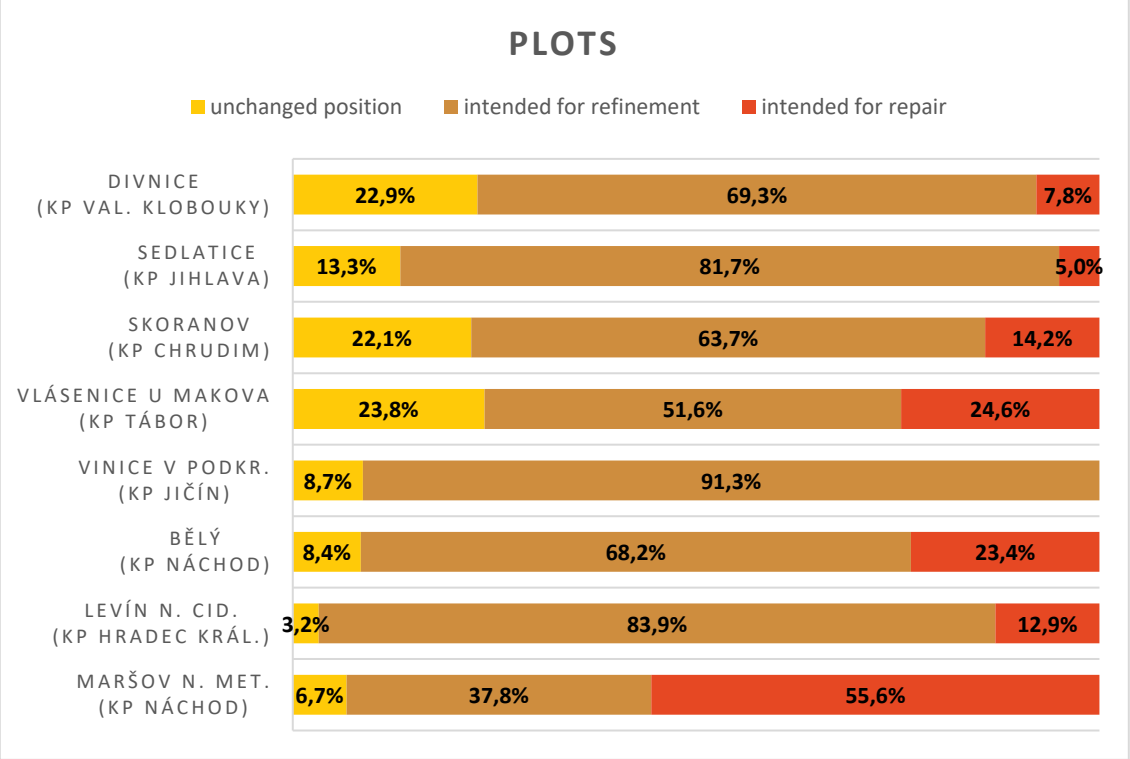

Fig. 4D – Comparative charts of the subject cadastral units

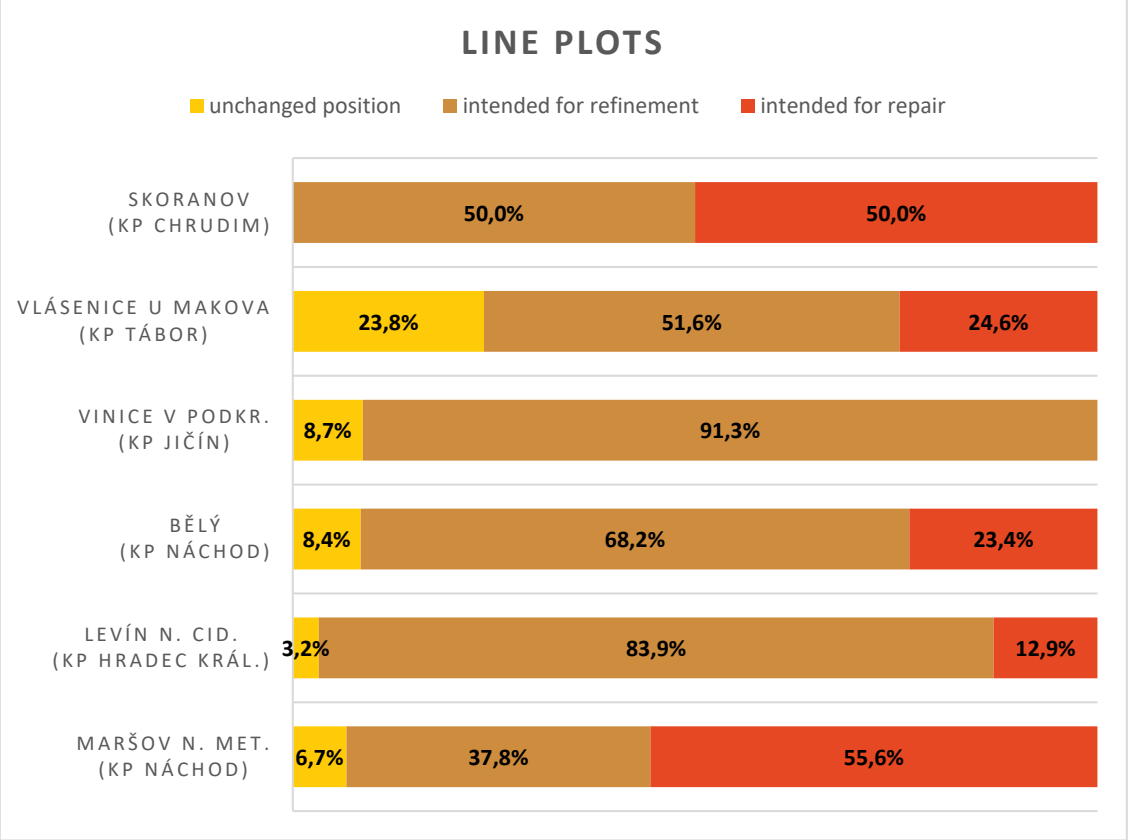

Fig. 4E – Comparative charts of the subject cadastral units

CONCLUSION

Testing of the displacements of detailed points before and after the mapping clearly confirmed that the digitised cadastral maps always show a certain number of detailed points whose displacement from the actual position is significantly greater than the distance that can be considered as a limiting condition for the refinement of the boundary by the owners. In particular, in areas that extend outside the built-up area of the municipality, this may involve up to one-third of the measured points. In such a location, it makes sense to carry out a new mapping as soon as possible. At the same time, however, the testing has surprisingly revealed a significant number of detailed points that, in the existing cadastral maps, meet the parameters for a detailed point with quality code 3 with a mean coordinate error of mxy = 0.14 m. In addition, a relatively large number of detailed points are technically perfect because their image on the map lies within 0 to 10 cm of the actual position. In these cases, we can already speak directly of a coincident point. The only reason for the change in its position in the new mapping is that the connection to the coordinate system is different, or the prism is attached to the fence post differently, etc.

Specific objects in the cadastral map are linear plots on one side and buildings on the other side. In the case of buildings, these are very often oversized buildings, which in the end only cause a shift in the map by insulation. Another widespread case is the exact position of the main building extended by a specific annexed part, and only the last group are twisted or positionally differently shifted buildings. These are always in the minority. Very often, one can also encounter a correctly depicted part of a building clearly visible from the road with one or more corners in the back part towards the yard or garden wrong, which logically could not be oriented when the digitised map was created and was therefore only vectorised using the refined grid of the previous land registration map.

In the case of linear parcels such as roads, paths, streams or rivers, whether they are located in the intravilane or extravilane, the cadastral map produced by the reworking of the stable cadastre is significantly inaccurate.

The following (Figures 5 - 10) are examples of the shift of the position of the objects under study in selected cadastral areas. The original cadastral map created by the reworking (KMD) is in grey, and the new digital cadastral map, after mapping used for accuracy testing, is in blue. Geostore V6 software was used for the analysis.

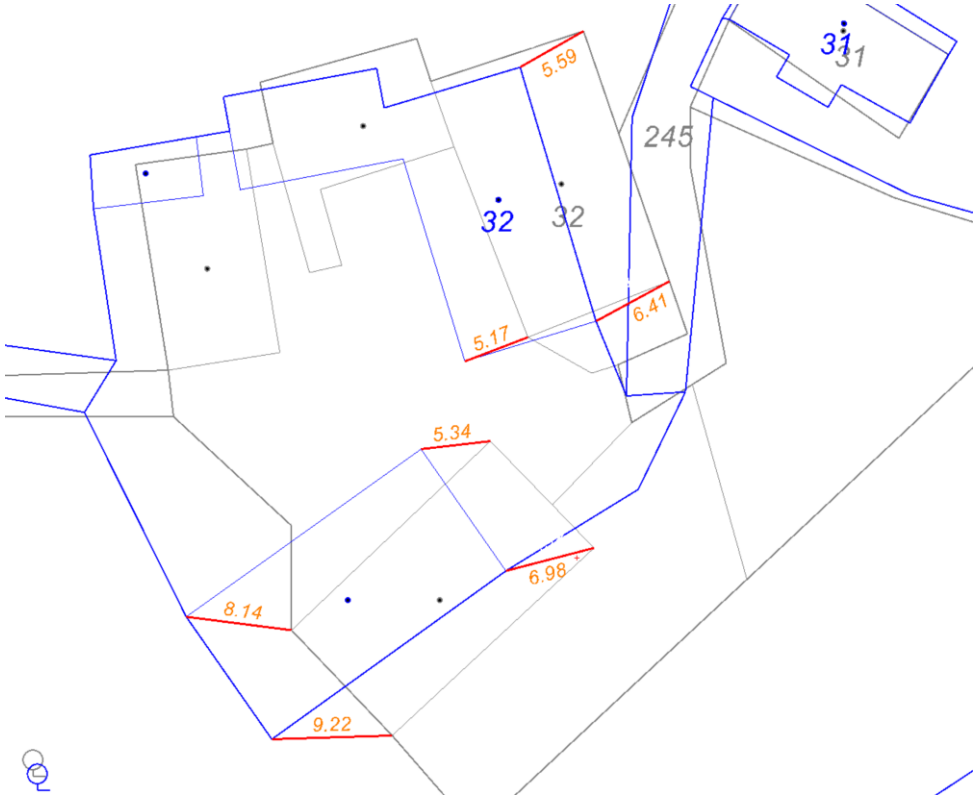

Fig. 5 – c. u. Maršov nad Metují – gross error of curled and displaced homestead in KMD map

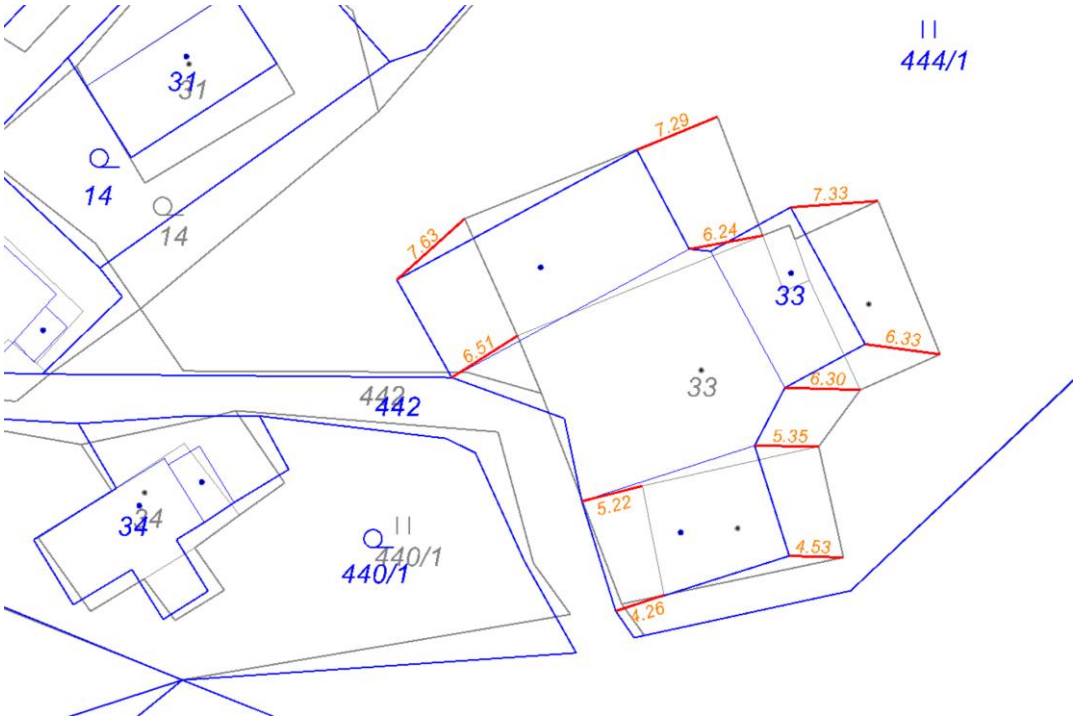

Fig. 6 – c. u. Bělý – an example of a twisted building and a gross error in position (No. 33)

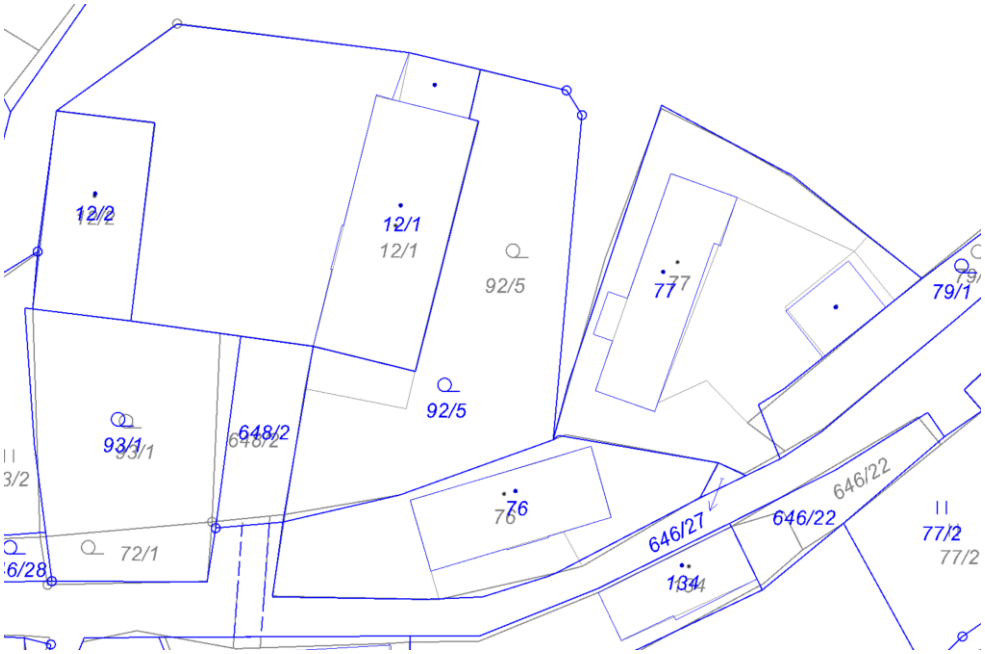

Fig. 7 – c. u. Bělý – positionally accurate sample of KMD map

Fig. 8 – c. u. Vinice v Podkrkonoší – positionally correct property boundaries in KMD

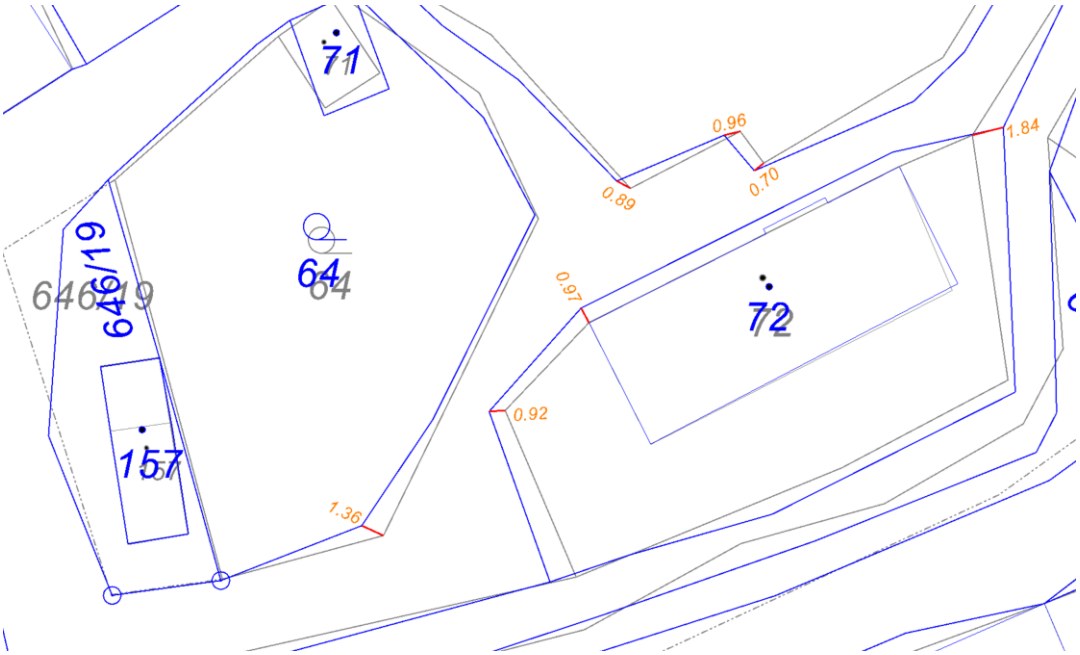

Fig. 9 – c. u. Bělý – boundary shifts within the "refinement" derogation

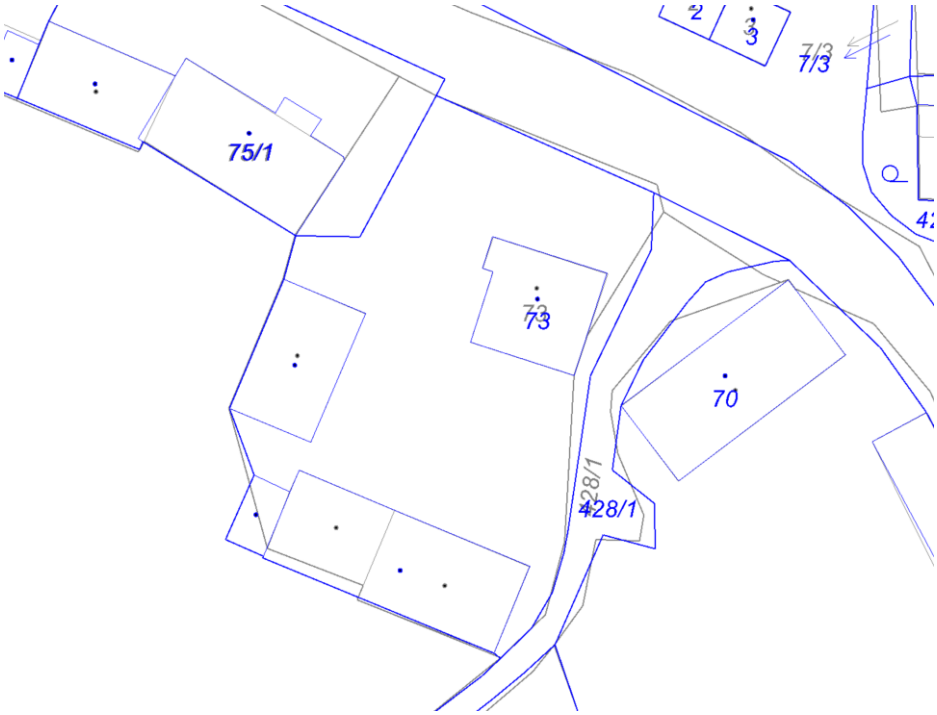

Fig. 10 – c. u. Vlásenice u Makova – correctly displayed buildings and error in the road rendition (No. 428/1)

DISCUSSION

This article deals with an unpublished topic and is an original topic for which there are no previous sources to build on. It is an innovative theme, and the aim is not only to provoke a discussion on the positional accuracy of digitised cadastral maps but, in particular, to approach the question of the need for new cadastral mapping from a technical point of view as a next step. The reason why the area of the positional accuracy of cadastral maps created by the redrawing from the stable cadastral system has been rarely addressed in the long term may be precisely because the maps are gradually being replaced by new mapping [10]. However, the pace of mapping is so slow that the use of these data is suggested for research into the actual positional accuracy of digitised cadastral maps.

REFERENCES

[1] Act on the Cadastre of Real Estate (Cadastral Act), No. 256/2013 Coll.

[2] Digitisation of cadastral maps and further procedure of cadastral register renewal (in Czech). Online. ČÚZK – Státní správa zeměměřictví a katastru. 2023. Available at: https://www.cuzk.cz/Katastr-nemovitosti/Digitalizace-a-vedeni-katastralnich-map/Digitalizace-katastralnich-map/Digitalizace-katastralnich-map.aspx [cit. 2024-05-25].

[3] Instructions for the Cadastral Register Restoration and Transfer, No. ČÚZK-01500/2015-22

[4] Outlook for the Activities of Cadastral Offices in the Field of Technical Data Management until 2030 (in Czech). Online. ČÚZK – Státní správa zeměměřictví a katastru. 2019. Available at: https://www.cuzk.cz/Katastr-nemovitosti/Digitalizace-a-vedeni-katastralnich-map/Vyhled-cinnosti-KU-v-oblasti-spravy-TU.aspx [cit. 2024-05-25].

[5] Navratil, G., Hafner, J. and D. Jilin (2010). Accuracy Determination for the Austrian Digital Cadastral Map (DKM). Fourth Croatian Congress on Cadastre with international participation –Proceedings. Zagreb, 2010. pp 171–181. ISBN 978-953-97081-8-2.

[6] Seidlová, A. and J. Chromčák (2017). Types of Cadastral Maps in Slovak Republic and Accuracy of the Land Area. RSP 2017 – XXVI R-S-P Seminar 2017 Theoretical Foundation of Civil Engineering. MATEC Web of Conferences, vol. 117. DOI: 10.1051/matecconf/201711700148.

[7] Karabin, M., Luczynski, R. and M. Karabin-Zych (2017). A Cadastral Map in Poland – the Proposal Based on Analysis of Cadastral Maps in Selected Countries. SGEM Conference Proceedings, Vol. 17, Issue 22. DOI: 10.5593/sgem2017/22/S09.002. ISSN 1314-2704.

[8] Decree on the Cadastre of Real Estate (Cadastral Decree), No. 357/2013 Coll.

[9] Services of the map server – cadastral map data (in Czech). Online. ČÚZK – Mapový server ČÚZK. 2023. Available at: https://services.cuzk.cz [cit. 2024-05-14].

[10] Overview of completed and planned operate renewals by mapping and revisions (in Czech). Online. ČÚZK – Státní správa zeměměřictví a katastru. 2020. Available at: https://services.cuzk.cz/prehled-mapovani-a-revize/mapovani-dokoncene [cit. 2024-05-14].

CIVIL ENGINEERING JOURNAL

Article no. 12

THE CIVIL ENGINEERING JOURNAL 2-2024

CONSTRUCTION METHODS AND APPLICATION OF TBM IN SHENGLI TUNNEL OF TIANSHAN MOUNTAIN UNDER POOR GEOLOGICAL CONDITIONS

Zhao Zhenping[1,2], Chen Jianxun[3], Geng Qi[4], Li Dong[1], Huang Dengxia[1], Luo Yanbin[3], Liu Weiwei[3], Mu Shaoping[4], Peter Anesu Kanhenga[4] and Wu Teligen[1]

1. *CCCC Central-South Engineering Company, LTD, Changsha, Hunan 410114, China, email: 230188190@seu.edu.cn*
2. *School of Civil Engineering, Southeast University, Nanjing, Jiangsu 211189, China*
3. *Highway School, Chang'an University, Xi'an, Shaan Xi 710064, China*
4. *School of Construction Machinery, Chang'an University, Xi'an, Shaan Xi 710064, China*

ABSTRACT

When a tunnel boring machine (TBM) excavates in poor geological conditions like fracture zones, soft rock with high ground stress, hard rock with high ground stress, and water inrush ground, severe problems such as surrounding rock collapse, convergence, rock burst and water and mud outburst are usually encountered. These problems existed in the Tianshan Shengli Tunnel project in Xinjiang, China. Several methods and techniques were adopted to reduce the construction risks and improve the construction efficiency. The seismic wave reflection long-distance geological forecasting method was employed to forecast and predict these adverse geological conditions. The pre-reinforcement construction method was employed on the surrounding broken rocks in front of the tunnel face to lower the risks of tunnel collapse and machine jamming. A combined steel arch was applied to prevent tunnel arch collapse. An artificial cap method was applied to prevent the jamming caused by high-ground stress soft rock. Measures such as spraying water on the tunnel face and drilling stress holes were employed to prevent rock bursts caused by high-ground stress in hard rock. Implementing the advanced pipe shed method during water influx, sudden mud, and other working conditions reduced the risk of groundwater damage to equipment and lowered risks to personnel safety. The successful application of these techniques can provide a reference for TBM tunnel construction in similar ground conditions.

KEYWORDS

TBM, Poor geology, Geological forecasting, Tunnel face pre-reinforcement, Advanced pipe shed method

INTRODUCTION

In recent years, the Full-face Tunnel Boring Machine (TBM) has been widely used for hard rock tunnel construction. A Full-Face Tunnel Boring Machine (TBM) is an engineering device that crushes rock by rotating and pushing the cutter head. It excavates the entire tunnel cross-section in a single pass and has other advantages, such as high construction speed and reliable quality, to mention a few. Recently, it has been popular in highway, railroad, hydraulic tunnels, and other tunneling projects [1].

TBM construction requires strict geological conditions, the machine is sensitive to surrounding rock conditions and is often prone to low tunneling efficiency [2, 3]. During tunnel excavation, unfavorable geological conditions can be encountered, such as fault fracture zones, high-stress soft rock, rock bursts, and water and mud intrusions. More severe problems such as

surrounding rock collapse, convergence, rock burst, and water and mud outbursts are usually encountered, resulting in a hazardous and difficult construction process heavily affecting TBM efficiency.

Construction measures under a fault fracture zone:

Addressing the issue of tunnel collapse constructed under a fault fracture zone, Chen et al. [4] put forward the collapse remediation program of "chemical grouting filling in collapsed cavities + chemical grouting reinforcing in loose bodies + spraying anchors supporting + dense arch supporting + overrunning grouting reinforcing". Yang et al. [5] proposed measures to prevent landslides: setting up meandering guide pits, pre-strengthening strata, increasing support strength, optimizing construction methods, and strengthening monitoring and measurement. Longlong et al. [6] used surface grouting, grouting inside the cave, and pipe shed to address landslide issues. Tong et al. [7] employed surface directional holes to improve the surrounding rock conditions, enabling smooth excavation through the fault fracture zone. Chen et al. [8] proposed a design method of pipe shed support parameters to ensure the safe construction of the tunnel and rock stability of the tunnel face in the fault fracture zone. The above studies mainly address the issue of tunnel collapse under a fault fracture zone by grouting reinforcement, strengthening support, and pipe shed support, to mention a few. Further research is needed on forecasting and predicting the surrounding rock conditions in front of the tunnel face and exploring the efficacy of using combined steel arches to mitigate landslides.

Construction measures under high-stress soft rock conditions:

To address the issue of soft rock deformation, enhancing the stiffness of initial support is crucial in controlling significant deformations in high-stress soft rock tunnels [9]. Liu et al. [10] conducted a systematic analysis of the failure mechanism of short anchor support in high-ground stress soft rock tunnels and demonstrated the necessity of lengthening the length of the anchor in high-stress soft rock tunnels. Wang et al. [11] proposed a design scheme based on active support with the combination of prestressed long and short anchor ropes + W-type steel belt + flexible fiber mesh, effectively controlling the deformation of surrounding rock. To mitigate initial support deformation, elevation arch bulging, and secondary lining compression collapse during the construction of high-stress soft rock tunnels, Zheng et al. [12] put forward the measures of elevation arch curvature optimization - early support double-layer steel frame - secondary lining reinforced lining - the perimeter of the hole limiting anchors and so on. Han et al. [13] searched for the optimal reserved deformation through the curvature of the characteristic curve for stress relief. The above research mainly controls the deformation of the surrounding rock by enhancing the support stiffness, and reserves deformation amount to release stress, controlling the release trend of deformation energy of the surrounding rock. However, there is relatively little research on solutions to the occurrence of jamming when there is significant deformation in the surrounding rock in front of the face.

Construction measures under high-ground stress hard rock conditions:

After the occurrence of a strong rock burst, the main beam of the tunnel boring machine got buried, and the construction progress was delayed [14]. Li et al. [15] set up reasonable spacing of tunnels to reduce the probability of rock bursts and used microseismic monitoring to assess the risk of rock bursts. In the slight rock burst and severe rock burst sections, Wang et al. [16] and He et al., [17] used water sprinkling or flooding and stress holes for stress relief, respectively. Li et al. [18] used steel pipe plates instead of steel arch support to improve the initial support operation efficiency and support capacity in the section prone to intense rock bursts and installed the whole annular steel pipe plate in the shield. The above research prevents rock bursts by setting tunnel spacing and microseismic detection and uses methods such as watering and stress holes to weaken the damage caused by rock bursts. However, there is relatively little research on the transformation of TBM water spraying systems under rock burst conditions.

Construction measures under the conditions of water and mud outbursts:

Water outbursts in the tunnel occur near the main channel of groundwater, and the magnitude of the water outburst is significantly related to the amount of rainfall [19]. Shi et al. [20] carried out

overrunning small conduit grouting and secondary grouting at the tunnel vault and precise grouting at the tunnel foot and lower part of the tunnel, which can effectively reduce the occurrence of tunnel disasters, such as water surge and mud outbursts. To mitigate water and mud outbursts, Liu et al. [21] constructed drainage channels consisting of drainage wells and connecting channels to make pressurized karst water flow to the surface by itself to address water gushing and mud bursting. Lang et al. [22] proposed a water discharge treatment plan of "temporarily shelving the inclined well, high-pressure water discharge in the main cave work area, implementing in phases, and steadily approaching the head of the inclined well" to realize the safe discharge of the water in the inclined well. The above studies mainly control water and mud outbursts by grouting and plugging reinforcement and setting up the drainage. However, fewer researchers have used the over-advance pipe shed method to deal with surging water and mud-surge conditions.

This paper uses the Tianshan Shengli Tunnel project in Xinjiang, China, as a case study to address challenges encountered during construction in adverse geological conditions. It proposes construction measures such as over-advance geological forecast, pre-reinforcement construction method for tunnel face, reinforcement construction methods for the surrounding rock at the TBM gripper shoe, over-advance pipe shed method and the artificial cap method, and so on. These measures aim to achieve a holistic approach to prevention before, during, and after construction, ensuring both construction quality and the safety of personnel and equipment while enhancing construction efficiency.

OVERVIEW OF THE PROJECT AND MAJOR ISSUES

Wuwei Expressway is an integral part of China's highway G0711 Urumqi to Ruoqiang and Xinjiang across the Tianshan Mountains, connecting the north and south of Xinjiang's transportation trunk line.

Among them, the Tianshan Shengli Tunnel is the control project of Wuwei Expressway; the tunnel is 22105m long, the maximum depth is about 1150m, the import elevation is about 2767m, and the export elevation is about 2900m. The technical standard is designed according to a two-way, four-lane highway design at 100km/h. The tunnel is located near the No.1 glacier of Tianshan Mountain.

The tunnel is located in the Tianshan No.1 glacier. the tunnel has 16 fracture zones, fracture zones affect a length of 2000m, the core section length of 768m, rock burst section length of 3940m. The surrounding terrain is complex and variable, the tunnel geologic cross-section is shown in Figure 1. Water-rich fault fracture zone, soft rock with high ground stress, hard rock with high ground stress, and water inrush ground are the unique poor geology of this tunnel, severe problems such as surrounding rock collapse, convergence, rock burst, and water and mud outbursts are usually encountered.

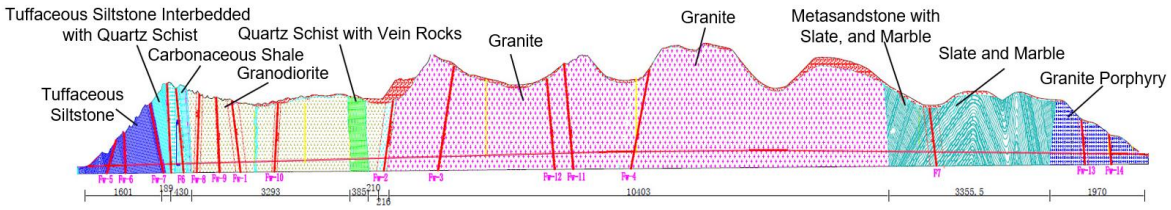

Fig. 1 - Geological longitudinal section of the tunnel

TBM CONSTRUCTION TECHNOLOGY AND APPLICATION IN FAULT FRACTURE ZONE

Long-range geologic forecasting method for seismic wave reflection

The seismic wave reflection long-distance geologic prediction method is used to detect the exact condition of the strata in front of the TBM face. This technique utilizes the seismic reflection

wave and surround wave to detect the geological conditions in front of the tunnel face. During the propagation of the seismic wave generated by the source to the tunnel front, the rock's relatively large acoustic impedance interfaces will generate reflected waves, and the relatively small acoustic impedance interfaces will generate wrap-around waves, collectively called seismic echo waves. The equipment collects seismic echo data from the tunnel's surrounding rock. The interface position, spatial distribution, polarity, and energy of the echo are extracted through the professional processing system, and combined with the comprehensive analysis of the tunnel geologic survey data, the purpose of the tunnel geologic advance prediction is realized.

Taking the mileage pile number PK76+108~PK76+208 of the Tianshan Shengli Tunnel project in Xinjiang, China, as an example, this project adopts the TGP (Tunnel Geology Prediction) Tunnel Geology Advance Prediction System for tunnel geology prediction work. The system is developed by the Beijing Institute of Hydropower Physical Exploration. Through the work of over-advance geological prediction, the three-component original record map of seismic wave (as shown in Fig. 2(a)) and the three-dimensional spatial cross-section scanning result map (as shown in Fig.2(b)(c)(d)) are obtained.

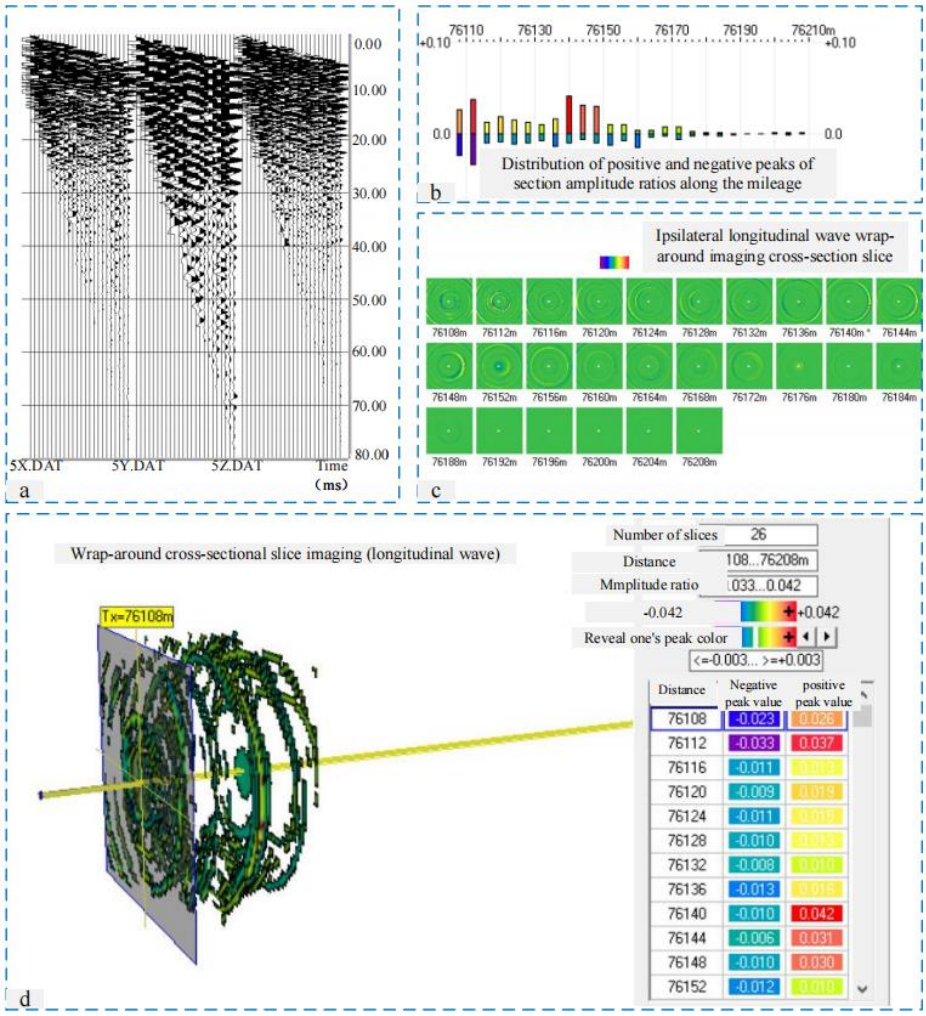

Fig. 2 (a) - The three-component original record map of the seismic wave;(b), (c), (d) the three-dimensional spatial cross-section scanning result map

The construction method of grouting pre-reinforcement on the tunnel face

According to the results of the over-advanced geological forecast and prediction, the fault fracture zone in front of the tunnel face is pre-reinforced in advance, and then the TBM will dig

through it, as shown in Figure 3(a)(b). The construction method of grouting pre-reinforcement on the face can also be used in the construction of a water-rich subgrade.

The Manual handheld YT28-type hand air drilling rig drilled and grouted holes at the gap between the tool and the cutter plate. In the front of the tunnel face, twenty-two deep grouting holes were strategically arranged, each with a depth of 10m, as shown in Figure 3(c)(d). The grouting pipe adopts D25 fibreglass anchors with grouting holes. In situations where the surrounding rock is broken, and hole formation is difficult to achieve, the self-entry fibreglass anchors are used. The grouting material adopts chemical grouting, cement water glass slurry, and cement slurry. The initial grouting pressure ranges from 1.2-1.5 times hydrostatic pressure, and the inal pressure is 2-3 times hydrostatic pressure. The length of the grouting hole is about 4m, and the length of each cycle of grouting is 4m; 2m is excavated after the completion of grouting, and 2m is reserved without excavation for the next cycle of lapping.

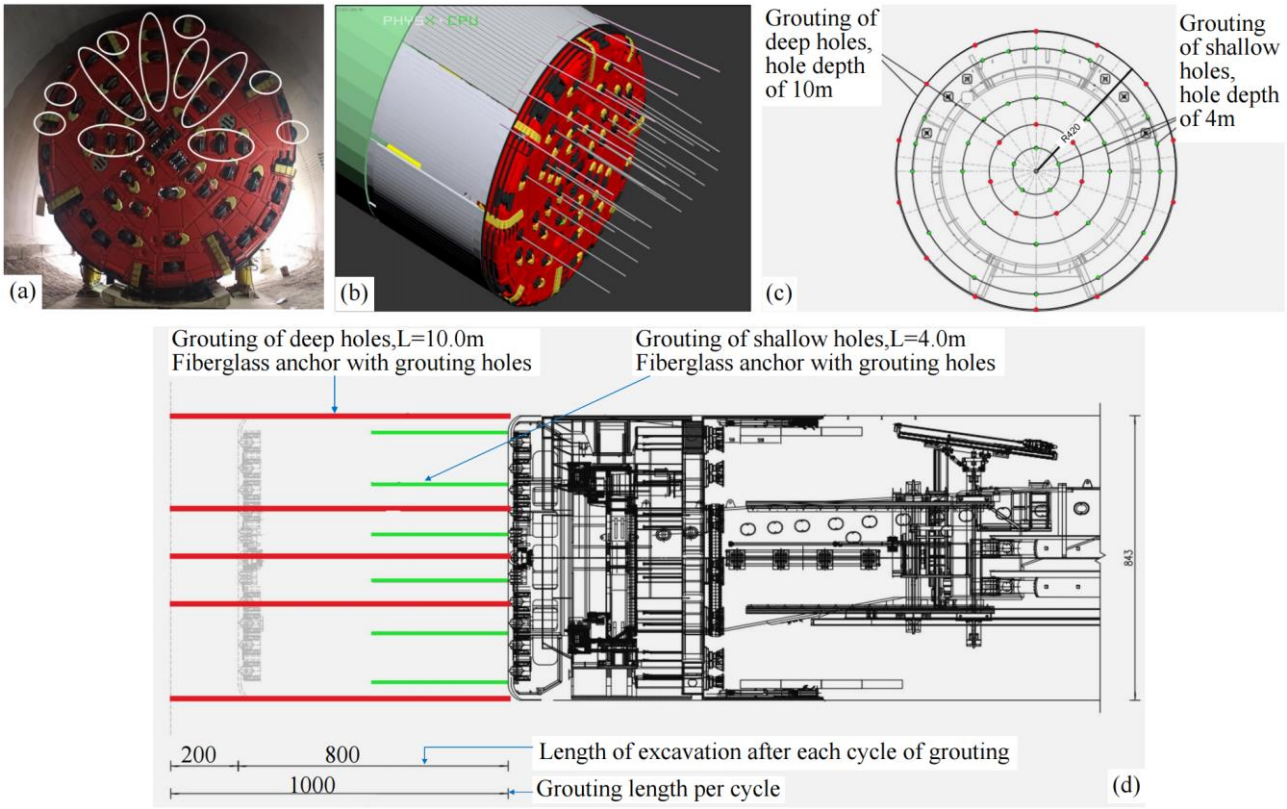

Fig. 3 (a)(b) - Schematic diagram of grouting on tunnel face;(c), (d) design drawing of overtopping grouting on tunnel face

The construction method for reinforcement of surrounding rock at TBM gripper shoe

In the event of a localized slump in the tunnel sidewall, adjustments are made to the support force of the TBM gripper shoe to alleviate pressure on the surrounding rock. Concurrently, the thrust and propulsion speed of the TBM is reduced accordingly, allowing the TBM to pass through the slumped section without stopping. In cases where the sidewall is relatively weak, the TBM gripper shoe is padded with sleepers to increase the grounding area, before proceeding. If the surrounding rock strength at the support boots is insufficient to provide thrust, a YT28 hand air drilling rig is deployed to drill holes at the support boots. The reinforcement method is φ42mm×3.0m grouting small conduit with a longitudinal and transverse spacing of 120cm, as shown in Figure 4. The grouting slurry is cement slurry. Cement grouting materials mainly include: cement, water, admixtures, admixtures, etc. Its water-cement ratio is generally 0.8:1 and 0.6 (or 0.5):1. The cement

strength grade of grouting should not be less than P42.5, and acid-resistant cement should be used for harmful groundwater caverns. The TBM water supply system is used for water supply, the water quality meets the requirements of drinking water, and the temperature of the slurry mixing water shall not be higher than 40 ℃. For the section with complex geological conditions, sand, fly ash and other admixtures can be mixed into the cement slurry. The cement grouting equipment adopts 4 sets of double-barrel vertical mortar high-speed mixers (2 sets standby), 4 sets of 250/50 grouting pumps (2 sets of standby), and 1 set of DXHB-10II. multi-function fine stone concrete pumps. The 250/50 grouting pump is a multi-cylinder plunger grouting pump with a maximum working pressure of 5Mpa. The grouting equipment is arranged near the TBM post-supporting and connecting bridges.

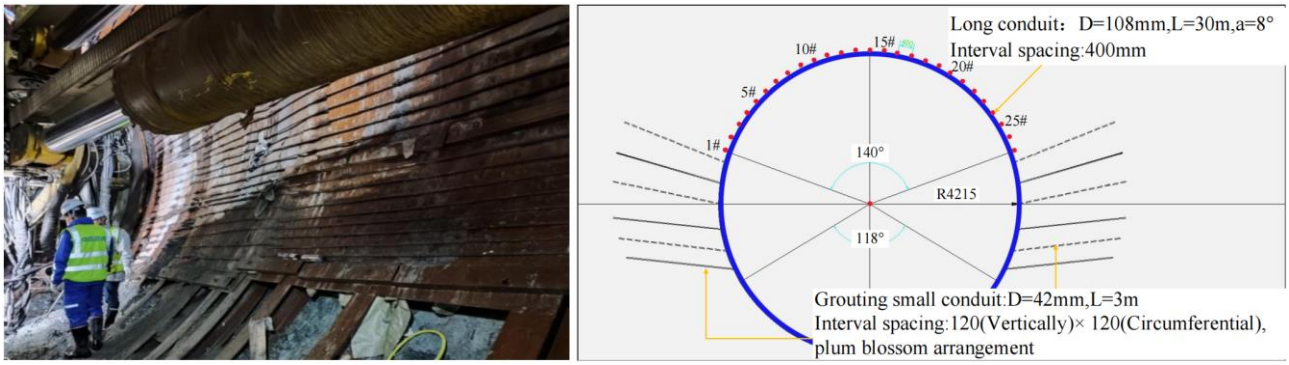

Fig. – 4 Construction site diagram and schematic diagram of the surrounding rock reinforcement at the TBM gripper shoe

Construction measures for collapsing rock surrounding the arch based on combined steel arches

In cases where a substantial amount of slag removal is required after the collapse of a large amount of rock, and the duration of slag removal is prolonged, it becomes highly unfavorable for TBM to pass through the fault fragmentation zone. To address this, a combined steel arch is employed to intercept the slag and rock debris from the collapsed body, ensuring the swift and safe passage of the TBM. , as shown in the figure (as shown in Figure 5(a)). The combined steel arch is symmetrically installed from bottom to top; the specific sequence is bottom pipe piece → side pipe piece → top pipe piece (the first ring and the second ring), and the subsequent rings are assembled in the order of top pipe piece → side pipe piece → bottom pipe piece. After the first and second rings are assembled, to enhance the stability, two locking anchor rods are set at the arch foot position of the side pipe pieces on both sides, and the locking anchor rods adopt 3m long φ22 drug coil anchor rods. After the combined steel arch is positioned, 8cm thick steel plate pads are installed to adhere to the rock surface, and the auxiliary push cylinder of the assembling machine tightens the steel arch, connecting the transverse and circumferential devices, respectively, to form a whole. Table 1 shows the parameters of each component of the steel arch, and Figure 5(c) shows the scheme of the combined steel arch.

On the exterior of the top pipe piece of the combined steel arch, several holes are reserved at intervals of 5m from high to low. These holes are designated for burying the exhaust pipe, blowing and filling the buffer layer pipe, and concrete backfill pipe, as shown in Figure 5(b). The exterior of the hole pipe is sealed with geotextile to prevent blocking of the hole pipe when spraying concrete. The grouting pipe should be inserted into the highest point of the collapsed cavity body, and the

concrete transfer pump is used to fill C25 fine stone concrete or fibre concrete into the collapsed cavity body from the reserved grouting holes, as shown in Figure 5(d).

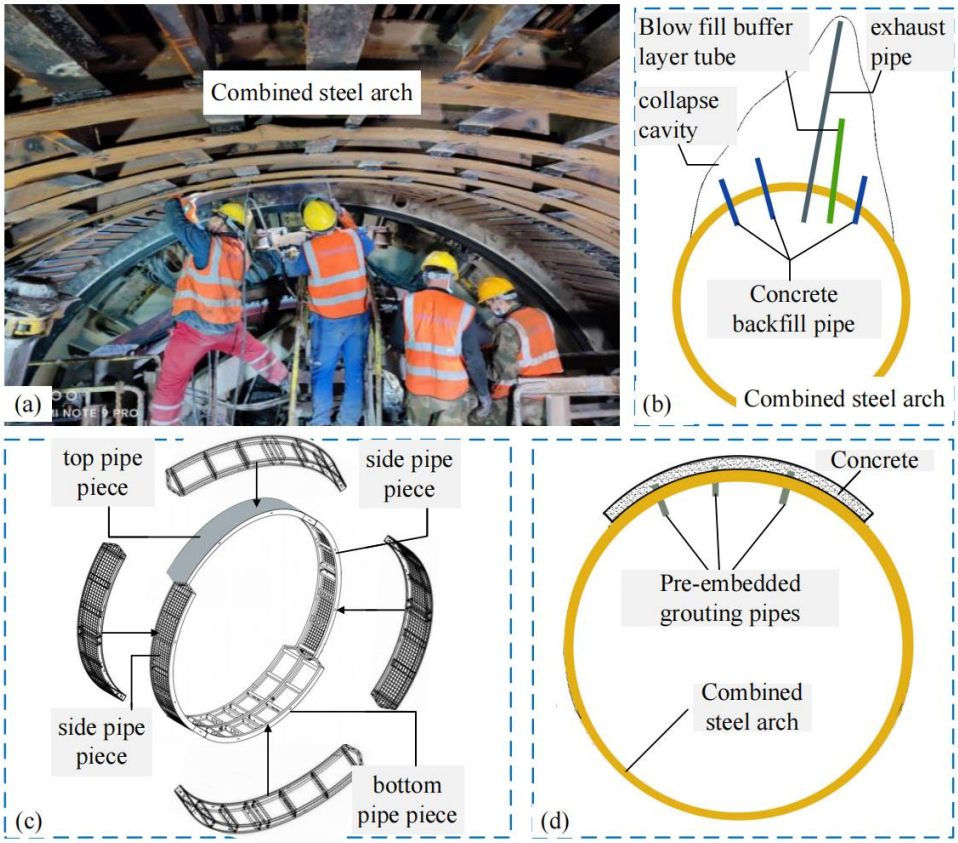

Fig. 5 - (a) Combined steel arch construction site; (b) layout of pre-buried pipes ;(c) combined steel arch construction program diagram; (d) concrete backfill schematic

Tab. 1 - Parameters of each component of combined steel arch

Item	Makeup	Quantity (Ring)	Weight (Kg)	Segment arc length (m)
Top pipe piece	Annular rib: 20b channel steel Longitudinal stiffener: I20 I-beam Outside: 10mm steel plate	1	1006.24	6.46m/ piece
Side pipe piece	Annular rib: 20b channel steel Longitudinal stiffener: I20 I-beam Outside: A10 steel mesh	2	626.04	6.46m/ piece
Bottom pipe piece	Annular rib: 20b channel steel Longitudinal stiffener: I20 I-beam, removable	1	569.62	6.46m/ piece

TBM CONSTRUCTION TECHNOLOGY AND APPLICATION IN HIGH-GROUND STRESS SOFT ROCK SECTION

Measures to cope with large deformations high-ground stress in soft rock

When surrounding rock convergence deformation is severe, the TBM's expansion function is utilized to increase the excavation diameter through the overbreak cutter, which helps increase the amount of reserved deformation. Once the surrounding rock emerges from the shield, timely initial support is applied. Measures such as encrypting steel arch, spraying steel fiber concrete, and applying anchor cables strengthen the support. In instances where the bearing capacity of the tunnel wall is insufficient to provide enough counterforce to the support boots, a combination of spray anchor network, steel arch, and concrete joint support is utilized to reinforce the parts of the cave wall before excavation. When encountering significant and rapid convergence deformation in the soft surrounding rock, leading to the TBM shield becoming stuck, the thrust of the TBM digging is increased. Waste oil and other lubricants are also injected into the shield to reduce friction. Immediate application of the initial support system follows after passing through the affected area.

TBM drifting solution under deformed soft rock

When there is a significant deformation of the surrounding rock in front of the tunnel face, which makes the TBM prone to jamming risk, the "artificial cap method" is adopted to over-excavate from the position of the cutter plate. The excavation adopts the method of reserving the core soil ring through artificial division excavation, and TBM digs the core soil. TBM lagged behind the manual excavation surface to shorten the manual slagging distance. The TBM begins digging 3m behind the manual excavation surface and excavates forward manually. When the manual excavation encounters surrounding broken rock, which affects construction safety, it is reinforced by overrunning small conduits or chemical grouting before excavation.

Among them, the "artificial hat method" refers to further expanding the excavation scope based on a small guide hole and expanding the space radially in the range of 150°～220° from the upper center of a small guide hole circle. To facilitate manual work, the outer radial direction of the pipe sheet or shield shell is generally taken as 1500 mm~1700 mm. Support parameters are selected: System anchor L=3m/Φ22@1.0m×0.5m. The H150 steel arch is made of single or multi-layer steel sections with a spacing of @0.5m. The longitudinal connection of the steel arch is made of the U12 channel steel with a pitch of @1.0m. Reinforcing steel mesh with double layer Φ10@10cm×10cm. The lining is made of C40 concrete with a thickness of 30cm.

TBM CONSTRUCTION TECHNOLOGY AND APPLICATION IN HIGH-GROUND STRESS HARD ROCK SECTION

Modification of water spray system for TBM cutter under high-ground stress hard rock conditions

Construction under high-ground stress hard rock sections is prone to rock explosion, threatening the safety of construction personnel and equipment. To mitigate this risk, the TBM cutter spray system uses water to soften the surrounding rock. However, the original TBM cutter spray system has drawbacks, such as a high failure rate of rotary joints, prone-to-clog nozzles, and limited water spray volume. As a result, the cutter spray system was upgraded to a system that is less susceptible to failures and has a higher water output capacity.

The use of a single pipe pump to the blade water spray system water supply, with an 11KW booster pump from the tank direct water supply (as shown in Figure 6(a)(b)), the water output from the original 120L per minute into the current 380L per minute. 1.5-inch water supply pipe will be thickened for the original 2-inch high-pressure water pipe, give up the original blade water spray nozzle and rotary joints from the back of the blade to install a spray system on the blade for the full-coverage spraying, as shown in the figure. After the transformation, the cutter spray system water

spray volume increased, effectively reducing the risk of rock explosion, and the water supply pipe blockage is reduced, the cooling makes the tool wear and tear, reducing the delay caused by the failure of the downtime, and improve the construction efficiency.

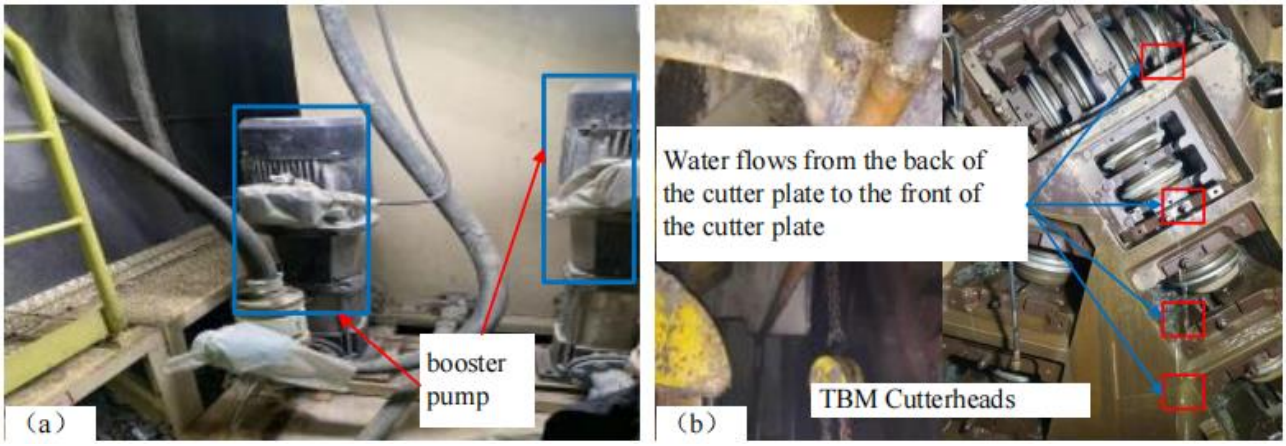

Fig. 6 - (a) Add a booster pump;(b) TBM cutter head water spray system retrofitted to the back of the cutter head

Construction measures for rock burst

To reduce the risk of rock explosions, the first countermeasure involves utilizing a cutter spray system and high-pressure water pipe behind the shield to spray water and soften the peripheral rock (as depicted in Figure 7(a)). This action facilitates stress release and adjustment. Subsequently, within the 120° arch range, H150 steel arches are employed along with Φ22 steel rows to reinforce joint support (as shown in Figure 7(b)). The longitudinal spacing of the arches is set at 0.9m. Finally, steel fiber concrete is sprayed with a thickness of 15cm (as illustrated in Figure 7(c)). The second measure involves preemptively drilling stress-release holes before excavation and then drilling radial stress-release holes after excavation. These stress-release holes are drilled perpendicular to the rock wall (as shown in Figure 7(d)).

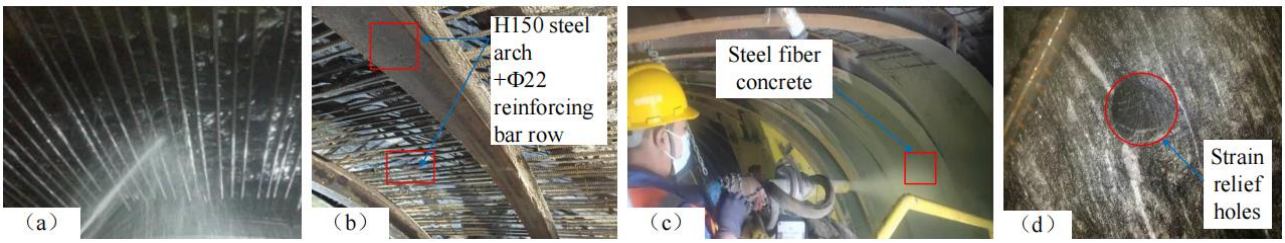

Fig. – 7 (a) Water jetting to soften the surrounding rock;(b) Combined support of H150 steel arches and Φ22 reinforcing bar row; (d) Strain relief holes

TBM CONSTRUCTION TECHNOLOGY AND APPLICATION IN WATER-SURGE AND MUD-SURGE SECTION

Construction Measures for Surging Water and Mud Surging Section

Construction of a small-scale water-surge section: water seepage from surrounding rock is in the form of dripping and linear seepage, while the TBM continues to excavate normally. In the process of digging, the anchor drilling machine that comes with the TBM is used to set up drainage holes at the water outlet, bury conduits to drain water and set up blind ditches or water cut-off rings if the event of poor water conduction.

Construction of large-scale water influx section**:** The water influx flow ahead of the tunnel face is assessed using overrunning geological forecasting methods. If the bottom of the tunnel does not meet the operating conditions, excavation must stop. Overrunning conduits and grouting are employed to block and treat the influx. Additionally, temporary high-power submersible pumps and pipelines are installed to pump water away from the TBM, ensuring at least a 50m area is adequately supported. If there is no substantial improvement in the surrounding rock conditions at the tunnel face despite these measures, the TBM's equipment is utilized to reinforce the tunnel face with overrunning grouting. If conditions still do not improve, the cutter is retracted, and access to the tunnel face is gained from the shield by drilling winding holes. Subsequently, the overrunning pipe shed method is implemented to support and block water influx.

Sudden mud section construction: A pre-predictive geological forecast is conducted to gain an in-depth understanding of the engineering geological conditions. This helps detect the geological conditions ahead of the tunnel face. To prevent the mud influx from compromising the safety of the TBM equipment and personnel, the pre-pre-pipe shed grouting method is adopted to pre-strengthen the surrounding rock before excavation.

Construction measures of over-advance pipe shed method in water surging and mud surging sections

The over-advance pipe shed method is employed to support, grout, and reinforce the surrounding rock while also plugging water influx and mud bursts. A schematic overrun pipe shed reinforcement diagram, is shown in Figure 8(a).

The over-advance pipe shed adopts L=25m, Φ=108mm, δ=6mm seamless steel pipe with a section length of 2m (matching with the drill pipe of the overrun drilling rig), and the joints are connected by wire fasteners with a wire fastener length of 15cm, and D=6mm grouting holes are drilled on the steel pipe with a longitudinal spacing of 15cm, and a plum blossom type of holes, and the length of the flower pipe section is 15.25m, as shown in Figure 8(b)

Within the 100° tunnel arch, the circular spacing is set at 40cm, with an external insertion angle of 8°. A total of 19 holes are arranged, as illustrated in Figure 8(c)(d). Following the completion of each cycle of pipe shed construction, the excavation proceeds by 10.1 meters. The sequence of pipe shed construction is from bottom to top, with a long steel pipe installed after drilling each hole.

Given the surrounding rock conditions of the water surge and mud break section, the grouting process adopts chemical grouting. Chemical grouting material mainly refers to polyurethane (polyurethane: PM-200, composed of white and black materials). The technical parameters of chemical grouting materials are shown in Table 2. The grouting equipment adopts a YZB-200/13 double-group material pump and 3SNS high-pressure grouting machine, which is simple in process, easy to clean for operation, convenient for transportation, suitable for multiple people to operate separately, which is conducive to speed up the progress of the project.

Initially, the grouting pressure is 1.2-1.5 times the static water pressure, and the termination pressure is 2-3 times the static water pressure. According to the actual situation of the site, the grouting pressure will be increased to the maximum allowable pressure to ensure the density of the grouting and increase the effective diffusion range. The grouting process is allowed to continue without interruption.

Tab. 2 - Technical parameters of chemical grouting materials

Product characteristics	Component A (Bevedol WF)	Component B (Bevedan)
Appearance	Light yellow liquid	Dark brown liquid
Viscosity (23±2℃)/mPa.s	200~400	200~400
Specific gravity (23±2℃) kg/m3	1020±10	1230±30
Use ratio (volume ratio)	1:1	
Full curing time (23±2℃)/S	40±5	
Foaming property	It is not foaming in itself and will react to foaming in contact with water	
Maximum compressive strength /MPa	60~80	
Maximum tensile strength /MPa	>10	
Maximum bond strength /MPa	>5	
Flame retardant property	Non-flame retardant	

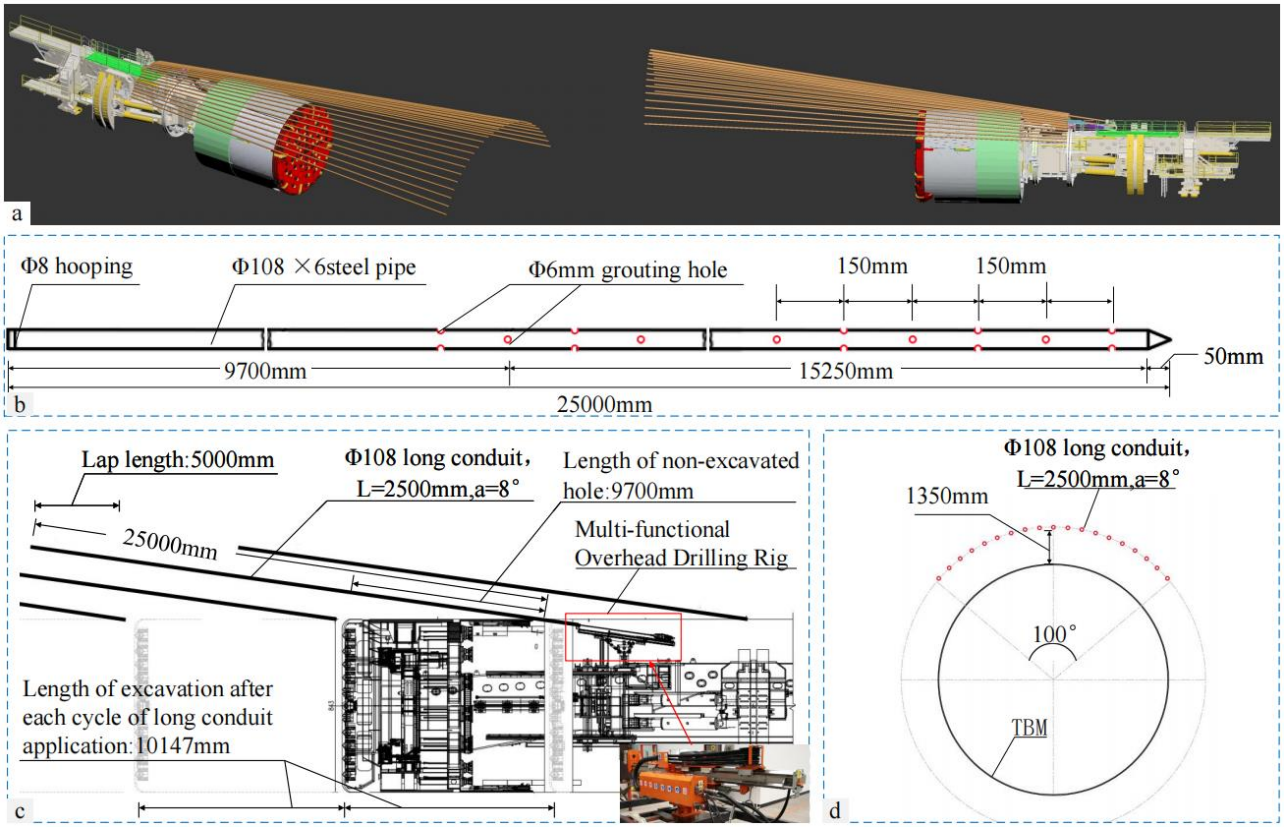

Fig. 8 - (a) Schematic diagram of over-advance pipe shed reinforcement;(b) Steel pipe sample drawing;(c) Section drawing of pipe shed reinforcement;(d) Sectional view of the upper 100 ° range of the pipe shed reinforcement cutter plate

CONCLUSIONS AND DISCUSSION

When the TBM encounters a fault fracture zone, the seismic wave reflection long-distance geological forecast method is employed to forecast and predict the condition of the surrounding rock ahead of the tunnel face. Based on the over-advanced geological forecast and prediction results, the fault fracture zone in front of the tunnel face is pre-reinforced. If the strength of the surrounding rock at the TBM support boot is insufficient to provide thrust, the rock at the support boot is reinforced by drilling and grouting. In cases where a large amount of slag removal is required and the time for slag removal is prolonged after the peripheral rock collapses, the combined steel arch is used to intercept the slag and rocks of the collapsed body, ensuring the quick and safe passage of the TBM.

When the TBM encounters a soft rock section with high stress, it utilizes the TBM's expanding excavation function to increase the reserved deformation volume. This is achieved by enlarging the diameter of the excavation through the overbreak cutter, addressing issues of severe peripheral rock convergence and deformation. In cases where the convergent deformation of the soft surrounding rock is significant and rapid, resulting in the TBM shield becoming stuck, measures are taken to increase the TBM digging thrust and inject lubricants such as waste butter outside the shield to reduce friction force. If the TBM becomes stuck due to the deformation of the surrounding rock in front of the tunnel face, the artificial cap method is adopted to excavate ahead of the cutter plate position.

When the TBM traverses a hard rock section with high stress to mitigate the risk of rock explosion, it employs the cutter spraying system and a high-pressure water pipe behind the shield to spray water on the surrounding rock, softening it. Additionally, stress relief holes are drilled as a precautionary measure. However, the original cutter spray system of the TBM presents challenges such as a high failure rate of rotary joints, easy clogging of nozzles, and limited water spray volume. Consequently, the cutter spray system has been redesigned. Following the remodeling, the cutter spraying system boasts increased water spraying volume, reduced clogging of the water supply pipe, and diminished tool wear. These improvements enhance construction efficiency.

When the TBM traverses the construction section affected by water surges and mud bursts, it employs the overrun pipe shed method to support the area. This involves grouting to reinforce the surrounding rock and constructing water plugging. The overrun pipe shed consists of seamless steel pipe with grouting holes drilled into the steel pipe, arranged in a plum blossom pattern. An overrun drilling machine is utilized to drill holes in the tunnel arch to install the steel pipe. Given the surrounding rock conditions of the water surge and mud burst section, the grouting process utilizes chemical grouting.

REFERENCES

[1] Xu P., Huang J., Zhou J.B., et al., 2020. 3D Numerical simulation of the interaction between rock mass and shield TBM passing through the fault fracture zone. Modern Tunnelling Technology, vol. 57(06): 63-69.

[2] Zhang J.M., Shi K.B., DALAYIHAN Bahetebieke et al., 2023. Evaluation and prediction of TBM′s geological adaptability based on variable-weight set pair-multidimensional linked normal cloud model. Tunnel Construction, vol. 43(04): 645-657.

[3] Xie, W., et al., 2023. Fast perception of rock mass strength and integrity in TBM tunnelling using in-situ penetration test. Tunnelling and Underground Space Technology, vol. 141.

[4] Cheng S.L., Wang L.C., Hu H.Q., et al., 2023. Fault and fracture zone collapse treatment technology for open tunnel boring machine applied in beijiang water diversion project. Tunnel Construction, vol. 43(12): 2122-2132.

[5] Yang J.H., Sheng K., Zhou J., et al., 2023. Mechanism and prevention of tunnel collapse through water-rich fault fracture zone. Journal of Engineering Geology, vol. 31(01): 248-257.

[6] Longlong, C., et al., 2023. Characteristics and treatment measures of tunnel collapse in fault fracture zone during rainfall: A case study. Engineering Failure Analysis, vol. 145.

[7] Tong R.J., Zheng S.T., Wu Y.J., et al., 2022. Key technology of advance pre-grouting of ground directional holesto shield roadway passing fault and broken zone. Coal Science and Technology, vol. 50(06): 196-203.

[8] Chen P., Ma X.Q., Long J., et al., 2022. Method of designing pipe roof support parameters for tunnel in fault zone. Journal of Yangtze River Scientific Research Institute, vol. 39(12): 62-67.
[9] Ma D., Sun Y., Wang W.X., et al., 2021. Key technologies for controlling large deformation of soft rock tunnels with high geostress. Tunnel Construction, vol. 41(10): 1634-1643.
[10] Liu Y.P., Xia C.C., Wu F.B., et al., 2020. A combined support technology of long and short bolts of soft rock tunnels under high ground stresses. Chinese Journal of Rock Mechanics and Engineering, vol. 39(01): 105-114.
[11] Wang W.P., Li J.F., Yan P.B., et al., 2023. Design practice of prestressed anchor cable support technology for soft rock with extremely high geostress and large deformation in muzhailing tunnel. Tunnel Construction, vol. 43(S1): 313-322.
[12] Zheng Y., Guo P., Wang L.J., et al., 2023. Key technologies for treating high ground stress and large deformation of soft rock in daliangshan tunnel of Yunlin expressway. Tunnel Construction.
[13] Han C.L., Xu C., Xia C.C., et al., 2023. Design of reserved deformation for soft rock tunnels with high geostress. Tunnel Construction, vol. 43(11): 1916-1923.
[14] Zhang, Q., et al., 2023. Microseismic characteristic and development mechanism of fault-slip rockburst in a deep-buried TBM excavated tunnel: A case study. Tunnelling and Underground Space Technology, vol. 142.
[15] Li, P., et al., 2023. Rockburst and microseismic activity in a lagging tunnel as the spacing between twin TBM excavated tunnels changes: A case from the Neelum-Jhelum hydropower project. Tunnelling and Underground Space Technology, vol. 132.
[16] Wang K., 2021. Overview of state-of-art of rockburst prediction and prevention techniques for deep-buried tunnels. Tunnel Construction, vol. 41(02): 212-224.
[17] He, S., et al., 2021. Damage behaviors, prediction methods and prevention methods of rockburst in 13 deep traffic tunnels in China. Engineering Failure Analysis, vol. 121.
[18] Li, Z., et al., 2022. Research on the difficulties and countermeasures of TBM tunnel construction in plateau railway. Journal of Railway Engineering Society, vol. 39(9): 70-78.
[19] Fu, K., et al., 2023. Karst hydrogeological characteristics and construction disease analysis of a high-speed railway tunnel. Journal of Railway Engineering Society, vol. 40(10): 86-92.
[20] Shi, Z., et al., 2023. Failure mechanism analysis for tunnel construction crossing the water-rich dense fracture zones: A case study. Engineering Failure Analysis, vol. 149.
[21] Liu, N., et al., 2022. Geological investigation and treatment measures against water inrush hazard in karst tunnels: A case study in Guiyang, southwest China. Tunnelling and Underground Space Technology, vol. 124.
[22] Lang Z.J., Li M.Y., Qiao H.Y., 2023. Key technologies for treating large-scale water and mud inrush in inclined shaft work area of super-long tunnels. Modern Tunnelling Technology, vol. 60(05): 224-233.

CIVIL ENGINEERING JOURNAL

Article no. 13

THE CIVIL ENGINEERING JOURNAL 2-2024

RESEARCH ON CONSTRUCTION TECHNOLOGY OF LARGE-DIAMETER SHIELD TUNNEL IN SHALLOW COVER SECTION OF RED STRATA GEOLOGY

Jian Ouyang[1], Haijun Wang[1], Xin Dong[1], Dawei Hu[2], Kexin Zhang[3] and Xingwei Xue [4]

1. *Engineering Department, Guangzhou Expressway Co., LTD, Guangzhou, China*
2. *Tunnel Engineering Department, China Railway Fourth Survey and Design Institute Group Co., LTD, Wuhan, China*
3. *Shenyang Jianzhu University, School of Transportation and Surveying Engineering, Department of Bridge and Tunnel Engineering, Shenyang, China; jt_zkx@sjzu.edu.cn*
4. *Shenyang Jianzhu University, School of Transportation and Surveying Engineering, Department of Bridge and Tunnel Engineering, Shenyang, China*

ABSTRACT

This paper is based on the construction of the Haizhuwan Tunnel in Guangzhou, which passes through predominantly mudstone and sandstone red strata geology. Excavation is carried out using a slurry balance shield tunneling machine with both atmospheric pressure and pressurized cutterheads, and real-time excavation parameters recorded by the shield equipment are collected and statistically analyzed. Discovery: In the initial shallow-buried excavation section, the total thrust of the shield machine increased as the tunneling distance increased. By continuously adjusting the excavation parameters during construction, the shield machine gradually tended towards a stable operating state, leading to a gradual reduction in the range of thrust fluctuations. East Line: After excavating the reinforcement area, the increase in cutterhead torque is significant, leading to a more pronounced adaptation process for the shield machine. The cutterhead torque fluctuates more on rings 20 to 65 on the East Line, showing greater variability. This situation is related to the wear of the cutterhead and the condition of the shield machine equipment on the East Line. West Line: After excavating the reinforcement area, the cutterhead torque is initially reduced, with a slow and continuous increase in torque from rings 20 to 65, eventually stabilizing at around 12 MN·m. Throughout the excavation process, the shield machine on the East Line maintained a relatively high excavation speed within the reinforced soil at the face, with an average of 7.76 mm/min. As the machine excavated beyond the reinforcement area, the overall excavation speed of the shield machine slowed down. The excavation speed from ring 21 to ring 65 was primarily controlled between 2 to 6 mm/min, with an average of 4.49 mm/min, showing a relatively stable overall change.

KEYWORDS

Shield tunnel, Complex red strata geology, Shallow buried section, Excavation parameters, Atmospheric pressurized, Pressurized cutterhead

BACKGROUND

China's research on large diameter shield tunneling technology started later than that of foreign countries. In 1994, China introduced a large diameter shield with a diameter of Ø11.22m from

Mitsubishi Heavy Industries of Japan for the construction of the south section of the Yantai East Road tunnel in Shanghai. This model was successfully applied in Shanghai's homogeneous soft ground, laying a technical foundation for the application of large diameter shield tunnels in China [1-3]. Subsequently, by tracking the progress of shield tunneling technology overseas, China began to research the application technology of large-diameter and super-large-diameter shields in tunnel construction [4-8]. In the 21st century, driven by large-scale construction projects in the country, various models and specifications of shield tunneling machines have entered the tunnel construction field in large numbers, providing a wealth of engineering application experience and technology for the localization of shield tunneling equipment [9-12]. The Shanghai Shangzhong Road Tunnel was the first to use a super large-diameter slurry shield tunnel boring machine with a diameter of 14.87 meters. Subsequently, the Shanghai Changjiang Road Tunnel used two 15.43-meter diameter shield tunneling machines, and Nanjing Weiqi Road used two 14.96-meter diameter shield tunneling machines. This marked the successive construction of large-diameter shield tunneling projects in China, indicating the widespread application of super large-diameter shield tunneling projects in China [13]. Currently, China has become the primary market for super large-diameter shield tunneling projects in the world. In 2015, the Tuen Mun Tunnel in Hong Kong was constructed using a slurry shield tunnel boring machine with a diameter of 17.6 meters, making it the world's largest diameter shield tunnel currently in operation [14].

According to statistical analysis of construction cases, the super large-diameter shield tunneling machines used in China are mainly of European and Japanese origin, with European machines accounting for over 60%. In recent years, with the rapid advancement of domestic shield tunneling technology, domestically produced machines have fully occupied the market in new construction projects in China. In the field of super large diameter shield tunneling, domestic machines have achieved complete independent research and development, with some technologies taking a leading position [15-17]. In terms of shield tunnel types, 90% of them are slurry shield tunnels, as slurry shield tunnels have better safety and geological adaptability in coping with complex geological conditions such as high-water pressure, varying soil hardness, and developed fractures [18].

Currently, both domestic and foreign scholars have conducted extensive research on the correlation between shield tunneling process parameters and the physical properties of rock and soil. However, most of them focus on theoretical calculations and the establishment of prediction models, and statistical analysis of a large amount of measured data is not common. In addition, the shallow buried shield tunnel has the characteristics of high buried depth, and the ground movement is obvious due to the loss of the bottom layer in the construction process, which has a great impact on the surrounding environment. Therefore, higher requirements are put forward for excavation, drainage, grouting and other methods, and the construction difficulty is increased. Therefore, this article is based on the Guangzhou Haizhuwan Tunnel project. The geological conditions in this section are unique, with the shield tunneling section consisting of red strata geology, primarily composed of muddy sandstone. The 1-65 ring of shield tunneling is shallow buried section, and the construction conditions are more complicated. The Haizhuwan Tunnel is divided into east and west lines, each using different types of tunnel boring machines (TBM) - one with a constant pressure cutterhead and the other with a pressurized cutterhead. The study collects and statistically analyzes six tunneling parameters recorded in real time by the shield tunneling equipment, and investigates their patterns of change.

INTRODUCTION TO ENGINEERING BACKGROUND

This project is the Haizhuwan Tunnel project, with the main line designed from chainage EK0-415.730 to EK3+933.057, with a total length of 4348.787 m. The starting point of the main line design of this project connects to the existing Dongxiaonan Viaduct. The route extends southward and passes through the Pearl River Lijiao Waterway, Luoxi Island, and Sanzhixiang Waterway in the form of a double-tube single-layer shield tunnel. After the shield tunnel ends at the northern end of

Nanpu Road, it continues to pass through Nanpu Road in the form of a buried tunnel and emerges on the surface, connecting to the bridge of the southern section of the project.

The design adopts the planned centerline revised according to the urban planning standards. The starting point connects to the Dongxiaonan Viaduct with a dual 4-lane bridge. After crossing Nanzhou Road, it descends to the ground, and passes under the Pearl River Lijiao Waterway, Luoxi Island, and Sanzhixiang Waterway using shield tunneling. Moving southward, it goes through Nanpu Road in an underground buried tunnel, then emerges on the surface to connect to the bridge of the southern section of the project. The total length of the tunnel is 3463.057 m, with the shield tunnel section being 2077 m long and the cut-and-cover section being 1386.057 m long. The shield tunnel has an outer diameter of 14.5 m and is designed to accommodate a dual 6-lane configuration. The minimum horizontal radius for the shield tunnel section is 1000 m, while for the onshore section it is 450 m, and for the Dongxiao South Viaduct, it is 160 m. The typical minimum clearance between adjacent tunnel sections is generally not less than 1.0 times the tunnel diameter, while the clearance at the beginning and ending sections is usually controlled at around 0.6-0.7 times the tunnel diameter. The minimum spacing for the gradient change points within the tunnel is 342.467m, which meets the specified regulatory requirements. The mainline has a minimum gradient of 0.3% and a maximum longitudinal slope of 4%. The vertical curve's minimum radius for the viaduct section is 3000 m, meeting the design speed requirement of 60km/h. For the tunnel section, the minimum radius for the vertical curve is 3800 m, also meeting the design speed requirement of 60 km/h. The strata crossed by the shield tunnel section are mainly composed of strong, moderate, and slightly weathered silty sandstone. The longitudinal section layout is shown in Figure 1.

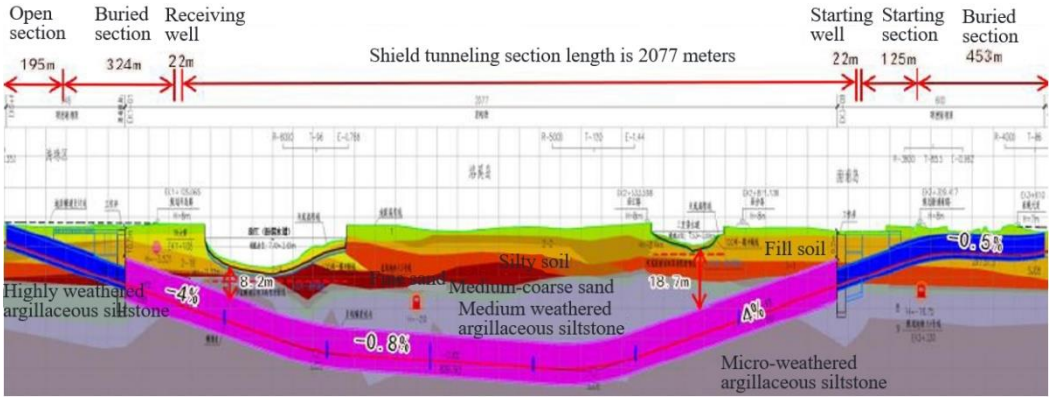

Fig. 1 – Illustration of the geological conditions in the shield tunnel section of Haizhuwan

The shield tunneling method is used for the middle section of the tunnel. The shield section has a circular cross-section with an outer diameter of 14.5 m, an inner diameter of 13.3 m, and a segment thickness of 0.6 m. The cross-sectional layout is shown in Figure 2.

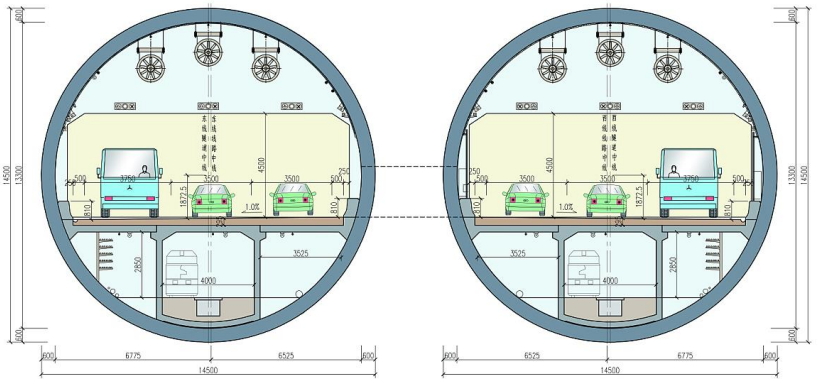

Fig. 2 – Cross-sectional diagram

OVERVIEW OF SHIELD TUNNELING MACHINE

Two slurry shield tunneling machines are used in the shield tunneling section. The excavation diameter of the shield tunneling machine is 15.07 m. The shield tunneling machine in the East line is divided into a main machine and 4 auxiliary cars behind it. The shield tunneling machine in the West line is divided into a main machine and 5 auxiliary cars behind it, with a maximum excavating speed of 50 mm/min. The technical parameters of shield machine is shown in Table 1, and the technical parameters of cutter head of shield machine is shown in Table 2.

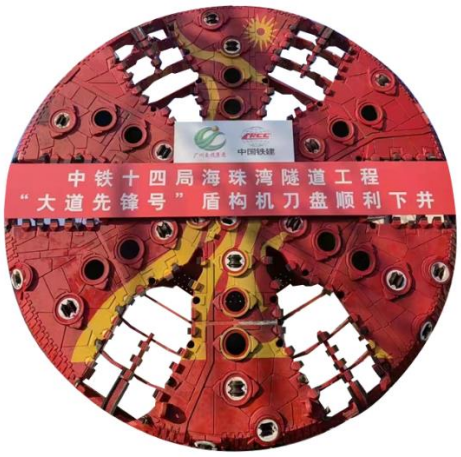

Fig. 3 – The layout diagram of the western line disc cutter (atmospheric pressure)

Fig. 4 – The layout diagram of the eastern line disc cutter (under pressure)

Tab. 1 - Technical parameters of shield machine

Herrenknecht slurry balance tunnel boring machine		China Railway Construction Heavy Industry Corporation with a mud-water balance shield tunnel boring machine	
Cutterhead diameter (m)	15.07	Cutterhead diameter (m)	15.07
Total length (m)	152	Total length (m)	128
Total weight (t)	4495	Total weight (t)	4300
Total power (kW)	11200	Total power (kW)	9755
Main drive power (kW)	5600	Main drive power (kW)	5600
Rated torque (kN.m)	42972	Rated torque (kN.m)	42784
Operating pressure (bar)	9	Total thrust (kN)	222173

Tab. 2 - Technical parameters of cutter head of shield machine

Herrenknecht slurry balance tunnel boring machine		China Railway Construction Heavy Industry Corporation with a mud-water balance shield tunnel boring machine	
Cutter opening rate (%)	30	Cutter opening rate (%)	35
Knives	246	Knives	387
Edge scraper	12	Edge scraper	16
Atmospheric pressure replaceable scraper	50	Center hob	6
Pressure replaceable center hob	12	Front hob	77
Atmospheric pressure replaceable front hob	60	Edge hob	22
Atmospheric pressure replaceable edge hob	4	Wide cutter	180
Ordinary scraper	150	Edge scraper	16
Plain side scraper	12	Over cutter	2

STRENGTHENING MEASURES AT THE DEPARTURE END HEAD

The clear dimensions of the departure work shaft pit are: length of 22 m, width of 54 m, height of 25.10 m, with a subsequent length of 126 m (114m for the east line). It has an underground four-story double-box structure and is constructed using an open-cut method in the order of excavation. The excavation support structure adopts a 1.2 m underground diaphragm wall combined with internal support bracing as the shoring scheme, and the bottom of the pit is reinforced with a skirt edge combined with struts. The starting shaft end uses Φ850 mm@ 600 triple-axis mixing piles, with a row of Φ800 mm @ 600 triple jet grouting piles for reinforcement near the working shaft. The reinforcement length is 20 m, and the reinforcement depth extends 1m below the strong weathered silty sandstone. An 800 mm thick plain wall is closely placed around the reinforcement body, extending to 5 m below the shield tunnel lining structure. The lower end reinforcement uses grouting, with the grouting range extending to the bottom of the mixing reinforcement body and 5 m below the

structure bottom. The reinforcement width extends 5 m on both sides of the structure outline, with the installation of dewatering wells. The mixing pile reinforcement of the work shaft should be completed before the excavation of the foundation pit, while the jet grouting piles should be constructed after the completion of the structural filling and before the start of the shield tunneling. As shown in Figure 5 and Figure 6.

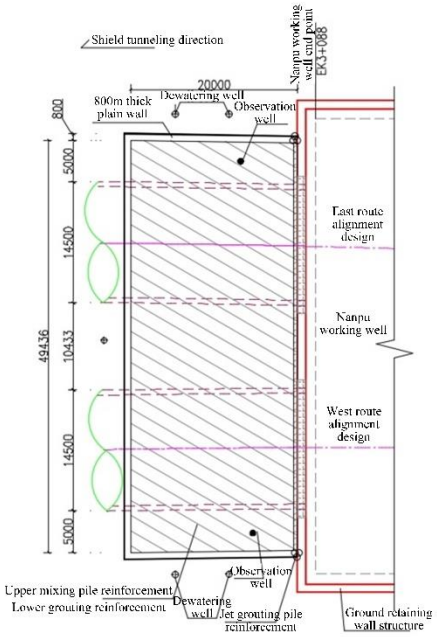

Fig. 5 – Plan view of the reinforcement at the starting shaft end

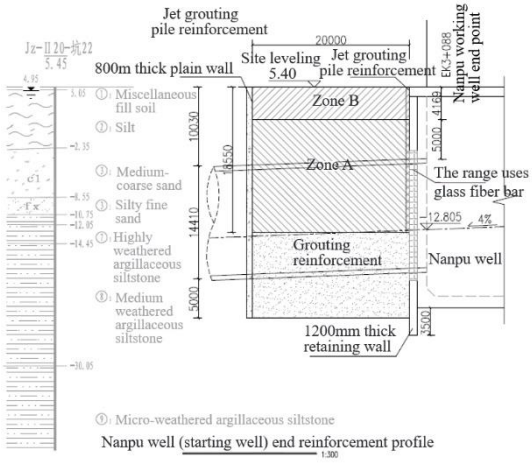

Fig. 6 – Section view of the reinforcement at the starting shaft

ANALYSIS OF THE EXCAVATION PARAMETERS IN THE SHALLOW BURIAL SECTION

Analysis of the thrust force of the tunnel boring machine

The variation curve of the thrust force of the tunnel boring machine in the process of excavating rings 1-65 in the shallow burial section can be found in Figure 7.

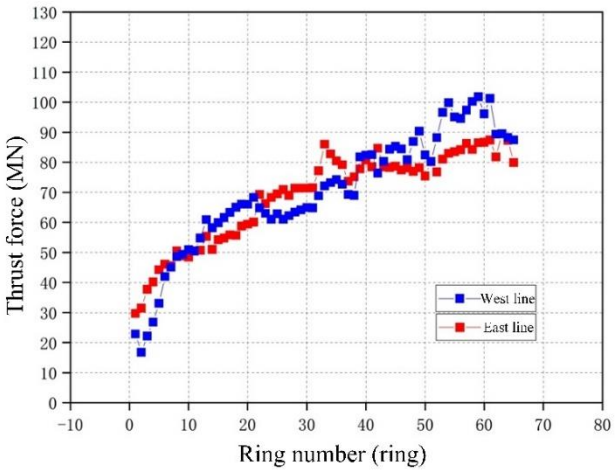

Fig. 7 – Graph of thrust variation in shallow burial section

It can be seen from Figure 7 that after the start of the tunnel boring machine on the west line, there are stage differences in the variation of thrust in the shallow burial section. During the tunnel boring process from ring 001 to ring 020, due to the stable soil in the front-end reinforcement area, the thrust force of the tunnel boring machine continues to increase to 70 MN. However, it is limited by the initial reaction frame and the stability of the cutterhead, so the thrust is controlled at a relatively low level. During the tunnel boring process from ring 021 to ring 032, as the tunnel boring machine excavates out of the front-end reinforcement area and encounters significant changes in geological conditions, the thrust force of the tunnel boring machine shows a slow decreasing trend, with an average thrust force of 64.3 MN. During the tunnel boring process from ring 033 to ring 065, as the tunnel boring machine operates at increasing depths and mainly encounters silty sandstone formations, the thrust force of the tunnel boring machine continues to steadily increase. Due to the rapid changes between soft and hard rock and soil formations in this section, the cutterhead experiences uneven loading, leading to significant eccentric loads and overturning moments on the cutterhead. When passing through the interface between soft and hard rock and soil formations, the cutterhead will experience high lateral impact loads, resulting in noticeable fluctuations in thrust force during excavation in this geological layer.

After the launch of the shield tunnel boring machine in the eastern section, the thrust force of the tunnel boring machine in the shallow-buried section overall continues to steadily increase. During the tunnel boring process from ring 001 to ring 020, the tunnel boring machine is located in the front-end soil reinforcement area, with good geological engineering properties. In the initial ten rings, the thrust force of the tunnel boring machine continuously and rapidly increases to 50 MN. In the subsequent ten rings, as the tunnel boring machine is about to excavate out of the front-end reinforcement area, the thrust force tends to increase slowly due to significant changes in geological conditions. During the tunnel boring process from ring 021 to ring 050, as the tunnel boring machine operates at increasing depths, it mainly enters silty sandstone formations. The thrust force of the tunnel boring machine continues to steadily increase. During the initial rings of tunnel boring, after the tunnel boring machine adapts to the normal soil layers, the thrust force increases from 60MN to 70 MN in stages. In the subsequent ten rings, the thrust force remains at 70 MN to ensure the stability of the tunnel boring machine excavation. The variation in thrust from rings 030 to 050 is an adaptive process for the tunnel boring machine to adjust to the new geological conditions. In the initial rings, the thrust increases from 70 MN to 86 MN in stages. However, due to the thrust not matching the geological conditions, the value gradually decreases afterwards, eventually stabilizing at 80kN. In the tunnel boring process from ring 051 to ring 065, the thrust of the tunnel boring machine continues to steadily increase. Due to rapid changes between soft and hard rock and soil formations in this section, uneven loading on the cutterhead causes the cutterhead to bear significant eccentric loads and overturning moments. When the cutterhead passes through the interface between soft and hard rock and soil, significant lateral impact loads are generated. In this geological layer, the thrust of the tunnel boring machine fluctuates significantly, with the thrust maintained at 80 to 90 MN.

In the initial shallow-buried excavation section, the total thrust of the tunnel boring machine increases with the excavation distance, and the excavation parameters are continuously adjusted during construction. The tunnel boring machine gradually reaches a stable operating state, resulting in a gradual reduction in the range of thrust fluctuations. Overall, due to the smaller curve radius on the western line, the total thrust on the western line is higher than that on the eastern line.

When the tunnel boring machine passes through the reinforcement zone at the starting end, the thrust increases rapidly due to the greater strength of the soil in the reinforced area. A comparison of the thrust variation curves between the eastern and western lines reveals that the thrust gradually increases with the increase of excavation distance, displaying a basic linear change. When excavating in the formations outside the reinforcement zone, both the eastern and western lines experience a certain degree of fluctuation in thrust, and the magnitudes of the fluctuations are essentially the same between rings 20 and 40. Subsequently, the thrust of both the eastern and western lines continues to increase. The thrust of the tunnel boring machine on the eastern line

gradually increases from 80.8 MN to 89.5 MN, while the thrust of the tunnel boring machine on the western line gradually increases from 82.41 MN to 101.83 MN. On the one hand, the thrust required for the disc cutters to crush the rock mass increases significantly with the increase in the proportion of the rock mass at the cutter face; on the other hand, in the composite soil-rock formations, the disc cutters wear out fast, leading to severe abnormal wear and a decrease in the rock-breaking ability of the cutterhead. During the excavation process in the shallow-buried section, the thrust of the cutterhead with constant pressure on the western line is between 69MN and 101.83 MN, while the thrust of the cutterhead with pressure on the eastern line is between 71 MN and 89.5 MN.

Cutterhead Torque Analysis.

The change curve of the cutterhead torque in the process of tunneling from ring 1 to ring 65 in the shallow-buried section is shown in Figure 8.

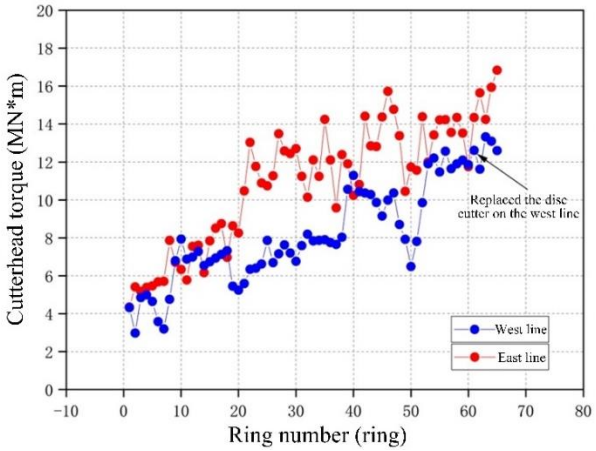

Fig. 8 – Cutterhead torque variation diagram in shallow-buried section

It can be seen from Figure 8 that the cutterhead torque of the westbound shield machine remains relatively stable overall during the tunneling process in the shallow-buried section. However, due to the limitations of the initial reaction frame and the stability of the cutting edge, the thrust is controlled at a relatively low level. During this period, the cutterhead torque frequently experiences sharp increases or decreases, with frequent fluctuations, while the distribution of the adjacent ring formations remains unchanged. This indicates significant differences in the flowability of the muck and the improvement effects in the adjacent ring chambers. During the tunneling of rings 001 to 020 of the shield tunnel, this section is for the stabilization of the end face. The soil is stable, and the cutterhead torque is continuously adjusted, fluctuating around 4 MN·m, and then steadily increasing to 7 MN·m. During the tunneling of rings 021 to 038 of the shield tunnel, as the shield machine excavates beyond the end face reinforcement zone, there is a significant change in the ground conditions, and the cutterhead torque shows a slow increasing trend. In the tunneling of rings 039 to 065 by the shield tunneling machine, as the depth of the shield machine increases, the shield machine mainly enters the mudstone and siltstone formations. The cutterhead torque continues to steadily increase. Due to the rapid changes between soft and hard rock and soil, the disc cutters bear uneven forces, resulting in significant eccentric loads and overturning moments on the cutterhead. The cutterhead torque fluctuates noticeably during tunneling in this formation.

After the start of the shield tunneling on the eastern line, there are phase differences in the overall variation of the cutterhead torque in the shallow buried section. In the tunneling of rings 001 to 020 by the shield tunneling machine, the shield machine is in the face soil reinforcement area, and the ground engineering properties are good. The cutterhead torque steadily increases to 8 MN·m in this section. In the tunneling of rings 021 to 065 by the shield tunneling machine, the shield machine continues to adjust to the new ground conditions after entering. The cutterhead torque

fluctuates noticeably during tunneling in this formation, with the cutterhead torque maintained at 10 to 16 MN·m.

In the initial shallow-buried tunneling section, as the tunneling distance increases, the tunneling parameters are continuously adjusted during construction. The cutterhead torque of the twin-shield tunneling machines is constantly fluctuating. The cutterhead torque can to some extent infer the working state of the main shaft and the wear of the tools. Overall, the cutterhead torque of the shield tunneling machine on the eastern line is higher than that of the western line.

When the shield tunneling machine passes through the initial face reinforcement area, the thrust of the twin-shield tunnels continues to increase due to the higher soil strength in the reinforcement zone. By comparing the thrust variation curves of the eastern and western lines, it can be observed that the thrust gradually increases with the tunneling distance, showing a generally linear trend. During tunneling in the strata outside the reinforcement area, both the eastern and western lines exhibit a certain degree of thrust fluctuation. Specifically, after tunneling out of the reinforcement area, the cutterhead torque of the eastern line undergoes a significant increase, leading to a more pronounced adaptation process of the shield machine. Between rings 20 and 65, the cutterhead torque of the eastern line shows greater fluctuations and more pronounced dispersion, which is correlated with the wear of the cutterhead tools and the condition of the shield machine on the eastern line. In contrast, the western line experiences an initial decrease in cutterhead torque after tunneling out of the reinforcement area, with a gradual and steady increase in torque between rings 20 and 65, ultimately stabilizing at around 12 MN·m.

Tunneling speed.

The variation curve of the tunneling speed of the west line during rings 1 to 65 of the shallow-buried section excavation process can be seen in Figure 9.

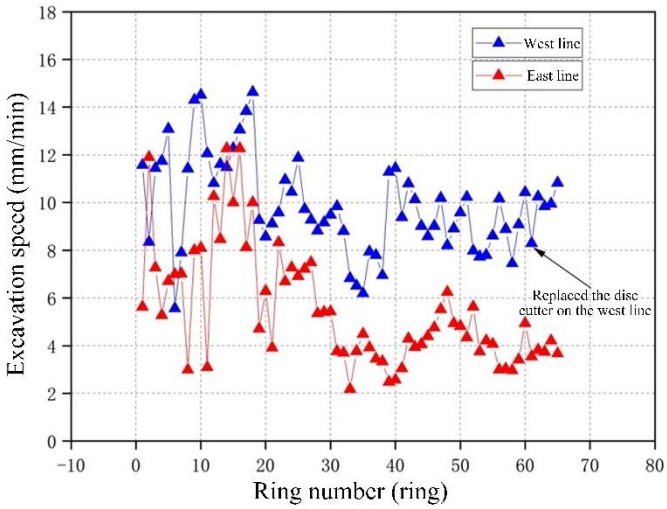

Fig. 9 – Variation of tunneling speed in the shallow-buried section

From Figure 9, it can be observed that compared to the fluctuation range of the total thrust and cutterhead torque of the west line shield machine mentioned earlier, the tunneling speed of the shield machine in the shallow-buried initial section has a higher degree of dispersion, with average and standard deviation values of 9.85 and 1.99 for the tunneling speed respectively. Throughout the entire excavation process, the tunneling speed within the face soil reinforcement area remains at a relatively high level, with an average of 11.37 mm/min. As the shield machine advances beyond the reinforcement area, the overall tunneling speed slows down, with the tunneling speed in rings 021 to 065 mainly controlled within the range of 6 to 12 mm/min, and averaging 9.18 mm/min.

Compared to the fluctuation range of the total thrust and cutterhead torque of the east line shield machine mentioned earlier, the tunneling speed of the east line shield machine shows a similar trend to the west line, with a higher degree of dispersion. The average and standard deviation of the tunneling speed are 5.49 and 2.44 respectively. Throughout the entire excavation process, the tunneling speed of the east line shield machine within the face soil reinforcement area also remains at a relatively high level, with an average of 7.76 mm/min. As the shield machine advances beyond the reinforcement area, the overall tunneling speed slows down, with the tunneling speed in rings 021 to 065 mainly controlled within the range of 2 to 6 mm/min, averaging 4.49 mm/min.

Starting from the shallow-buried starting section, the tunneling speeds of the dual-line shield machines both increase rapidly. Due to the need for the shield machine to gradually adapt to the surrounding strata in the initial stages of tunneling, the tunneling speed fluctuates greatly. As the dual-line shield machines excavate beyond the soil reinforcement area at the face, the ground conditions become more complex. Therefore, the tunneling speed of the shield machines gradually slows down and tends to stabilize with mild fluctuations. Furthermore, the shield machine has gradually adapted to the surrounding strata, so the fluctuations in tunneling speed are relatively stable. The average and standard deviation of tunneling speed for the west line are 9.85 and 1.99 respectively, while for the east line are 5.49 and 2.44. During the tunneling in the shallow-buried starting section, the tunneling speed of the east line shield machine is significantly lower than that of the west line shield machine.

Cutterhead rotation speed

The variation curve of cutterhead rotation speed for rings 1 to 65 during the tunneling process in the shallow-buried section of the west line can be seen in Figure 10.

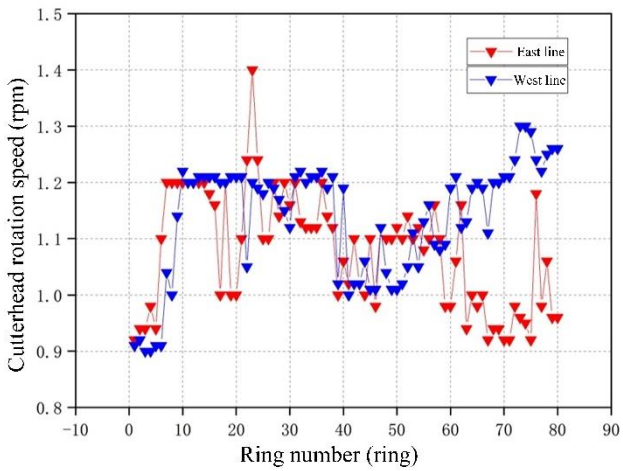

Fig. 10 – Cutterhead rotation speed variation in the shallow-buried section

From Figure 10, it can be seen that after the start of the west line shield tunneling, the rotation speed of the cutterhead continues to increase to 1.2 rpm during the excavation of the end soil reinforcement section. From rings 10 to 40, the cutterhead rotation speed is mainly maintained at around 1.2 rpm with minimal fluctuations. After ring 40, when the shield machine enters the complex strata with variations in soil hardness, in order to reduce the disturbance to the surrounding soil during excavation, the cutterhead rotation speed is reduced from 1.2 rpm to 1.0 rpm in the lower layer of this strata. As the proportion of rock mass on the cutting face increases, the rolling cutter in the complex strata wears out quickly, experiences severe abnormal wear, and the rock-breaking ability of the cutterhead decreases. The cutterhead rotation speed gradually increases to 1.2 rpm. Due to the need for constant adjustments to adapt to the strata, there is significant fluctuation in the cutterhead rotation speed during excavation in this strata.

After the start of the east line shield tunneling, the rotation speed of the cutterhead continues to increase to 1.2 rpm during the excavation of the end soil reinforcement section. From rings 10 to 30, the cutterhead rotation speed is mainly controlled at around 1.2 rpm, showing significant fluctuations. After ring 30, in order to better adapt to different strata conditions, the cutterhead rotation speed is reduced from 1.2 rpm to around 1.1 rpm. With the increasing proportion of rock mass at the face, the rolling cutter in the composite strata wears out quickly and exhibits severe abnormal wear, resulting in reduced rock breaking efficiency of the cutterhead. As a result, the cutterhead rotation speed fluctuates continuously between 0.9 and 1.2 rpm.

In the initial shallow-buried excavation section, the cutterhead rotation speed is continuously adjusted during construction as the excavation progresses. The cutterhead rotation speed fluctuates significantly between 0.9 and 1.2 rpm. The average cutterhead rotation speed for the shield machine in the west line is 1.11 rpm, while in the east line, it is 1.10 rpm. Overall, the cutterhead rotation speed in the east line shows a higher level of dispersion compared to the west line.

Cutting water pressure and air bubble chamber pressure

The variation curves of cutting water pressure and air bubble chamber pressure in the excavation process of rings 1-65 in the shallow-buried section of the west line can be seen in Figure 11.

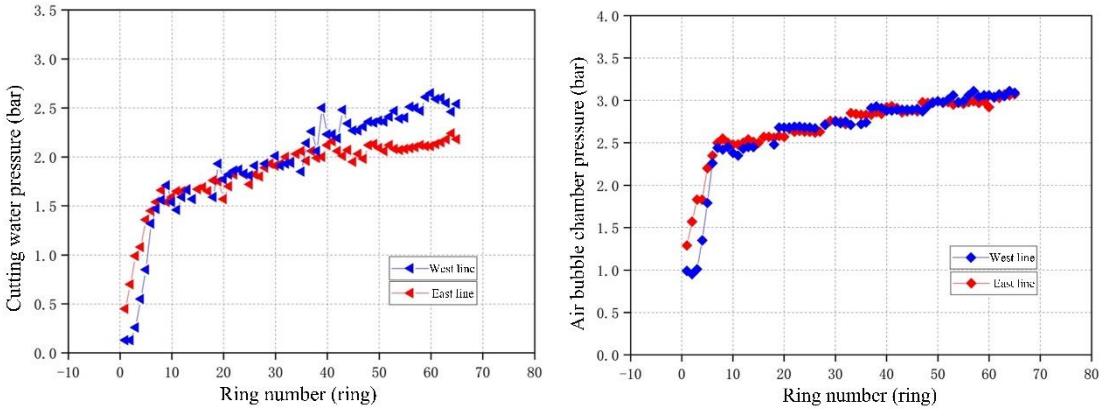

(a) Cutting water pressure *(b) Air bubble chamber pressure*

Fig. 11 – Cutterhead rotation speed variation in the shallow-buried section

According to Figure 11, it can be seen that with the continuous increase of the excavation distance of the west line shield tunnel, the tunnel depth also increases accordingly. Therefore, the cutting water pressure and ai bubble chamber pressurer bubble chamber pressure of the shallow-buried starting section of the west line shield tunnel both show an overall increasing trend. During the excavation of rings 001 to 010 of the shield tunnel, due to being in the end soil reinforcement zone, the cutting water pressure and air bubble chamber pressure of the west line shield tunnel both increased rapidly. The cutting water pressure increased from 0.13 bar to 1.54 bar, and the air bubble chamber pressure increased from 0.99 bar to 2.38 bar. In the subsequent rings 011 to 065, the cutting water pressure and air bubble chamber pressure continued to increase, but compared to the first ten rings, the rate of increase slowed down, with smaller fluctuations and a more stable trend.

The cutting water pressure and air bubble chamber pressure of the shallow-buried starting section of the east line shield tunnel follow the same pattern as the data for the west line tunnel, with both values gradually increasing. During the excavation of rings 001 to 010 of the shield tunnel, the cutting water pressure and air bubble chamber pressure of the east line shield tunnel both increased rapidly. The cutting water pressure increased from 0.45 bar to 1.59 bar, and the air bubble chamber pressure increased from 1.29 bar to 2.48 bar. In the subsequent rings 011 to 065, the cutting water

pressure and air bubble chamber pressure continued to increase, but compared to the first ten rings, the rate of increase slowed down.

The cutting water pressure and air bubble chamber pressure of the shallow-buried starting section of the east and west lines both show a gradually increasing trend. The standard deviations of the cutting water pressure in the shallow-buried starting section of the east and west lines are 0.34 and 0.6, respectively, indicating that the west line cutting water pressure has a higher degree of dispersion compared to the east line cutting water pressure; the standard deviations of the air bubble chamber pressure in the shallow-buried starting section of the east and west lines are 0.34 and 0.50, respectively, indicating that the west line air bubble chamber pressure has a higher degree of dispersion compared to the east line air bubble chamber pressure.

Grouting volume

The curve showing the changes in the grouting volume of the west tunnel boring machine in rings 1 to 65 of the shallow-buried section is shown in Figure 12.

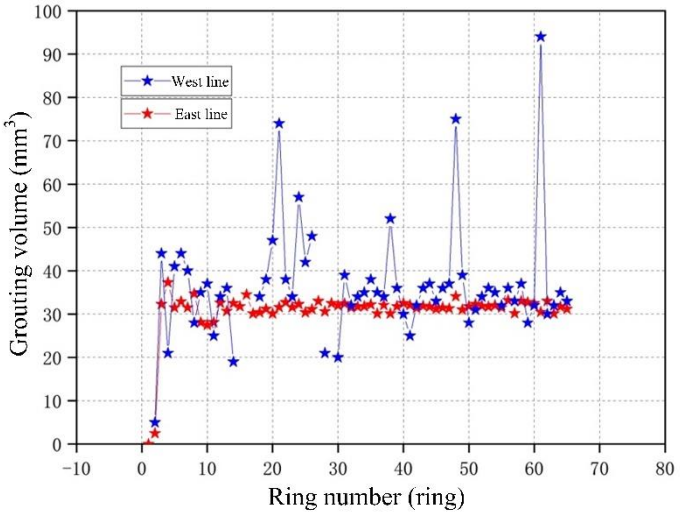

Fig. 12 – C Graph of grouting volume changes in the shallow-buried section

As can be seen from Figure 12, the average grouting volume of the west tunnel boring machine is 36.66 m^3, showing a trend of fluctuation around the average throughout the entire excavation process of the shallow-buried starting section. The average grouting volume of the east tunnel boring machine is 30.76 m^3. Throughout the entire excavation process of the shallow-buried starting section, except for the initial 3 rings, the grouting volume at the remaining segment lining rings remains relatively stable.

The grouting volumes of the east and west tunnel boring machines in the shallow-buried starting section remained within specific values, with fluctuations in the data corresponding to different ring numbers. The standard deviations of the grouting volumes for the east and west tunnel boring machines in the shallow-buried starting section are 5.50 and 13.21 respectively, indicating that the grouting volume of the west tunnel boring machine has a higher level of dispersion compared to the east tunnel boring machine.

ANALYSIS OF GROUND SURFACE SETTLEMENT MONITORING SECTION RESULTS

The ground surface settlement caused by shield tunnel excavation is essentially the cumulative soil loss caused by shield tunnel construction. In order to study the dynamic process of ground surface settlement during shield tunnel construction, five transverse monitoring sections, DB1 (0 m

from the starting shaft), DB2 (20 m from the starting shaft), DB3 (40 m from the starting shaft), DB4 (60 m from the starting shaft), and DB5 (80 m from the starting shaft), were selected as target surfaces. The dynamic relationship curves between ground surface settlement and the excavation face advancement process are shown in Figures 13 to 17.

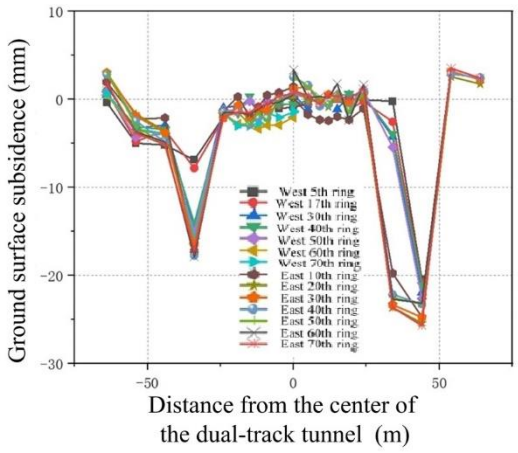

Fig. 13 – Settlement curve of transverse monitoring section DB1

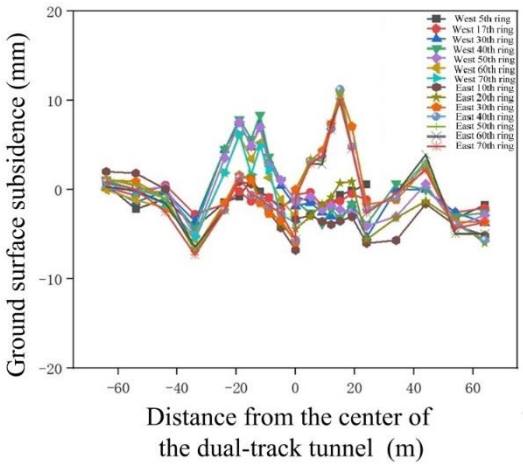

Fig. 14 – Settlement curve of transverse monitoring section DB

From Figure 13 and Figure 14, it can be seen that before the shield tunneling machine reaches the section, there is no significant ground settlement. With the excavation of the west line (leading tunnel) and the east line (following tunnel) shield tunnels, as the transverse monitoring sections DB1 (0 m away from the originating shaft) and DB2 (20 m away from the originating shaft) are both located within the initial section head reinforcement zone, reinforcement measures such as bored piles ensure the formation of cement soil in the reinforcement zone, with good engineering properties. No significant ground settlement occurred near the axis of the twin tunnels and the excavation sections, indicating the reasonable and effective implementation of the measures taken, ensuring the safe progress of the originating construction. After the shield tunneling machine of the east line tunnel passes through, significant settlement occurred at the edge of the originating shaft and the head reinforcement zone due to the apparent difference in soil properties. The maximum settlement on the west side of section DB1 is about 18 mm, and on the east side is about 26 mm, the maximum settlement on the west side of section DB2 is about 7 mm, and on the east side is about 6 mm.

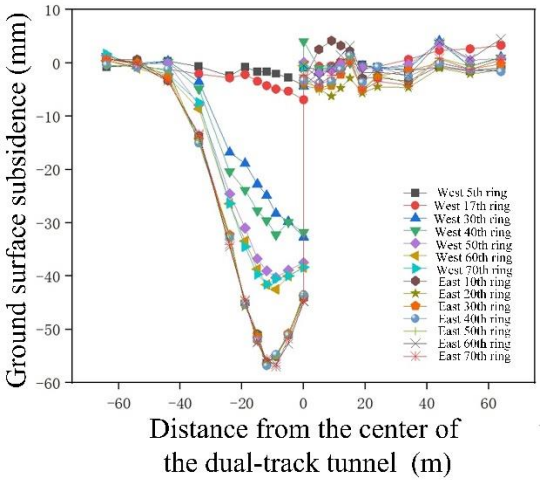

Fig. 15 – Shows the settlement curve of transverse monitoring section DB3.

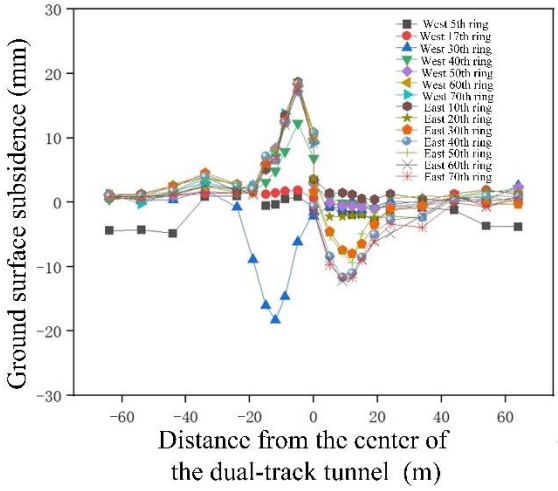

Fig. 16 – Shows the settlement curve of transverse monitoring section DB4.

From Figure 15, it can be seen that with the excavation of the shield tunnel of the west line (leading tunnel), there is no significant settlement on the ground surface before the shield tunnel machine of the west line arrives at the section. After the DB3 section (40 m from the starting shaft), surface settlement gradually occurs. When the tunnel machine reaches Ring 20, it crosses the monitoring section DB3. At this point, the surface settlement of the DB3 section significantly increases, and the settlement values and settlement rates at the tunnel axis are noticeably greater than those on both sides of the tunnel. As the shield tunnel machine of the west line crosses the section, the settlement curve develops into a normal distribution curve. The single-line excavation of the west line tunnel conforms to the settlement law of the Peck theory. The maximum transverse surface settlement value of 42.51 mm is obtained at the axis of the west line tunnel, with a settlement trough width of approximately 44m, conforming to the settlement trough theory. This indicates that tunnel excavation will cause lateral differential settlement on the ground surface.

With the excavation of the shield tunnel of the east line (trailing tunnel), monitoring data shows that before the shield tunnel machine arrives at the section, there is approximately 4.18 mm of ground uplift at the axis of the east line tunnel section. As the construction progresses, when excavating to Ring 20, the shield tunnel machine crosses the monitoring section, and the surface settlement of the DB3 section significantly increases. The surface settlement values and settlement rates at the tunnel axis are noticeably greater than those on both sides of the tunnel. At this point, the maximum transverse surface settlement value of 6.24 mm is obtained at the axis of the east line tunnel, with a settlement trough width of approximately 15 m. As the shield tunnel machine of the east line crosses the section, after the grouting is completed, the strata slowly undergo consolidation and rheology, eventually reaching a new stress equilibrium, and the ground surface stabilizes. Due to the disturbance of the surrounding soil caused by the excavation of the west line tunnel, the surface settlement values overlap with those generated during the excavation of the east line tunnel. The position of the maximum settlement point shifts towards the centerline of the two tunnels, ultimately reaching a maximum settlement value of 56.96 mm. The width of the settlement trough continues to increase, and the final shape remains V-shaped.

Based on the results of the engineering geological exploration, it is believed that before the shield tunnel machine reaches the monitoring section DB3, the settlement is mainly caused by consolidation of the overlying soft soil layer. When the shield tunnel machine crosses the section until grouting is completed at the tail of the shield, shear stress is generated at the interface between the shield and the soil, as the diameter of the shield tunnel machine is slightly larger than the outer diameter of the tunnel lining, and simultaneous grouting cannot instantly fill the gap between the

tunnel lining and the soil. The surrounding soil rapidly moves towards the gap, leading to a rapid occurrence of surface settlement, which can be considered as instantaneous settlement. After grouting is completed, the strata slowly undergo consolidation and rheology, eventually reaching a new stress equilibrium, and the ground surface stabilizes. It can be seen that significant surface settlement occurs during the shield tunnel crossing the section and before grouting is completed at the shield tail.

From Figure 16, it can be seen that as the shield tunnel of the west line (leading tunnel) is excavated, there is no significant surface settlement before the shield tunnel machine of the west line reaches the section. Subsequently, surface settlement gradually occurs at the DB4 section (60 m from the starting well). When excavation reaches ring 30, the shield tunnel machine crosses the monitoring section, and surface settlement at the DB3 section significantly increases. The maximum lateral surface settlement value at the axis of the west line tunnel is 18.31 mm, with a settlement trough width of approximately 34 m. The surface settlement value and settlement rate at the tunnel centerline are significantly greater than those on both sides of the tunnel. As the shield tunnel machine of the west line crosses the section, the area near the west line tunnel gradually transitions from settlement to uplift. The maximum lateral surface uplift value within the west line tunnel is 18.07 mm.

As the shield tunnel of the east line (trailing tunnel) is excavated, the monitoring data shows that there is approximately 1.23 mm of ground uplift at the axis of the east line tunnel before the shield machine reaches the section. When excavating to ring 30, the shield tunnel machine crosses the monitoring section, and surface settlement at the DB4 section significantly increases. The surface settlement value and settlement rate at the tunnel centerline are significantly greater than those on both sides of the tunnel. At this time, the lateral surface settlement value at the axis of the east line tunnel is 7.95 mm. As the shield tunnel machine of the east line crosses the section, after the grouting is completed, the strata slowly undergo consolidation and rheological changes, eventually reaching a new stress equilibrium, and the ground surface stabilizes. Due to the disturbance caused by the excavation of the west line tunnel, the surface settlement values generated during the excavation of the east line tunnel are superimposed. The position of the maximum settlement point shifts towards the centerline between the two tunnels, resulting in a maximum settlement value of 12.24 mm. The settlement trough shows a V-shaped pattern.

Compared to the previous three sections, in the lateral monitoring process of this section, there is a significant ground uplift near the axis of the west line tunnel. Based on the results of engineering geological exploration and grouting volume data in the shallow buried section (see Figure 12), it is believed that the main cause of surface settlement is the drastic fluctuation in grouting volume during the excavation of the west line tunnel. From Figure 12, it can be seen that the grouting volume for the west line tunnel from ring 29 to ring 30 is 20m3 each, while the average grouting volume for the west line shield tunnel is 36.66 m^3, indicating a significant undersupply of grouting volume. When the west line tunnel advances to ring 31 to ring 35, significant surface settlement has occurred. It is reasonable to increase the control of grouting at this point. However, due to insufficient grouting in the earlier rings, a sudden increase in grouting volume at this stage causes the strata to quickly undergo rheological changes, leading to surface uplift. The grouting volume for the west line tunnel shows a significantly higher level of dispersion compared to the grouting volume for the east line tunnel, indicating that the control of surface settlement during the excavation of the east line tunnel is clearly better than that of the west line tunnel. It can be seen that it is highly important to make reasonable adjustments and controls to excavation parameters during shield tunneling.

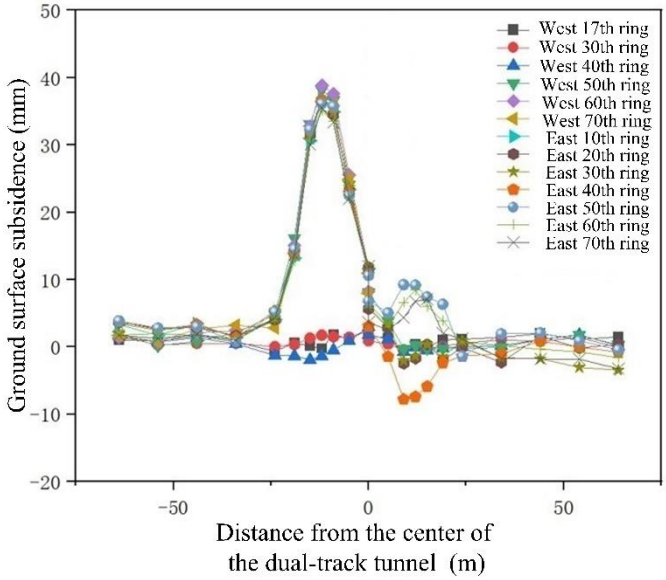

Fig. 17 – Shows the settlement curve of transverse monitoring section DB4.

From Figure 17, it can be seen that as the excavation of the west line (leading tunnel) shield tunnel progresses, monitoring data before the arrival of the shield machine at the section of the west line tunnel axis shows that a ground uplift of approximately 1.73 mm occurs at the west line tunnel axis. When excavating through ring 40, the shield machine crosses the monitoring section. The surface settlement of DB3 section significantly increases, with the maximum lateral surface settlement value obtained at the west tunnel axis reaching 1.94 mm. The settlement trough width is approximately 34 m, and the surface settlement value and settlement rate at the tunnel axis are significantly greater than those on both sides of the tunnel. As the shield machine of the west line tunnels through the section, the area near the west line tunnel gradually changes from settlement to uplift. The maximum lateral surface uplift value of 38.85 mm is achieved on the inside of the west line tunnel.

As the shield tunnel of the east line (trailing tunnel) is excavated, there is no apparent surface settlement before the shield machine reaches the section. When excavating to ring 40, the shield machine crosses the monitoring section, and the surface settlement of the DB5 section significantly increases. Due to the disturbance of the surrounding soil caused by the excavation of the west line tunnel, the surface settlement values generated during the excavation of the east line tunnel are superimposed. The position of the maximum settlement point shifts towards the centerline of the two tunnels. At this point, the maximum lateral surface settlement value of 7.8 mm is obtained at the inner measuring point of the east line tunnel axis. As the shield machine of the east line tunnels through the section, after grouting is completed, the strata slowly undergo consolidation and rheological changes, eventually reaching a new stress equilibrium, and the surface stabilizes. The maximum settlement value eventually reaches 3.37mm, and the settlement trough appears in a V shape.

Similar to section DB4, during the lateral monitoring process of the measuring points in this section, there is also a noticeable surface uplift near the axis of the west line tunnel. This is mainly caused by improper adjustment of the grouting volume in the excavation parameters. The grouting volume of the west line is relatively more dispersed compared to that of the east line. In this section, the advantage of the east line tunnel in controlling surface settlement throughout the excavation process is more evident, further confirming the importance of properly adjusting and controlling excavation parameters.

CONCLUSION

(1) In the initial shallow-buried excavation section, as the excavation distance increases, the total thrust of the shield machine is continuously adjusted during construction. The shield machine gradually reaches a stable operational state, resulting in a gradual reduction in the fluctuation range of the thrust values. Overall, due to the smaller curve radius of the west line, its total thrust is higher than that of the east line.

(2) After the excavation and reinforcement zone on the east line, the cutterhead torque experiences significant growth, leading to a more noticeable adaptation process for the shield machine. The fluctuation of the cutterhead torque is greater in rings 20 to 65 on the east line, showing higher levels of dispersion. This situation is correlated with the wear of the cutterhead and the condition of the shield machine equipment on the east line. On the west line, after the excavation and reinforcement zone, the cutterhead torque is initially decreased. From ring 20 to ring 65, the torque gradually and slowly increases, eventually stabilizing around 12 MN·m.

(3) The excavation speed of the shield machine on the east line displays a similar trend to that on the west line, with a higher level of dispersion. The average and standard deviation of the excavation speed are 5.49 and 2.44, respectively. During the entire excavation process, the shield machine on the east line maintains a relatively high excavation speed within the end soil reinforcement zone, with an average of 7.76 mm/min. As the excavation progresses beyond the reinforcement zone, the overall excavation speed of the shield machine slows down. In rings 021 to 065, the excavation speed is mainly controlled between 2 to 6 mm/min, with an average of 4.49 mm/min. Overall, the speed changes more steadily.

(4) In the initial shallow excavation section, the cutterhead speed is continuously adjusted during construction as the excavation progresses. The cutterhead speed fluctuates noticeably between 0.9 to 1.2 rpm. The average cutterhead speed for the shield machine on the west line is 1.11 rpm, while the average cutterhead speed for the shield machine on the east line is 1.10 rpm. Generally, the cutterhead speed on the east line has a higher level of dispersion compared to the west line.

(5) The water pressure at the cutting face and the air bubble chamber pressure in the initial shallow excavation sections of the east and west lines are showing a gradually increasing trend. The standard deviations of the water pressure at the cutting face in the initial shallow excavation sections of the east and west lines are 0.34 and 0.6, respectively, indicating that the water pressure at the cutting face on the west line has a higher level of dispersion compared to the east line. Similarly, the standard deviations of the air bubble chamber pressure in the initial shallow excavation sections of the east and west lines are 0.34 and 0.50, respectively, indicating that the air bubble chamber pressure on the west line has a higher level of dispersion compared to the east line.

REFERENCES

[1] Gou, Yuxuan, et al, “Experimental study on the mechanical response of metro shield tunnels obliquely crossing ground fissures”, Tunnelling and Underground Space Technology, vol. 132, pp. 104849, 2023, doi: 10.1016/j.tust.2022.104849

[2] Yi, Haiyang, et al, “Influence of long-term dynamic load induced by high-speed trains on the accumulative deformation of shallow buried tunnel linings”, Tunnelling and Underground Space Technology, vol. 84, pp. 166-176, 2019, doi: 10.1016/j.tust.2018.11.005

[3] Li, Chenyang, et al, “Deformation and failure analysis of metro shield tunnel induced by active ground fissure in Xi'an, China”, Engineering Failure Analysis, vol. 142, pp. 106776, 2022, doi: 10.1016/j.engfailanal.2022.106776

[4] Zhao, Mingji, et al, “Optimization of Construction Parameters and Deformation Characteristics of Large-Section Loess Tunnel: A Case Study from Xi’an Metro”, Advances in Civil Engineering vol. 2021, pp.1-21, 2021, doi: 10.1155/2021/6639089

[5] Guo, Kai, and Limao Zhang, “Multi-source information fusion for safety risk assessment in underground tunnels”, Knowledge-Based Systems, vol. 227, pp. 107210, 2021, doi: 10.1016/j.knosys.2021.107210

[6] Lu, Yao, et al, “Deformation characteristics and internal force analysis of shield hoisting construction of working shaft in silty clay strata: Case study in Jinan”, IOP Conference Series: Earth and Environmental Science, vol. 570, no. 5, 2020, doi: 10.1088/1755-1315/570/5/052044

[7] He, Siyue, et al, “A literature review on properties and applications of grouts for shield tunnel”, Construction and Building Materials, vol. 239, pp. 117782, 2020, doi: 10.1016/j.conbuildmat.2019.117782

[8] Chen, Ren-peng, et al, “Experimental study on face instability of shield tunnel in sand”, Tunnelling and Underground Space Technology, vol. 33, pp. 12-21, 2013, doi: 10.1016/j.tust.2012.08.001

[9] Jin, Dalong, et al, “Analysis of the settlement of an existing tunnel induced by shield tunneling underneath”, Tunnelling and Underground Space Technology, vol.81, pp. 209-220, 2018, doi: 10.1016/j.tust.2018.06.035

[10] Xue, Yadong, and Yicheng Li, “A fast detection method via region‐based fully convolutional neural networks for shield tunnel lining defects”, Computer‐Aided Civil and Infrastructure Engineering, vol.33, no.8, pp. 638-654, 2018, doi: 10.1111/mice.12367

[11] Liang, Rongzhu, et al, “Simplified method for evaluating shield tunnel deformation due to adjacent excavation”, Tunnelling and Underground Space Technology, vol.71, pp.94-105, 2018, doi: 10.1016/j.tust.2017.08.010

[12] Yin, Minglun, et al, “Effect of the excavation clearance of an under-crossing shield tunnel on existing shield tunnels”, Tunnelling and Underground Space Technology, vol.78, pp.245-258, 2018, doi: 10.1016/j.tust.2018.04.034

[13] Gong, Chenjie, et al, “Waterproof performance of sealing gasket in shield tunnel: A review”, Applied Sciences, vol. 12, no.9, pp.4556, 2022, doi: 10.3390/app12094556

[14] Huang, Hong-wei, Qing-tong Li, and Dong-ming Zhang, “Deep learning based image recognition for crack and leakage defects of metro shield tunnel”, Tunnelling and underground space technology, vol.77, pp.166-176, 2018, doi: 10.1016/j.tust.2018.04.002

[15] Liu, Dejun, et al, “Structural responses and treatments of shield tunnel due to leakage: A case study”, Tunnelling and Underground Space Technology, vol.103, pp.103471, 2020, doi: 10.1016/j.tust.2020.103471

[16] Zhang, Fengshou, Xiongyao Xie, and Hongwei Huang, “Application of ground penetrating radar in grouting evaluation for shield tunnel construction”, Tunnelling and Underground Space Technology, vol.25, no.2, pp.99-107, 2010, doi: 10.1016/j.tust.2009.09.006

[17] Zhang, J., and Qi, Y, “Research on the intelligent positioning method of tunnel excavation face”, Archives of Civil Engineering, vol. LXVIII, no.1, pp.431-441, 2022, doi: 10.24425/ace.2022.140178

[18] An, H., Song, Y., and Yang, D, “Experimental study of the effect of rock blasting with various cutting forms for tunnel excavation using physical model tests” Archives of Civil Engineering, vol.67, no.3, 2022, doi: 10.24425/ace.2022.140178

CIVIL ENGINEERING JOURNAL

Article no. 14

THE CIVIL ENGINEERING JOURNAL 2-2024

A COMPARATIVE ANALYSIS BETWEEN PERSONAL AND TERRESTRIAL LASER SCANNING FOR THE DOCUMENTATION OF HERITAGE SITES

Arli Llabani and Freskida Abazaj

Polytechnic University of Tirana, Faculty of Civil Engineering, Department of Geodesy, Street Muhamet Gjollesha, Tirana, Albania; arli.llabani@fin.edu.al; freskida.abazaj@fin.edu.al

ABSTRACT

This paper presents a comparative analysis of mobile and terrestrial laser scanning techniques in the 3D surveying of Bashtova castle in Albania, showcasing the integration's efficacy in capturing a comprehensive and accurate representation of this historical structure. Personal laser scanning (PLS), characterized by its mobility and ability to capture data while in motion, offers advantages in terms of efficiency and coverage of large areas. Conversely, terrestrial laser scanning (TLS), with its stationary setup and high precision, excels in capturing detailed information and intricate architectural features. Thanks to the research on the case study of the Bastova Castle in the article, it can be stated that the integration of data from PLS and TLS is seamless with the help of modern software while respecting the basic photogrammetric-geodetic rules and demonstrates the possibility of creating a complex 3D model, usable for further analyses for architects and conservation professionals, as well as for restorers and civil engineers. Research has shown that the difference between point clouds from PLS and TLS is within one centimeter.

KEYWORDS

PLS, TLS, Point Cloud, Accuracy, Bashtova castle, viDOC

INTRODUCTION

In the realm of heritage preservation and archaeological documentation, the marriage of cutting-edge technologies has become instrumental in unraveling the mysteries of historical structures or objects. Among these, the integration of PLS (personal laser scanning) and terrestrial laser scanning (TLS) stands out as a transformative approach, offering a synergistic solution to the challenges posed by the intricate architecture and expansive landscapes of castles [1].

Geodetic technologies have been used for a long time for the documentation of monuments and objects of heritage conservation. With the development of computer technology and new equipment, the speed and accuracy of documentation work have increased significantly. About 150 years ago, photography began to be used for documentation, and photogrammetry was developed. Electronic systems were gradually integrated into surveying after World War II, and in the 1970s satellite data began to be used in addition to aerial photographs. A major change occurred in the 1990s with the development of commercially available computer technology and the digitization of technology. Nowadays, electronic surveying systems (total stations, GNSS equipment), airborne systems, satellite systems, terrestrial and mobile laser scanning, and automated close-range photogrammetry from the ground and drones are used. The synergy of data from different instruments is a topic of research in many workplaces today [3].

This study delves into the application of this integrated methodology, focusing on the case study of Bashtova Castle. This castle, with its rich historical significance and complex architectural features, serves as a compelling canvas to explore the capabilities and effectiveness of combining mobile and terrestrial laser scanning for the comprehensive 3D surveying of castles.

The allure of castles lies not only in their historical narratives but also in the intricate details of their construction, both inside and out. However, traditional surveying methods often fall short of capturing the full scope of these structures. TLS and PLS, stationed on the ground, specialize in acquiring detailed and precise data about the castle's interiors and architectural nuances. This integrated approach promises a holistic understanding by combining the strengths of these technologies, overcoming challenges such as occlusions, inaccessibility, and the need for comprehensive datasets [4].

Nestled within a captivating landscape, this castle presents a microcosm of challenges that the integrated approach aims to address. As we embark on this exploration of Bashtova Castle, the study not only seeks to showcase the practical implementation of Aerial Photogrammetry and TLS / PLS but also endeavors to shed light on the broader implications for cultural heritage management, archaeological research, and the preservation of historical structures [5].

Through a meticulous examination of the integration process, data acquisition strategies, and the ensuing 3D model generation, this research aims to contribute valuable insights to the evolving field of castle surveying. The findings from the case study are anticipated to demonstrate the efficacy of this integrated methodology, providing a blueprint for future endeavors in unraveling the architectural tapestry of castles and, by extension, our shared cultural heritage [10, 15].

THE CASE PROJECT

This paper uses the castle of Bashtova as a case study. The Bashtova Castle is situated north of the Shkumbini River, three to four kilometers from Vile-Bashtove settlement.

Built in the fifteenth century, this fortress is a stunning example of the various civilizations that have passed through Albania. The location is 20 kilometers northwest of Lushnjë, 15 kilometers south of Kavajë, 36 kilometers north of Fier, and 40 kilometers southwest of Tirana.

It is the only castle in the Balkans to be constructed on a field. The castle is 60 by 90 meters in size and is aligned north to south in a quadrangular configuration. In the eighteenth century, the western portion was renovated. The two round towers to the east and north are 12 meters high, and the walls are nine meters high and one meter wide.

With some brick and tile woven into the structure, it is constructed out of native stone. Three of the seven towers of the Bashtova Castle—two circular and one rectangular—remain standing. This castle is believed to have had two stories, the first of which is subterranean. The shooting ports are still visible, and the castle includes an arcade-style fighting platform that is accessible by stairs. Three rows extend into the walls, while the towers have five rows.

Fig. 1 – Location of Bashtova Castle

INSTRUMENTS USED AND DATA CAPTURING

Selection of Instruments

The selection of instruments for Personal and Terrestrial Laser Scanning for the 3D surveying of the Fortress of Bashtova in Albania necessitated a strategic consideration of the site's unique characteristics and surveying objectives. PLS instruments, renowned for their ability to penetrate vegetation and capture detailed elevation data, were invaluable for mapping dense vegetation within and surrounding the fortress, providing insights into ecological dynamics and historical land use. On the other hand, TLS instruments, with their high precision and ability to capture fine details of structures, were instrumental in documenting the architectural intricacies of the fortress itself. Reduced funding and transportation issues have compelled the usage of smaller instruments. Larger laser scanners mounted on tripods or traditional total geodetic stations could not be used because of this. Therefore, portable measuring devices were used in conjunction with the most advanced geomatics techniques available today [16].

Instruments used

PLS is a basic type of laser scanning and it creates a 3D point cloud with a LiDAR device (Light Detecting and Ranging). It is capable of collecting millions of points in a short time period. For this reason, it is used in many applications such as project monitoring, building diagnostics, progress control, change detection, quality control, and creating part-built, and as-built models [17].

GoSlam RS100i is a PLS instrument and it was used to perform measurements. This PLS uses SLAM technology (simultaneous localization and mapping), which is real-time positioning and mapping technology joined with the IMU /inertial measurement unit). GoSlam RS100i has a scanning

radius of 120 meters and the ability to collect 320,000 points per second. It has a super large field of view angle 360 degree with a spatial point accuracy up to one cm.

Fig. 2 – GoSlam RS100i laser scanner (https://www.goslam.com/product/RS100).

A low-cost solution for mobile mapping can be the viDOC. The viDoc RTK Rover is a vital component of the mapping process, providing real-time kinematic (RTK) location to improve the accuracy of the mapping findings in comparison to the stock GNSS receiver contained in the iPhone. To provide centimetre-level location precision, the viDoc RTK Rover uses the RTK correction signals that are continuously monitored by the CORS stations from satellites. The viDoc RTK Rover is able to improve the system's positioning and receive real-time corrections by pairing it with the iPhone 13 Pro Max over Bluetooth. The accuracy of a VIDOC RTK (Real-Time Kinematic) rover can be quite high, as RTK technology is designed to provide centimeter-level precision in positioning data. When connected to any NTRIP service, the rover synchronized with PIX4Dcatch allows the generation of real-time, RTK-accurate georeferenced photos and 3D models. Studies have indicated that 3D models with an absolute precision of less than 5 cm can be obtained using viDoc RTK.

Fig. 3 – Vidoc RTK rover paired with a smartphone (DJI Ferntech)

Terrestrial Laser Scanning is a cutting-edge technology used to capture highly detailed three-dimensional (3D) data from terrestrial environments. It employs laser beams emitted from a scanning instrument towards an object or surface, measuring the time it takes for the laser pulses to return [19].

Faro Focus S70 Laser Scanner is a TLS instrument and it was used to perform measurements. With a maximum range of up to 70 meters (approximately 230 feet), the S70 can efficiently capture data from large-scale environments, such as buildings, industrial facilities, and outdoor landscapes. Portability is a cornerstone of the S70's design, allowing users to easily transport and deploy the scanner in diverse settings. The intuitive interface and seamless integration

with FARO's software ecosystem make operation straightforward, empowering users to process, analyze, and visualize captured data with ease.

The FARO S70 Laser Scanner utilizes Time-of-Flight (ToF) technology to capture highly accurate three-dimensional (3D) data from terrestrial environments.

Additionally, the FARO S70 integrates other advanced technologies such as rotating mirrors or prisms to direct the laser pulses, high-resolution cameras for capturing color information, and a positioning system (such as GPS or total station) to determine the scanner's location in space. These technologies work in tandem to ensure the scanner captures detailed and accurate 3D data efficiently and reliably.

The combination of ToF technology with these advanced features enables the FARO S70 Laser Scanner to deliver exceptional performance in terms of precision, speed, and versatility, making it a powerful tool for professionals across various industries. This device delivers a measurement accuracy of up to ±1 mm at a 10-meter range, which can slightly vary with increasing distances, ensuring minimal error margins even over its maximum range of 70 meters. The scanner's ability to capture up to 976,000 points per second allows for rapid and detailed data collection, essential for high-resolution 3D models. It performs reliably in various environmental conditions, including bright sunlight and complete darkness, thanks to its robust design and IP54 rating for protection against dust and water splashes. Operating effectively within a wide temperature range of -20°C to 55°C (-4°F to 131°F), the FARO Focus S70 is adaptable to diverse field conditions, ensuring consistent performance. This combination of precision, speed, and environmental resilience makes the FARO Focus S70 an invaluable tool for professionals in surveying, construction, architecture, and industrial applications requiring meticulous 3D documentation.

Fig. 4 – Faro Focus S70 Laser Scanner (https://www.faro.com/en/Products/Hardware/Focus-Laser-Scanners)

METHODS

Ground Control Points Marking

For geolocation of obtained point clouds, five ground control points (GCPs) as targets 60 cm x 60 cm dimensions were used. These GCP targets are easy identifiable on photos; these are placed on the ground within the boundary of the personal and terrestrial laser scanning and serve to possibility to georeference the created photogrammetrical model. For this study, five GCPs were selected and measured with GNSS Trimble R12i receiver, obtaining RTK data from the Albanian National GNSS System "ALBCORS. It is advisable to make the GCPs visible during the scanning area, which is achieved by using high-contrast colors and ensuring that the size of the control points

is sufficiently visible for the flight height at which the work is being performed. The size of the control points shall be determined by the scale of the image; the GCP for the TLS and PLS shall have a clearly identifiable center or point within the accuracy of the ground measurement, in this case approximately two centimeters. The size of the target should be at least 10 pixels for sufficient detection quality. The GCPs should be placed regularly at the edge of the observed locality and at least one in the middle due to model deformation. The accuracy of the ground control points (GCPs) measured using a total station is notably high, achieving an overall precision of approximately two centimeters. This level of accuracy is essential for ensuring the reliability and utility of the geospatial data derived from these points. To enhance the robustness of the measurements, a subset of GCPs was measured twice from different survey stations, allowing for cross-verification of the data. The observed differences in the measured coordinates from these repeat measurements are around 8 millimeters, which is well within the acceptable tolerance for high-precision surveying. This minor discrepancy highlights the consistency and reliability of the total station. The workflow involved meticulously setting up the total station at designated survey stations and precisely measuring the coordinates of each GCP. For validation, certain GCPs were remeasured from alternative stations, providing a means to verify and ensure the accuracy of the initial measurements. The consistency observed in the measurements underscores the effectiveness of the workflow and the reliability of the equipment used, confirming the GCPs as trustworthy benchmarks for high-accuracy geospatial tasks.

Fig. 5 – Ground Control Point distributed around the castle (Google Earth).

The coordinates of GCPs were obtained with one cm absolute accuracy in ETRS89 / Albania TM 2010 coordinate system (epsg:6870).

Tab. 1 - Coordinates of 5 Ground Control Points measured with Total Station

GCP	X (m)	Y (m)	H (m)
1	4,545,881.829	457,710.367	3.474
2	4,545,937.371	457,697.870	3.246
3	4,545,944.403	457,626.342	3.224
4	4,545,864.029	457,647.027	3.012
5	4,545,906.751	457,671.135	3.491

Personal and Terrestrial Laser Scanning

Plans and cross-sections of the fortification were the intended output of the documentation. So, spatial measurement was always the basis. Regarding methodology, all three technologies—PLS, Mobile Laser Scanning (MLS), and TLS—were employed. It must be acknowledged that each has benefits and drawbacks and that the objects for which they are used vary. Larger built-up regions are best mapped using the PLS because it is quick and portable; in the instance of the Vidoc Rtk Rover, there is no texture because the scanner utilized here lacks a camera and simply produces a non-textured point cloud with an accuracy of within 5 cm. [21].

TLS requires more work, but the Faro M70 laser scanner has texture and better accuracy. The drawback is that documentation is done more slowly than with PLS. Currently, photogrammetric documentation is produced at a very high and quick level using SfM or IBMR, which creates a point cloud in a manner comparable to laser scanners. The point cloud in photogrammetric technology is invariably textured. One could argue that photography is a type of scanning as well, albeit one that uses a matrix of detectors and typically does so in an erratic order. Photogrammetry uses pixels and lines rather than metric units, thus you will need to add a scale bar or measure at least one distance on the object [22].

Measurements were conducted using the PLS instrument GoSlam RS100i. This PLS makes use of SLAM (simultaneous localization and mapping) technology, which combines the IMU (inertial measurement unit) with real-time positioning and mapping capabilities. With a scanning radius of 120 meters, the GoSlam RS100i can gather 320,000 points in a second. With a spatial point accuracy of up to 1 cm, it boasts an incredibly broad field of view, spanning 360 degrees. GoSlam took 58 minutes to acquire the data about the castle.

The iPhone 13 Pro Max's high-resolution camera and light detection and ranging (LiDAR) technology were utilized to capture images and gather depth data, respectively. Together 3738 images were collected.

The Pix4Dcatch software was paired with the iPhone 13 Pro Max to enable real-time data gathering and analysis of the LIDAR point cloud data in the field. The Pix4Dcatch program was used to handle the LiDAR sensor data and produce a point cloud. To improve the geolocation accuracy of the mapping results, data from the viDoc RTK rover acquired through the VRS network was also utilised. Using LiDAR point cloud data, the Pix4Dcatch app on the iPhone 13 Pro Max created a preliminary depiction of the point cloud; however, additional image processing was required to create a high-resolution point cloud by providing additional camera sensor data.

Subsequently, the data collected by the iPhone 13 Pro Max was transferred to a computer that was running the Pix4Dmatic application in order to undergo additional processing. Through the integration of the LIDAR point cloud data with the image captured by the iPhone 13 Pro Max, the Pix4Dmatic software generated a more accurate and comprehensive representation of the road infrastructure. Furthermore, the software employed state-of-the-art algorithms and computer vision techniques to improve the accuracy of the mapping results.

The Pix4Dmatic application includes control points that were acquired by field-based georeferencing using GNSS receivers in addition to RTK GNSS data. This information was used to reference the locations in the point cloud that the user had marked and could easily differentiate. Pix4Dmatic's 3D model of the object space is extremely accurate and detailed thanks to its usage of photogrammetric image processing. The software automatically aligned the LIDAR point cloud and picture data, used the RTK GNSS and georeferencing data, and increased the accuracy of the mapping findings.

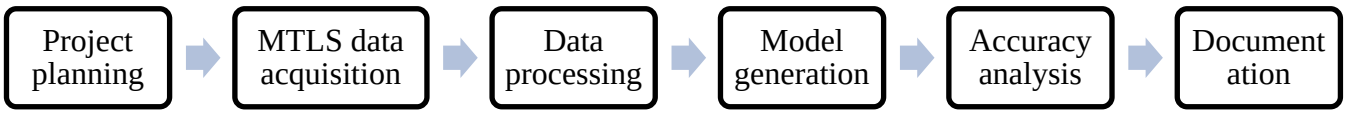

Fig. 6 – The workflow adopted for the study

The FARO S70 Laser Scanner collects extremely precise three-dimensional (3D) data of terrestrial environments using Time-of-Flight (ToF) technology. In order for ToF technology to function, laser pulses are directed at surfaces or objects, and the time it takes for the pulses to return is measured. The scanner generates point clouds, which are accurate three-dimensional depictions of the scanned area, by computing these distances. By working with Faro S70 laser scanner, only five scanner position were used, located in the center and in the corners of the fortress. The integration of ToF technology with these sophisticated functionalities empowers the FARO S70 Laser Scanner to yield remarkable results in terms of accuracy, velocity, and adaptability, rendering it an invaluable instrument for experts in several fields. It took 43 minutes to capture the data for the castle using the Faro S70 [24].

Fig. 7 – Laser Scanner Faro S70 during measurements inside the castle.

RESULTS

Personal Laser Scanning (PLS)

The GoSLAM Studio Flagship Version software was used to process personal laser scanning data. This software is specially designed and developed for the GoSLAM series of mobile 3D scanners, integrating device application and point cloud processing. It is also compatible with third-party device point cloud processing.

The program has eight fundamental features: coordinate transformation, automatic horizontal plane fitting, point cloud splicing, forward photography, automatic point cloud data report production, one-click point cloud denoising, shadow rendering, and point cloud encapsulation. To facilitate data access, GoSLAM incorporates one-click heap data production into bulk metering. Using GoSLAM Studio Flagship, the independently registered PLS point clouds of the castle were aligned. We combined all the data after this alignment to create a single point cloud. A set of spatially measured points is called a point cloud. Each pixel in digital photogrammetry is made up of two coordinates, X and Y. By using photogrammetric processing, it is possible to compute the point cloud from at least two overlapping photos of the same object. A typical point cloud is composed of millions of points,

which together form a 3D shape or view; the points can be coloured by a camera in laser scanning or directly from images in digital photogrammetry.

Fig. 8 – Point Cloud generated from PLS

viDOC

The LiDAR sensor created a point cloud of the region, which gave us a complete 3D representation of the object space and allowed us to understand the road infrastructure, while the camera took pictures of the road infrastructure. The mapping procedure was made more accurate and efficient by using the Pix4Dcatch app for image processing and automated alignment between the photos and LiDAR data. Pix4Dcatch software was used to process the data collected by the RTK Rover and iPhone 13 Pro Max, as depicted in Figure 2, and create a 3D reconstruction of the road infrastructure. The application used RTK data, LiDAR, and image alignment to improve the geolocation accuracy of the mapping results. The precision of the mapping results was further improved by the iPhone 13 Pro Max's capability to receive real-time modifications from the RTK Rover via Bluetooth connectivity.

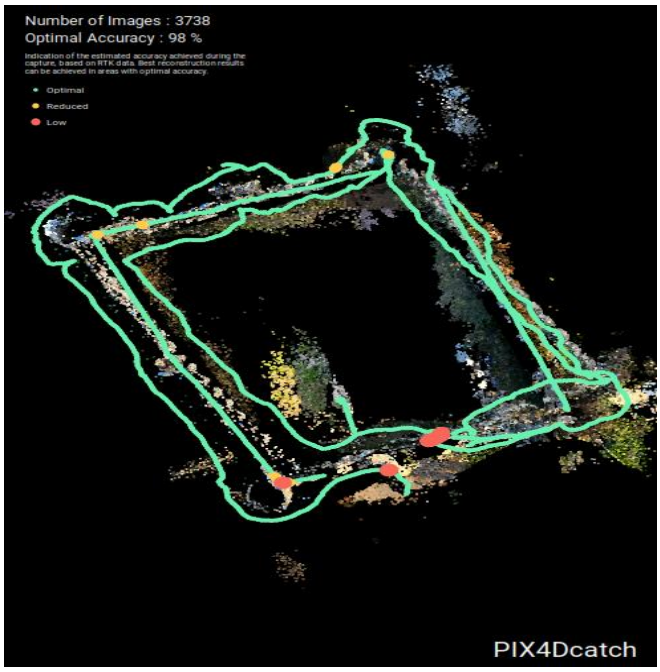

Fig. 9 – Results obtained in Pix4Dcatch

Fig. 10 – Point cloud generated in Pix4Dmatic

Accuracy assessment of viDOC

The absolute correctness of the point cloud data was assessed by contrasting manually measured RTK-GNSS ground control points with the digital relief model (DRM) created from the data. Point clouds created by mobile handheld terrestrial laser scanning need a common reference in order to be compared. In this instance, we used a standard digital relief model (DRM) for evaluation and chose to interpolate the data sets with irregular spacing, like point clouds, using the inverse distance weighting (IDW) technique. The optimal grid resolution for this experiment was determined using Equation 1, which can accurately compute the lowest grid resolution (p) based on the data density. Different DSM surfaces were generated at various grid resolution calculations for each dataset.

$$p = 0.5 * \sqrt{\frac{1}{D}} \quad (1)$$

where D is the average point density (number of points/dm2)

Every RTK-GNSS GCP elevation (ZGCP) and the elevation of the point at the same position (ZDRM) in DRM were compared to determine the elevation difference. ZGCP represents the GCP points with their elevation (Z), while ZDSM represents the points identified in the digital relief model along with their elevation. Additionally, using the vertical differences between the observed RTK-GNSS control points (ZGCP) and the points on the DRM surface at corresponding coordinates, the root mean square error (RMSE) and standard deviation (SD) were calculated. These points are dispersed over the research region and unrelated to the point cloud and DRM creation. This is how the RMSE and SD were computed:

$$RMSE = \sqrt{\frac{\sum_{i=1}^{n}(Z_{GCP}(X_i - Yi) - Z_{DRM}(X_i - Yi))}{n}} \quad (2)$$

$$SD = \sqrt{\frac{\sum_{i=1}^{n}(Z_{GCP}(X_i - Yi) - Z_{DRM}(X_i - Yi) - \mu)}{n-1}} \quad (3)$$

To evaluate absolute accuracy, manually measured RTK-GNSS data were employed. The calculated error statistics for DSM surfaces with respect to each ground control point are shown in Table 1. The table shows that all statistical values are below five centimeters barrier. There were not many changes between the point cloud data that came from each system, according to an analysis of the error statistics of the two systems.

Tab. 2 - Error values of point cloud data

Min (m)		Max (m)	SD (m)	RMSE (m)
-0.08		0.021	0.026	0.048

Terrestrial Laser Scanning

The Faro Scene software was used to process terrestrial laser scanning data. This software is a versatile and robust platform developed by FARO Technologies, renowned for its excellence in 3D measurement and imaging technology. Designed to process, manage, analyze, and visualize 3D point cloud data from various sources, including laser scanners and drones.

Terrestrial laser scanning has become a common tool for documenting monuments, but it has also resulted in a significant surge in data. In two days, more than 16 GB of data—including photographic ones—were collected. In the best-case scenario, a report is generated, and the scans are automatically merged based on the correlation. However, a significant overlap of scans is required, and this can only be done with expertise. For less complicated items, sets of connected scans are formed that need to be manually linked into one using tie points. For more complex objects, the scans join well automatically based on overlap, usually more than 50%. Still, the end product is a 3D model with texture that is of a respectable caliber.

FARO Scene offers a comprehensive suite of tools and features. From efficient data import and management to advanced registration and alignment capabilities, the software empowers users to seamlessly integrate and manipulate large datasets with ease. Its powerful visualization and analysis tools enable precise navigation through point cloud environments, allowing for detailed measurements, annotations, and modeling directly within the software. With seamless export options and compatibility with industry-standard formats, FARO Scene facilitates interoperability with other software applications, ensuring flexibility and efficiency in diverse workflows across industries such as architecture, engineering, construction, and forensics.

After the expedition, all five scans were processed using the Faro Scene program. The totally automated "cloud-to-cloud" technique of joining the gathered scans was based on correlation.

Between four scanner stations, eight linkages were discovered. Due to the Faro S70 laser scanner's ability to make measurements that are reasonably accurate across short distances, the final combined point cloud it produced was designated as the reference measurement.

Fig. 11 – Point Cloud generated from TLS

Comparison of PLS and TLS

Point clouds were generated and transferred to the CloudCompare program from laser scanners. The TLS measurement was chosen as the reference point cloud because, out of the three approaches, it was the most accurate and complicated. According to the computational report, the average overlap is more than 78%, and the differences after automatically connecting four observed point clouds approach only 1 cm. The final point cloud produced by TLS and the point cloud produced by PLS were compared.

Comparing point clouds in CloudCompare software involves a systematic process to analyze and visualize the similarities and differences between multiple datasets. After importing the point clouds into the software, users can utilize various tools and functionalities to conduct the comparison. Cloud-to-cloud distance analysis allows for the measurement of the discrepancy between corresponding points in different datasets, enabling the identification of areas of divergence or alignment. Additionally, registration algorithms can be employed to align the point clouds for accurate comparison, utilizing features such as Iterative Closest Point (ICP) or manual point picking. Visualization tools such as color mapping and slicing enable users to visualize and interpret the comparison results effectively. By leveraging these capabilities, CloudCompare empowers users to conduct comprehensive analyses of point cloud data, facilitating informed decision-making in various fields such as archaeology, geology, and engineering. The point cloud obtained from TLS measurements was used as the reference point cloud. As can be seen from figures 12 and 13, both point clouds are very similar; the peripheral parts are different, which is logical. They contain dissimilar parts. We obtained a mean RMS of 1.15 cm and std. dev was 1.56 cm.

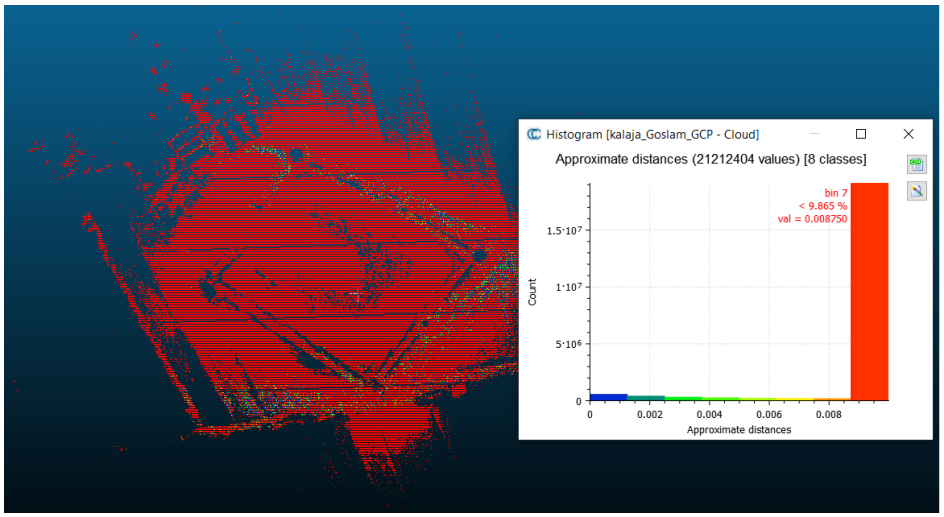

Fig. 12 – Distance computation and histogram in Cloud Compare

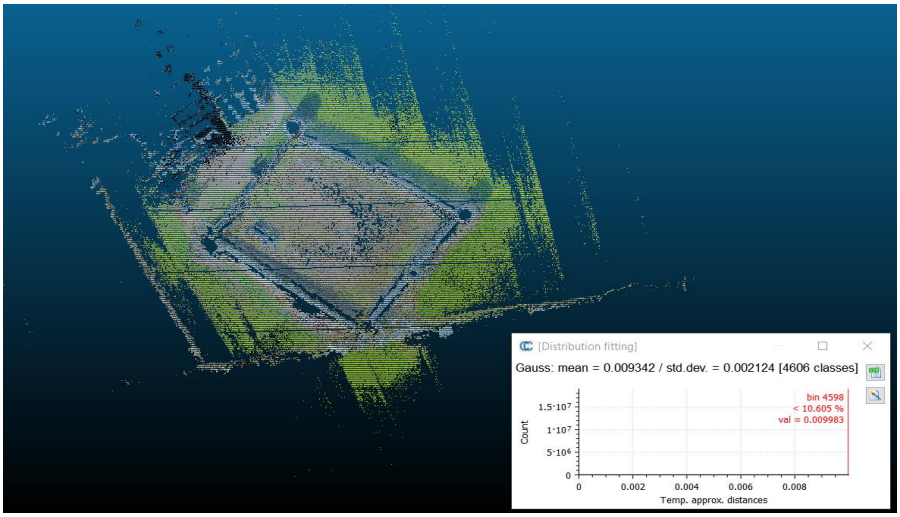

Fig.13 – Results obtained in Cloud Compare

CONCLUSION

TLS and PLS offer distinct advantages and should ideally be selected or combined based on the desired level of accuracy, data coverage, and visual detail needed to preserve and study cultural heritage areas effectively.

PLS technology generate direct point measurements. This makes it the preferred choice when precise dimensional information is critical, such as for intricate architectural elements. It is also economical and perfect for the detailed scanning of objects. The precision is based on IMU and the time of measurement, and of course on complexity of movement; the absolute accuracy can be 1-3cm based on using of GCPs.

Using of iPhone 13 Pro Max with a viDoc RTK Rover was easy to use and sufficiently accurate. The absolute accuracy of the point cloud data was evaluated by hand measurements acquired from a GNSS device. The results demonstrate that the vertical precision of the iPhone-viDoc point cloud data was substantially higher, with error values approaching the centimeter level. The georeferencing of the dataset was completed satisfactorily at the centimeter scale. This suggests that all three approaches may be used to extract road borders and evaluate cross-slopes with a high degree of accuracy. The exact correctness of the point cloud data is determined by comparing manually measured RTK-GNSS ground control points (GCPs) with digital relief models

(DRMs) created from the point cloud data.. The results also show that the iPhone-viDoc point cloud data can be used in place of UAV-LiDAR data for these reasons. PPK application on the viDoc RAW data may be investigated in future studies in an effort to improve the testing and reach even higher georeferencing accuracy. The study provides useful information regarding the mapping and appraisal of heritage sites using low-cost mobile mapping techniques like viDOC.

Personal laser scanning systems, such as handheld or backpack-mounted devices, often provide high-resolution point clouds with exceptional detail, particularly in confined or inaccessible areas. However, the accuracy of PLS may be influenced by factors such as operator skill, motion artifacts, and limited range. In contrast, TLS systems offer superior precision and accuracy over larger areas due to their fixed position and advanced scanning capabilities. Despite this, TLS may struggle with capturing intricate details in complex environments or areas with occlusions. One of the primary advantages of PLS is its portability and flexibility.

PLS systems can be easily transported and deployed in diverse settings, allowing for rapid data collection and on-site processing. This agility is particularly advantageous for documenting heritage sites with challenging terrain or restricted access, where TLS may be impractical or time-consuming to set up. However, the mobility of PLS comes at the cost of reduced scanning range and potential limitations in coverage compared to TLS. The cost of equipment, software, and personnel training is a critical factor in choosing between PLS and TLS for heritage site documentation.

PLS systems generally have a lower initial investment compared to TLS, making them more accessible to smaller organizations or projects with limited budgets. However, ongoing expenses related to maintenance, calibration, and data processing may offset these initial savings over time. In contrast, TLS systems require a larger upfront investment but offer economies of scale for large-scale projects and long-term data archival. Both PLS and TLS generate point cloud datasets that can be integrated with other surveying techniques, such as photogrammetry or ground-based measurements, to create comprehensive 3D models of heritage sites. The complementary nature of these methods enables researchers to combine the strengths of each approach and mitigate their respective weaknesses. For instance, PLS may be used for capturing fine-scale details and textures, while TLS provides accurate geometric data for structural analysis and conservation planning.

The results of the study showed that the TLS offers a constant accuracy than PLS for the documentation of cultural heritage areas. After analyzing our results, we found that there is a one centimeter difference between the point clouds obtained from TLS and PLS. It should be added that the PLS and TLS will not deliver data from the upper parts of the object if it is used as a mobile device carried by the operator. By comparing the point clouds derived from TLS and UAV in CloudCompare software, we obtained a mean RMS of 1.15 cm and std. dev was 1.56 cm. In general, we can recommend both technologies for the documentation of the heritage sites.

REFERENCES

[1] Uysal M, Toprak A.S, Polat, N (2015) DEM Generation with UAV Photogrammetry and Accuracy Analysis in Sahitler Hill. Measurement, 73, 539–543., https://doi.org/10.1016/j.measurement.2015.06.010

[2] Balázsik V, Tóth Z, Abdurahmanov I (2021) Analysis of Data Acquisition Accuracy with UAV. International Journal of Geoinformatics, Vol. 17 Issue 1, p1-10. 10p.m https://doi.org/10.52939/ijg.v17i1.1697

[3] Mulakala J (2019) Measurement Accuracy of the DJI Phantom 4 RTK & Photogrammetry. https://iopscience.iop.org/article/10.1088/1755-1315/1123/1/012015/pdf

[4] Przybilla H.J, Baeumker M (2020) RTK and PPK: GNSS-Technologies for Direct Georeferencing of UAV Image Flights. In Proceedings of the FIG Working Week 2020, Amsterdam, The Netherlands https://www.researchgate.net/publication/341312887_RTK_and_PPK_GNSS-Technologies_for_direct_georeferencing_of_UAV_image_flights

[5] Akgul M, Yurtseven H, Gulci S, Akay A.E (2018) Evaluation of UAV and GNSS-Based DEMs for Earthwork Volume. Arab. J. Sci. Eng., 43, 1893–1909. https://doi.org/10.1007/s13369-017-2811-9

[6] Mohammadi M, Rashidi M, Mousavi V, Karami A, Yu Y, Samali B (2021) Quality evaluation of digital twins generated based on UAV photogrammetry and TLS: bridge case study. Remote Sens. https://doi.org/10.3390/rs13173499
[7] Guo M, Sun M, Pan D, Wang G, Zhou Y, Yan B, Fu Z (2023) High-precision deformation analysis of yingxian wooden pagoda based on UAV image and terrestrial LiDAR point cloud. Herit Sci.;11(1):1. https://doi.org/10.1186/s40494-022-00833-z
[8] Remondino F (2011) Heritage recording and 3D modeling with photogrammetry and 3D scanning. Remote Sens.;3(6):1104–38. https://doi.org/10.3390/rs3061104
[9] Logothetis S, Delinasiou A, Stylianidis E (2015) Building information modelling for cultural heritage: a review. ISPRS Ann Photogramm Remote Sens Spatial Inf Sci.; II-5/W3:177–83. https://doi.org/10.5194/isprsannals-II-5-W3-177-2015
[10] Yastikli N (2007) Documentation of cultural heritage using digital photogrammetry and laser scanning. J Cult Herit.;8(4):423–7. https://doi.org/10.1016/j.culher.2007.06.003
[11] Moon D, Chung S, Kwon S, Seo J, Shin J (2019) Comparison and utilization of point cloud generated from photogrammetry and laser scanning: 3D world model for smart heavy equipment planning. Autom Constr.; 98:322–31. https://doi.org/10.1016/j.autcon.2018.07.020
[12] Kwoczynska B, Piech I, Polewany P, Gora K (2018) Modeling of sacral objects made on the basis of aerial and terrestrial laser scanning. In: 2018 Baltic geodetic congress (BGC Geomatics) p. 275–82. https://doi.org/10.1109/BGC-Geomatics.2018.00059
[13] Hassan, A.T.; Fritsch, D. Integration of Laser Scanning and Photogrammetry in 3D/4D Cultural Heritage Preservation—A Review. Int. J. Appl. Sci. Technol. 2019, 9, 16. https://doi.org/10.30845/ijast.v9n4p9
[14] Albertz, J. A Look Back: 140 Years of Photogrammetry. Photogramm. Eng. Remote Sens. 2007, 73, 504–506.
[15] Aicardi, I.; Chiabrando, F.; Lingua, A.M.; Noardo, F. Recent trends in cultural heritage 3D survey: The photogrammetric computer vision approach. J. Cult. Herit. 2018, 32, 257 266. https://doi.org/10.1016/j.culher.2017.11.006
[16] Erdelyi, J.; Kopacik, A.; Kyrinovic, P. Construction control and documentation of facade elements using terrestrial laser scanning. Appl. Geomat. 2018, 10, 113–121.https://doi.org/10.1007/s12518-018-0208-4
[17] Wang, Y.; Chen, Q.; Zhu, L.; Liu, L.; Zheng, L. A Survey of Mobile Laser Scanning Applications and Key Techniques over Urban Areas. Remote Sens. 2019, 11, 1540. https://doi.org/10.3390/rs11131540
[18] Haala, N.; Alshawabkeh, Y. Combining Laser Scanning and Photogrammetry—A Hybrid Approach for Heritage Documentation, Proceedings of the 7th International conference on Virtual Reality, Archaeology and Intelligent Cultural Heritage VAST'06, Nicosia, Cyprus, 30 October–4 November 2006; Ioannides, M., Arnold, D., Niccolucci, F., Mania, K., Eds.; Eurographics Association: Goslar, Germany, 2006; pp. 163–170. https://doi.org/10.2312/VAST/VAST06/163-170
[19] Jaafar, H.A.; Meng, X.; Sowter, A.; Bryan, P. New approach for monitoring historic and heritage buildings: Using terrestrial laser scanning and generalised Procrustes analysis. Struct. Control. Heal. Monit. 2017, 24, e1987. https://doi.org 10.1002/stc.1987
[20] Pritchard, D.; Sperner, J.; Hoepner, S.; Tenschert, R. Terrestrial laser scanning for heritage conservation: The Cologne Cathedral documentation project. ISPRS Ann. Photogramm. Remote Sens. Spat. Inf. Sci. 2017, 2, 213–220. https://doi.org/10.5194/isprs-annals-IV-2-W2-213-2017
[21] Rodríguez-Gonzálvez, P.; Jiménez Fernández-Palacios, B.; Muñoz-Nieto, Á.L.; Arias-Sanchez, P.; Gonzalez-Aguilera, D. Mobile LiDAR System: New Possibilities for the Documentation and Dissemination of Large Cultural Heritage Sites. Remote Sens. 2017, 9, 189, https://doi.org/10.3390/rs9030189
[22] Pavelka, K.; Šedina, J.; Pavelka, K., Jr. Knud Rasmussen Glacier Status Analysis Based on Historical Data and Moving Detection Using RPAS. Appl. Sci. 2021, 11, 754. https://doi.org/10.3390/app11020754
[23] Bouček, T.; Stará, L.; Pavelka, K.; Pavelka, K., Jr. Monitoring of the Rehabilitation of the Historic World War II US Air Force Base in Greenland. Remote Sens. 2023, 15, 4323. https://doi.org/10.3390/rs15174323
[24] Pavelka, K.; Šedina, J.; Pavelka, K., Jr. Knud Rasmussen Glacier Status Analysis Based on

Historical Data and Moving Detection Using RPAS. Appl. Sci. 2021, 11, 754. https://doi.org/10.3390/app11020754

[25] Matoušková, E.; Pavelka, K.; Smolík, T.; Pavelka, K., Jr. Earthen Jewish Architecture of Southern Morocco: Documentation of Unfired Brick Synagogues and Mellahs in the Drâa-Tafilalet Region. Appl. Sci. 2021, 11, 1712. https://doi.org/10.3390/app11041712

[26] Pix4D, Pix4Dmapper 4.1 User Manual. Lausanne, 2020

[27] Faro Technologies, Faro Scene User Manual. Florida, 2023

CIVIL ENGINEERING JOURNAL

Article no. 15

THE CIVIL ENGINEERING JOURNAL 2-2024

RESEARCH ON OPTIMIZATION OF MOTORWAY ROUTE DESIGN SCHEME IN MOUNTAIN AREAS BASED ON ENTROPY WEIGHT-TOPSIS MODEL

Yunwei Meng[1], Zhenyu Quan[1], Kang Chen[2], Binbin Li[1], Guangyan Qing[3] and Zhongshuai Liu[4]

1. *College of Traffic and Transportation, Chongqing Jiaotong University, Chongqing400074, China; 514346081@qq.com*
2. *School of Civil and Engineering, Chongqing Jiaotong University, Chongqing400074, China; 2606011182@qq.com*
3. *China Merchants Roadway Information Technology (Chongqing) Co., Ltd., Chongqing400067, China; 379544277@qq.com*
4. *China Merchants Chongqing Communications Technology Research & Design Institute Co., Ltd., Chongqing, 400067, China; 499151250@qq.com*

ABSTRACT

During the design process of a new mountainous motorways, multiple route schemes are often proposed for a comprehensive design effort. Each route scheme will have its advantages and disadvantages, so it is often difficult to choose a route scheme. Usually the expert decision method is used to screen the route schemes, but this method mainly relies on the personal experience of experts, and it is difficult to measure the criteria, which can lead to the embarrassing situation that different experts do not agree on the choice of the routes. In order to optimize the route scheme for the design process of mountainous motorways and improve the efficiency and scientificity of route scheme selection, evaluation indicators were selected from traffic safety, construction economy, and environmental friendliness. The Entropy Weight Method (EWM) was used to assign the weight of the evaluation indicators. By improving the Technique for Order Preference by Similarity to an Ideal Solution (TOPSIS), the problem of subjective opinions and excessive reliance on objective data by designers in the multi factor evaluation process was overcome. An EWM-TOPSIS evaluation model was proposed. By analyzing specific examples of mountainous motorway construction, research results were obtained. The results indicate that the model can reflect the designer's intention towards the route scheme and the actual construction project. There is a high degree of consistency with the expert's empirical judgment, which verifies the feasibility and accuracy of the model. This model can provide reliable reference and basis for the decision-making of motorway route schemes in mountainous areas.

KEYWORDS

Mountainous motorway, Route design scheme, EWM-TOPSIS Model

INTRODUCTION

The support role of motorway construction to the national economy is becoming increasingly evident with the development of society. In China, the construction of motorways in mountainous areas is vigorously underway. The design process can determine the direction and operational level of the motorway, and plays a decisive role in the construction of mountainous motorways [1]. The route scheme is the beginning of road design, and leads to other professional design work such as

roadbed, pavement, bridges, and tunnels. In the design process of mountainous motorways, especially in the early stage of route selection, designers need to consider factors such as the difficulty of construction, environmental benefits, economic benefits, investment costs, and vehicle safety, passenger comfort and travel time in the later operation process, while also taking into account factors such as the topography and geological conditions, weather and climate conditions, and local socio-economic development level of the region where the motorway is located.

The geological and topographical conditions of mountainous motorways are complex, and the construction requires a large amount of work, resulting in high costs. In the construction and operation process of mountainous motorways, there may be various problems that need to be solved, and the generation and feasible solutions of these problems are closely related to the route scheme selection. An excellent route scheme refers to a centerline that is technically feasible, economically reasonable, environmentally friendly, and able to meet the needs of multiple parties between the determined starting point and ending point, based on the natural geographical environment, socio-economic environment, technical standards, etc. A scientific and reasonable route plan is the key to achieving the social, economic, and environmental benefits of motorways. A poor route scheme will result in an increase in engineering quantity and construction difficulty. In the later operation stage, there will also be adverse consequences such as high energy consumption, high traffic safety risks, and high maintenance costs. Therefore, route scheme selection is the most important part of the entire design task. In the design process, multiple route schemes are often proposed, which is the result of comprehensive consideration of multiple factors. For multiple schemes, due to different focus areas, there are often difficult to choose optimal route scheme. Given this, scholars have conducted extensive research on this topic.

Regarding the geographical environment where the highway is located, Chen compared and selected route schemes from various aspects such as technical indicators, engineering scale, and cost, social and environmental impact based on the Moyu-Hotan motorway project as an example in desert oasis of Xinjiang, China. After comprehensive analysis, it proposed a recommended scheme [2]. Cao conducted a systematic analysis of the specific impacts of motorway construction on the natural environment, ecological resources and social environment in the selection of design routes in a reservoir area of the Yellow River in China [3]. Through the theoretical method of multiple indicator comprehensive evaluation, it established an environmental impact assessment index system and evaluation model for the motorway route scheme. It screened indicators from environmental impact and technical and economic aspects, and determined 15 evaluation indicators. Wang proposed that at the beginning of conducting route scheme research, it is necessary to understand the regional characteristics and constraints of the project location, sort out the project characteristics and difficulties, propose targeted countermeasures, and then determine the principles of route scheme [4]. Based on comprehensive selection concepts such as standards, terrain, geology, safety and cost, multiple scheme comparisons are proposed. After comparing technical and economic indicators, the recommended plan is ultimately selected to improve the quality of the plan. Zhang et al. introduced the spatial data analysis technology and intelligent evolutionary algorithm of Geographic Information System (GIS) into the road routing process in permafrost regions of the Qinghai-Xizang Plateau to solve the problem of road routing in complex geographical environments [5]. Zhang et al. proposed a scheme optimization method which could realize by using quantum particle swarm algorithm in view of the comparison between through mountain highway and winding mountain highway in mountain highway route selection [6]. GIS, raster space analysis and Google Earth are also commonly used software tools which can be used for rough selection of route design schemes [7][8]. Some highway route selection schemes focus on economic indicators [9].

Regarding the determination of indexes used in the evaluation of route schemes, the following methods have been mainly used. Analytic Hierarchy Process (AHP) method is used to determine the weights of various indexes [10]. An improved Fuzzy Analytic Hierarchy Process (FAHP) method is adopted to calculate weights [11] [12]. The method that combines AHP and GIS is used [13]. The weights of each index are determined by combining AHP with EWM [14]. The method of combining AHP with variable weight calculation is used to determine index weights [15].

A multiple-criteria weighting method is applied, which involves combining multiple weighting methods to determine the weights of each index comprehensively [16].

In terms of comparing and selecting route schemes, the following methods have been mainly used. Fuzzy Comprehensive Evaluation Method [17], a comparison made by listing and comparing each item one by one [4], Cloud Model Theory [18], TOPSIS method [19] and improved TOPSIS method [20], game decision model [21], Preference Ranking Organization Method for Enrichment Evaluations method [22].

In the evaluation of route schemes, the determination of index weights plays a crucial role and is also the focus of research. In previous studies, the methods used either relied too heavily on experts' experiences, required a lot of effort for 3D modeling, or could be influenced by subjective factors. Thus, there is still no widely accepted method for evaluating route schemes for motorways in mountainous areas, indicating that the evaluation of route schemes is a sustained and worthy research topic. This paper uses EWM to determine the weights of indexes and TOPSIS model to calculate the proximity values of each scheme for optimal selection, which avoids the limitations of consulting a large number of experts and ensures the scientificity of the evaluation results [23].

METHODS

The EWM-TOPSIS evaluation method used in this article can be summarized into 6 steps, as shown in Figure 1. The first step is to screen and determine the primary evaluation indexes for the design scheme of mountainous motorway routes. The second step is to screen and determine the secondary evaluation indexes. The third step is to form an index set. The fourth step uses the EWM to calculate the weights of each index. The fifth step is to use the optimized TOPSIS to construct a calculation evaluation model and calculate the relative closeness values of each route design scheme and the ideal solution. The sixth step is based on the size of the relative closeness values, optimal route scheme is decided.

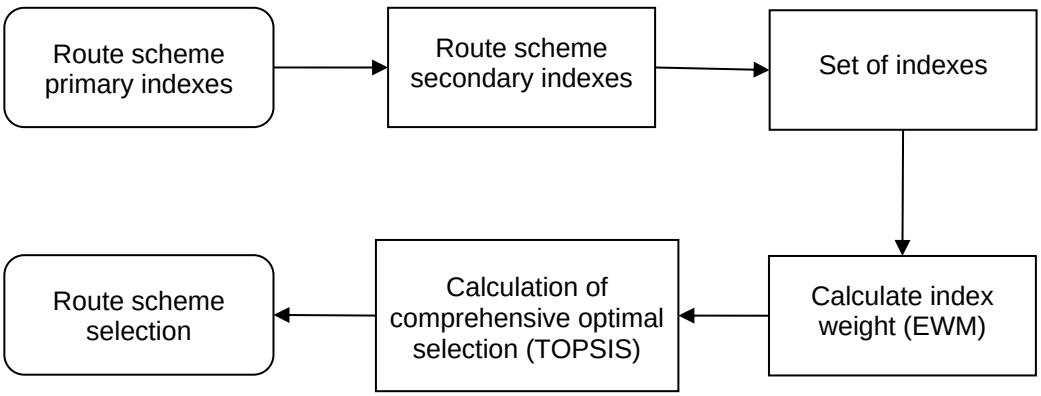

Fig. 1 – Steps of comprehensive optimization selection for route schemes

Evaluation indexes

AHP method is used for establishment of an index system. According to the degree of profit and loss of the objective, evaluation indexes can be divided into several types. A satisfactory route design scheme for a mountainous motorway needs to achieve the goals of traffic safety, good economic benefits, and ecological friendliness. Therefore, safety, economy, and ecology are set as the target. Based on the goals that need to be achieved, evaluation indexes should be constructed from the perspectives of alignment, cost, and environment, which are the primary indexes. In the selection of evaluation indexes, it keeps being consistent with the design indicators proposed in Technical Standard of Highway Engineering and Design Specification for Highway Alignment in order to facilitate the adoption of designers [24] [25].

In the design process of mountainous motorways, horizontal curves are one of the commonly used alignment types. The horizontal curves consist of circular curves and spiral. Their length and radius directly affect the safety and driving comfort of traffic [26] [27], and are also closely related to the visual physiological and psychological load levels of drivers. It is generally believed that the larger the radius and length of the horizontal curve, the higher the safety of driving [28]. Therefore, horizontal curve indexes can be used as the profit-type indexes in the alignment. Based on the same consideration as the horizontal curve, the radius value of the vertical curve can also be used as the profit-type index. The steep slope section is a traffic accident-prone section. In the design of mountainous motorways, the route scheme is often restricted by the terrain and has to use greater grade. It is generally believed that the larger the grade, the more unfavorable to traffic safety [29]. Therefore, the maximum grade can be used as one of the loss-type indexes of the alignment. The composite slope is an important alignment index for comprehensive evaluation of traffic safety [30], which is the combination value of horizontal and vertical cross. The extreme value usually appears where horizontal curves and steep slopes are combined. It is determined according to the design speed of the motorway. The composite slope is an interval-type index.

The construction and installation cost is that the project construction party needs to raise for the construction. This index belongs to the loss-type. Generally, there is a large amount of excavation and filling work in the construction of mountainous motorways, and the excavation work is usually more than the filling work, which will cause a lot of waste materials, not only increasing the excavation cost but also increasing the disposal cost. The filling and excavation balance degree is the ratio of the waste materials to the difference between the excavation and filling before and after soil and rock mass allocation. This index belongs to the interval-type, and 0 is the optimal value. The construction volume of the high-fill and deep excavation section is huge and is also the focus of the later operation and management stage. This index belongs to the loss-type. The length of tunnels is a loss-type index that the construction party strives to control. The separated roadbed is a design work that compromises with the terrain. Compared with the integral roadbed, its cost is lower. Therefore, the length ratio of the separated roadbed can be used as a profit-type index.

For the environmental evaluation index of mountainous motorways, the spatial are divided into open, closed and semi-closed form, which are expressed by the ratio of the height to length in the roadside space, which is degree of closure. The larger this index, the narrower the driving vision, and the more unfavorable it is for safety [31], which is a loss-type index. The slope masonry ratio is the ratio of the exposed masonry to the whole slope area in the surface area of the roadside slope. It is found that the raw and dull masonry structure will increase the psychological load of the driver, which is unfavorable to the driving safety, and this index is loss-type. In the construction of mountainous motorways, there are often adverse geological sections, including landslide slopes, karst caves, debris flows, etc. If the motorway route passes through these sections, there will often be serious hidden dangers, and the impact of motorway construction on the environment will be significant. Therefore, the adverse geological section ratio is proposed as an index, which is the ratio of the length of the adverse geological section to the length of the motorway, and is a loss-type index. The primary and secondary indexes are listed as shown in Table 1.

Tab. 1 - Set of indexes used for route design scheme evaluation

Primary indexes	Secondary indexes		Unit	Type
Alignment	Minimum radius of a horizontal curve	A1	m	Profit-type
	Minimum length of a spiral	A2	m	Profit-type
	Minimum length of a horizontal curve	A3	m	Profit-type
	Minimum radius of crest vertical curve	A4	m	Profit-type
	Minimum radius of sag vertical curve	A5	%	Profit-type
	Minimum length of vertical curve	A6	m	Profit-type
	Maximum grade	A7	%	Loss-type
	Maximum composite slope	A8	%	Interval-type
Cost	Construction and installation costs	C1	Billion yuan	Loss-type
	Cut volume	C2	10000m3	Loss-type
	Balance of filling and cutting	C3	%	Interval-type
	High fill and heavy cut section ratio	C4	%	Loss-type
	Maximum tunnel length	C5	m	Loss-type
	Separate roadbed length ratio	C6	%	Profit-type
Environment	Degree of closure	E1	%	Loss-type
	Slope masonry ratio	E2	%	Loss-type
	Adverse geological section ratio	E3	%	Loss-type

In order to not overlooked the impact of indicators with excessively small or too large values on the route scheme, it is necessary to develop a reasonable calculation method for index values. In actual cases, there may be more than one poor alignment or special section, such as small radius curve and steep grade. If the design speed is different, the required radius of the horizontal curve for the route also varies. When the design speed is 80km/h, a small radius curve refers to a curve with a radius less than 400m. In order to comprehensively consider the influence of multiple small radius curves on the overall route scheme, the formula for calculating the minimum radius of a horizontal curve for the profit-type index is as follows:

$$A = \min(b) \cdot \frac{1}{1+n} \tag{1}$$

Formula (1) is also applicable for calculating other indexes under the influence of multiple poor alignments or special sections on the overall scheme, such as the minimum lengths of horizontal and vertical curves, which are profit-type indexes. A represents this type indexes while $min(b)$ represents the minimum value of a certain indexes. n represents the number of poor alignments or special sections in the route scheme, and it is counted when its design value reaches the general value specified by the techinical standards.

For loss-type indexes such as $A7$, the formula is as follows:

$$A = \max(b) \cdot (1+n) \tag{2}$$

$max(b)$ represents the maximum value of a certain index in the route scheme.

For interval-type indexes such as $A8$, the formula is as follows:

$$A = \max(b) + \frac{1}{n} \cdot \sum_{i=1}^{n} ni \tag{3}$$

$max(b)$ represents the maximum value of a certain indexe in the route scheme. ni represents the specific value of the index corresponding to the i-th poor alignment or special section.

The above describes the principles for determining indexes considering the overall impact of multiple poor alignments or special sections within a route scheme. For other single indexes, it can be obtained directly or indirectly from the design drawings.

Weight of evaluation indexes

In the assigning weights to the above evaluation index, the influence of subjective factors cannot be completely avoided, but the relationship between various indexes should be fully considered. Therefore, the EWM is adopted to minimize the subjective tendency of designers. Entropy is a physical quantity that characterizes the disorderly distribution of information and reflects the amount of information. Entropy weight, on the other hand, reflects the amount of useful information carried and transmitted by each index. The greater the useful information carried and transmitted, the higher its entropy weight [32]. The method and steps for calculating the weights of evaluation indexes through EWM are outlined below.

(1) Assuming that there are m route design schemes to be evaluated and n indexes in each scheme, a matrix R is established.

$$R' = (r'_{ij})_{m\times n} \tag{4}$$

(2) After the normalization process, the matrix R is obtained.

If an index is positive,

$$r_{ij} = \frac{r'_{ij} - \min\{r'_{ix}\}}{\max\{r'_{ix}\} - \min\{r'_{ix}\}} \tag{5}$$

If an index is negative,

$$r_{ij} = \frac{\max\{r'_{ix}\} - r'_{ij}}{\max\{r'_{ix}\} - \min\{r'_{ix}\}} \tag{6}$$

$$R = (r_{ij})_{m\times n} \tag{7}$$

(3) Calculate the weight of each index,

$$f_{ij} = \frac{r_{ij}}{\sum_{i=1}^{n} r_{ij}} \tag{8}$$

Where f_{ij} denotes the element in row i-th column j-th.

(4) Determine the entropy of the index,

$$H_j = -k\sum_{i=1}^{m} f_{ij} \ln f_{ij}, k = \frac{1}{\ln m} \tag{9}$$

(5) Calculate the entropy weight of each index,

$$W_j = \frac{1 - H_j}{n - \sum_{j=1}^{n} H_j} \tag{10}$$

(6) The index weight vector is $W = (w_1, \ , w_n)$, from which the weight matrix P is constructed.

$$P=\begin{pmatrix} w_{11} & 0 & \cdots & 0 \\ 0 & w_{22} & \cdots & 0 \\ \vdots & \vdots & \ddots & \vdots \\ 0 & 0 & \cdots & w_{nn} \end{pmatrix} \tag{11}$$

Routed design scheme evaluation model

TOPSIS evaluation method is a multi-attribute decision analysis method suitable for evaluating multiple route design schemes until the optimal route scheme is found, allowing decision-makers to more accurately grasp the differences between various schemes [33]. This evaluation method can flexibly handle the types of evaluation indicators, and any outliers on the evaluation indicators will not affect the evaluation results. It can consider the interdependence between indicators. After determining the weights of evaluation indicators, the improved TOPSIS model is convenient for evaluating route design schemes.

(1) Initial judgment matrix.

There are M route design schemes, and which denote $M=(m_1,\ ,m_n)$, and each scheme has N evaluation indexes which denote $N=(n_1,\ ,n_n)$. Then the decision matrix A is denoted as

$$A=\ (a_{ij})_{m\times n} \tag{12}$$

(2) Positive management for indexes.

For loss-type indexes, $N_x=(a_{ix})$, the following formula is used for positive management.

$$\tilde{a}_{ix}=\max\{a_{ix}\}-a_{ix} \tag{13}$$

For interval-type indexes $N_y=(a_{iy})$, the positive management is performed using the following formula.

$$W=\max\{\mu-\min\{x_{iy}\},\max\{x_{iy}\}-\nu\} \tag{14}$$

$$\tilde{a}_{iy}=\begin{cases} 1-\dfrac{\mu-a_{iy}}{W}\ ,a_{iy}<\mu \\ 1\quad\ ,\mu<a_{iy}<\nu \\ 1-\dfrac{a_{iy}-\nu}{W}\ ,a_{iy}>\nu \end{cases} \tag{15}$$

Where μ,ν represents the upper and lower limits of the interval.

For interval-type indexes $N_z=(a_{iz})$, the positive management is performed using the following equation.

$$M=\max\{|a_{iz}-a_{best}|\} \tag{16}$$

$$a_{iz}=1-\frac{|a_{iz}-a_{best}|}{M} \tag{17}$$

Where abest is the best value for the interval-type index.

(3) Standardization of the judgment matrix.

The normalized metrics are dimensionless to obtain the standard matrix X, with the following equation.

$$x_{ij} = \frac{a_{ij}}{\sqrt{\sum_{i=1}^{n} a_{ij}^2}} \tag{18}$$

(4) Weighting of the standard matrix.

The weighting matrix Z is obtained by multiplying the standard matrix X with the weight matrix obtained in EWM by P.

$$Z = XP \tag{19}$$

(5) Calculation of the minimum and maximum ideal solutions.

Minimum ideal solution,

$$Z^- = (Z_1^-, Z_2^-, \ldots, Z_n^-) = (\min\{z_{i1}\}, \min\{z_{i2}\}, \ldots, \min\{z_{in}\}) \tag{20}$$

Maximum ideal solution,

$$Z^+ = (Z_1^+, Z_2^+, \ldots, Z_n^+) = (\max\{z_{i1}\}, \max\{z_{i2}\}, \ldots, \max\{z_{in}\}) \tag{21}$$

(6) Calculation the distance from each scheme to the minimum and maximum ideal solution.

Distance from the minimum ideal solution,

$$D_i^- = \sqrt{\sum_{j=1}^{n} (Z^- - Z_{ij})^2} \tag{22}$$

Distance from the maximum ideal solution,

$$D_i^+ = \sqrt{\sum_{j=1}^{n} (Z^+ - Z_{ij})^2} \tag{23}$$

(7) Calculating the relative proximity values of each solution to the ideal solution.

$$C_i = \sqrt{\frac{D_i^-}{D_i^- + D_i^+}} \tag{24}$$

The route design schemes are ranked based on the size of their relative proximity values. The larger the value, the closer the route design scheme is to the ideal solution, resulting in a higher ranking. This model enables the determination of the priority ranking for each route design scheme for mountainous motorway.

FAHP method

In design work, designers often use the Fuzzy Analytic Hierarchy Process to select route design schemes, which is a common method and will not be repeated here for its calculation process. The FAHP method relies heavily on the subjective experience of experts, and the calculated results sometimes make it difficult for decision-makers to make up their minds. The purpose of listing the FAHP method here is to first calculate a preferred route scheme, and then use the EWM-TOPSIS method, forming a comparison between the two calculation methods.

CASE STUDY

Overview of construction of motorways in mountainous areas

The D-F-W Motorway, situated in the mountainous and hilly terrain of Chongqing, China, is currently in design process. The motorway connects to already established motorways at its starting and ending points. The project's technical specifications are extensive, with the Mingyue Mountainous Tunnel section serving as a two-way six-lane road, boasting a width of subgrade 33.5m, while the remaining sections are two-way four-lane roads with a width of subgrade 26m. The design speed for the section between the starting point and Yanjiang Motorway is set at 100km/h, while the rest is designed for 80km/h. The total length of the route is about 160km.

Proposal of route design schemes

In the preliminary design stage, when the mountainous motorway passes through Jilong Town, the designer studied and proposed five route plans, named as the Feasibility route, K, C11, C12, and C13. The project owner must choose one route plan from them as the basis for the construction drawing design, and each route design plan is shown in Figure 2.

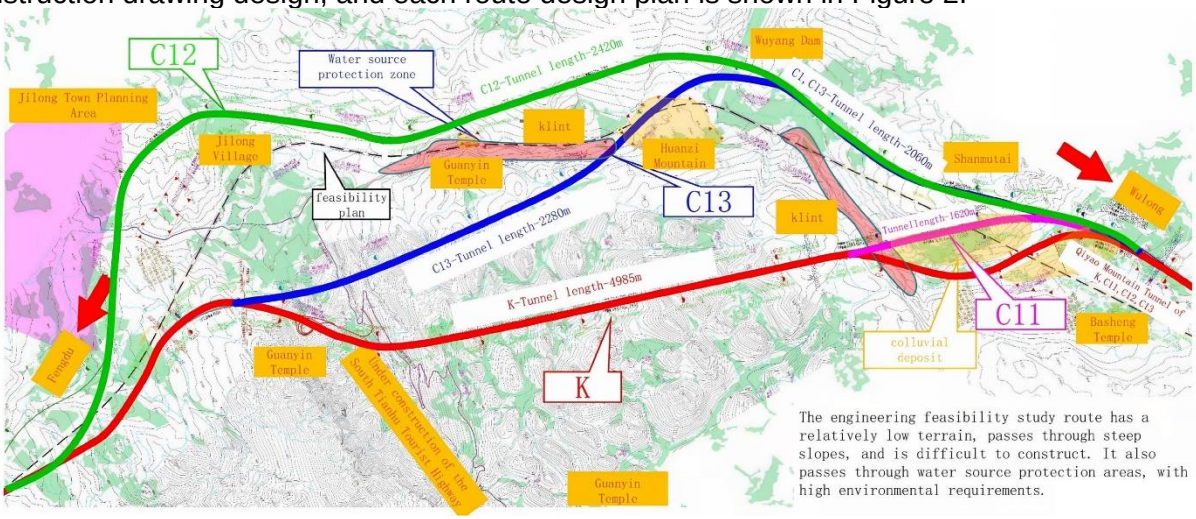

Fig. 2 – Plan of each line scheme

In Figure 2, the feasible route is located in a valley, with an overall low elevation. After passing the Guanyin Temple section, it passes through as an embankment bridge, with a steep slope and many control factors, leading to significant implementation difficulties. Additionally, there will be an extra-long tunnel with a total length of 7,600 meters, which will cause significant environmental disturbance to the first-level water source protection area. Therefore, during the on-site survey stage of the design work, the scheme was found to be not feasible. Next, it is necessary to study four route design schemes. This section of the motorway cannot avoid passing through unfavorable geological sections such as landslide deposits. After detailed work by the designer, the evaluation indexes of the four route design schemes are shown in Table 2.

Tab. 2 - Value of indexes for each design scheme

Primary indexes	Secondary Indexes	K	C11	C12	C13
Alignment	A1	2050	2050	2520	2663
	A2	104	112	90	94
	A3	354	340	286	326
	A4	12000	12000	13000	12500
	A5	7000	7000	5500	6000
	A6	266	331	348	331
	A7	2.5	2.5	3.51	2.98
	A8	3.62	3.62	4.38	4.17
Cost	C1	17.985	18.881	20.387	20.135
	C2	192.289	176.715	242.431	209.004
	C3	10.6	15.9	7.5	9.1
	C4	20.6	16.1	23.4	25.9
	C5	4985	4985	2420	2280
	C6	4.3	4.5	5.8	6.1
Environment	E1	54.7	82.2	32.3	33.6
	E2	11.9	6.7	19.6	22.8
	E3	9.7	1.3	2.1	2.8

Based on the index value, a radar chart can be presented to more intuitively reflect the differences among the route schemes, as shown in Figure 3. Each route scheme has its own advantages and disadvantages. It is difficult to select excellent route design schemes. Here, the model presented in this article is used to select the optimal route scheme.

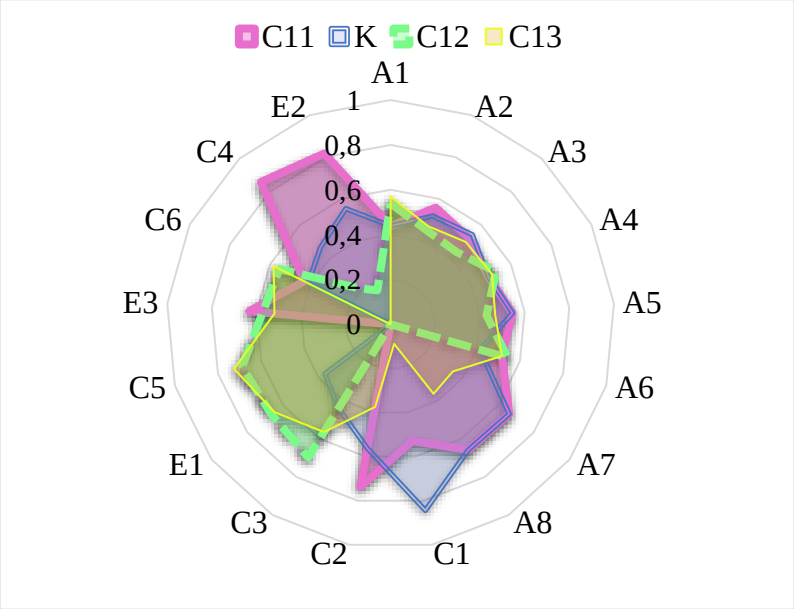

Fig. 3 – Radar chart of evaluation indexes

RESULTS

Evaluation result using FAHP method

The designer uses the Fuzzy Analytic Hierarchy Process to select the route design scheme, and the scoring results are shown in Tables 3-6. There are 20 experts recruited, all of whom are senior engineers with a working experience of no less than 20 years. Among them, 5 are in the alignment major, 5 are in the cost major, 5 are in the environmental major, and 5 are in the bridge and tunnel major. Based on the scoring results, the weights of the primary and secondary indexes

are calculated as shown in Table 7. It can be seen that the cost has the highest weight in the primary indexes, followed by the linear indicator. The highest weight among the secondary indexes is the construction and installation cost, and the weight of each environmental index is greater than that of the alignment index. This indicates that cost indexes are significantly more valued by experts, while alignment indexes can make compromises when meeting the specification and standard.

Tab. 3 - Expert scoring of primary indexes

Primary index	Alignment	Cost	Environment
Alignment	0.5	0.3	0.65
Cost	0.7	0.5	0.85
Environment	0.35	0.15	0.5

Tab. 4 - Expert scoring of alignment indexes

Alignment indexes	A1	A2	A3	A4	A5	A6	A7	A8
A1	0.5	0.7	0.75	0.55	0.6	0.7	0.4	0.45
A2	0.3	0.5	0.55	0.35	0.4	0.5	0.2	0.25
A3	0.25	0.45	0.5	0.3	0.35	0.45	0.15	0.2
A4	0.45	0.65	0.7	0.5	0.55	0.65	0.35	0.4
A5	0.4	0.6	0.65	0.45	0.5	0.6	0.3	0.35
A6	0.3	0.5	0.55	0.35	0.4	0.5	0.2	0.25
A7	0.6	0.8	0.85	0.65	0.7	0.8	0.5	0.55
A8	0.55	0.75	0.8	0.6	0.65	0.75	0.45	0.5

Tab. 5 - Expert scoring of cost indexes

Cost indexes	C1	C2	C3	C4	C5	C6
C1	0.5	0.75	0.7	0.55	0.65	0.7
C2	0.25	0.5	0.45	0.3	0.4	0.45
C3	0.3	0.55	0.5	0.35	0.45	0.5
C4	0.45	0.7	0.65	0.5	0.6	0.65
C5	0.35	0.6	0.55	0.4	0.5	0.55
C6	0.3	0.55	0.5	0.35	0.45	0.5

Tab. 6 - Expert scoring of environment indexes

Environment indexes	E1	E2	E3
E1	0.5	0.35	0.45
E2	0.65	0.5	0.6
E3	0.55	0.4	0.5

Tab. 7 - Weight of each index calculated by FAHP

Primary indexes	Weight	Secondary indexes	Weight
Alignment	32.08%	A1	4.44%
		A2	3.39%
		A3	3.13%
		A4	4.17%
		A5	3.91%
		A6	3.39%
		A7	4.96%
		A8	4.70%
Cost	47.08%	C1	9.45%
		C2	6.62%
		C3	7.19%
		C4	8.88%
		C5	7.75%
		C6	7.19%
Environment	20.83%	E1	5.90%
		E2	8.25%
		E3	6.68%

According to the weights in the FAHP method, the evaluation results of the four route design schemes are shown in Table 8. In the evaluation results, the C12 and C13 schemes were eliminated, while the scores of the K scheme and C11 scheme were relatively close. In order to obtain more accurate evaluation results, a combination of EWM-TOPSIS model will continue to be used for further research.

Tab. 8 - Evaluation results obtained by FAHP method

Scheme	K	C11	C12	C13
Score	0.46	0.49	0.36	0.39

Evaluation result using EWM-TOPSIS model

The weights of each index are calculated using the EWM as shown in Table 9. The cost index has the highest weight, accounting for 56.96% of the total weight. The weight of the environmental index is 26.31%, while the alignment index has the smallest proportion, accounting for 16.73%.

Tab. 9 - Weights of each index calculated by EWM

Primary indexes	Weight	Secondary indexes	Weight
Alignment	16.73%	A1	0.18%
		A2	0.09%
		A3	0.08%
		A4	0.01%
		A5	0.13%
		A6	0.12%
		A7	8.12%
		A8	7.99%
Cost	56.96%	C1	13.24%
		C2	8.06%
		C3	7.60%
		C4	10.50%
		C5	17.28%
		C6	0.29%
Environment	26.31%	E1	7.97%
		E2	11.09%
		E3	7.25%

In the EWM-TOPSIS model, the proximity of each route scheme obtained using the weights of indexes calculated is shown in Table 10. The results show that the proximity value of the C11-scheme is the highest, at 0.3812. The proximity value of the K-scheme is 0.2757. The values of C12 and C13 schemes are 0.2143 and 0.2288, respectively, indicating that even if the tunnel length decreases, it is still not enough to offset the contribution of other factors, and the proximity values of these two schemes differ significantly from that of the C11 and K schemes. This also demonstrates that the results obtained using the EWM-TOPSIS model proposed in this paper are consistent with the expert experience.

Tab. 10 - Relative proximity values for each scheme by EWM-TOPSIS

K	C11	C12	C13
0.2757	0.3812	0.2143	0.2288

CONCLUSION

In response to the problem of difficult selection of route schemes for mountainous motorways, it selected 17 evaluation indexers that refer to alignment, cost, and environmental characteristics, and proposed a comprehensive optimization EWM-TOPSIS model. This model was applied in a mountainous motorway project in Chongqing, China, and more intuitively determined the route design scheme than the FAHP method commonly used by designers, verifying the rationality of the model. Due to the difficulty in obtaining some data in the case study, such as the construction period and the interference of the project to surrounding residents, the evaluation index system constructed in this article needs to be improved in subsequent research. The use of EWM can quantitatively calculate the weight of indexes, which can reflect the objectivity of the method, but it cannot completely eliminate subjective bias factors, especially in the construction of mountainous motorways. The opinions of experts who have worked for many years are still important for design work.

ACKNOWLEDGEMENTS

This research was supported by National Key Research and Development Program of China(Project No.2022YFC3002603), Natural Science Foundation of Chongqing, China(Project No. cstc2019jcyj-msxmX0342), Graduate Joint Training Base Construction Project of Chongqing (Project No. JDLHPYJD-2020029).

REFERENCES

[1] Xu J., 2018. Road Survey and Design. China Communications Press Co. Ltd. Beijing, China

[2] Chen J., 2018. An example of route scheme comparison and selection in the desert oasis area of Xinjiang. Transportation World, (26), pp.45-47. http://dx.doi.org/10.16248/j.cnki.11-3723/u.2018.26.018

[3] Cao Z., 2021. Research on the optimal route scheme of highways in the Gongboxia Reservoir area of the Yellow River considering environmental impacts. [Master's thesis, Lanzhou Jiaotong University]. Lanzhou Jiaotong University. http://dx.doi.org/10.27205/d.cnki.gltec.2021.000222

[4] Wang J., 2022. Comparison and optimization of route schemes for complex sections of highways in mountainous areas. Transportation World, 621(27), pp.121-123.

[5] Zhang C., Yang K., Wang S., Yang H., & Shao G., 2016. Highway intelligent route selection method in permafrost region of Qinghai-tibet Plateau. Journal of Traffic and Transportation Engineering, 16(4), pp.14-25. http://dx.doi.org/10.19818/j.cnki.1671-1637.2016.04.002

[6] Zhang C., Xiang Y., Lin X., Zhang K., & Zhou Y., 2022. Slope combination design of highway superelevation transition section considering slope drainage. Journal of Railway Science and Engineering, 19(8), pp.2278-2286. http:// dx.doi.org/10.19713/j.cnki.43-1423/u.t20210985

[7] Zhao X., 2021. Research on road route selection design based on Google Earth intelligent system. Journal of Physics: Conference Series, 2023(1), p.012013. http://dx.doi.org/10.1088/1742-6596/2023/1/012013
[8] Yang J., & Zhou Z., 2021. Highway route selection based on raster space analysis algorithm under geological cisaster background. Advances in Transportation Studies, 54, pp.195-202. https://doi.org/10.53136/979125994054413
[9] Sarı F., & Sen M., 2017. Least cost path algorithm design for highway route selection. International Journal of Engineering and Geosciences, 2 (1), 1-8. https://doi.org/10.26833/ijeg.285770
[10] Zhu H., & Chen Y., 2013. Route selection of expressway based on VE and AHP. Applied Mechanics and Materials, 357–360, 2420–2425. https://doi.org/10.4028/www.scientific.net/amm.357-360.2420
[11] Lu H., & Wu Z., 2020. Optimization and application of highway route schemes based on the FAHP evaluation system. Highway Engineering, 45(6), 149-154. http://dx.doi.org/10.19782/j.cnki.1674-0610.2020.06.024
[12] He X., 2021. Application of fuzzy analytic hierarchy process and three-dimensional terrain model in traffic routes selection. Journal of Physics: Conference Series, 2083(2), p.022027. http://dx.doi.org/10.1088/1742-6596/2083/2/022027
[13] Sameer Y. M., Abed A. N., & Sayl K. N., 2021. Highway route selection using GIS and analytical hierarchy process case study Ramadi Heet rural highway. Journal of Physics: Conference Series, 1973(1), p.012060. https://iopscience.iop.org/article/10.1088/1742-6596/1973/1/012060
[14] Cheng X., Guan D., & Xia J., 2021. Research on the route selection of expressways based on IAHP-EWM. Highway, 66(2), pp.63-68.
[15] Kang Y., Chen S., Zhang C., Wang Z., & Tan H., 2019. Highway route optimization based on variable weight calculation. Journal of University of South China (Natural Science Edition), 33(4), pp.44-48.
[16] Mondal M. S., Garg R. D., Pandey V., & Kappas M., 2021. Route alignment planning for a new highway between two cities using geoinformatics techniques. Egyptian Journal of Remote Sensing and Space Science, 24(3), pp.595-607. https://doi.org/10.1016/j.ejrs.2021.05.003
[17] Yang S., 2021. Application of fuzzy comprehensive evaluation in route scheme comparison of highway engineering. Highway and Automobile Transport, (5), pp.91-94.
[18] Han F., Liu Z., Li L., Yin W., & Wu J., 2022. Study on ecological risk evaluation and optimum selection of desert expressway schemes based on the two-dimensional cloud model. Mathematical Problems in Engineering, 2022, pp.1-13. https://doi.org/10.1155/2022/1361861
[19] Liu C., Wang Q., & Cao Z., 2022. An Intelligent Optimization Method for Highway Route Selection Based on Comprehensive Weight and TOPSIS. Plos One, 17(2). e0262588. https://doi.org/10.1371/journal.pone.0262588
[20] Liang X., & Meng X., 2019. An extended ftopsis method for freeway route selection in the pre-feasibility study stage. Physica A: Statistical Mechanics and Its Applications, 526, p.120871. https://doi.org/10.1016/j.physa.2019.04.107
[21] Huang Y., & Zeng Q., 2008. Game decision-making model of highway route selection scheme. Journal of Changsha Railway University (Social Science Edition), 28(1), pp.225-230.
[22] Vilke S., Krpan L., & Milkovic M., 2018. Application of the multi-criteria analysis in the process of road route evaluation. Tehnicki Vjesnik-Technical Gazette, 25(6), 1851-1859. https://doi.org/10.17559/TV-20170530085451
[23] Huang W., Shuai B., Sun Y., Wang Y., & Antwi E., 2018. Using entropy-TOPSIS method to evaluate urban rail transit system operation performance: the China case. Transportation Research Part A-policy and Practice, 111, pp.292-303. https://doi.org/10.1016/j.tra.2018.03.025
[24] CCCC FIRST HIGHWAY CONSULTANTS CO.LTD, 2014. Technical Standard of Highway Engineering, China Communications Press Co. Ltd. JTG B01-2014.
[25] CCCC FIRST HIGHWAY CONSULTANTS CO.LTD, 2017. Design Specification for Highway Alignment, China Communications Press Co. Ltd. JTG D20-2017.
[26] Geng Y., Zhou H., Gong X., Ma Y., & Chen X., 2021. Evaluation of pavement runoff and driving safety on highway curve segment. Baltic Journal of Road and Bridge Engineering, 16(4), 176-191. https://doi.org/10.7250/bjrbe.2021-16.544

[27] Sil G., Nama S., Maji A., & Maurya A. K., 2020. Effect of horizontal curve geometry on vehicle speed distribution: a four-lane divided highway study. Transportation Letters-the International Journal of Transportation Research, 12(10), pp.713-722. https://doi.org/10.1080/19427867.2019.1695562
[28] Zhang H., Zhang M., Zhang C., & Hou L., 2021. Formulating a GIS-based geometric design quality assessment model for Mountain highways. Accident Analysis and Prevention, 157, p.106172. https://doi.org/10.1016/j.aap.2021.106172
[29] Lan S., Liu Y., Liu B., Sheng P., Wang T., & Li X., 2011. Effect of slopes in highway on traffic flow. International Journal of Modern Physics C, 22(4), pp.319-331. https://doi.org/10.1142/S0129183111016270
[30] Zhang H., Li G., & Xie X., 2022. Research on route selection of cross-mountain highway based on quantum particle swarm optimization. Seventh International Conference on Electromechanical Control Technology and Transportation (ICECTT 2022); 123025H (2022) https://doi.org/10.1117/12.2646024
[31] Meng Y., Zhang X., Qing G., Wang C., Luo J., & Gong W., 2021. Study on the characteristics of visual and mental workload under driving in the spatial domain of mountainous expressways. Journal of Wuhan University of Technology (Transportation Science & Engineering), 45(03), 403-407.
[32] Shang T., Sheng Q., & Bai J., 2019. Safety evaluation of tunnel-interchange sections based on entropy weight matter-element model. Science Technology and Engineering, 19(12), 333-338.
[33]Chen P., 2021. Effects of the entropy weight on TOPSIS. Expert Systems with Applications, 168, p.114186. https://doi.org/10.1016/j.eswa.2020.114186

CIVIL ENGINEERING JOURNAL

Article no. 16

THE CIVIL ENGINEERING JOURNAL 2-2024

EVALUATING FISH PASSAGE EFFICIENCY IN VERTICAL SLOT FISHWAYS USING THE ANALYTIC HIERARCHY PROCESS

Li Jiang and Yuheng Zhai

North China University of Water Resources and Electric Power, School of Water Conservancy, Zhengzhou, East Road Jinshui 136, China; zhaiyuheng@gmail.com

ABSTRACT

Based on the Analytic Hierarchy Process (AHP), a comprehensive evaluation system has been developed to assess the performance of vertical slot fishways. This system incorporates 30 factors related to fish passing efficiency, thereby facilitating a detailed analysis of hydraulic characteristics, engineering layout, operation management, and monitoring. For its practical application, the vertical slot fishway at the Laolongkou Hydro-junction project's comprehensive evaluation was assessed and consequently rated as "Operating Excellently". This rating accurately reflects the fishway's operational status. The case study demonstrates that the established index system and the model calculation method are capable of thoroughly considering the operational conditions of fishways and the applicability of the model. Moreover, the methodology offers valuable experiences and guidance for creating evaluation systems in various other water conservancy project sectors.

KEYWORDS

Analytic hierarchy process (AHP), Vertical slot fishway; Fish passing efficiency; Comprehensive evaluation

INTRODUCTION

The fishway is a project designed to mitigate the damage to the aquatic ecosystem caused by water conservancy projects. It has gained an increasingly important role as advocacy for ecological protection grows.

Researchers have found that different types of fish are attracted to varying flow velocities and patterns. These variations are present at the entrance of the fishway and throughout the fishway chambers [1]. Through experiments, researchers concluded that the main environmental factors affecting fish passage are flow velocity, discharge, upstream water level, and transparency [2]. They proposed: (1) The key points of fishway entrance design include entrance location, entrance flow, flow pattern, entrance structure, the number of entrances, and the entrance working water level; (2) Induction facilities, such as water replenishment facilities and fish barriers, can help improve entrance efficiency; (3) The key points in the design of the main structure are to ensure that the slope, fishway length, flow velocity, turbulent kinetic energy, and other indicators are moderate to prevent fish fatigue; (4) Strengthen the assessment of fish passage facility effectiveness [3]. Researchers have identified that the effectiveness of a fishway is determined by the upstream water level and the fishway's water temperature. Optimal function occurs only when both conditions satisfy the necessary fishway requirements [4]. It has been found that the upward movement of fish is related to season, water temperature, and discharge [5]. In comparing and selecting design plans, factors considered include topography and geology, operation management, and fish migration patterns, which influence the choice of fish passage facility plans [6]. Researchers have found that by conducting hydrodynamic model experiments and implementing measures including the addition of guide vanes, adjusting the width of gaps, and altering the proportions of the fish pass dimensions, the water flow characteristics in the fishway have been significantly enhanced. The direction of flow

distribution is more uniform, and the scale of the resulting counter currents and eddy zones is moderate [7]. The researchers, utilizing staggered arrangements of reed modules, have engineered a fish passage that mimics the natural environment; physical model experiments revealed that these vegetation modules efficiently decelerate the water flow, generating a current akin to that of natural watercourses [8]. Researchers have discovered that placing pylons in the center of fish passages can significantly reduce the size of recirculation zones and decrease the energy of turbulence, with a maximum reduction of up to 18% [9]. Researchers have found that the position of vertical slots can adjust the specific location of the main flow zone within the pool chamber, which in turn influences the layout, size of the recirculation zones, and the overall characteristics of the flow field [10]. Researchers, through studies combining model experiments and numerical simulation methods at three different flow rates, have demonstrated that juvenile silver carp tend to avoid areas with turbulence intensities of 8.5 to 9.2 cm/s during their movement, and prefer waters with turbulence intensities ranging from 5.25 to 8.40 cm/s [11]. Researchers found that the number of fish collected at the outlet of the Ice Harbor fishway is positively correlated with the water level at the dam [12]. In a study of a fishway in Australia, it was noted that environmental factors are associated with fish passage efficiency, with salinity accounting for 21%, flow velocity for 38%, and surface water temperature for 11% [13]. In the Alaskan Steep-pass fishway, researchers observed a significant positive correlation between water temperature and the number of fish passing through [14]. A study on lamprey revealed that the rate of fish entering the fishway increases with temperature [15]. Furthermore, researchers found that water flow velocity within the fishway is positively correlated with fish passage efficiency, while the slope and length of the fishway are negatively correlated with passage efficiency [16]. The researchers' model experiments show that by adjusting the width of the pool, the slope of the fishway, and the roughness of the bottom, it can be confirmed that the flow patterns are significantly influenced not only by the slope and the width of the pool but also by the roughness of the bottom. At the same time, the flow coefficient is constrained by the slope and width of the pool chamber and is not significantly related to the magnitude of the flow and the degree of roughness [17]. According to the researchers' observations, the Iberian barbel fish tend to choose areas with lower turbulence energy as their resting zones and then proceed to move through areas with higher velocity and turbulent energy along the main current [18]. Researchers have found that catfish tend to linger longer in regions where the turbulent energy ranges between 0.02 to 0.043 m^2/s^2, suggesting that this level of turbulence is preferred by the catfish [19]. Researchers have found that Reynolds shear stress, τ_{uv}, exerts the greatest influence on fish movement, particularly in fish of smaller size with less swimming capability. This observation is notably pronounced [20]. Judging from current research, many experts and scholars have conducted numerous experiments and identified many factors that affect the efficiency of fish passage. However, due to the multitude of influencing factors, there is currently no scientific, effective, and systematic method for combining these factors to comprehensively evaluate fishway efficiency.

Therefore, based on the Analytic Hierarchy Process (AHP), this paper establishes a vertical slot fishway operation evaluation system considering 30 factors for the fishway's operation.

METHODS

In this study, the Analytic Hierarchy Process (AHP) was primarily used to establish a fishery efficiency evaluation system. In the 1970s, Professor T. L. Saaty [21], an American operations researcher, proposed the Analytic Hierarchy Process (AHP), a method that incorporates both qualitative and quantitative assessments for decision-making. It is designed to tackle evaluation issues involving a variety of scenarios, criteria, and objectives, especially suited for systems that are large in scale, complex in structure, diverse in goals, and abundant in qualitative factors.

ESTABLISHING AN EVALUATION SYSTEM VIA THE ANALYTIC HIERARCHY PROCESS

Basic Principles

The main principle adopted by the Hierarchical Analysis Method is to gradually decompose a complex issue into multiple levels. Starting from the ultimate goal, it identifies and breaks down the various influencing factors that impact the goal, step by step, thereby constructing a hierarchical diagram. Within this diagram, elements at each level correspond to a set of relative importance criteria. These criteria can be assessed through quantitative analysis in order to calculate the relative weight of each criterion, which then guides the selection of the optimal plan or decision-making.

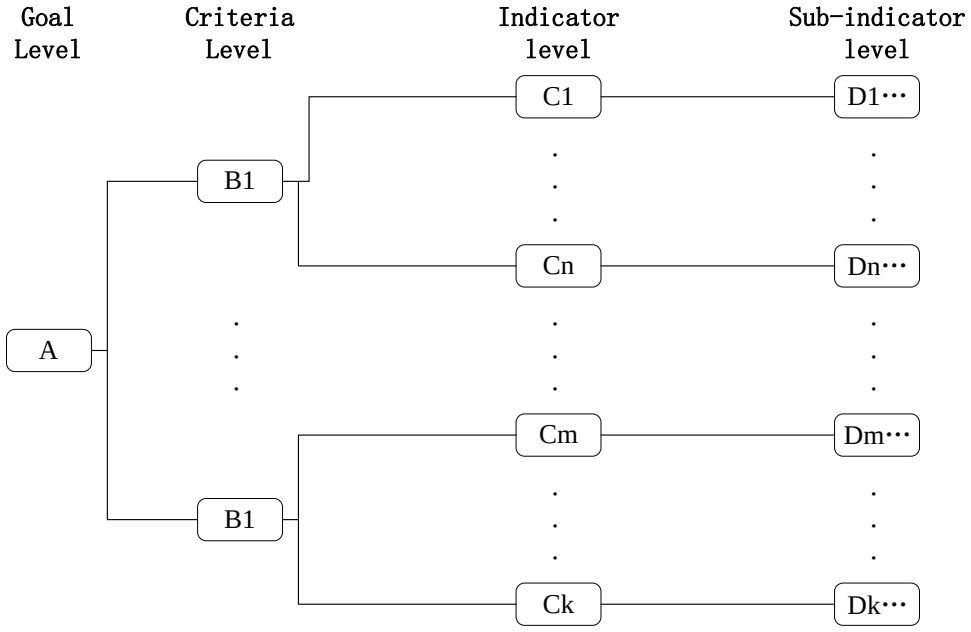

Fig.1 - Structure concept diagram of AHP

Implementing the Hierarchical Analysis Method involves the following steps:

1. Creating a hierarchical model: Based on the nature and key characteristics of the problem to be solved, a tiered model structure is formed, which is refined into different levels step by step.
2. Selecting criteria and factors: For each level, determine the relevant evaluation criteria and key factors.
3. Establishing the judgment matrix: Build a judgment matrix based on the relative importance of each criterion and factor. The size of the matrix is determined by the number of relevant factors, and the values in the matrix reflect the relative importance between factors, typically expressed on a scale of 1 to 9.
4. Calculating weight values: Use mathematical methods to obtain the weight values of each criterion and factor, which are usually presented in the form of a vector.
5. Consistency verification: Conduct a consistency check on the constructed judgment matrix to ensure the reasonableness and accuracy of the obtained weights, thereby increasing the scientific application of the method.
6. Synthesizing weights: By integrating the weights at various levels, we ultimately obtain a weight vector that represents the importance of each factor in the overall structure, which then assists in the assessment of plans or decision-making.

Overall, the Hierarchical Analysis Method is a practical tool for solving complex decision-making problems and is widely applicable to multiple aspects such as investment choices, strategic planning, product development, project management, and risk assessment.

Tab.1 - Construction form of judgment matrix

	C1	C2	⋯	Cn
C1	C11	C12	⋯	C1n
C2	C21	C22	⋯	C2n
⋮	⋮	⋮		⋮
Cn	Cn1	Cn2	⋯	Cnn

Tab. 2 - Judgment matrix scale

Quantitative scale	Qualitative description
1	Two factors have equal importance.
3	One factor is slightly more important than the other.
5	One factor is moderately more important than the other.
7	One factor is significantly more important than the other factor.
9	One factor is extremely important, almost to the sum of all other factors.
2,4,6,8	Intermediate Judgment Value

System Establishment

The evaluation of fishway operation needs to include as many factors as possible that can affect the operation from an overall perspective, including the impact of hydraulic characteristics, engineering layout, and operation management and monitoring. Therefore, combined with existing research conclusions, an evaluation system for fishway operation has been established based on the current mainstream evaluation methods. The results are shown in Table 1.

Tab .3 - Vertical slot fishway operation evaluation system

Goal Level	Criteria Level		Indicator level		Sub-indicator level	
Vertical slot fishway operation evaluation system	B1	Hydraulic characteristics	C1	Water depth	D1	Water depth at entrance
					D2	Head difference between the upstream and the downstream
					D3	Water depth in fishway
			C2	Flow rate	D4	Inlet flow rate
					D5	Maximum flow rate
					D6	Flow velocity amplitude
					D7	Outlet flow rate
			C3	Discharge	D8	Maximum discharge
					D9	Runoff volume
			C4	Other characteri-stics	D10	Water temperature
					D11	Transparency
					D12	Salinity
					D13	Sand content
					D14	PH
					D15	Turbulence kinetic energy
					D16	Vortex
	B2	Engineering layout	C5	Fishway import	D17	Location
					D18	Import quantity
					D19	Hydraulic jump
			C6	Inside the fishway	D20	Slope
					D21	Total length
					D22	Length of each level
					D23	Vertical slot width
			C7	Fishway exit	D24	Export quantity
					D25	Auxiliary facilities
	B3	Operation management and monitoring	C8	Management	D26	Management level
					D27	Operational model
			C9	Monitor	D28	Species of fish
					D29	Number of fish passed
					D30	Seasonal differences

ESTABLISH EVALUATION INDICATORS AND ASSESSMENT CRITERIA

Quantitative Criteria for Determining Hydraulic Characteristics

1) The Standardized Criteria for Determining Water Depth Quantitatively

Establishing standards based on the ratio of the operational water depth determined by design or measurement to the optimum swimming depth for key fish species.

Tab.4 - Quantitative Evaluation Standards for Water Levels

	A	B	C	D	E
D1	＞0.80	0.80~0.70	0.70~0.60	0.60~0.50	＜0.50
D2	＞0.80	0.80~0.70	0.70~0.60	0.60~0.50	＜0.50
D3	＞0.80	0.80~0.70	0.70~0.60	0.60~0.50	＜0.50

2) Quantitative Determination Criteria for Flow Rate

Developing standards based on the designed or measured operating flow velocity and the optimal swimming flow velocity ratio of the main fish species.

Tab.5 - Quantitative assessment standards for flow rate

	A	B	C	D	E
D4	0.9~1.1	0.8~0.9, 1.1~1.2	0.7~0.8, 1.2~1.3	0.6~0.7, 1.3~1.4	＜0.6, ＞1.4
D5	0.9~1.1	0.8~0.9, 1.1~1.2	0.7~0.8, 1.2~1.3	0.6~0.7, 1.3~1.4	＜0.6, ＞1.4
D6	0.9~1.1	0.8~0.9, 1.1~1.2	0.7~0.8, 1.2~1.3	0.6~0.7, 1.3~1.4	＜0.6, ＞1.4
D7	0.9~1.1	0.8~0.9, 1.1~1.2	0.7~0.8, 1.2~1.3	0.6~0.7, 1.3~1.4	＜0.6, ＞1.4

3) Quantitative Assessment Standards for Discharge

Establish standards based on the ratio of the designed or measured operational flow rate to the preferred flow rate for the primary fish species.

Tab.6 - Discharge quantitative assessment standards

	A	B	C	D	E
D8	0.9~1.1	0.8~0.9, 1.1~1.2	0.7~0.8, 1.2~1.3	0.6~0.7, 1.3~1.4	＜0.6, ＞1.4
D9	0.9~1.1	0.8~0.9, 1.1~1.2	0.7~0.8, 1.2~1.3	0.6~0.7, 1.3~1.4	＜0.6, ＞1.4

4) Quantitative Assessment Standards for Other Characteristics

Tab.7 - Quantitative assessment standards for other attributes

	A	B	C	D	E
D10	Best Temperature (±1℃)	Optimal Temperature (±5℃)	Critical Activity Temperature （±10℃)	Unsuitable Temperature （±15℃)	Extreme Temperature （±25℃)
D11	Turbid Water	/	/	/	Clear Water
D12	Specific Fish Species targeted Plan				
D13	Specific Fish Species targeted Plan				
D14	7.12~7.20	/	7.04~7.12, 7.20~7.34	/	＜7.04, ＞7.34
D15	＜0.15 m²/s²	0.15~0.2 m²/s²	0.2~0.3 m²/s²	0.3~0.5 m²/s²	＞0.5 m²/s²
D16	without eddy	There are a few small eddies.	Occasional large eddies	Fixed occurrence of whirlpools.	The water flow is particularly turbulent.

Establishing Quantitative Judgment Criteria for Engineering Layout

1) Fishway Import Quantitative Assessment Criteria

The entrance of the fishway is crucial for allowing fish to enter the fishway, and its location, the number of entrances, and the water leap conditions have a significant impact on the efficiency of the fishway operation. Optimizing the placement of the entrance, the number of entrances, and the water leap conditions can greatly improve the operational efficiency of the fishway, facilitating the smooth migration and protection of fish.

Tab.8 - Fishway Entrance Quantitative Evaluation Criteria

	A	B	C	D	E
D17	The best location is far away from power stations and other hydraulic structures.	The location is suitable, far away from power stations and other hydraulic structures.	The location is average, not far from power stations and other hydraulic structures.	The location is poor, very close to power stations and other hydraulic structures.	The location is very poor, very close to power stations and other hydraulic structures.
D18	more than one	one	/	/	/
D19	no-water jump phenomenon	/	minor water splash effects		significant water splash effects

2) Quantitative Criteria for Inside the Fishway Assessment

The length of the pool chamber within a fishway, as well as the total length and slope of the fishway, are crucial factors influencing the migration of fish. Additionally, the width of the vertical slots plays a key role in determining the successful passage of migrating fish through the fishway.

Tab.9 - Quantitative Evaluation Criteria for Inside the Fishway

	A	B	C	D	E
D20	＜2°	2°~4°	4°~6°	6°~8°	＞8°
D21	＜200m	200~300m	300~400m	400~500m	＞500m
D22	＜3m	3~3.5m	3.5~6m	6~8m	＞8m
D23	＜0.35m	/	0.35~0.5m	/	＞0.5m

3) Quantitative Criteria for Fishway Exit Assessment

Tab.10 - Quantitative Evaluation Standards for Fishway Exit

	A	B	C	D	E
D24	more than one	one	/	/	/
D25	There are floating debris barriers.	/	/	/	No floating debris barriers

Operation, Management, and Monitoring of Quantitative Determination Standards

1) Management of Quantitative Determination Standards

Tab.11 - Management of Quantitative Assessment Standards

	A	B	C	D	E
D26	Excellent	Good	Average	Below average	Below standard
D27	Beneficial management	/	Partially effective management	/	Ineffective management

2) Monitoring Quantitative Determination Standards

The standards for the types and quantities of migratory fish should be based on the percentage of the fish species and quantities passing through fishways to the total number and species of upstream migrating fish in the basin. Seasonal variations should be considered based on the number of months when major fish migrations occur each year to establish standards.

Tab.12 - Monitoring Quantitative Assessment Standards

	A	B	C	D	E
D28	90%~100%	75%~90%	60%~75%	50%~60%	＜50%
D29	85%~100%	75%~85%	60%~75%	50%~60%	＜50%
D30	＞4 months	3~4 months	2~3 months	1~2 months	＜1 month

INTEGRATED EVALUATION METHOD

Construct the Judgment Matrix

Use the AHP method to determine the weight of each factor, to compare the importance of the various indicators, and to quantify the significance of each factor [22].

Through multi-channel research, 10 expert evaluation forms were collected. These forms underwent screening and analysis, after which the sum-product method was applied to address the problem. The formula for the sum-product method is as follows:

$$\int_{a_1}^{b_1}\int_{a_2}^{b_2}\cdots\int_{a_n}^{b_n} f(x_1,x_2,\cdots,x_n)dx_1dx_2\cdots dx_n = \int_{a_1}^{b_1}\int_{a_2}^{b_2}\cdots\int_{a_{n-1}}^{b_{n-1}}\left[\int_{a_n}^{b_n} f(x_1,x_2,\cdots,x_n)dx_n\right]dx_{n-1}\cdots dx_1 \quad (1)$$

Assessment of Consistency in Judgement Matrices

After constructing the judgment matrix, it is essential to verify that the weights are credible and reasonable by performing a consistency test to determine if the matrix satisfies the required consistency criteria.

To determine whether the matrix satisfies consistency, it should be evaluated based on the Consistency Ratio (CR), which is the ratio of the Consistency Index (CI) to the Random Index (RI). The CI is calculated using the maximum eigenvalue and the order of the matrix, while the RI is derived from a standardized table corresponding to the matrix's order, as shown in Table 11. Generally, if CR is less than 0.1, the judgment matrix is considered consistent; otherwise, if CR is 0.1 or greater, the judgment matrix is not consistent, and adjustments to the matrix are necessary before recalculating and analyzing it again.

Tab. 13 - Random Index (RI) Values [21]

Order n	1	2	3	4	5	6	7	8	9	10
RI	0	0	0.52	0.89	1.12	1.26	1.36	1.41	1.46	1.49

Weight Calculation in Evaluation Systems

First, we carry out the weight calculation for the criteria layer of the vertical slot fishway operation evaluation system, which includes hydraulic characteristics, engineering layout, operation management, and monitoring. The corresponding judgment matrix is as follows:

$$A=\begin{bmatrix} 1 & 1.33 & 2.5 \\ 0.75 & 1 & 2 \\ 0.4 & 0.5 & 1 \end{bmatrix} \quad (2)$$

After the calculation, the weights for the criteria layer—which comprises hydraulic characteristics, engineering layout, operation management, and monitoring—are as follows:

$$[0.4634 \quad 0.3551 \quad 0.1815] \quad (3)$$

The maximum characteristic root is 3.000, the CI is 0.000, and the RI is 0.520. The calculated CR is 0, which is less than 0.1, indicating that the judgment matrix passes the consistency test.

Similarly, the weights of the indicator layer and the sub-index layer within the vertical slot fishway operation evaluation system have been calculated. The corresponding judgment matrix and the results are presented in Table12 as follows:

Tab.14 - Computed Weights for the Indicator Layer and Sub-Indicator Layer

Criteria Level	The judgment matrix		Indicator level	Weight	Consistency Test
B1	$\begin{bmatrix} 1 & 0.625 & 1.5 & 1.5 \\ 1.6 & 1 & 2.33 & 2 \\ 0.667 & 0.667 & 1 & 0.667 \\ 0.667 & 0.500 & 1.5 & 1 \end{bmatrix}$	(4)	C1	0.2565	CI=0.005 RI=0.89 CR=0.006<0.1
			C2	0.3885	
			C3	0.1561	
			C4	0.1989	
B2	$\begin{bmatrix} 1 & 2 & 2.5 \\ 0.5 & 1 & 2 \\ 0.4 & 0.5 & 1 \end{bmatrix}$	(5)	C5	0.5174	CI=0.012 RI=0.52 CR=0.024<0.1
			C6	0.3042	
			C7	0.1784	
B3	$\begin{bmatrix} 1 & 0.652 \\ 1.533 & 1 \end{bmatrix}$	(6)	C8	0.3947	CI=0 RI=0
			C9	0.6053	
Indicator level	**The judgment matrix**		**sub-indicator level**	**Weight**	**Consistency Test**
C1	$\begin{bmatrix} 1 & 2.143 & 1.5 \\ 0.467 & 1 & 1.154 \\ 0.667 & 0.867 & 1 \end{bmatrix}$	(7)	D1	0.4712	CI=0.014 RI=0.52 CR=0.027<0.1
			D2	0.2613	
			D3	0.2675	
C2	$\begin{bmatrix} 1 & 0.8 & 1.4 & 2 \\ 1.250 & 1 & 2.667 & 3 \\ 0.714 & 0.375 & 1 & 1.5 \\ 0.500 & 0.333 & 0.667 & 1 \end{bmatrix}$	(8)	D4	0.2796	CI=0.006 RI=0.89 CR=0.007<0.1
			D5	0.4062	
			D6	0.1825	
			D7	0.1317	
C3	$\begin{bmatrix} 1 & 1.385 \\ 0.772 & 1 \end{bmatrix}$	(9)	D8	0.5807	CI=0 RI=0
			D9	0.4194	
C4	$\begin{bmatrix} 1 & 6.5 & 2.091 & 3.6 & 2 & 1.667 & 3.5 \\ 0.154 & 1 & 0.267 & 0.677 & 1.154 & 0.286 & 0.429 \\ 0.478 & 3.750 & 1 & 1.7 & 2.333 & 0.6 & 1.6 \\ 0.278 & 1.5 & 0.588 & 1 & 0.8 & 0.308 & 0.4 \\ 0.5 & 0.867 & 0.429 & 1.25 & 1 & 0.4 & 2.3 \\ 0.6 & 3.5 & 1.667 & 3.25 & 2.5 & 1 & 2.143 \\ 0.286 & 2.333 & 0.625 & 2.5 & 0.435 & 0.467 & 1 \end{bmatrix}$	(10)	D10	0.2950	CI=0.058 RI=1.36 CR=0.092<0.1
			D11	0.0567	
			D12	0.1579	
			D13	0.0714	
			D14	0.1050	
			D15	0.2128	
			D16	0.1012	

C5	$\begin{bmatrix} 1 & 7.5 & 3.125 \\ 0.133 & 1 & 0.588 \\ 0.320 & 1.7 & 1 \end{bmatrix}$	(11)	D17 D18 D19	0.6954 0.1049 0.1997	CI=0.007 RI=0.52 CR=0.013<0.1
C6	$\begin{bmatrix} 1 & 1.067 & 1.154 & 0.364 \\ 0.938 & 1 & 1.250 & 0.692 \\ 0.867 & 0.8 & 1 & 0.588 \\ 2.75 & 1.444 & 1.7 & 1 \end{bmatrix}$	(12)	D20 D21 D22 D23	0.1978 0.2269 0.1900 0.3853	CI=0.019 RI=0.89 CR=0.022<0.1
C7	$\begin{bmatrix} 1 & 0.88 \\ 1.136 & 1 \end{bmatrix}$	(13)	D24 D25	0.4681 0.5319	CI=0 RI=0
C8	$\begin{bmatrix} 1 & 1.6 \\ 0.625 & 1 \end{bmatrix}$	(14)	D26 D27	0.6154 0.3846	CI=0 RI=0
C9	$\begin{bmatrix} 1 & 1.143 & 0.364 \\ 0.875 & 1 & 0.455 \\ 2.750 & 2.2 & 1 \end{bmatrix}$	(15)	D28 D29 D30	0.2265 0.2231 0.5504	CI=0.007 RI=0.52 CR=0.014<0.1

The assessment model built on this premise is complex, with numerous factors impacting the operational efficiency of fishways. However, due to variations in the construction location, environment, and design management of fishways, not all factors are considered in the assessment model. Additionally, certain functionalities are challenging to monitor and indicators are difficult to determine, which hinders the formation of quantifiable results. In such scenarios, it is necessary to eliminate unconsidered or non-quantifiable indicators from the model and recalculate the weights accordingly.

Quantitative Grading and Composite Scoring

The article quantifies sub-indicator levels by referencing various engineering evaluation systems, with scores presented in Table13.

Tab.15 - Sub-indicator Level Quantification Chart

Level	Non-quantifiable Metrics	E	D	C	B	A
score	0	1	2	3	4	5

After obtaining the quantitative data for various indicators, one can calculate the comprehensive score S_{sum} of the fishway operation level using the following formula.

$$S_{sum}=\sum_{i=1}^{n}\sum_{j=1}^{m_i} W_i \times W_{ij} \times S_{ij} \tag{16}$$

In the formula,'S_{sum}' is the comprehensive score of the operational level, 'n' is the number of indicators; 'm_i' is the number of sub-indicators under each indicator; 'W_i' is the weight of the indicator; 'W_{ij}' is the weight of the sub-indicator; 'S_{ij}' is the score of the sub-indicator.

After calculating the comprehensive score of the fishway operation assessment using the formula, the grade of the evaluated project can be determined according to Table14.

Tab.16 - Comprehensive Scoring Table for Fishway Operational Efficiency

Comprehensive score	Level	Judgment Conclusion
0~1.0	Totally Srapped	The fishway project is in a completely scrapped state, with all indicators failing to meet the requirements. It needs to be redesigned, demolished, and rebuilt.
1.0~2.0	Operating Marginally	The actual operation condition is poor, and most indicators do not meet the design requirements, which seriously affects the normal operation of the fishway. It needs to be decommissioned and overhauled, and the entire fishway needs to be monitored for a long time after reuse.
2.0~3.0	Operating Normally	More than half of the actual operating conditions meet the design requirements. The indicators that do not meet the requirements have only a slight impact on the operation of the fishway. It is necessary to improve certain aspects, optimize the operating status, and conduct long-term monitoring of the overall fishway.
3.0~4.0	Operating Well	Most of the actual operations align with the design specifications, but a small number of indicators do not meet the requirements, which have a minimal impact on the overall operation of the fishway. Regular monitoring of individual components is sufficient.
4.0~5.0	Operating Excellently	The actual operation conditions meet the design requirements, and all data monitoring is normal.

Computational Procedure for Evaluating the Efficiency of Fishway Operations

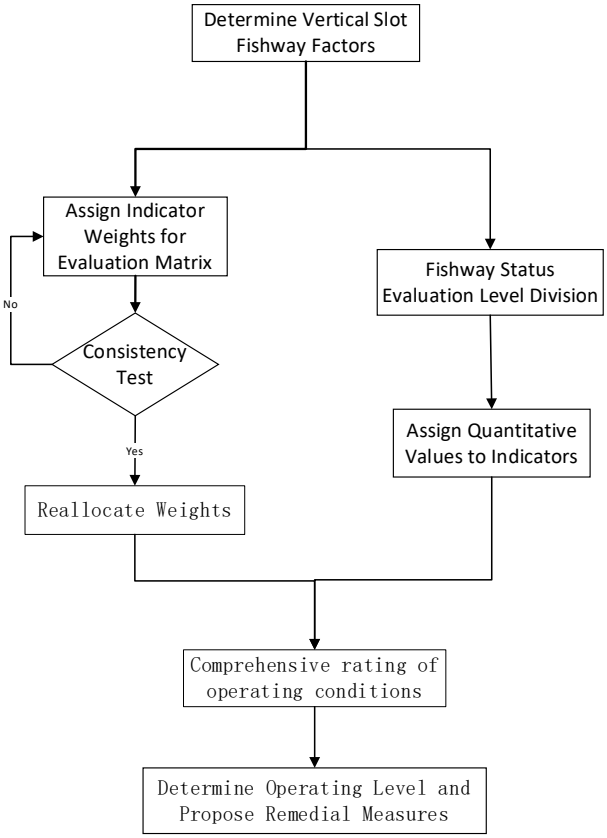

Fig.2 - Vertical Slot Fishway: Operation Evaluation & Calculation Flowchart

CASE ANALYSIS

Basic parameters

The fish passage project for the Laolongkou Hydro-junction is situated in the middle and lower reaches of the Hunchun River. The highest water level for fish in the reservoir is 109 m; the highest normal tailwater level downstream from the reservoir is 82 m, resulting in a design water level difference of 27 m. The main migratory fish species in the Hunchun River include masu salmon, common salmon, humpback salmon, and Japanese lamprey. There are also anadromous species such as the ridge head fish, Asian smelt, and dace. The period from mid-August to mid-October marks the upstream migration season for spawning adult fish, while mid-April to mid-May is the season for juvenile fish to descend to the sea, following the current [23,24].

Fig.3 - Site View of the Fishway Project at Laolongkou

Indicator Weight Reassignment and Scoring

Based on the basic parameters and monitoring values described in the data for the case, the weight coefficients for parameters or indicators that are unlisted or cannot be quantified are set to zero, and the weights of the indicators are redistributed. The coefficients for D4, D6, D7, D9, D10, D11, D12, D13, D14, D26, and D27 are zero. Consequently, the weights for C9, D5, and D8 are set to one. The weights for D15 and D16 undergo redistribution. After calculation, the weight ratio of the two sub-indices is:

$$[0.6818 \quad 0.3182] \tag{17}$$

Next, each sub-indicator is individually scored. The scores are detailed in Table15.

Tab.17 - Table of Comprehensive Scores for Sub-indicators [23-27]

Indicator level	Sub-indicator level	Parameters & Data	Score
C1	D1	The normal operating water depth is between 2.9 and 3.9 m.	4
	D2	The maximum water level difference is 27m.	2
	D3	The water depth of the fishway ranges from 0.6 to 2.2 m.	5
C2	D5	The maximum flow rate is 2.35 m/s.	3
C3	D8	The maximum discharge is 1.65 m^3/s.	5
C4	D15	The turbulent kinetic energy range is from 0.01 to 0.12 m^2/s^2.	5
	D16	There are no obvious vortices.	5
C5	D17	The fishway is arranged within the spillway.	4
	D18	There is one fish inlet.	4
	D19	There are no obvious water jumps in the channel.	5
C6	D20	The bottom slope of the fishway is 1:10.	3
	D21	The total length of the fishway is 281.6m.	4
	D22	The spacing between partitions in the fishway is 3.2 m.	4
	D23	The width of the vertical slots in the fishway is 0.32 m.	5
C7	D24	The fishway has five outlets at varying heights.	5
	D25	The exit is equipped with gates, trash racks, protective fences, and an auxiliary water supply system.	5
C9	D28	The main migratory fish species include salmon, lamprey, and beachhead fish.	4
	D29	The theoretical maximum capacity of the fishway is 7,000 fish per day.	5
	D30	The main fishing season occurs from August to October each year.	4

Comprehensive ratings and reviews

According to formula (2), the comprehensive score of the fishway operation assessment for the project is calculated as:

$$S_{sum}=\sum_{i=1}^{n}\sum_{j=1}^{m_i} W_i \times W_{ij} \times S_{ij} = 4.12 \quad (18)$$

Referring to Tab.5, the comprehensive score table for fishway operation evaluation, it is determined that the operation level of the fishway project is 'Operating Excellently.' The actual operating conditions meet the design requirements, and all data monitoring is normal.

CONCLUSION

(1) This study references assessment theory and draws on existing methods to establish for the first time an operational evaluation analysis based on the Analytic Hierarchy Process for vertical slot

fishways. This method encompasses three main categories - hydraulic characteristics, engineering layout, operational management, and monitoring - including a total of 30 factors.

(2) Based on the literature of numerous fishway studies, the study adopted a five-level classification method to divide the operational efficiency grades of vertical slot fishways, providing a qualitative description for each corresponding grade. Using a scale of 1 to 9, the weights of each indicator were evaluated, criteria were established, and a comprehensive score was given to the performance of each indicator for the vertical slot fishway operation.

(3) After presenting a method for assessing the operation of vertical slot fish passages, the passageway project at the Laolongkou Hydraulic Junction was examined as a case study. Using actual measured data from the project and applying it to the evaluation system for the efficiency of vertical slot fishway operation, the project was rated as ' Operating Excellently ' in its operation, which confirmed the validity and reliability of the proposed assessment system.

ACKNOWLEDGEMENTS

This work was supported by North China University of Water Resources and Electric Power.

REFERENCES

[1] Muchun L., Dongya L., Hongzhi K., 2023. Research on fish passage optimization design method based on fish passing effect evaluation. Water Resources Planning and Design: 56-61.
[2] Jie L., Xinhui L., Shuli Z. et al., 2019. Study on the Efficiency of Influencing Factors of Xiniu Fishway in the Lianjiang River. Journal of Ecology and Rural Environment, vol. 35: 8.
[3] Yiqun H., Lu C., Xiaojuan C. et al., 2020. Design Points and Effectiveness Evaluation for Fish Passage. Environmental Impact Assessment, vol. 42: 19-23.
[4] Yanyan Z., Zhenjun H., Yong H. et al., 2017. Analysis on the efficiency of fishway for the low-head gate dam. Journal of Hydraulic Engineering, vol. 48: 748-756.
[5] Shouning X., 2022. Research on the effect of fish passage in the fishway project of Shaping II Hydropower Station. Yangtze River, vol. 53: 95-98.
[6] Jian S., Yueping C., Lei L. et al., 2023. Scheme Comparison and Selection of Fish Passage Facilities for DG Hydropwer Station in Tibet. Water Power, vol. 49: 5-8.
[7] Shuangke S., Mingyu D., Yingyong L. Hydraulic Design Study of the Shangzhuang New Gate Vertical Slot Fishway in Beijing City. National Conference on Hydraulics and Hydroinformatics, ate 2007.
[8] Guangning L., Shuangke S., Zhihong Q. et al., 2019. Layout of Fishway Entrance in the Tailrace Channel of a Power Station. Transactions of the Chinese Society of Agricultural Engineering, vol. 35: 81-89.
[9] Songtao L., Guangning L., Kai S. et al., 2024. Exploration of the Fish Passage Efficiency of Vertical Slot Fishway Pile Structures. Journal of Hydroecology: 148-158.
[10] Binru Z., Huichao D., Guiwen R. et al., 2017. The Influence of Vertical Slot Position on the Hydraulic Characteristics of Vertical Slot Fishways. Advances in Science and Technology of Water Resources, vol. 37: 69-73+83.
[11] Jiquan S., Jibao W., Wei H. et al., 2018. The Relationship between Swimming Behavior of Juvenile Bighead Carp and Response to Turbulence Intensity. Chinese Journal of Ecology, vol. 37: 1211-1219.
[12] Lee J. W., Yoon J. D., Kim J. H. et al., 2015. Efficiency Analysis of the Ice Harbor Type Fishway Installed at the Gongju Weir on the Geum River using Traps. Environmental Biology Research, vol. 33: 75-82.
[13] Stuart I. G., Berghuis A. P., 2010. Upstream passage of fish through a vertical-slot fishway in an Australian subtropical river. Fisheries Management & Ecology, vol. 9: 111-122.
[14] Haro A., Odeh M., Castro-Santos T. et al., 1999. Effect of Slope and Headpond on Passage of American Shad and Blueback Herring through Simple Denil and Deepened Alaska Steeppass Fishways. North American Journal of Fisheries Management, vol. 19: 51-58.
[15] Castro-Santos T., Cotel A., Webb P. W., 2009. Fishway evaluations for better bioengineering -- an integrative approach. challenges for diadromous fishes in a dynamic globalenvironment.

[16] MALLEN⅄OOPER M., Stuart I. G., 2007. Optimising Denil fishways for passage of small and large fishes. Fisheries Management and Ecology, vol. 14: 61-71.
[17] Ballu A., Calluaud D., Pineau G. et al., 2017. Experimental study of the influence of macro-roughnesses on vertical slot fishway flows. Houille Blanche: 9-14.
[18] E., Quarant, C. et al., 2017. Turbulent flow field comparison and related suitability for fish passage of a standard and a simplified low-gradient vertical slot fishway. River Research and Applications, vol. 33: 1295-1305.
[19] Tan J., Gao Z., Dai H. et al., 2018. Effects of turbulence and velocity on the movement behaviour of bighead carp (Hypophthalmichthys nobilis) in an experimental vertical slot fishway. Ecological Engineering, vol. 127: 363-374.
[20] Silva, AT, Santos et al., 2011. EFFECTS OF WATER VELOCITY AND TURBULENCE ON THE BEHAVIOUR OF IBERIAN BARBEL (LUCIOBARBUS BOCAGEI, STEINDACHNER 1864) IN AN EXPERIMENTAL POOL-TYPE FISHWAY RID F-9022-2010. River Research and Applications, vol. 2011,27(3): 360-373.
[21] Shanshan J., 2023. Research on Evaluation and Improvement of Teacher's Professional Ability Based on Analytic Hierarchy Process. Agricultural Mechanization Using ＆ Maintenance: 6-11+88.
[22] Yi S., 2023. Evaluation of urban drainage pipe network operation performance based on analytic hierarchy process. Shanxi Water Resources: 176-178+184.
[23] Dejing S., Hui J., Changtao G. et al., 2008. Design of a fishway for Lao Long Kou hydro-junction project. Marine Fisheries Research, vol. 29: 92-97.
[24] Design code for fish passage facilities in hydropower projects (2015). vol NB/T 35054-2015. CN-NB,
[25] Xian-nyu Z., Jinghui J., 2015. Fishway design of Laolongkou Water Conservancy Project in Jilin Province. Changchun Inst Tech (Nat Sci Edi): 82-84+110.
[26] Yuhui C., Xingzu X., 2010. Fishway design of Laolongkou Water Conservancy Project in Jilin Province. Jilin Water Resources: 1-4.
[27] Li G., Ligao B. B., Xiangpeng M. et al., 2015. Study on Hydraulic Characteristics of Fishway for Laolongkou Hydro-junction Project. Water Resources and Power, vol. 33: 73-76+96.

CIVIL ENGINEERING JOURNAL

Article no. 17

THE CIVIL ENGINEERING JOURNAL 2-2024

ST. VITUS CATHEDRAL AT PRAGUE CASTLE DURING THE PERIOD OF NORMALIZATION

Martin Šnorbert

Czech Technical University in Prague, Faculty of Civil Engineering, Department of Architecture, Thákurova 7, 166 29 Prague 6 - Dejvice, Czech Republic; martin.snorbert@fsv.cvut.cz

ABSTRACT

This paper deals with the building modifications in the building of the Cathedral of St. Vitus, St. Wenceslas, St. Adalbert and St. Mary during the period of normalization - the 1970s and 1980s. This period has so far been neglected by researchers, although many articles and publications have been written about the history, development and artistic decoration of the cathedral. Normalization, like the entire period of communist rule in Czechoslovakia, meant the oppression of church leaders, the suppression of sacred themes in religious buildings and in everyday life. Nevertheless, the cathedral was the scene of necessary reconstruction works, as well as modifications aimed at improving the use of space and interventions based on the change of the Roman Catholic liturgy.

St. Vitus Cathedral is the most important Catholic church in the Czech Republic, formerly in Czechoslovakia, and even earlier in the Czech Kingdom. Its construction, spanning almost 700 years, demonstrates the development in culture, technical possibilities, architectural and building art. The cathedral is an essential part of the Prague Castle complex and the Hradčany panorama. Prague Castle was and still is the center of secular and ecclesiastical power. This connection was symbolically fulfilled by the most important ruler ceremonies (coronations, funerals, marriages, christenings), which took place in the cathedral.

One of the most beautiful and most photographed views of Hradčany is dominated by the silhouette of Prague Castle and especially the cathedral. The St. Vitus Cathedral rises from the base formed by the uniform design of the facades of Prague Castle, which was created during the reign of Empress Maria Theresa. For a long time, the cathedral itself looked like a torso, as only the bell tower with a Renaissance and later Baroque helmet was built. The transept and the towers in the facade were not completed until the late 19th and early 20th centuries.

On the basis of archival research, interviews with witnesses and the study of specialist literature, the reader is introduced to the interventions in St. Vitus Cathedral and the associated change in the space for the celebration of the liturgy, as well as the space for ordinary visitors to this church during the period under study. Further attention is given to the unrealised designs and other sacred buildings in the grounds of the Castle.

KEYWORDS

Prague Castle, St. Vitus Cathedral, Sacral Buildings, Building Modifications, Reconstruction, Liturgical Modifications, Normalization

INTRODUCTION

Between 1948 and 1989, Czechoslovakia was ruled by the Communist Party, which enforced the totalitarian character of Czechoslovakia and later the Czechoslovak Socialist Republic. An anti-religious policy was applied. It was manifested by the crackdown on religious men and women in the 1950s, the suppression of religious and Christian themes from ordinary public life, the emphasis on atheistic education of children and youth, and the holding of civil ceremonies [1],[2]. One of the typical elements of the communist persecution was "the dilapidation, sanitation and profanation of existing

sacred buildings, efforts to minimize sacred architecture, and, on the contrary, alternative offerings in the form of civil ceremonies and quasi-sacred spaces" [1]. At the turn of the 1950s and 1960s, some churches were even expropriated (for example, the Basilica of St. George at Prague Castle) [1], [3]. In the 1960s, "there was a gradual relaxation of the cultural policy of the state, which heralded the development and significant success of Czechoslovak artistic creation, the adoption of Western cultural patterns and a broad social relaxation" [1]. In 1968 the believers rode the wave of enthusiasm of the whole society, they also experienced a very intense period when they expected the correction of the state's ecclesiastical policy. This period was followed by the so-called normalization, when there was a return to "the violent suppression of expressions of discontent and dissent in the public space, the displacement and real persecution of groups of citizens with different and critical views, although the draconian nature was not equal to that of the 1950s" [1]. For the Church, normalization meant the end of promising prospects; it was once again persecuted by the state, this time in the form of working for the widespread atheization of civil society, rather than through public trials of Church leaders [1], [4].

St. Vitus Cathedral is the seat of the Archbishop of Prague, the highest representative of the Czech Roman Catholic Church. Quite naturally, together with Prague Castle, "it has become a kind of the center and heart of the Czech lands, an obvious sign of Czech national and state identity" [5]. The cathedral is also a major attraction for tourists from all over the world. The pre-Romanesque rotunda, dedicated to St. Vitus and built by Prince Wenceslas, gradually became a chapter, bishop's and finally archbishop's church. It has undergone two major structural and architectural transformations from a Romanesque Basilica from the late 11th century to a magnificent torso of a Gothic cathedral [6]. The Czech national revival led to ideas for the completion of the extensive western part of this building. The completion took place from the end of the 19th century until 1929 on the occasion of the St Wenceslas Millennium (900 years since the martyrdom of St Wenceslas). The medieval construction of the cathedral and the 19th and 20th century completions, the artistic decoration of the exterior and interior, the liturgical and musical programme became an important "part of the artistic and social discourse, a symbolic and cultural phenomenon. It retained its position even in times that were not conducive to the development of cultural and religious activities, and it has not lost its significance even today" [7].

The strategic location in the middle of the castle, where first the prince, later the king and the president resided, brought the connection of secular and ecclesiastical power, thus another important and functional characteristic of St. Vitus Church. "It became the site of the most important ceremonies associated with the life and function of the monarch - coronation ceremonies, royal funerals, marriages and baptisms. Meetings and assemblies connected with the function of the feudal state and its internal and foreign policy were held here" [6].

The Cathedral of St. Vitus together with Prague Castle form the dominant feature of the so-called Hradčany panorama. The most frequently observed and recorded view of Hradčany is from the Charles Bridge or from the embankment leading from the National Theatre to the Charles Bridge, as shown in the attached picture Figure 1. Several towers rise above the small historic houses of the Lesser Town (St. Nicholas Church, St. Thomas Church, Lesser Town Bridge Tower, and others), the horizontal roofline of Paccasi's South Wing (rebuilding and unification of the facades under Maria Theresa) rises above them, and the main motif is the richly articulated silhouette of St. Vitus Church [8].

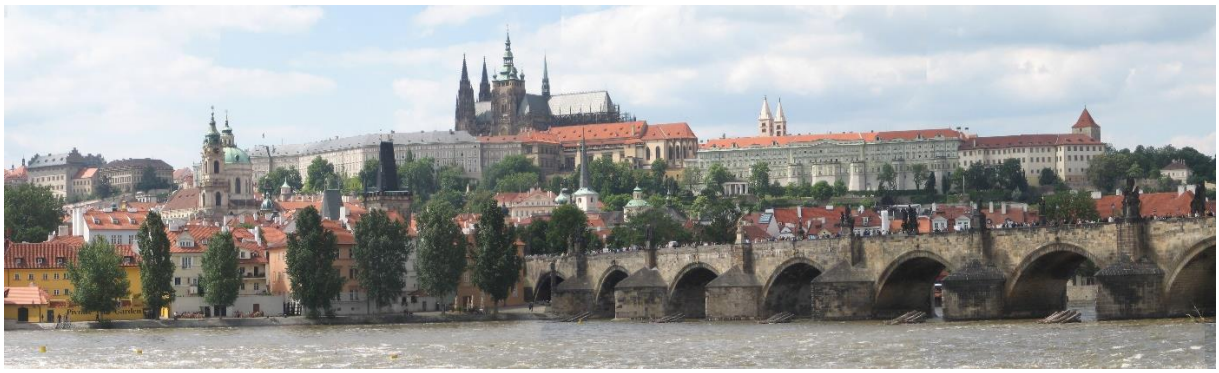

Fig. 1 – Hradčany panorama (Prague Castle, Charles Bridge, Lesser Town) [9]

SACRAL BUILDINGS AT PRAGUE CASTLE IN HISTORY

The Rotunda of St. Vitus was built by Prince Wenceslas as the third Christian building at Prague Castle and the fifth in the then Czech Principality [7]. The oldest Christian building in the Castle was the Church of Our Lady. According to tradition, it was built during the reign of Prince Bořivoj at the end of the 9th century, and rather surprisingly it was built outside the central part of the future Přemyslid Castle. Around 920, a second Christian building, the Basilica of St. George, was founded on the eastern elevation (today's St. George Square) [10]. "In 972-973, when the Prague bishopric was founded, the rotunda of St. Vitus became the bishop's church. It is very likely that the bishop must have been given space to build his residence at that time, first in wood, later in stone, with the Chapel of St. Moritz. It looks as if the space that would become the spiritual center of the country during the 11th century had already been defined in this early period" [7].

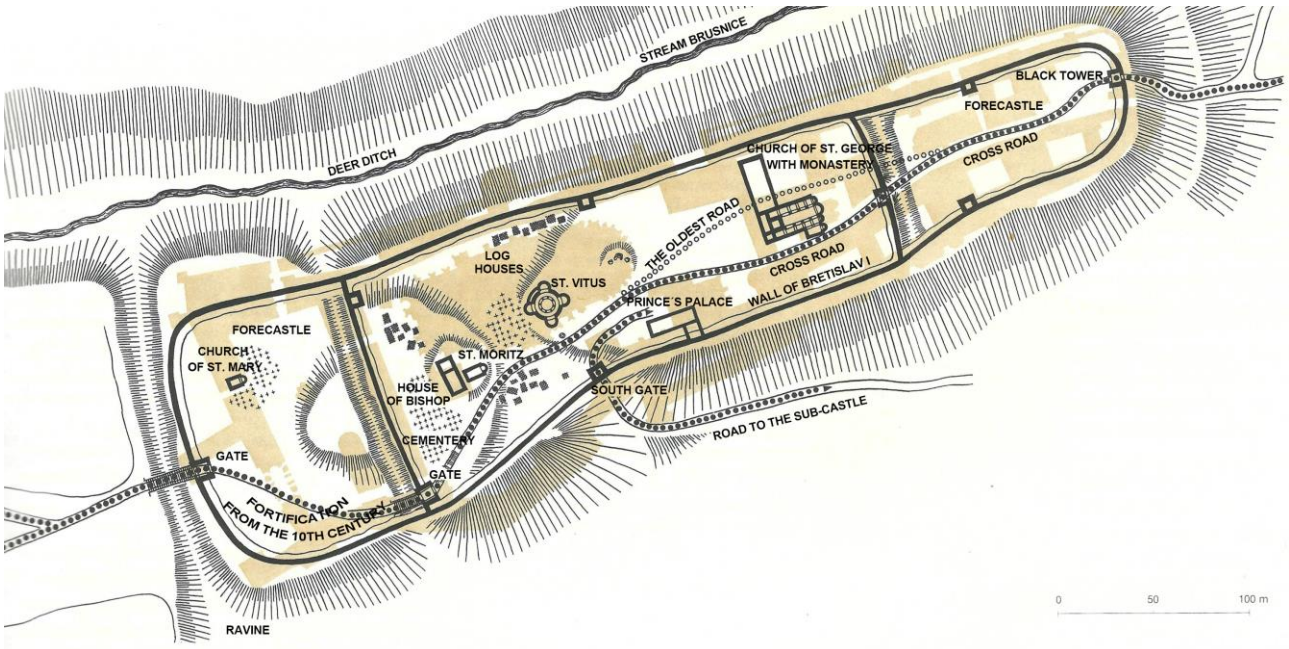

Fig. 2 – Reconstruction of a pre-Romanesque hillfort – the predecessor of today's Castle. The main buildings are: the princely palace, the rotunda of St. Vitus, the three-nave basilica of St. George, the bishop's house with the chapel of St. Moritz, several towers and gates, log buildings of peasants and servants, cemeteries. Colour suite according to the stable cadastre of 1879 [8]

Subsequent rulers of the Přemyslid family supplemented the ground plan of Prague Castle with other sacral buildings, see Figure 2. The Rotunda of St. Vitus ceased to be sufficient, and it was

decided to replace it with a new church. Starting in 1060, a two-chambered, three-aisled Romanesque Basilica with two towers, crypts, a transept and several attached or related chapels was built over a period of about 30 years. By the second half of the 13th century, the episcopal complex with the basilica had been extended by several other buildings. On the north side of the basilica a chapter house with an ambit and the chapel of St. Thomas was added. The Romanesque bishop's house with the Chapel of St. Moritz was gradually expanded to the west. In the south, the basilica was connected by a long corridor with the church of St. Bartholomew (located in the excavation area under the third courtyard, excavations were carried out in 1920-1922). The disappearance of parts of this complex was related to the construction of the Gothic cathedral [7]. In the second half of the 12th century, Prince Spytihnev built a new princely palace in the south and also new walls, which were essentially part of the palace. The castle chapel of All Saints was added to the eastern side of the palace [11]. In 1142, the church and the monastery of St. George burned down, after which both buildings were rebuilt. "The original short, three-aisled basilica with a crypt under the altar was extended (...) and a south tower was added to the north tower" [8]. To the east of the basilica, a monastic hospital with the Church of St. John the Baptist was built, but it soon disappeared, see Figure 3.

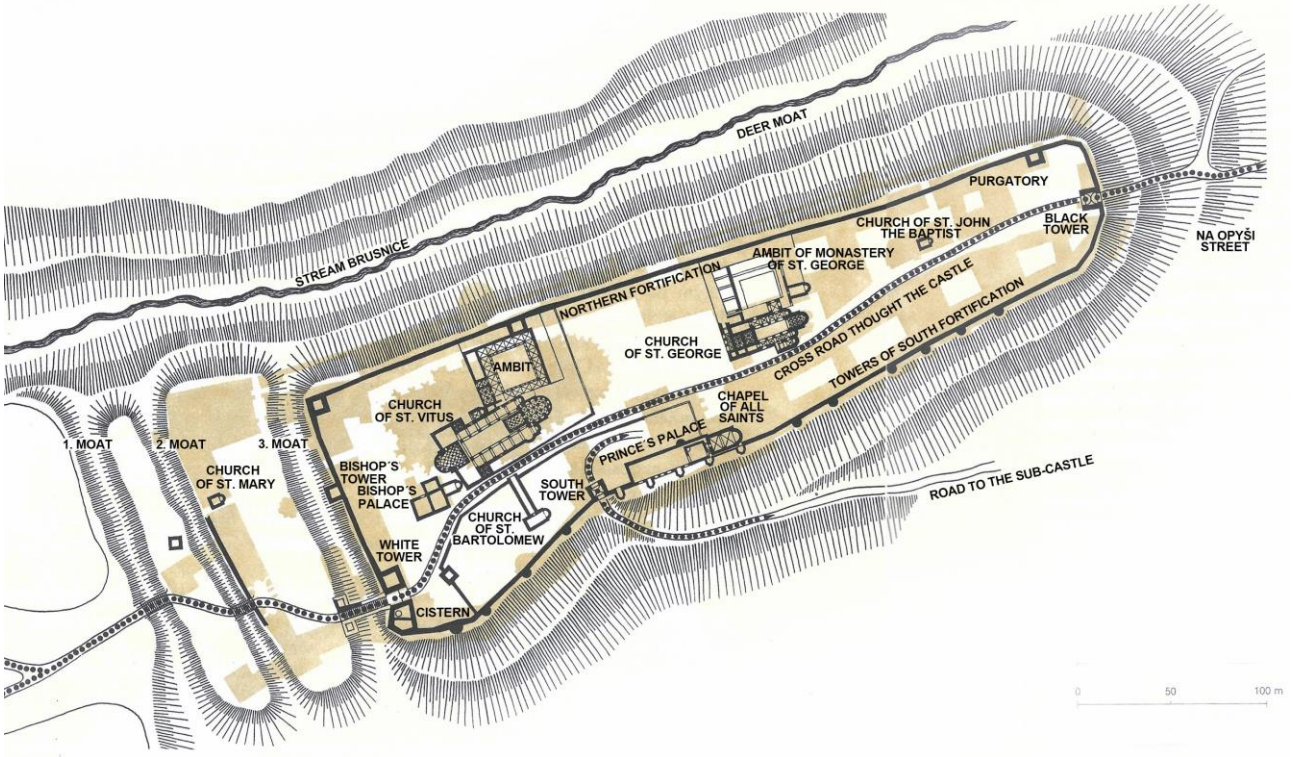

Fig. 3 – Reconstruction of Prague Castle during the last Přemyslids at the end of the 13th century, drawn in the contour lines of today's Castle. Three main buildings stand out: the Romanesque Basilica of St. Vitus with the bishop's house next door, the three-nave Church of St. George with the monastery and the paradise court, and the princely palace, which is flanked on the south side by the wall. It is reinforced by square towers, 2 of which are the gates of the Castle, the White (west) and the Black (east) [8]

The reign of Charles IV (1346-1378) brought unprecedented prosperity to the Bohemian lands, but also to Prague Castle. The old Romanesque castle, similar to the German Falci, was rebuilt according to the principles of French Gothic. A Gothic church of All Saints was built on the eastern side of the palace on the site of the original Romanesque chapel. The builder was Petr Parléř and his model was the Sainte-Chapelle in Paris. Unfortunately, the church was severely damaged by fire in 1541 and the subsequent rebuilding was done in a soberer Renaissance style. It has

retained this appearance to the present day, serving as the private chapel of the adjacent Institute of the Nobility since the mid-18th century [8]. The monarch had the Chapel of Our Lady created within the first floor of the royal palace and was also instrumental in the elevation of the Prague bishopric to an archbishopric. The foundation stone of the new cathedral was laid on 21 November 1344. The famous French architect Matthias of Arras was chosen for the construction, but he died prematurely (1352) and the construction was continued by an unknown master. At the same time the old basilica was being demolished [12]. By the time the new young architect, Peter Parléř, arrived, the nine pillars of the arcade around the choir, the eight choir chapels at the end of the church and the eight bays of the choir gallery had already been built [7]. Petr Parléř completed the sacristy with the treasury, built the chapel of St. Wenceslas, the south vestibule (Golden Gate) with a new sacristy on the first floor, completed the perimeter chapels on the north and south sides, and began the construction of the Great South Tower. Work on the cathedral was stopped by the Hussite wars. During the Jagiellonian reign, many successful and high-quality building interventions are associated with the name of Benedikt Ried (Rejt). He was responsible for the creation of Vladislav Hall, a magnificent Gothic airy hall with ribbed vaulting and Italian Renaissance windows. During the construction of this hall, the partitions between the three existing rooms on the floor of the royal palace were demolished. The original hall, the Chapel of the Virgin Mary and the Charles Room were thus lost [8]. Towards the end of the 15th century a new oratory was built in the cathedral in place of the Luxembourg oratory (probably under the direction of Hans Spiess or Benedikt Ried) [7]. Vladislav Jagiellon attempted to complete the cathedral, and the north tower was founded (Figure 4) [13]. Only a part of the new tower was built, it was badly damaged by fire, so it was demolished and the construction was never continued. A huge fire in 1541 also affected the cathedral, the fire spreading from the Great South Tower, which was temporarily covered with a shingled roof. The fire subsequently spread to the roof of the western part, with the entire roof trusses burnt and the interior furnishings damaged [7]. The fire also affected the church and the monastery of St. George.

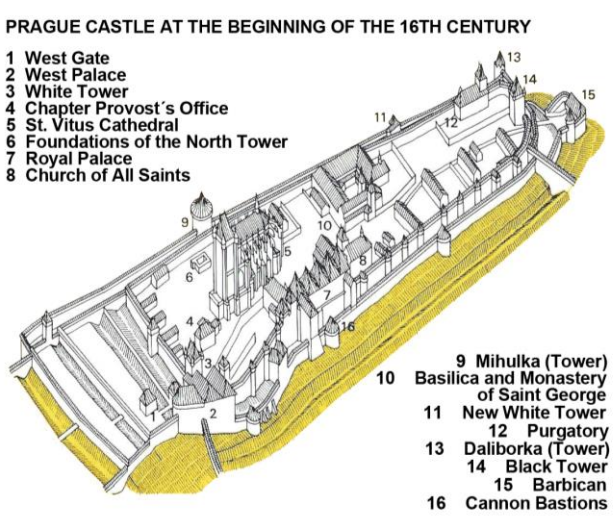

Fig. 4 – Prague Castle during reign of Vladislav Jagellonsky (early 16th century) [14]

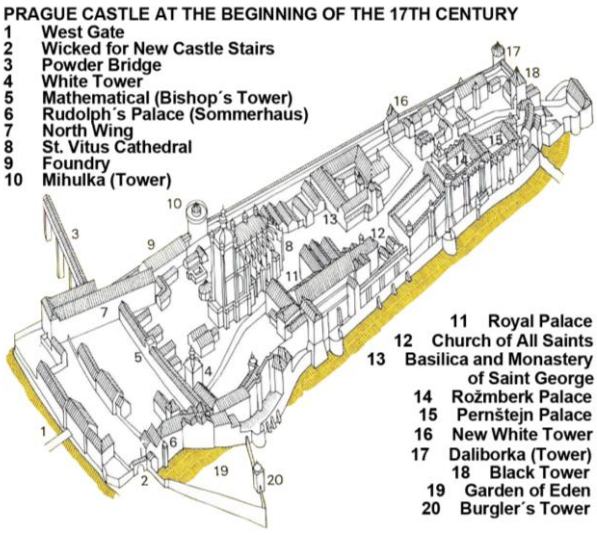

Fig. 5 – Prague Castle during reign of Rudolf II (early 17th century) [14]

The aforementioned fire facilitated the arrival of the Renaissance in the area of Prague Castle. From 1541 to the middle of the 19th century, the silhouette of the cathedral did not change significantly. Around 1560, a Renaissance porch and the complex Renaissance helmet of the Great South Tower (architect Bonifác Wohlmuth) were added (Figure 5) [8]. The helmet was replaced in 1769-1771 by a Baroque cupola which remains on the cathedral to this day. The high choir was covered by a much lower roof with three spires [13]. A temporary wall was built to the west of the Gothic cathedral before the Hussite period. Between the wall and the cathedral was the Chapel of the Holy Trinity adjacent to the Great Tower (demolished 1887) and the central Renaissance chapel

of St. Adalbert (demolished 1879) [7]. The nave of the cathedral consisted of a Renaissance royal mausoleum, which was and still is surrounded by an iron grille [15]. During the Baroque period (after the Battle of White Mountain in 1620), new furnishings were created, new decorations were added to the chapels and altars (mural, paintings) [7]. The Baroque period brought the reconstruction of the main façade of St. George's Basilica (around 1671) and also a new building of the Chapel of St. John of Nepomuk (1718-1722, F. M. Kaňka), which was added to the façade of the basilica. The early Baroque façade has been preserved to this day. The Archbishop's Palace moved outside the Prague Castle but remained very close to Hradčany Square [8].

The reign of Maria Theresa and Joseph II in the second half of the 18th century meant the reconstruction of the Castle into office space and a change of the facade towards the city. Nicolo Pacassi created a single long façade in the French Classical style, a façade that has survived to the present day [8]. The Chapel of the Holy Cross was built in 1758-1763 on the site of the building office with the kitchen in the second courtyard, according to the same architect's design. The marble high altar with statues of angels and the Crucifixion painting have survived. The other furnishings date from 1852-1856, when the church was refurbished for the exciseman Ferdinand [14]. Joseph II abolished the monastery of St. George and had it converted into a barracks, and the basilica began to decay [8].

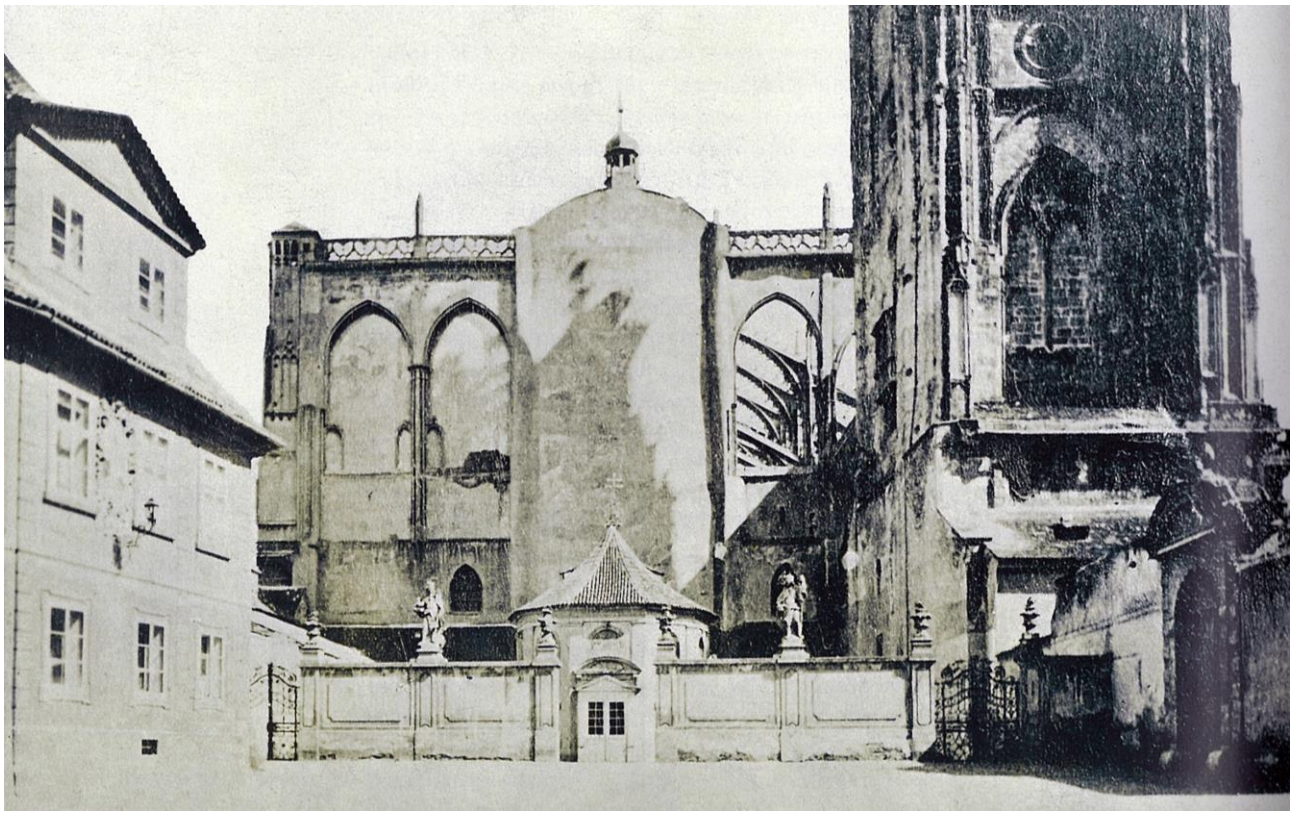

Fig. 6 – St. Vitus Cathedral with the Chapel of St. Adalbert, 1860s [16]

The middle of the 19th century brought ideas for the completion of St. Vitus Cathedral. The condition of the cathedral at this time can be seen in figure 6. In 1859, the Unity for the completion of the main cathedral of St. Vitus at Prague Castle was founded, and in 1873 the foundation stone of the completion was laid. The first builder of the cathedral was Josef Andreas Kranner in 1861. He built a stonework on St. George's Square, in the first phase he started with the repairs of the medieval part - he began with the reconstruction of the choir chapels, then he dealt with the placement of the neo-Gothic gargoyles, finally the work moved to the high choir and its support system. After Kranner's death, Josef Mocker became the second builder. He presented a new plan for the completion of the cathedral - a five-aisle version (as opposed to Kranner's three-aisle version), a west front with two

towers and three portals. Mocker worked on his concept until his death in 1899, commissioning additional gargoyles and sculptural decoration. He added neo-Gothic altars to the interior, restored the royal oratory, and modified the choir for the high altar. The last builder was Kamil Hilbert, who reworked some parts of the design and completed the whole process of completion by 1929. He continued the reconstruction of the tower, built the staircase to the first and second bell towers, finished some chapels, and the restoration of St. Wenceslas Chapel was a major task. He often used the motif of a spiral staircase [7].

The period after the Second World War, and especially with the advent of the communist regime, is associated with the decay, sanitation and profanation of existing sacral buildings [1]. There was no dilapidation and destruction at Prague Castle, but there were several adaptations and conversions of church buildings. This was related to the process of desacralization. The premises were to serve other than ecclesiastical purposes. This was to symbolically contribute to the separation of the state from the church. The cathedral began to be referred to as a mere burial place of Czech kings, and even the transfer of the crown jewels to other premises was considered [17]. The Church of All Saints was modified in 1952-1953, the Baroque grille was moved from its original position separating the chancel from the nave to a new position, which closed off the space of the Baroque tomb of St. Procopius. A Baroque Gothic organ was installed in the same building in 1964. They were transferred from the church in Skapce near Klabruby [14]. A Memorial to the History of the Czechoslovak People was to be built in the Monastery of St. George (considerations began in 1959, the project ran from 1961-1967), but due to construction complications this project was never completed. Another example was the conversion of the Chapel of the Holy Cross into a jewellery store, a project that was undertaken by the architect Studený in 1960. Another example was the reconstruction of the refreshment chapel in the Kajetán Garden according to the implementation project by architect Hrubý in 1966. At the turn of the 1950s and 1960s, churches were also expropriated as part of the atheisation process. In the Castle, this concerned the Basilica of St. George [3].

The newly elected first communist president, Klement Gottwald, attends a Te Deum mass in the cathedral in 1948. It was the last time a communist president attended a solemn mass, other presidents preferred other rituals after their election. In the 1950s, the primary religious character of the cathedral was suppressed. The spiritual center moved to several Prague churches where popular priests preached [7]. According to Government Decree No. 55/1954 Coll. on the protected area of Prague Castle, all real estate (including church buildings) became the property of the Czechoslovak state. In 1957 it was stipulated by contract that "the Metropolitan Chapter will continue to take care of the management and preservation of the internal facilities of the Metropolitan Cathedral" [18]. The interior furnishings, except for the objects of worship, were handed over to the administration of the Office of the President of the Republic. There were many disagreements between these two institutions in the administration of the Cathedral, as their rights and duties were not clearly defined. There were few spiritual activities in the cathedral, which improved only in the second half of the 1960s with the arrival of the apostolic administrator František Tomášek, which was of course also related to the social change [7].

The artistic activity in the St. Vitus Cathedral was very limited, the last action connected with the Unity was the completion of the south portal according to the architectural competition won by Jan Sokol and Josef Wagner. The work had been going on since 1950, completed in 1959 only under the direction of Sokol, as the sculptor Wagner died in 1957. Of the few other completed projects, mention can be made of the carving and installation of the relief tympanums of the west portals, the central one was installed in 1953, the southern one in 1956 and the northern one in 1966. During the total renovation of St. Wenceslas Chapel, which took place between 1964-1967, new stained-glass windows were installed by the well-known Libenský and Brychtová duo and Josef Soukup [7].

SACRAL BUILDINGS AT PRAGUE CASTLE IN THE PERIOD UNDER STUDY

Even during the period of normalisation, the process of desacralisation begun in the 1950s and described above was not stopped. Adaptations and conversions of religious buildings continued. Most of them did not serve their original purpose. After the unsuccessful project of the Memorial of the History of the Czechoslovak People in the monastery of St. George, it was decided to use this monastery for the needs of the National Gallery. Between 1969-1975 the monastery was adapted for exhibition purposes for the exposition of old Czech art from the Middle Ages to the end of the Baroque period (fig. 7 and 8). "Professor František Cubr and architect Josef Pilař designed the restoration to create a set of exhibition spaces. The sightseeing circuit was extended to include part of the ambit and the chapel area. In the interior and on the south façade, the architecture of the various stages of development was retained. The western and southern parts of the ambit, together with the Paradise Court, served as entrance and relaxation areas (...) The monastery was previously composed of several smaller rooms, which was not suitable for exhibition purposes. The partitions between the rooms were demolished and the whole space was unified" [19].

Fig. 7 – View of the exposition in the monastery of St. George – Gothic part [20]

Fig. 8 – View of the exposition in the monastery of St. George – Baroque part [21]

Another sacral space within the monastery of St. George was also newly designated for exhibition purposes - the Chapel of St. Anne. The implementation project was completed in 1973 by the aforementioned architects. The Chapel of the Holy Cross was used as a treasury, and only after the revolution (in 1991) was the entrance and information system of this chapel redesigned. The architect Miloslav Burian was in charge of it [22]. In the Church of All Saints, restoration work was carried out in the late 1980s (1987-1988). The younger paintings were removed and the original gilding was restored [14].

MODIFICATIONS IN THE CATHEDRAL IN THE PERIOD UNDER STUDY

The end of the 1960s was marked by social relaxation, and in 1969 a funeral mass was celebrated in honour of the late Cardinal Beran, who had died in Rome. It was considered to bring his body back to Bohemia, to the cathedral. The new people in the Communist Party leadership, however, did not want this to happen, and they had been trying for more consistent atheist propaganda since childhood. Their attitude towards the cathedral remained the same even during this period, as evidenced by the words of historian Jiří Burian, who was employed in the Office of the President of the Republic, in 1975: "St. Vitus Cathedral, as part of the National Cultural Monument - Prague Castle - has been the subject of constant care by the socialist state for two decades, which has maintained it as a jewel of Czech architecture, the scene of significant events in national history and an unrepeatable collection of cultural values of the past" [6].

The beginning of the 1970s brought serious thoughts about adjustments to the liturgical space, which should adapt to the liturgical requirements arising from the Second Vatican Council, which took place between 1962 and 1965. This modification was completed in 1973 and will be discussed in more detail in the following chapter. The celebration of the St. Adalbert's Millennium in the same year was greatly reduced. The year 1978 played an important role for the further development and promotion of the importance of the cathedral in the eyes of the faithful, when the Archbishop of Cracow, Karol Woltyla, was elected Pope and chose the names John Paul II. He encouraged Cardinal Tomášek and the whole community of the faithful to greater activity. In the 1980s, there was a growing interest in spirituality, especially in large cities and intellectual circles. The cathedral became "a space of spiritual resistance to the regime, moreover, naturally connecting the Catholic faithful with people of other beliefs" [7]. Once again, it became a spiritual centre during major church festivals and celebrations of the country's patrons. Masses of people gathered in the cathedral and its immediate surroundings, even turning into spontaneous demonstrations at the end of the 1980s, which, of course, did not please the state authorities [7].

The prevailing view of scientific communism was that of the temple as a historical monument and burial place of Czech rulers. This is probably why very few new interventions were made in the cathedral, but restoration work and many repairs were carried out. In the 1970s this included a new altar table by Professor Jan Sokol in connection with liturgical reforms. In the 1980s, the only new work of art was a figural sculpture of Agnes (the future saint) by Karel Stádník. It was placed in the chapel of the Bartons of Dobenín [7].

Unfortunately, repairs and maintenance work were not carried out in the 1950s and 1960s, although the Department of Historic Preservation (later the Department) of the Office of the President of the Republic often pointed this out. The beginning of the repair’s dates back to 1968-1969, when the Central Bohemian Enterprise for the Conservation and Restoration of Cultural Monuments repaired the top floor, the roof of the Great South Tower and structurally secured the Royal Oratory [7]. Pavel Mošťák was the architect of the reconstruction of the Renaissance gallery of the tower, and other collaborators took part in the project. The architect Karel Kovář and Marie Plachtová were responsible for the survey, the statics were designed by Dr. Jan Rudolf, the scaffolding by Miroslav Hurych, and the budget by Matěj Drofa. Photo documentation was provided by academic painter and restorer Jiří Novák. The technical report described "the reconstruction of the surface treatment of the Renaissance gallery of the main tower of St. Vitus with the creation of a suspended scaffolding system (fig. 9 and 10) for the survey and repair of the tower helmet" [23]. The report began with a brief historical overview of previous modifications to the tower. It assessed the condition at the time and proposed a solution: "In recent decades, the plastered surface of the arcaded gallery has deteriorated to the point that it threatens the safety of traffic and the plastic members of the lower structure at the exposed location of the main south portal with the so-called Golden Gate. Also, the copper cover of the tower is considerably loose at the joints as a result of rotten formwork" [23].

The actual design of the individual modifications is described in detail, firstly the surface treatment of the gallery arcade of the main tower (careful removal of the plaster, cleaning of the exposed brickwork - with emphasis on washing out the salt deposits, dampening of the brickwork, spraying with hydraulic mortar and filling the joints, execution of a one-layer plaster with a tightened surface - manually processed using an oak and then iron trowel, restoration repair of the plastic links of the ionic heads with new plaster, execution of the internal plastering according to the same principles, cleaning of the reinforced concrete structure's surface, finally careful cleaning of the gallery of tower from all impurities, all surfaces preserved about a month after the end of the work with a mist hydrophobizing spray LUKOSIL L). The recipe for the preparation of the new mortar was also described here. This was followed by adjustments to the plumbing work, as the Gothic profiles of the medieval section overhanging the outer outline of the Renaissance arcade were to have their plywood and brick covers removed and replaced with covers of hard copper sheeting. A detailed survey of the copper bath was also to be carried out. The last reference was to the modification of

the stonework (products). It was proposed to clean the stone parapets, stone repairs to minor damage, and treatment with multiple saturation with lime water solution [23].

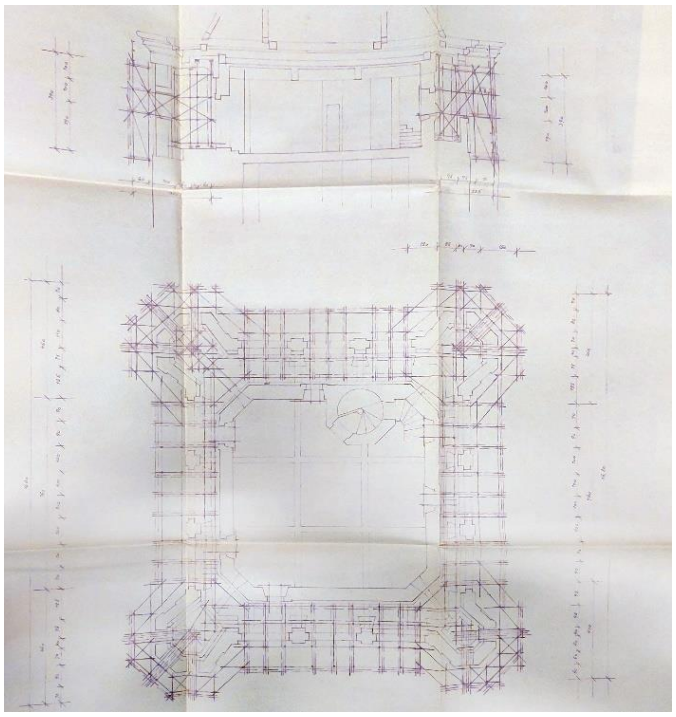

Fig. 9 – St. Vitus Church – perimeter scaffolding of the gallery – floor plan and vertical section [24]

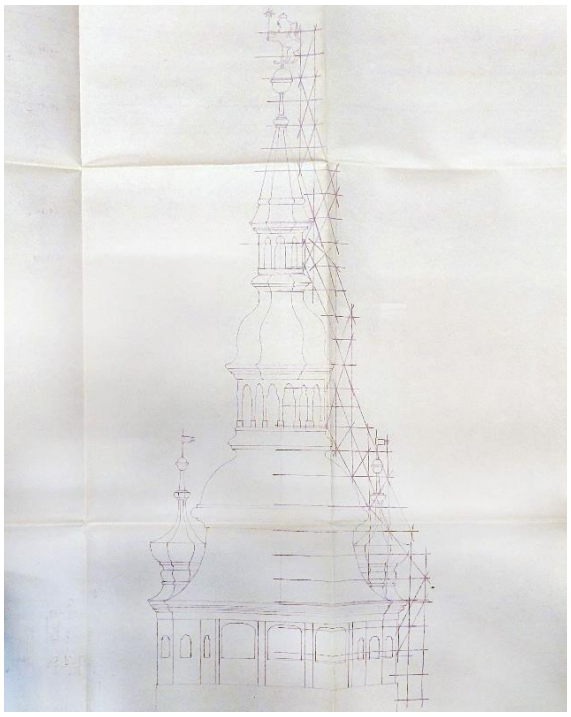

Fig. 10 – St. Vitus Church – perimeter scaffolding of the gallery – view of the scaffolding [24]

The following year was full of explorations, measurements and tests with new materials (e.g. artificial sandstone). In the following years, loose stone elements were brought down, weeds and trees were removed, the sandstone surface was cleaned and joints were restored, without the use of scaffolding. Businesses with climbers were used. The wooden trusses of the choir and Great Tower, as well as the steel truss over the completed section, were treated in this way until 1974 [7].

Already in 1972, due to the fall of the cross cover, a protective scaffolding was erected, which was gradually enlarged, and as other stone elements also fell down, this led to systematic care of the entire shell and the support system under the direction of the Štuko cooperative. The repair of the first pillar was not completed until November 1977. Between 1978 and 1985, seven more pillars were successfully repaired. This was followed by the reconstruction of the main roof between 1985 and 1989, during which the slate roofing was replaced. It was possible to extract rock from the same quarries as in the 19th century. The pattern was also preserved, which is made up of stencils with two colours. The interior underwent changes during an extensive electrical renovation in 1983-1987. An archaeological survey was associated with this action. In the following period between 1988-1991, interior defects were removed and conservation of the exterior parts was resumed [7].

THE MOST SIGNIFICANT MODIFICATION

The greatest change in the interior of the cathedral came in the early 1970s, when it had to be modified in response to the liturgical reforms of the Second Vatican Council. It took place, as the name suggests, at the Vatican, and had four sessions from October 1962 to December 1965. It brought about a major liturgical reform, bringing many initiatives to express the Church's relationship to the ever-evolving world, to other faiths, to individual believers. The Council made possible the use of national languages in the liturgy (previously the Mass had been celebrated in Latin), provided more space for reading from the Bible, dealt with liturgical singing and music, emphasized the

simplification of the rites, their greater clarity and shortening, but also the active participation of the faithful. The new conception of liturgy brought requirements for the worship space, and more detailed requirements were provided by the publication of liturgical instructions. A huge change occurred in the celebration of the Mass, as the priest now served facing the people. This change necessitated a new altar in the form of a table (mensa) as the center of the presbytery, and an elevated place called the ambo was to be created for the reading and singing of biblical texts. The nave of the church is also described, but it did not undergo major changes [1].

The Archbishopric of Prague, and hence the Metropolitan Chapter, requested modifications in the interior of the cathedral according to the liturgical reform. The request argues that the altar is too far from the pews where the faithful sit. Thus, there is no active participation of all the faithful and the formation of a community during the service [25]. The Department of Heritage Conservation (part of the Office of the President of the Republic) had drawn up conservation guidelines stating that "any attempt to reanimate and functionally adapt the cathedral space must be based on a historical and architectural-spatial analysis of the cathedral interior" [26]. The question of the modifications was discussed on behalf of the Metropolitan Chapter by its canon Miroslav Vlček, while the architectural aspect was entrusted to Professor Jan Sokol, who had been thinking about changes to the cathedral's interior (fig. 11 and 12) for some time [7]. Archival documents show that interior work began in December 1972 and was completed in June of the following year [27].

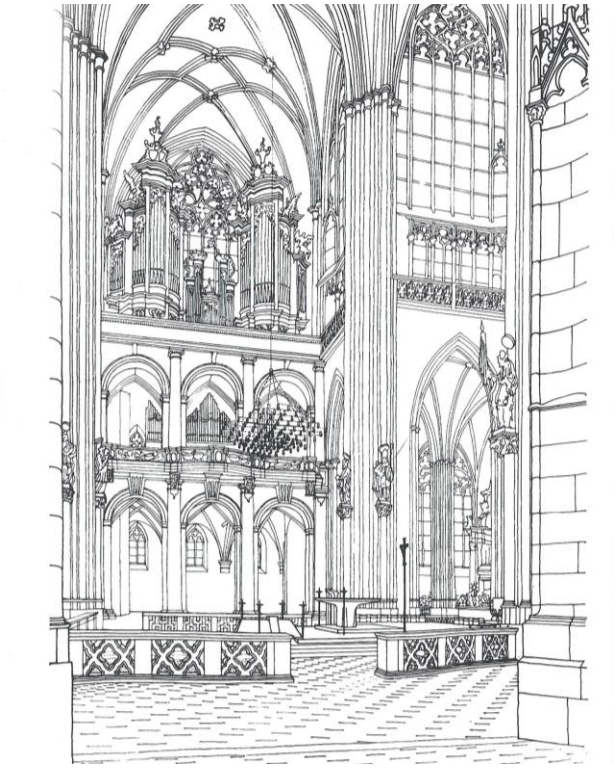

Fig. 11 – Perspective of the Considered Altar in the Nave Crossing of the Cathedral [28]

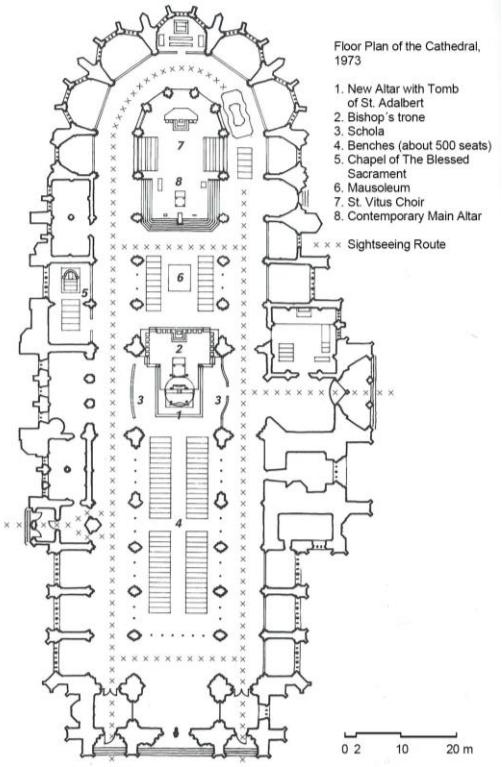

Fig. 12 – Considered Plan of the Cathedral, 1973 [28]

Sokol's ideas about the St. Vitus Cathedral did not correspond to the perception of the then communist society. For him, the cathedral represented above all the first church in Czechoslovakia, a sacred object. Sokol had been thinking about interior modifications for a long time. The original design was drawn up after the Second World War. He considered moving the royal mausoleum in front of the organ chancel to the north arm of the nave. A new high altar would have been built on the vacant site, which would have included the tomb of St. Adalbert. In a new design in the 1970s, he continued with the original ideas, but abandoned the idea of moving the mausoleum and no longer considered a table altar because of liturgical regulations. He would have used the mausoleum as a

backdrop for the new altar and as a separating element between the new and older sections. The new mensa (mensa Domini = altar table) was to be located at the crossing of the nave, was to become the spiritual center of the cathedral, and was to house the tomb of St. Adalbert. It was also to be used during visiting hours. The center of the cathedral would be closed to tourists, while the side aisles would be used for sightseeing tours. This proposal received the support of the Archbishopric, but the Conservation Commission (more accurately called the Subcommission for History, Art History and Archaeology) gave its opposition [28].

Another opportunity was provided by his collaboration with Canon Miroslav Vlček to create a new altar according to the conclusions of the Second Vatican Council. Sokol tried to extend this task to the reconstruction of the entire choir (presbytery), which demonstrates his efforts to save at least some of the previous study. He proposed an extension of the choir platform where a new altar could be placed along with a lectern (ambo) and cross. A new staircase would be built in front of the podium leading to the side aisles. The bishop's throne was going to be placed on the enlarged stage of the main altar, which was built by Josef Mocker. He was not too fond of this altar, but there was no possibility of removing it, so he wanted to use it as a backdrop to the cathedral. From the back of the altar, a stone spiral staircase leads to the upper porch, where the monstrance was formerly displayed. Behind these stairs was the tomb of St. Adalbert. In the space between the main altar and the tomb, a back room with church supplies was built. Sokol proposed to remove this facility and to remove the staircase by the main altar in order to restore dignity to this part of the church. He again submitted his plans to the castle monuments, but again received a negative opinion [28].

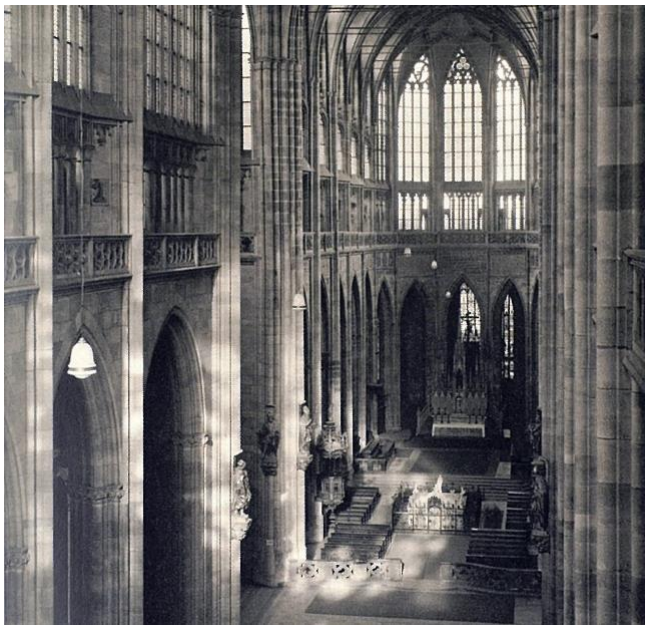

Fig. 13 – View of the church presbytery in the 1920s [29]

Fig. 14 – View of the Presbytery after Modifications Designed by Architect Jan Sokol [30]

Although the grandiose ideas did not come to fruition in the end, at least a relatively minor but significant modification of the presbytery (the space for priests and assistants) with a new altar table and lectern (ambo) was implemented (fig. 14). Architect Sokol, in cooperation with architect Jan Fröml, used a simple but inventive solution. He envisaged the mensa as a marble altar slab supported by six legs made of gold-plated steel I-profiles, see Figure 15). The altar was successfully constructed, but the marble slab was replaced by a slab of Romanian limestone during the execution, to the displeasure of Sokol [28].

Fig. 15 – Altar Table and Pulpit, Gilded Rolled Profiles, Limestone Slab [30]

CONCLUSION

The history of Prague Castle has been associated with sacral buildings since the earliest times; over the centuries several new ones have been built, several have disappeared and several have changed their original function. The Rotunda of St. Vitus was the third building of this type to be built on the Castle grounds, which was first converted into a basilica and then into a cathedral. It became the spiritual center of the Bohemian kingdom, and later of Czechoslovakia and the Czech Republic. The exception was the period of the communist regime, which includes the period under study (1970s and 1980s). During this period, there was an attempt to suppress the religious dimension as much as possible and, on the contrary, to give priority to its other functions - a burial place of Czech rulers, a document of outstanding Gothic and Neo-Gothic architecture, a repository of other cultural and historical monuments of the past, a tourist attraction. It was not until the end of the 1980s that the restoration of a leading role in the spiritual direction of Prague and the whole country was brought about.

The communist government marked a period of decline and disinterest for church buildings. Sacred monuments fell into disrepair, were destroyed, and were converted for other profane purposes (exhibition halls, music halls, etc.). The transformation of religious buildings did not avoid the Castle either. An unambiguous example of this principle is the approach to the Monastery of St. George, which was first to become a Memorial to the History of the Czechoslovak People and eventually became the exhibition space of the National Gallery. Thanks to its presence on the Castle grounds, the sacred buildings were spared dilapidation, although, for example, repairs and building maintenance of the cathedral were neglected in the 1950s and 1960s despite the proclaimed care of the socialist state. However, the period under review brought about a change in this respect and systematic restoration and conservation work began to take place.

The times did not favour the construction of new religious buildings or new interventions in them. Apart from the interventions in the context of conversions, the only significant modification was the new design of the presbytery with the altar table and lectern (ambo) in the Church of St. Vitus by Professor Jan Sokol. This architect worked on the interior of the cathedral for several years, first after the Second World War and then especially in the 1970s, when new liturgical regulations appeared in connection with the Second Vatican Council.

ACKNOWLEDGEMENTS

This article was supported by the CTU Student Grant Competition No. SGS24/033/OHK1/1T/11

REFERENCES

[1] Sklenar M., 2022. Postaveny navzdory: vznik nových římskokatolických sakrálních staveb v českých zemích v letech 1948-1989 (Built in Spite of: The Creation of New Roman Catholic Sacral Buildings in the Czech Lands in 1948-1989), Brno, (Centrum pro studium demokracie a kultury = Centre for the Study of Democracy and Culture) 496 pp. (written in Czech)

[2] Balik S., Hanus J., 2013. Katolická církev v Československu 1945-1989 (The Catholic Church in Czechoslovakia 1945-1989), Brno, (Centrum pro studium demokracie a kultury = Centre for the Study of Democracy and Culture) 400 pp. (written in Czech)

[3] Cuhra J., Ateizace a výchova k vědeckému světonázoru (Atheization and Education for a Scientific Worldview) In: Cuhra J., Cerna M., Devata M., Hermann T., Kourova P., 2020. Pojetí a prosazování komunistické výchovy v Československu 1948-1989 (The Concept and Promotion of Communist Education in Czechoslovakia 1948-1989), Praha (Prague), Ústav pro soudobé dějiny AV ČR (Institute for Contemporary History of the Academy of Sciences of the Czech Republic) 308 pp. (written in Czech)

[4] Blazek P. et al, 2005. Opozice a odpor proti komunistickému režimu v Československu 1968-1989 (Opposition and Resistance to the Communist Regime in Czechoslovakia 1968-1989), Praha (Prague), p. 67-78 (Dokořán = Wide Open Publication House) 352 pp. (written in Czech)

[5] Kuthan J., Royt J., 2022. Katedrála sv. Víta, Václava a Vojtěcha: svatyně českých patronů a králů (The Cathedral of St. Vitus, Wenceslas and Adalbert: the Shrine of Czech Patrons and Kings), Praha (Prague), page 29 (Nakladatelství Lidové noviny = Lidove noviny Publishing House) 692 pp. (written in Czech)

[6] Neubert K., Burian J., 1987. Katedrála sv. Víta na Pražském hradě (St. Vitus Cathedral at Prague Castle), Praha (Prague), (Odeon = Odeon Publishing House) 150 pp. (written in Czech)

[7] Marikova-Kubkova J., 2019. Katedrála viditelná a neviditelná: průvodce tisíciletou historií katedrály sv. Víta, Václava, Vojtěcha a Panny Marie na Pražském hradě (The Cathedral Visible and Invisible: A Guide to the Thousand-year History of the Cathedral of St. Vitus, St. Wenceslas, St. Adalbert and St. Mary at Prague Castle), Praha (Prague), (Hilbertinum – Společnost Kamila Hilberta = Hilbertinum – Kamil Hilbert Society) 928 pp. (written in Czech)

[8] Vancura J., 1976. Hradčany, Pražský hrad (Hradčany, Prague Castle), (SNTL = State Publishing House of Technical Literature) 320 pp. (written in Czech)

[9] Pražský hrad (Prague Castle) - Wikipedia (online). (cit. 2024-04-08). Available from https://cs.m.wikipedia.org/wiki/Pra%C5%BEsk%C3%BD_hrad (written in Czech)

[10] Becker J., Frolik J., Petrickova J., 2000. Nejstarší sakrální architektura Pražského hradu: výpověď archeologických pramenů (The Oldest Sacral Architecture of Prague Castle: Testimony of Archaeological Sources), Praha (Prague), p. 94-144 (Peres = Peres Publishing House) 450 pp. (written in Czech)

[11] Carek J., 1947. Románská Praha (Romanesque Prague), Praha (Prague), page 70 (Universum = Universum Publishing House) 486 pp. (written in Czech)

[12] Streit J., 1958. Divy staré Prahy (Wonders of Old Prague), Praha (Prague), page 45 (Mladá fronta = Mlada Fronta Publishing House) 344 pp. (written in Czech)

[13] Libal D., Zahradnik P., 1999. Katedrála svatého Víta na Pražském hradě (The Cathedral of St. Vitus at Prague Castle), Praha (Prague), (Unicornis = Unicornis Publishing House) 207 pp. (written in Czech)

[14] Chotebor P., 1994. Pražský hrad – podrobný průvodce (Prague Castle – Detailed Guide), Praha (Prague), (Pražské nakladatelství Jiřího Poláčka = The Prague Publishing House of Jiri Polacek) 184 pp. (written in Czech)

[15] Krcalova J., Renesance (Renaissance) In: Benesovska K., Merhautova A et al., 1994. Katedrála sv. Víta v Praze: K 650. výročí založení (St. Vitus Cathedral in Prague: 650th Anniversary), Praha (Prague), (Academia = Academia Publishing House) 283 pp. (written in Czech)

[16] Archiv Pražského hradu, fond Sbírka fotografií Stavební správy Pražského hradu, inv. č. 1009b, foto: Zikmund Reach (Archive of Prague Castle, Prague Castle Building Administration Photograph Collection, inv. no. 1009b, photo: Zikmund Reach).
[17] Rollová V., 2019. Pražský hrad na cestě ke komunistické utopii (1948-1968) (Prague Castle on the Road to Communist Utopia (1948-1968)), Praha (Prague), (UMPRUM = Publishing House of Academy of Arts Architecture and Design in Prague) 264 pp. (written in Czech)
[18] Archiv Kanceláře prezidenta republiky, 6121/2, Stavební záležitosti a údržba IV., Katedrála sv. Víta, stavební úpravy, Katedrála – přehled o majetkoprávních vztazích, č. j. 402 377/74, rekapitulace vývoje majetkoprávních vztahů ke katedrále sv. Víta, Praha, květen 1974, s.3. (Archive of the Office of the President of the Republic, 6121/2, Construction and Maintenance IV, St. Vitus Cathedral, Constructional Alterations, Cathedral - Overview of Property Relations, No. 402 377/74, Recapitulation of the Development of Property Relations to St. Vitus Cathedral, Prague, May 1974, p.3.) (written in Czech)
[19] Snorbert M., Architektonické intervence v areálu Pražského hradu v 70. letech 20. století (Architectural Interventions in the Area of Prague Castle in the 1970s) In: Perinkova M., Juttnerova S., Videcka L., eds. 2022. 14. Architektura v perspektivě 2022 (14th Architecture in Perspective 2022), Ostrava, Vysoká škola báňská – Technická univerzita v Ostravě (University of Mining and Metallurgy – Technical University of Ostrava) 250 pp. (written in Czech)
[20] Archiv Národní galerie, Dokumentace výstav Národní galerie, 1976–1980, Sbírka starého umění (stálá expozice) (1980) – karton č.1, i.č. 7, foto Marie Šonková (National Gallery Archives, Documentation of National Gallery Exhibitions, 1976-1980, Collection of Old Art (permanent exhibition) (1980) - card no. 1, i.no. 7, photo Marie Šonková).
[21] Archiv Národní galerie, Dokumentace výstav Národní galerie, 1976–1980, Sbírka starého umění (stálá expozice) (1980) – karton č.1, i.č. 7, foto Vladimír Fyman (National Gallery Archives, Documentation of National Gallery Exhibitions, 1976-1980, Collection of Old Art (permanent exhibition) (1980) - card no. 1, i.no. 7, photo Vladimír Fyman).
[22] Archiv Pražského hradu. Nová plánová sbírka, 1918-2001, ev. č. 14 (Archive of Prague Castle. New Plan Collection, 1918-2001, ev. no. 14). (written in Czech)
[23] Archiv Pražského hradu. Nová plánová sbírka, sign. 10 201 Katedrála sv. Víta, Pražský hrad – katedrála sv. Víta, rekonstrukce renesančního ochozu věže, Technická zpráva, inv. č. 360 (Archive of Prague Castle. New Plan Collection, 10 201 St Vitus Cathedral, Prague Castle – St Vitus Cathedral, Reconstruction of the Renaissance Gallery of the Tower, Technical Report, inv. no. 360). (written in Czech)
[24] Archiv Pražského hradu. Nová plánová sbírka, sign. 10 201 Katedrála sv. Víta, Chrám sv. Víta – ochoz věže obvodové lešení, inv. č. 361 až 364 (Archive of Prague Castle. New Plan Collection, 10 201 St Vitus Cathedral, St. Vitus Church – Tower Gallery, Perimeter Scaffolding, inv. no. 361 to 364). (written in Czech)
[25] Archiv Kanceláře prezidenta republiky, 6121/1, Stavební záležitosti a údržba II., dopis představitelů Metropolitní kapituly u sv. Víta, Praha, 23.6.1971 (Archive of the Office of the President of the Republic, 6121/1, Construction and Maintenance II, Letter from Representatives of the Metropolitan Chapter of St. Vitus, Prague, 23 June 1971). (written in Czech)
[26] Archiv Kanceláře prezidenta republiky, 6121/1, 6121/1, Stavební záležitosti a údržba IV., Katedrála sv. Víta II, Památkové směrnice pro úpravu interiéru katedrály sv. Víta na Pražském hradě (Archive of the Office of the President of the Republic, 6121/1, Building Affairs and Maintenance IV, St. Vitus Cathedral II, Monumental Guidelines for the Interior of St. Vitus Cathedral at Prague Castle). (written in Czech)
[27] Archiv Kanceláře prezidenta republiky, 6121/1, 6121/1, Stavební záležitosti a údržba III., předání dokončené investice, 12.6. 1973 (Archive of the Office of the President of the Republic, 6121/1, Construction and Maintenance III, Handover of Completed Investment, 12 June 1973). (written in Czech)
[28] Sokol J., Sokol V., 2004. Moje plány: paměti architekta (My Plans: Memoirs of an Architect), Praha (Prague), (Triáda = Triada Publishing House) 341 pp. (written in Czech)
[29] Uměleckoprůmyslové museum v Praze, inv. č. GF50962, foto Josef Sudek (Museum of Decorative Arts in Prague, inv. no. GF50962, photo Josef Sudek)
[30] Správa Pražského hradu, foto Jan Gloc (Prague Castle Administration, photo by Jan Gloc)

CIVIL ENGINEERING JOURNAL

Article no. 18

THE CIVIL ENGINEERING JOURNAL 2-2024

FINITE ELEMENT SIMULATION ANALYSIS OF CURVILINEAR CONTINUOUS BEAM BRIDGE JACKING AND TRANSLATION CONSTRUCTION

Xilong Zheng[1], Jinshuo Yan[2], Peng Li[3], Wei Li[1] and Qiong Wang[4]

1. *School of Civil and Architectural Engineering, Harbin University, No.109 Zhongxing Road, Harbin, Heilongjiang Province, China; sampson88@126.com*
2. *School of Transportation and Surveying Engineering, Shenyang Jianzhu University, No. 25 Hunnan Zhong Road, Shenyang, Liaoning Province, China*
3. *Engineering Department, Shenyang Zhongyuan Traffic Investigation Design Engineering Service Co., Ltd., No.888 Puhe Road, Shenyang, Liaoning Province, China*
4. *School of Civil and Architectural Engineering, Harbin University, No.109 Zhongxing Road, Harbin, Heilongjiang Province, China*

ABSTRACT

This paper investigates the issue of beam misalignment in curved continuous beam bridges. Taking the D0 to D6 spans of the viaduct as the basis, the main influencing factors causing misalignment in curved beam bridges are analyzed and the causes of transverse and longitudinal misalignment in curved beam bridges are calculated and analyzed using Midas/Civil finite element simulation software. The results indicate that the main influencing factor causing misalignment in the operation of curved continuous beam bridges is the system temperature, with the displacement caused by it being larger than the cumulative displacement caused by self-weight, construction phase, gradient load, vehicle load, and bearing settlement. During operation, the failure of expansion joints changes the boundary conditions of the beam, preventing the bridge from freely expanding and contracting longitudinally under temperature load. As a result, the transverse displacement increases to 2-3 times the normal working state of the expansion joint, leading to beam misalignment.

KEYWORDS

Continuous beam bridge, Jacking simulation, Translation simulation, Misalignment, Simulation analysis

INTRODUCTION

Small and medium-span bridges account for approximately 88% of the total number of highway bridges in our country, and due to their large quantity, they deserve more attention in terms of daily maintenance and repair work [1-3]. Due to the fact that many of these bridges were built in the previous century, they were limited by the technology available at that time. As a result, their design load standards and capacity are inadequate to meet current requirements [4-7]. Currently, in China, the majority of funds allocated for highway bridge construction are focused on major bridge projects. As a result, there is limited funding available for small and medium-span bridges. For those smaller bridges that cannot meet current traffic demands, it is nearly impossible to demolish and reconstruct them on a large scale. Instead, it is necessary to modify these existing bridges, making them

compliant with current traffic requirements [8-11].

To better renovate small and medium-span bridges and ensure their efficient service to the people, it is crucial to address the common structural defects. However, there is still insufficient attention given to these issues. One such concern is the significant problem of lateral displacement in the superstructure, which severely affects the normal functioning of the bridges. In particular, small and medium-span curved continuous beam bridges are more prone to such displacements due to their complex structure and load characteristics under long-term effects [12]. Analyzing the causes of bridge lateral displacement is of great significance for improving the efficiency of treating this issue, reducing structural defects in small and medium-span bridges in China, and ensuring the safety of bridges during their operational phase [13-15]. This article will establish bridge models using finite element software to identify the influencing factors contributing to beam displacement. The objective is to analyze the extent to which these factors impact the lateral and longitudinal displacements of the bridge.

INTRODUCTION TO ENGINEERING BACKGROUND

The design load level for the elevated bridge is Class A. The main span of the bridge consists of 119 segments. This study mainly focuses on the displacement analysis of spans D0 to D6. The upper structure of spans D0 to D6 is a continuous curved box girder made of ordinary reinforced concrete, with a span combination of 20+4×25+20=140 m. The box girder is a twin-box six-cell structure with a height of 1.4 m. The total width of spans D0 to D6 is 27 m, and the width distribution is as follows: 0.5 m crash barrier + 12.0 m roadway + 2.0 m median strip + 12.0 m roadway + 0.5 m crash barrier. The lower structure consists of pier D1 to D5#, which are column-type bridge piers, and pier D6 is a prestressed concrete inverted T-shaped cap beam pier. The substructure also includes reinforced concrete rectangular abutments. The aerial view of the elevated structure is shown in Figure 1, and the elevation, plan, and cross-sectional views of the bridge are shown in Figure 2 - Figure 4. The cover beam and retaining block are provided at the expansion joint position, and the cover beam and retaining block are not provided at the other positions.

Fig. 1 – Aerial view of the elevated bridge

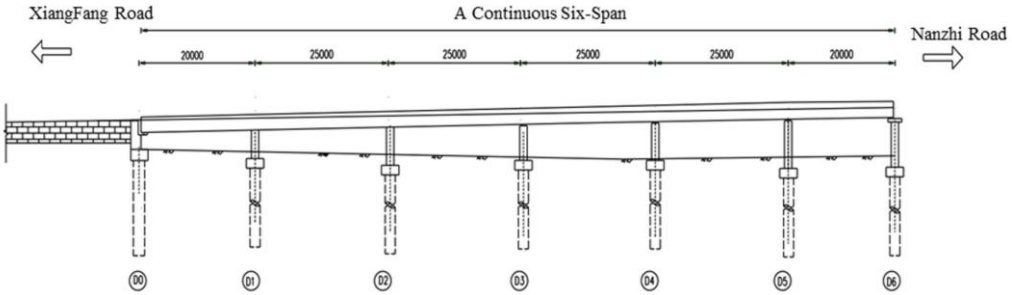

Fig. 2 – Bridge elevation layout diagram (unite: mm)

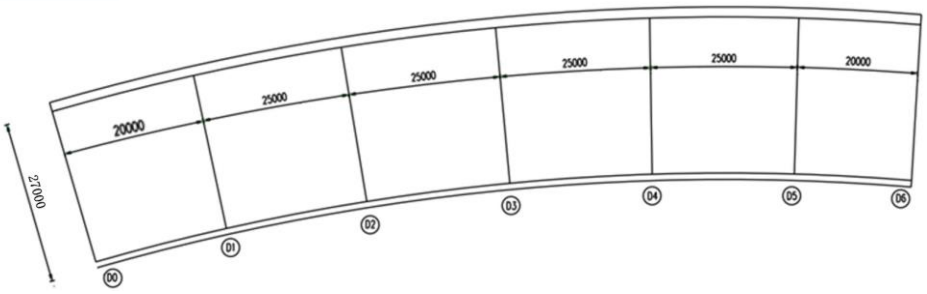

Fig. 3 – Plan layout diagram (unite: mm)

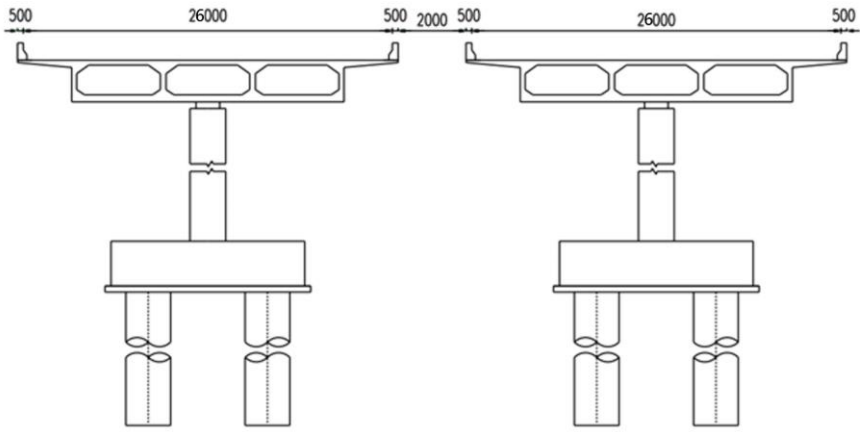

Fig. 4 – Cross-section layout diagram (unit: mm)

OFFSETTING DEFECT

(1) During the inspection of a curved continuous beam bridge, significant lateral displacement of the main beam towards the outside of the curve was observed. The D6# pier box beam exhibited the most noticeable lateral displacement, with a measured lateral displacement at the end of the continuous box beam of at least 90 mm at the outer side of the curve abutment. Due to this lateral displacement, the continuous box beam has caused severe structural damage to its lower bearings, the bridge piers, and even the adjacent ramp bridge. At the end of the 6# pier cap beam (outer side of the curved beam), the retaining block has fractured under the lateral pressure exerted by the main beam, posing a risk of falling as shown in Figure 5.

Fig. 5 – Diagonal splitting of bridge abutment cap beam block

(2) ¨ The lateral displacement of the curved girder bridge will cause the steel plate on the bearing to move along with it. Inspection revealed that there is a common phenomenon of outward sliding movement of the upper steel plate in the bidirectional movable bearings, and in some severe cases, there is a 40 mm displacement between the upper steel plate and the steel basin, as shown in Figure 6 and Figure 7.

Fig. 6 – Compression deformation of lateral restraining steel bar

Fig. 7 – Sliding of upper steel plate out of steel basin by 40 mm

(3) The lower outer surface of the bridge pier column has several semi-circular cracks, as shown in Figure 8. The maximum width of the cracks is 0.26 mm. The crack distribution schematic is shown in Figure 9. The analysis indicates that this is due to the presence of fixed basin-type bearings above the bridge pier. The lateral displacement tendency of the main beam is constrained by the fixed bearings. According to the principle of force interaction, the main beam exerts radial forces on the bearings in the crawling direction, causing a transition of the bridge pier column from an axially compressed state to an eccentrically compressed state and even resulting in tensile stress in the outer concrete.

Fig. 8 – Bottom half-ring crack in bridge pier concrete

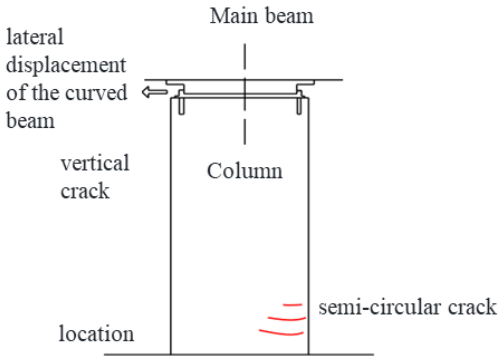

Fig. 9 – Schematic diagram of crack in bridge pier column

MODEL ESTABLISHMENT

The process of bridge jacking and translation may appear simple, but the selection of construction schemes and the control standards during construction are extremely complex. The main challenge lies in how to control the displacement and stress of the beam within a reasonable range during the construction process, without causing damage to the beam. To address this issue, a focused analysis is conducted on the causes of beam deformation and stress during construction, in order to identify corresponding avoidance measures.

Simulation of the Boundary for Curve Continuous Beam Jacking

(1) Selection of jacking method. Bridge jacking techniques can be divided into two categories: integral jacking and partial jacking. Due to the fact that the D0~D6 spans of the Elevated Bridge consist of a 6-span continuous beam structure, and considering the relatively large jacking height required for this project, the integral jacking method is adopted to minimize damage to the beam. The jacking process mainly includes installing temporary supports, jacking the beams, replacing bearings, and releasing the oil from the jacks. The specific operational steps are illustrated in Figure 10.

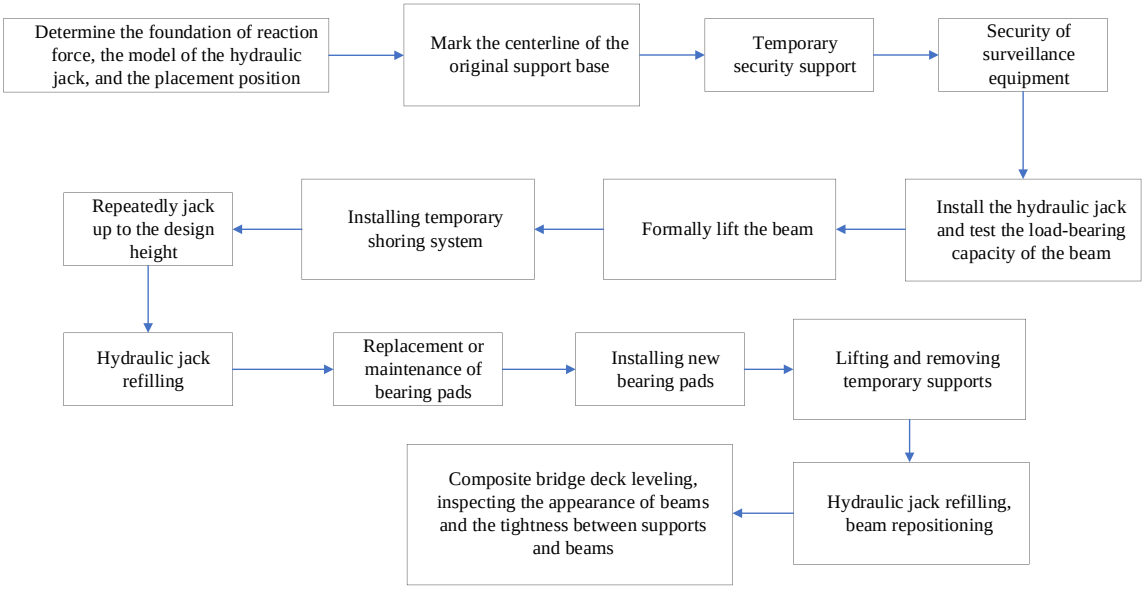

Fig. 10 – Jacking construction steps

(2) In the process of synchronously jacking a bridge, the main control is the variation of the beam stress values generated by the height difference during the start of synchronous jacking and the final placement of the beam. Therefore, the simulation of the supports is controlled by node displacement to achieve the desired effect.
(3) The main beam supports of the original bridge design adopt the form of GPZ8000 pot rubber bearings. Therefore, this paper simulates the bridge supports using compressed springs.
(4) Br 80% of the stress uplift force and lifting height design.

Based on the size of the beam and considering the effects of various adverse loads, the rated lifting force of the jack is increased by 200% as a safety margin. When lifting the bridge, a 650 t hydraulic jack with mechanical locks is used. The method of staged synchronous lifting is adopted.

Simulation of The Translation Boundary of a Curved Continuous Beam Bridge.

(1) The bridge displacement construction method adopts the whole top pushing and resetting construction method.
(2) During the vertical boundary simulation of bridge displacement and resetting construction, the pot rubber bearings have been removed. Horizontal sliding devices are used as vertical supports for the beam structure during the displacement construction. Polyethylene PTFE sheets are applied with silicone oil to reduce friction during construction. Therefore, during the simulated process of top pushing and displacement, compressed rigid supports are used to replace the vertical boundary conditions of the main beam.

(3) During the lateral boundary simulation of bridge displacement and resetting, the lateral boundary conditions of the beam are released. Under the thrust of the jacks, the beam overcomes the frictional resistance of the slide and moves towards the inner side of the arc. During the displacement process, the beam mainly undergoes rigid body motion; at the same time, the beam may experience small recoverable deformations. When the beam is translated to the contact with the stopper at the end of the beam and the bridge abutment, the stopper acts as a lateral rigid constraint. The beam will cease rigid body rotation and accompanied by significant recoverable deformations.

(4) The design of lateral top pushing force and displacement for the bridge. When the main beam is laterally pushed, considering the adverse factors such as temperature stress and the shear deformation of the bearings themselves, the principle of adding a 200% safety margin to the rated lifting force of the jacks is followed. For the displacement process, a 150 t jack is selected for controlled top pushing with graded control. The top pushing speed of the jacks during horizontal displacement should not exceed 1mm/min to ensure that the entire beam moves towards the inner side of the curve as per design requirements.

Control of The Uplift and Translation Reaction Forces.

During the uplift and translation resetting operation of the bridge under traffic closure, it is crucial to ensure that there is no void under the bearings. This means that the bridge, in its displaced state, must have a minimum reaction force of the jacks that is not less than 0 under the most unfavorable load combinations, controlled by hydraulic pressure. This is necessary to prevent the risk of beam overturning and to perform stress verification.

In the condition of traffic closure, the minimum reaction forces of each bearing of the bridge under the load combination of 1.2 dead load + 1.4 live load are shown in Figure 11.

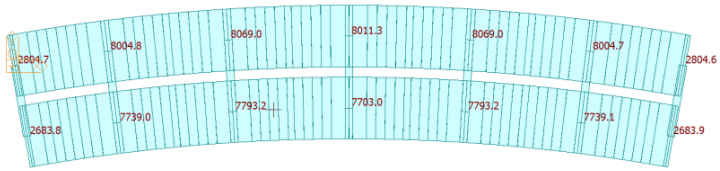

Fig. 11 – Bearing reaction forces

When the bridge reaches its maximum displacement of 90 mm under traffic closure, the minimum value of the inner-side bearing reaction force for a curved girder bridge is 2683.9 kN, and the support force of the jacks is greater than 0. Therefore, it can be concluded that when the beam displacement reaches 90 mm under traffic closure, the bridge support is in a safe condition.

In the condition where traffic is not controlled and vehicles travel along the original lanes, the reaction forces at each support position are shown in Figure 12. In this state, the minimum bearing reaction force is 2432.5 kN. Hence, it can be concluded that when the bridge is in a displaced condition without traffic control, the support forces decrease under the action of eccentric loads. If the bridge is not properly maintained and continues to operate in the displaced state, the displacement will continue to increase, and there is a risk of overturning under the action of eccentric loads.

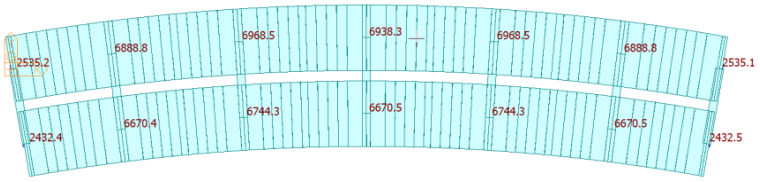

Fig. 12 – Bearing reaction forces

Hydraulic Lifting Stress Control

Traffic control is required during the construction of hydraulic lifting and translation to ensure construction safety and normal travel for the public. The stress increment generated at the most critical section during the construction process should be less than the stress increment generated by live loads at the same section.

Under the action of the most unfavorable eccentric load, tensile stress is generated at the upper edge of the main beam section as Pt, and compressive stress is generated in the main beam section as Pc. The stress of key section of main beam under carriageway load is simulated by finite element method. In the jacking process, there is uneven jacking between piers, which causes secondary internal force of the main beam, and the change of secondary internal force should be controlled. To ensure the safety and sufficient safety factor of the main beam during the hydraulic lifting and translation construction process, the stress variation at the most critical section is controlled to not exceed 80% of the stress increment under the action of live loads at the same section. Specifically, the incremental tensile stress at the most critical section of the main beam should not exceed 0.8 Pt, and the incremental compressive stress at the most critical section of the main beam should not exceed 0.8 Pc, which ensures the safety of the construction. The calculation results are shown in Figure 13.

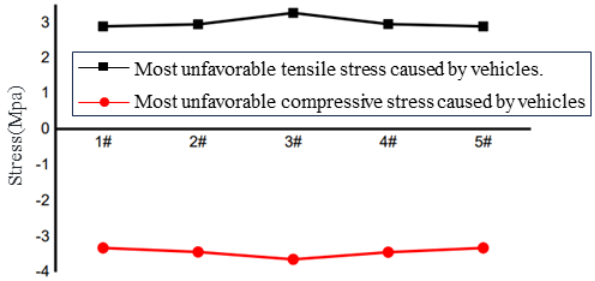

Fig. 13 – The stress limits during the bridge translocation and repositioning process

Using this stress control method is safer and more accurate compared to directly using the design value of concrete tensile strength as the construction stress control criteria.

SIMULATION ANALYSIS OF CURVED CONTINUOUS BEAM BRIDGE.

Simulation of the Jacking Process

In the jacking process of the bridge, a step-by-step jacking method is adopted, with a jacking increment of 5-10 mm per step. This study takes a step increment of 10 mm as an example to analyze the stress increment of each section under different jacking conditions. The specific conditions are listed in Table 1.

Tab. 1 - Simulation of Jacking Conditions

Operating condition	The jacking height
Operating condition one	10mm single-point jacking for Pier 0 and Pier 3
Operating condition two	Pier 0 jacked up by 10 mm, Pier 1 jacked up by 5 mm, Pier 3 jacked up by 10 mm, Pier 2 and Pier 4 jacked up by 5 mm
Operating condition three	Pier 0 jacked up by 10 mm, Pier 1 jacked up by 8 mm. Pier 3 jacked up by 10 mm, Pier 2 and Pier 4 jacked up by 8 mm
Operating condition four	Synchronized jacking up by 10 mm

(1) *Condition 1:* The single-point jacking of Piers 0 and 3 by 10 mm. The increment of stress and deformation of the main beam is shown in Figure 14 – Figure 17.

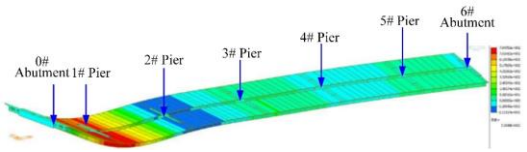

Fig. 14 – Stress distribution diagram of main beam (0# Abutment raised by 10mm)

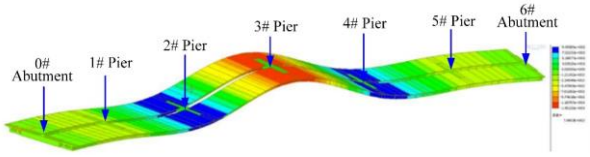

Fig. 15 – Stress distribution diagram of main beam (3# Pier cap raised by 10 mm)

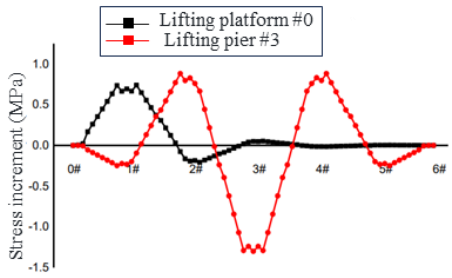

Fig. 16 – Increment of stress on the lower edge of the main beam during single point jacking

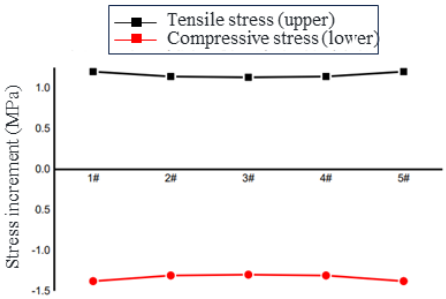

Fig. 17 – Increment of stress on main beam cross-sections for each pier during single point jacking

From the above figure, when the single point is raised to 10 mm, the main beam section at the 0# abutment is in an unconstrained state, resulting in no increase in the bottom stress increment. However, the adjacent main beam section at the 1# pier has a positive increase in bottom stress, indicating tensile stress, and the maximum stress value. When the single point is raised to 10 mm at the 3# pier, the bottom stress increment at the 3# pier is negative, indicating compressive stress and the maximum stress value, while the bottom stress increment at the adjacent piers 2# and 4# is positive, indicating tensile stress with relatively large stress values.

(2) *Condition 2:* The lifting height at the 0# abutment and the 3# pier is 10 mm, while the adjacent piers on the left and right have a lifting height of 5 mm. The stress increments and deformations of the main beam section are shown in Figure 18 - Figure 21.

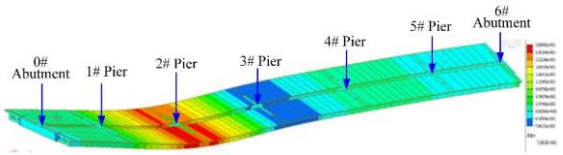

Fig. 18 – Stress distribution diagram of main beam (0# Abutment raised)

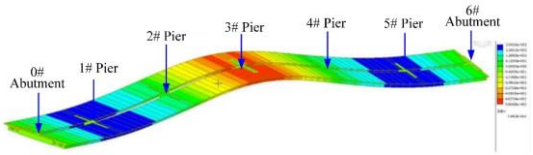

Fig. 19 –Stress distribution diagram of main beam (3# Pier raised)

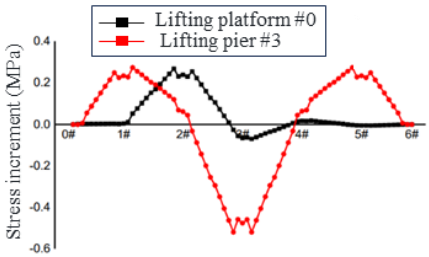

Fig. 20 – Increment of stress on the lower edge of the main beam (0# Abutment, 3# Pier raised)

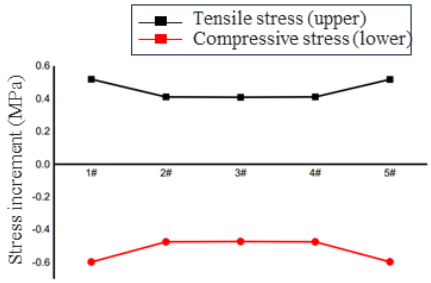

Fig. 21 – Maximum increment of stress on the main beam (1#~5# Pier raised)

From the above figures, it can be observed that when the 0# abutment is lifted to 10 mm and the 1# pier is lifted to 5 mm, the main beam section at the 0# abutment experiences no increase in bottom stress increment due to its unconstrained state. However, the bottom stress increment at the adjacent 1# and 2# piers undergo significant changes. When the 3# pier is lifted to 10 mm and both the 2# and 4# piers are simultaneously lifted to 5 mm, the stress increment across the entire bridge remains large.

(3) *Condition 3*: The lifting height at the 0# abutment and the 3# pier is 10 mm, while the adjacent piers on the left and right have a lifting height of 8 mm. The stress increments and deformations of the main beam section are shown in Figure 22 - Figure 25.

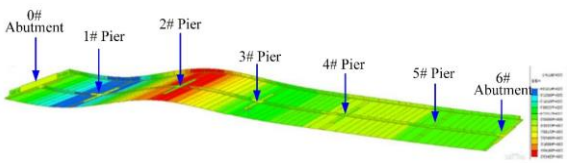

Fig. 22 – Stress distribution diagram of the main beam (0# Abutment raised)

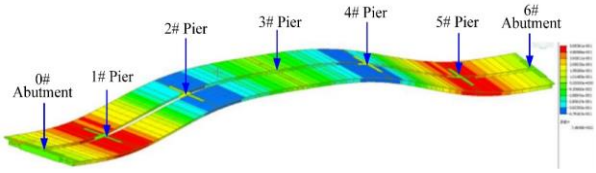

Fig. 23 – Stress distribution diagram of the main beam (3# Pier raised)

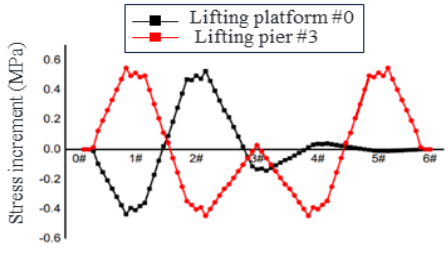

Fig. 24 – Increment of stress on the lower edge of the main beam (0# Abutment, 3# Pier raised)

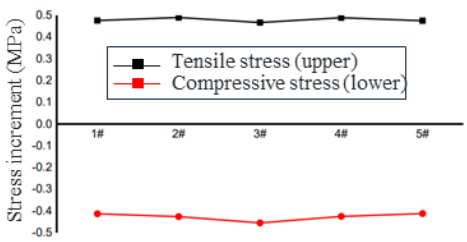

Fig. 25 – Maximum increment of stress on the main beam (1#~5# Pier raised)

From the above figures, it can be seen that when the 0# abutment is lifted to 10 mm and the 1# pier is lifted to 8 mm, the stress increments across the entire bridge are not significant. However, when the 3# pier is lifted to 10 mm and both the 2# and 4# piers are simultaneously lifted to 8 mm, the stress increment at the 3# pier is relatively large and compressive, while the stress increments at the other piers and abutments are relatively small.

(4) *Condition 4:* Synchronized lifting of the entire bridge by 10 mm, the stress increments of the main beam section are shown in Figure 26.

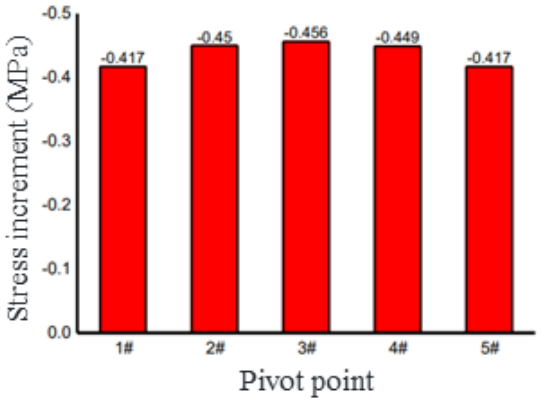

Fig. 26 – Increment of stress on the lower edge of the main beam during synchronized lifting

From the above figure, it can be observed that when the entire bridge is synchronously lifted by 10 mm, the stress increments at the piers 1# to 5# are relatively uniform and the magnitude of the stress increments is also similar.

SIMULATION ANALYSIS OF THE TRANSLATIONAL PROCESS

The translational process simulation is carried out by simulating the top pushing force through the application of concentrated forces. Multiple loading conditions are simulated based on different directions and magnitudes of the top pushing force. The details are as follows.

(1) *Condition 1:* During the translational process, the jacks exert equal pushing forces in a direction perpendicular to the beam end, pushing towards the inside of the curve. The angle between the pushing force direction and the tangent line of the curve is shown in Table. 2. When simulating the pushing force direction of the bridge using finite element software, the angle between the pushing force direction and the Y-axis is shown in Table 3. The displacement in the transverse, longitudinal, and vertical directions of the main beam is shown in Figure 27 - Figure 29. The maximum stress increments on the upper and lower edges, as well as the inner and outer sides of the main beam, are shown in Figure 30 - Figure 33.

Tab. 2 - Angle between the top-down direction at various support point locations and the normal of the curve

Pivot point	0# Abutment	#1 Pier	#2 Pier	#3 Pier	#4 Pier	#5 Pier	#6 Abutment
Angle (°)	-9.96	-7.16	-3.58	0	3.58	7.16	9.96

Tab. 3 - Angle between the top-down direction and the Y-axis at various support point locations

Pivot point	0# Abutment	#1 Pier	#2 Pier	#3 Pier	#4 Pier	#5 Pier	#6 Abutment
Angle (°)	0	0	0	0	0	0	0

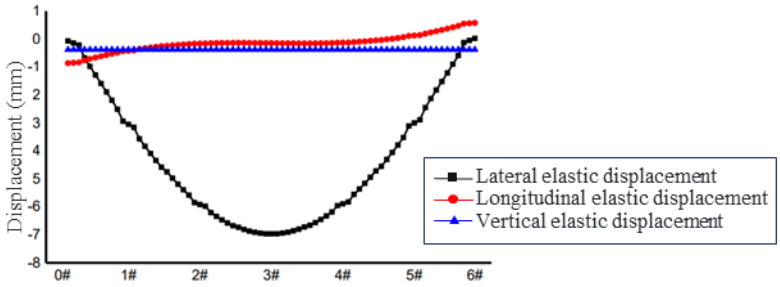

Fig. 27 – Three-dimensional elastic displacement of the main beam during translation process

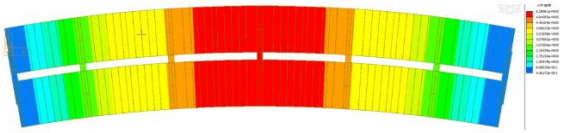

Fig. 28 – Deformation diagram of the main beam during translation process

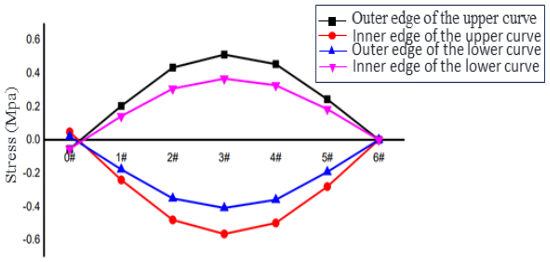

Fig. 29 – Stresses on upper and lower flanges, inner and outer sides of the main beam during translation process

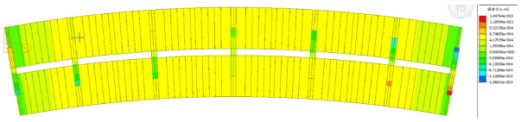

Fig. 30 – Stress distribution on the upper outer surface of the main beam section during translation process

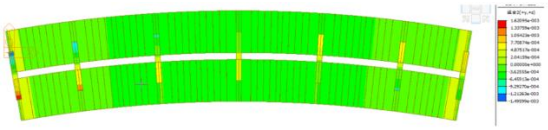

Fig. 31 – Stress distribution on the upper inner surface of the main beam section during translation process

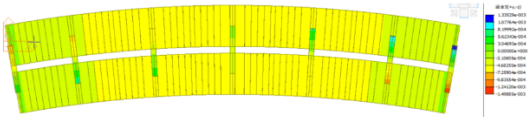

Fig. 32 – Stress distribution on the lower outer surface of the main beam section during translation process

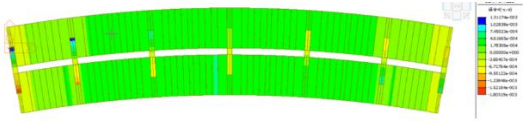

Fig. 33 – Stress distribution on the lower inner surface of the main beam section during translation process

(2) *Condition 2:* The pushing force is applied in the direction perpendicular to the main beam's line form, pushing towards the inside of the curve. The pushing force magnitude is the same for each

pier section. The angle between the pushing force direction and the curve's normal vector is shown in Table 4. When simulating the pushing force direction of the bridge using finite element software, the angle between the pushing force direction and the Y-axis is shown in Table 5.

Tab. 4 - Angle between thrust direction and curve normal at various support locations

Pivot point	0# Abutment	#1 Pier	#2 Pier	#3 Pier	#4 Pier	#5 Pier	#6 Abutment
Angle (°)	0	0	0	0	0	0	0

Tab. 5 - Angle between thrust direction and Y-axis at various support locations

Pivot point	0# Abutment	#1 Pier	#2 Pier	#3 Pier	#4 Pier	#5 Pier	#6 Abutment
Angle (°)	9.96	7.16	3.58	0	-3.58	-7.16	-9.96

The maximum deformation in the transverse, longitudinal, and vertical directions of the main beam is shown in Figure 34. The stress deformation cloud diagram of the main beam during translation is shown in Figure 35. The maximum stress increments on the upper and lower edges, as well as the inner and outer sides of the main beam, are shown in Figure 36.

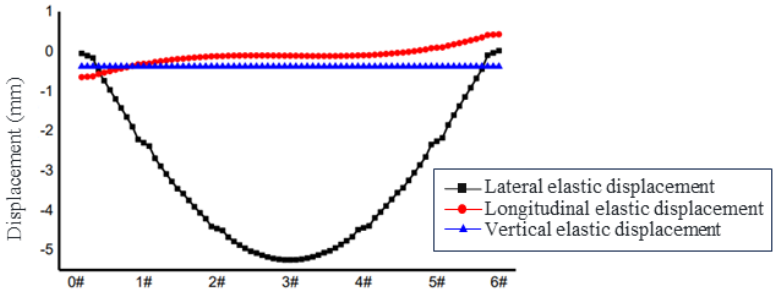

Fig. 34 – Three-dimensional elastic displacement of the main beam during translation process

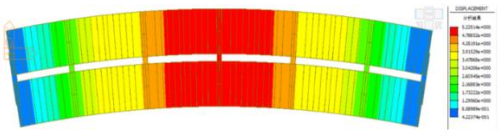

Fig. 35 – Deformation diagram of the translated main beam

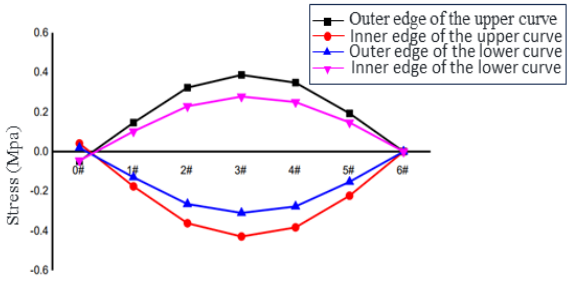

Fig. 36 – Stresses on the upper and lower flanges, inner and outer sides of the translated main beam

(3) *Condition 3:* The pushing force direction is along the line perpendicular to the beam end and pushing towards the inside of the curve. The maximum deformations in the transverse, longitudinal, and vertical directions of the main beam are shown in Figure 37. The stress deformation cloud diagram of the main beam during translation is shown in Figure 38. The maximum stress increments on the upper and lower edges, as well as the inner and outer sides of the main beam,

are shown in Figure 39.

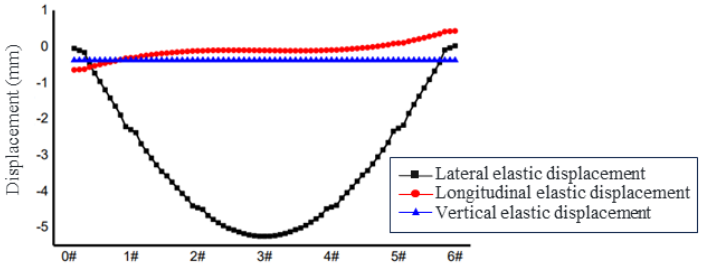

Fig. 37 – Three-dimensional elastic displacement of the main beam during translation process

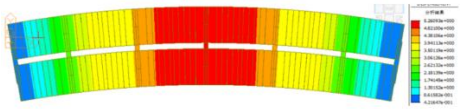

Fig. 38 – Deformation diagram of the translated main beam

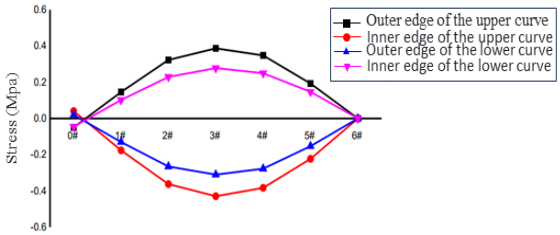

Fig. 39 – Stresses on the upper and lower flanges, inner and outer sides of the translated main beam

Condition 3, when compared to conditions 1 and 2, exhibits smaller stresses and elastic deformations during construction, ensuring the safety of the beam structure. However, controlling the pushing force of the jacks during the pushing operation in Condition 3 can be challenging. If not finely controlled, there is a possibility that the pushing force may not overcome the frictional resistance, resulting in the inability of the beam to rotate.

Condition 2, in comparison to condition 1, offers superior stress and deformation characteristics. With the project located on a curved surface with a radius of curvature of 400 m, when pushing forces are applied perpendicular to the beam's end line, significant horizontal bending deformations of the main beam will occur during the pushing process, and the radius of curvature will decrease.

CONCLUSION

Discussion on the rigid body state of the bridge during the lifting, translation, and resetting construction process, deriving a reasonable method for bridge lifting and translation construction, as well as establishing a model. Proposing stress limitation criteria during the lifting and translation process. Then, based on the aforementioned model establishment method, a finite element model of the actual bridge is established, and a simulation analysis is conducted on the lifting and translation process of the project. The following conclusions are reached:

(1) The beam section stresses were calculated by using node forced displacement simulation during the beam lifting construction phase. It was found that when the main beam was lifted at single point bridge abutment and pier locations, significant differences in the section stress values of the main beam were observed. At the same time, the closer the lifting height of the main beam at the pier and bridge abutment, the more similar the growth pattern of the section stress values. When synchronous lifting was employed, the stress values were all within 0.45 MPa and below the ultimate stress limit. Due to the large lifting height required for the project, it is necessary to control the stress differences. Therefore, the synchronous lifting construction method was adopted.

(2) During the translation construction phase of the beam, a concentrated force was applied to simulate the pushing force of a hydraulic jack. Combining with the model, the movement form and stress state of the beam under different pushing force directions and magnitudes during the translation process were discussed. Safety in construction and the difficulty of construction control were taken into consideration to derive a reasonable construction plan.

REFERENCES

[1] Zhai, Zhihao, Chengbiao Cai, and Shengyang Zhu. Implementation of Timoshenko curved beam into train-track-bridge dynamics modelling[J]. International Journal of Mechanical Sciences, 2023, 247: 108158.

[2] Linzell, D. G., and J. F. Shura. Erection behavior and grillage model accuracy for a large radius curved bridge[J]. Journal of Constructional Steel Research, 2010, 66(3): 342-350.

[3] Li, Ming, and Jingqiao Hu. Analysis of heterogeneous structures of non-separated scales using curved bridge nodes[J]. Computer Methods in Applied Mechanics and Engineering, 2022, 392: 114582.

[4] Tondini, Nicola, and Bozidar Stojadinovic. Probabilistic seismic demand model for curved reinforced concrete bridges[J]. Bulletin of earthquake engineering, 2012, 10: 1455-1479.

[5] Dimitrakopoulos, Elias G., and Qing Zeng. three-dimensional dynamic analysis scheme for the interaction between trains and curved railway bridges[J]. Computers & Structures, 2015, 149: 43-60.

[6] Wang, Jianwei, et al. Application of High-Viscosity Modified Asphalt Mixture in Curved Bridge Pavement[J]. Sustainability, 2023, 15(4): 3411.

[7] Seo, Junwon, and Daniel G. Linzell. Use of response surface metamodels to generate system level fragilities for existing curved steel bridges[J]. Engineering Structures, 2013, 52: 642-653.

[8] Kim, Woo Seok, Jeffrey A. Laman, and Daniel G. Linzell. Live load radial moment distribution for horizontally curved bridges[J]. Journal of Bridge Engineering, 2007, 12(6): 727-736.

[9] Zeng, Qing, Y. B. Yang, and Elias G. Dimitrakopoulos. Dynamic response of high speed vehicles and sustaining curved bridges under conditions of resonance [J]. Engineering Structures, 2016, 114: 61-74.

[10] Monzon, Eric V., Ian G. Buckle, and Ahmad M. Itani. Seismic performance and response of seismically isolated curved steel I-girder bridge[J]. Journal of Structural Engineering, 2016, 142 (12): 04016121.

[11] DeSantiago, Eduardo, Jamshid Mohammadi, and Hamadallah MO Albaijat. Analysis of horizontally curved bridges using simple finite-element models[J]. Practice Periodical on Structural Design and Construction, 2005, 10(1): 18-21.

[12] Ni, Yongjun, et al. Influence of earthquake input angle on seismic response of curved girder bridge[J]. Journal of traffic and transportation engineering (English edition), 2015, 2(4): 233-241.

[13] Wen, Q., et al. Control of human-induced vibrations of a curved cable-stayed bridge: Design, implementation, and field validation[J]. Journal of Bridge Engineering, 2016, 21(7): 04016028.

[14] Nevling, D., Daniel Linzell, and J. Laman. Examination of level of analysis accuracy for curved I-girder bridges through comparisons to field data[J]. Journal of Bridge Engineering, 2016, 11(2): 160-168.

[15] Zhang, Lixin, and Yin Gu. Seismic analysis of a curved bridge considering soil-structure interactions based on a separated foundation model[J]. Applied Sciences, 2020,10(12) :4260.

CIVIL ENGINEERING JOURNAL

Article no. 19

THE CIVIL ENGINEERING JOURNAL 2-2024

OPTIONS SELECTION AND IMPACT STUDY OF INTERCITY RAILWAY TUNNEL CONSTRUCTION UNDER AIRPORT INTERZONE

Ming Zhang

Henan University of Engineering, Institute of Civil Engineering, 1 Xianghe Road in Longhu, Xinzheng, Zhengzhou, China; mzhang@haue.edu.cn

ABSTRACT

The construction of the intercity railroad tunnel beneath the airport causes surface subsidence and affects the operation safety of the airport runway. It is necessary to comprehensively consider many factors to determine the optimal construction plan and control the impact within a safe range. This study employs theoretical analysis and numerical simulation to conduct a comprehensive comparison between the open excavation method and shield method, considering various factors. The findings reveal that: (1) Compared with the open excavation method, the shield method is more suitable for the construction of the interval tunnel crossing the airport under the conditions of groundwater and silty soil layer. (2) The open excavation meets the rapid timelines required by rail transit, and the total cost is close to two shield machines. When the shield method is used for construction, only one shield machine is preferred from reducing the total cost, and two shield machines are preferred from shortening the construction period. (3) The maximum ground settlement resulting from shield tunneling construction is 20mm, and the maximum vertical differential settlement perpendicular to the tunnel is 2.8cm, and the maximum differential settlement ratio is 0.93‰. Which meets the requirements of airport post-construction settlement and differential settlement and can ensure the seamless operation of the airport infrastructure amidst tunnel construction. The research results presented in this paper can serve as a reference for the optimization of tunnel construction scheme and the safety impact control in similar projects in the future.

KEYWORDS

Tunnel, Intercity railroad, Shield method, Open excavation method, Airport; Construction program

INTRODUCTION

In the context of integrating rail transportation into airport collection and distribution systems, the advent of subways and intercity railroads accessing airports has been increasingly significant. Globally, numerous instances exist of subway tunnels intersecting with airport infrastructure [1-6], albeit fewer examples are found regarding intercity railroads. Given the stringent environmental and safety requisites for projects involving intercity railroad tunnels under airports-where operation must proceed without halting flights-the selection of construction techniques is paramount. This necessitates a careful consideration of both the environmental constraints at the construction site and the scale of tunnel construction. The predominant construction methodologies include the box culvert jacking method, mining method, shield method, and open excavation method, among others.

The construction of a tunnel beneath an airport invariably leads to the loosening and disturbance of surrounding rock and soil, causing a radial movement towards the tunnel section and resulting in surface deformation and movement. For critical structures like airports, where

settlement control standards are strict, this can impede the normal functionality of runways (including taxiways and aprons), posing safety risks. Thus, it is crucial to choose the optimal construction method, predict surface movement and deformation during the tunnel construction, and assess the construction's impact on airport operations to ensure the safety and integrity of runway operations (taxiway and apron) throughout the tunnel construction phase.

The discourse on tunnel construction methods through airport areas has been enriched by several studies. Lu Xingbang et al [7] analyzed various construction methods for underground crossings in non-stop airport flight areas, highlighting the open excavation method's key technologies for Shanghai Pudong and Hongqiao airports' taxiway crossings. Jiang Xiaorui [8] explored the feasibility of employing the mining method for intercity railroad tunnel crossings under Guangzhou Baiyun International Airport and its taxiways through numerical analysis, presenting a comparative discussion on the shield and mining methods. Li Xinggao [9] examined the advantages, disadvantages, key technologies, and application scopes of different tunneling methods through airports (flight zones) with typical engineering cases. Yue Renhui [10] analyzed four different construction schemes for a major urban trunk road tunnel beneath the runway of Luogang Airport, employing finite element software to evaluate the pipe curtain + box culvert jacking method's impact on runway safety. Jiang Xiaorui [11], through numerical simulation of the Xinbai-Guangzhou Intercity Railway tunnel construction process under the airport taxiway, evaluated three different excavation methods, ultimately advocating for the upper and lower steps with reserved core soil method. Mi Sixing et al [12] conducted an examination of various schemes for underground crossing of the service lane in the runway area of Pudong Airport, and concluded the feasibility of implementing an underground crossing beneath Pudong Airport's existing runway.

The interaction between tunnels and surrounding soil is typically investigated through field monitoring, model tests, and numerical simulations. Field monitoring can be time-consuming, cumbersome, and may occasionally result in sensor damage. Model tests often simplify complex strata or detailed structures, which might not accurately represent real-world conditions [13-16]. Numerical simulations offer a more efficient means to model soil properties, subway tunnels, adjacent structures, and their interactions, despite requiring some simplifications in the calculation process. This method proves particularly effective for large-scale engineering problems. Ning Jiao et al. [17] conducted deformation analysis of a railway undergoing an under-crossing by a double shield tunnel in a composite stratum of soil and rock through numerical simulations. Liu Xiang et al [18] explored the subgrade settlements of four national railway lines affected by twin shield tunnel excavations, highlighting the correlation between shield machine operational parameters and subgrade settlements. Boonyarak [19] utilized an advanced hypoplasticity constitutive model for numerical back-analysis to discuss the influence zone of new tunnel excavations on existing tunnels. Yao Jianshi et al. [20] analyzed the effects of constructing a new shield tunnel under an existing high-speed railway on the settlement deformation and stress changes of the existing structure via ANSYS. Fei Ruizhen et al [21] combined centrifuge tests with three-dimensional numerical simulations to study the dynamic response of shield tunnel undercrossing an existing high-speed railway, examining the impact on the railway lines and tunnel structures and establishing control standards. Zhao Jinpeng et al [22] Investigated the effectiveness of umbrella arch in controlling deformation of the surrounding rock when a tunnel passes through wear and fragmented surrounding rock by using numerical modeling and field monitoring method. Wu Jingang et al [23] analyzed the mechanical characteristics of the piles and evaluated the reliability of the reinforcement measures by using finite element software to simulate the process of shield tunnelling through bridge piles.

However, research on the impact of tunnel construction on adjacent airports is limited. Yuan Xinpeng [24] applied three-dimensional numerical analysis to simulate the shield tunnel construction process for an intercity railroad under an airport roadway, identifying soil disturbance levels and the extent of construction impact. Li Zhijun [25] developed a three-dimensional model to calculate changes in surface settlement during shield tunneling under an airport runway, assessing the impact on runway operations. Xiao Ming [26] used three-dimensional numerical analysis to

investigate subsidence in the flight zone runway caused by shield construction of the Kunming Rail Transit Project, analyzing soil disturbance and the influence of tunnel depth on runway subsidence.

The above scholars mainly studied the tunnel construction scheme and construction impact of the accessing airport, but failed to comprehensively consider the navigation, technology, construction period, cost, construction impact and other factors. This paper leverages theoretical analysis and numerical simulations to assess the comparative viability of open excavation and shield tunneling methods beneath airports for intercity railroad projects. It aims to provide technical references for the design and construction of similar tunnel projects while ensuring the planning and safe operation of future airport areas.

PROJECT OVERVIEW

The Guangzhou-Dongguan-Shenzhen Intercity Railway (illustrated in Figure 1), originating from Xintang Station on the Guangzhou-Shenzhen Line 4, spans a length of 97.6 km. This route traverses through Guangzhou Xintang, Wanghong, Humen Railway Station, Jinsha and terminates at Shenzhen Airport. The airport section connected to the west side of Shenzhen Airport's T3 Terminal spans 1,800 meters, necessitating penetration through the existing Vertical Liaison Road and the proposed area to the west of the T3 Terminal's station apron. This construction phase is critical as it impacts the usage of the second runway and the operational launch of the T3 Terminal Building. Given the airport expansion project's current state and the planned operational launch, constructing the tunnel access to the T3 Terminal is constrained by the operation of the second runway, geological conditions, existing roadways, and the mandate to maintain uninterrupted flight operations, thereby complicating excavation and construction efforts. Consequently, it is essential to gather and analyze airport-related information and relevant management regulations to devise an appropriate construction strategy.

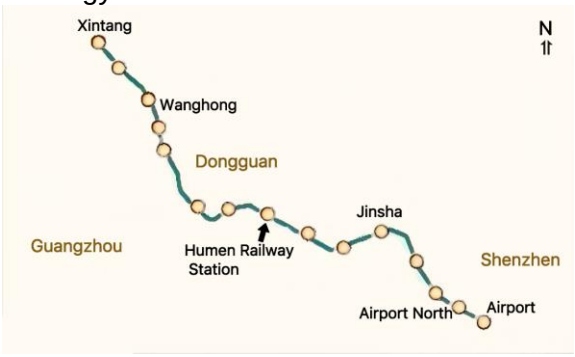

Fig.1 – Guangzhou-Dongguan-Shenzhen intercity railway line

Surrounding environmental conditions

The surrounding environment of the Shenzhen Airport section of the Intercity Railway extends from the north end of the T3 Terminal Building through the vertical connecting road and the west station site to the west side of the T3 Terminal. The surrounding environment is shown in Figure 2, Key points of the construction environment include: (1) the second runway and connecting road, which have been completed and are now operational, including road surface and navigational aids; (2) the vertical connecting road, designed to link the second runway with Terminals No. 1 and No. 2, is operational following the completion of its road surface; (3) the T3 Terminal Building has reached structural completion, with the west wing corridor's foundation constructed using prefabricated pipe piles approximately 30.0 meters deep; (4) on the south side of the T3 Terminal, construction has commenced on the foundation piles for the airport communication center and hotel, with deep foundation pit excavation reaching about 6.0 meters.

Chyba! Objekty nemohou být vytvořeny úpravami kódů polí.

Fig.2 – Surrounding environmental condition of Shenzhen Airport section of Guangzhou-Dongguan-Shenzhen-intercity railway

According to the Regulations on the Administration of Non-stop Construction of Civil Airports [27], once an airport's flight area becomes operational, it must be closed for management. Construction within this closed area must adhere to specific conditions: (1) Construction activities within 300 meters beyond the runway end and 60 meters alongside the runway centerline are prohibited during flight operations; (2) Construction equipment and vehicle heights in the aforementioned areas must not penetrate the obstacle limitation surfaces; and unless specially authorized, construction beyond the taxiway and aprons must maintain a distance of 7.5 meters from the roadway (aprons) plus half the wingspan of the largest aircraft type utilized at the airport.

Engineering geological conditions

Originally a combination of sea area and fishponds, the site underwent reclamation six months prior, followed by soft foundation treatment through the drainage consolidation preloading method. The ground elevation ranges from 3.0 to 3.4 meters, with the constructed road surface elevation between 4.0 and 5.0 meters. The stratigraphic sequence from top to bottom comprises:

(1) A sand filling layer beneath the reclaimed ground surface, predominantly consisting of medium-fine to medium-coarse sand with less than 5% mud content, measuring 5.0 to 6.0 meters in thickness and possessing a standard penetration number greater than 11, indicating a slightly dense to medium dense state.

(2) Muddy soil, which post-treatment transitions from fluid-plastic to soft-plastic, with water content reduced by 20% and in-situ shear strength exceeding 30 kPa over a thickness of 3.0 to 7.0 meters.

(3) The reserved apron area north of the T3 Terminal was backfilled with 4.0 meters of silt, totalling more than 12.0 meters in thickness, characterized by fluid-plasticity and unconsolidated state.

The groundwater level lies at 1.0 to 1.5 meters deep, interconnected with seawater and influenced by tidal changes, resulting in abundant water storage. Given these environmental and geological conditions around the Shenzhen Airport section of the Intercity Railway, coupled with the requirements for uninterrupted construction within the flight area, a comparative analysis of tunnel construction plans assesses the feasibility of construction and its impact on airport infrastructure.

COMPARISON AND SELECTION OF CONSTRUCTION SCHEME OF TUNNEL UNDER AIRPORT

Open excavation construction

Construction scheme analysis

Given the site's geological conditions, which include layers of sand filling and muddy soil rich in groundwater, the risk associated with foundation pit support is considerable. Drawing on the engineering experiences from the Shenzhen Airport deep foundation pit project, the depth of the foundation pit required for tunnel excavation via the open excavation method approaches 15.0m. The chosen foundation pit support structure comprises an underground continuous wall (or borehole occluding pile) reinforced with steel support across three tiers. The second tier of support is dismantled and replaced by the third after the construction of the footing slab and portions of the sidewall.

The primary construction sequence is as follows: installation of the underground continuous wall (or borehole occluding pile), layered soil excavation, tiered erection of steel supports, construction of the base plate and sections of the sidewall, swapping to the third layer of support, removal of the second support for the completion of the sidewall and top slab, backfilling, repairing holes reserved for the partition wall, and finalizing the main tunnel structure.

Influence of open excavation construction on the airport

The impact of open excavation tunnel construction on the airport primarily manifests in three areas:

(1) Construction Alongside the Vertical Connecting Road: The airport's flight area is categorized as 4F, accommodating a runway that is 3800m long and 60m wide, suitable for the world’s largest passenger airplane, the Airbus A380, with the Boeing 747-400 freighter being the largest aircraft currently operating. Given the enclosure and patrol road requirements, construction activities must maintain a minimum distance of 15m from the roadway for the 747 model and at least 30m for the A380. To ensure aircraft passage is not obstructed, an additional connecting road is required on each side of the construction site.

(2) Impact on the T3 Building: The construction necessitates reserving space along the west side of the apron for the rail transit line. The open excavation and subsequent backfilling delay the west apron of the T3 building’s availability by one year.

Cost and duration analysis

The demolition and reconstruction of the connecting road pavement, measured at a width of 30 meters, necessitate additional connecting road surfaces on either side to accommodate construction. Using several tunnel excavation projects with similar geological conditions in this region as benchmarks, the project's cost is analyzed as listed in Table 1, with direct expenses amounting to approximately RMB 329 million.

Tab. 1 - Project Cost Analysis on Open Excavation Method

Serial number	Item	Unit	Number	Unit cost /CNY	Total cost/ ten thousand CNY
1	Underground diaphragm wall	m^3	72000	1800	12960
2	Lock beam	m^3	3600	1100	396
3	Steel bracing	t	6440	8000	5152
4	Steel waist beam	t	1037	8000	830
5	Outward transport earth volume	m^3	432000	45	1944
6	Reinforced concrete structure	m^3	75600	1100	8316
7	Water proofing	m^3	90000	100	900
8	Earthwork backfilling	m^3	135000	50	675
9	Pavements removing	m^3	6750	200	135
10	Pavements recovery	m^3	6750	1000	675
11	New added pavement	m^3	4500	1000	450
12	Non-stop flight cooperation fee	Item	-	-	500
Total cost					32933

Several tunnel open excavation projects with similar geological conditions in this region are taken as reference, The analysis on the duration of open excavation method is shown in Table 2. Since the vertical connecting road section needs to be constructed upside down, it is the controlling duration of the project. It is estimated that constructing one side of the tunnel will take 7 months, with an additional 4 months required for two instances of connecting road surface restoration, culminating in a total construction period of 18 months. Factoring in the vertical contact road restoration, the overall construction timeline extends to 19 months. This schedule aligns with the rail transit project's opening timeline. However, due to the reversed construction of the connecting road, compliance with airport uninterrupted construction management regulations introduces significant uncertainty into the actual construction duration.

Tab. 2 - Construction Period Analysis of Open Excavation Method

Serial No.	Item	First year												Second year								
		1	2	3	4	5	6	7	8		10	11	12	1	2	3	4	5	6	7	8	9
1	Preparation for construction																					
2	First-sequence construction of connecting road																					
3	Connecting road recovery																					
4	Second-sequence construction of connecting road																					
5	Connecting road recovery																					
6	Open excavation of west station																					
7	West station pavement																					

Shield Method Construction

Analysis of construction scheme

The airport section's site is characterized by a significant depth of bedrock and a considerable thickness of pulverized clay and sandy clay layers, with a shallow burial depth. Furthermore, the absence of obstacles, such as abandoned building foundations, renders it well-suited for construction utilizing the shield tunneling method. The shield tunnel section for the airport segment of the intercity rail transit, as illustrated in Figure 3, boasts a track depth exceeding 15.5 m, a center spacing of 17.0 m, and an outer shield diameter of 8.5 m.

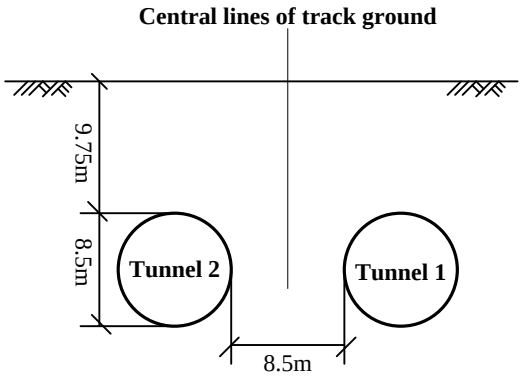

Fig.3 – Schematic drawing of shield design section

The shield tunnel construction for this project benefits from several favorable conditions: (1) The considerable depth of the site's bedrock and the presence of soft and weak strata through which the shield tunnel will pass, devoid of soft-hard interlayers and obstacles, makes it ideal for shield tunnel construction; (2) The construction process does not necessitate the dismantling and rebuilding of the vertical liaison road and the apron construction; (3) Concealed excavation construction facilitates uninterrupted navigation, ensuring that the construction does not impede the west apron road surface construction and its subsequent operational launch.

Numerical simulation analysis of the influence of shield construction on airports

The primary challenge in employing the shield tunneling method within the airport section is the potential impact on the existing roadway surface and the proposed roadway surface on the west apron of the T3 building. Consequently, this section focuses on calculating and analyzing both the ground settlement and the deformation of the shield tunnel during construction, ensuring minimal disruption to airport operations and infrastructure.

(1) *Model calculation*

As depicted in Figure 4, following the selection of the tunnel shield construction section, FLAC3D software is utilized to create a three-dimensional finite difference grid for the construction path. This grid encompasses a length of 160 m, a width of 137 m, and a depth of 33 m. Within the calculation domain, the Y-axis (longitudinal) represents the direction of shield tunneling, the Z-axis (vertical) points upwards, and the X-axis (horizontal) extends to the left. The site's soil model is categorized into 8 layers, with the dual tunnel model centrally positioned. Both the soil and grouting material, alongside the tunnel, are represented using hexahedral solid elements, whereas the lining segments are modelled with plate elements and the shield machine itself with shell elements.

In instances where displacement occurs between the shield advance and the surrounding soil, it's essential to establish a contact surface element between the shield's shell element and the adjacent soil element. This arrangement accounts for the surrounding soil filling the shield's tail gap and the outward soil expansion due to the shield tail grouting. A dislocation between the shield shell and the cured slurry at the rear necessitates a contact surface on the cross-section to simulate their separation accurately. For this purpose, the Goodman contact surface element, which is without thickness, is employed. The computational model is divided into 66,880 units and 71,400 nodes.

To minimize boundary effects on the calculation area, the model enlarges the surrounding grid and imposes constraints on each boundary. The X-direction movement is restricted at the X=60 and X=-77 side nodes; Y-direction movement at the Y=80 and Y=-80 side nodes. Rigid constraints are applied to the nodes on the Z=-20 plane at the model's base to emulate the bedrock's constraint on the site. The ground level is represented at Z=14 on the model’s top surface, designated as a constraint-free plane.

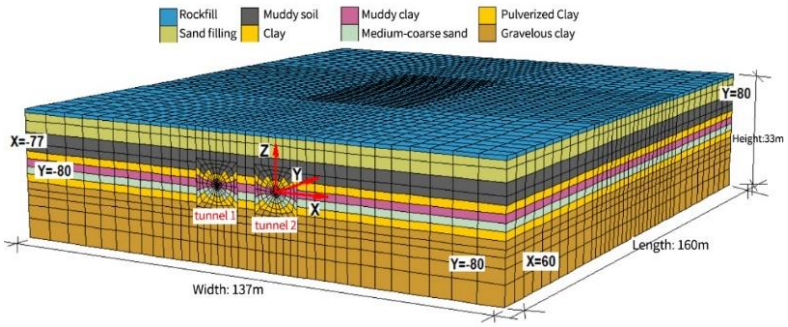

Fig.4 – Numerical simulation geometric model

(2) Parameters calculation

Current soil constitutive models for foundation pit and underground engineering analysis predominantly include the Duncan-Chang (DC) model, Mohr-Coulomb (MC) model, modified Cambridge (MCC) model, hardened soil (HS) model, and small strain hardened soil (HSS) model [28]. The DC model, a non-linear elastic framework, captures the soil's stress-strain non-linearity but fails to account for soil plastic strain or varying stress paths. The MCC, HS, and HSS models, which demand extensive parameterization often requiring complex stress-path testing, are more challenging to implement [29]. The Mohr-Coulomb (MC) model, by contrast, simplifies parameter acquisition and tends to overestimate construction-induced environmental deformations, thereby

ensuring safer estimated outcomes within acceptable engineering error margins [30]. It is the most commonly applied model in foundation pit and underground engineering analyses and serves as a preferred soil hardening model. Consequently, this model's soil employs the Mohr-Coulomb criterion's elastic-plastic framework.

Based on survey [31] and test data [32], the calculation parameters are outlined in Table 3. The shield shell, grouting layer material, and lining segments of the shield machine adhere to the elastic criterion, with stiffness and Poisson's ratio for steel and concrete derived from the elastic model. The shield shell's elastic modulus is 3.45×10^5 MPa with a Poisson's ratio of 0.2. The segment utilizes C50 concrete, and the calculation parameters for both grouting material and lining segments are detailed in Table 4.

(3) *Simulation on construction process*

Reflecting the operational principles of a soil-pressure balance shield, the numerical simulation incorporates the thrust and torque effects of the shield machine on the cutting face. Given that soil units ahead of the cutting face are disturbed by the excavation process, a reduced-strength unloading unit is established. Additionally, a shield tube sheet structure unit is incorporated to emulate the lining effect of the shield, with relevant mechanical parameters set to simulate the interactive dynamics between the tube sheet and the surrounding tunnel rock. The simulation unit's mechanical properties are adjusted to represent the shield machine's propulsion process.

Tab. 3 - Physical and Mechanical Parameters for Soil Layer

Name of rock and soil	Depth /m	Constitutive model	*w* /%	Internal friction angle *φ* /	Cohesion force *c*/ kPa	Elasticity modulus *E*/MPa	*v*	Volume modulus *K*/MPa	Shear modulus *G* /MPa	ρ_{sat} / (g·cm^{-3})	tensile strength *T*/kPa	expansion angle *ψ*/
Rockfill	0～1	Mohr coulomb	-	40	0.1	14	0.3	11.7	5.4	2.30	0.1	0
Sand filling	1～6	Mohr coulomb	-	30	0.1	9.4	0.3	7.8	3.6	1.80	0	5
Muddy soil	6～11	Mohr coulomb	59.3	1.2	14.5	2.67	0.35	2.96	0.98	1.64	0	0
Clay	11～13	Mohr coulomb	29.6	20	35	5.9	0.35	6.6	2.2	1.94	1	0
Muddy clay	13～15	Mohr coulomb	40.8	15	8	2.8	0.35	3.1	1.0	1.91	0.5	0
Medium-coarse sand	15～17	Mohr coulomb	16.6	25	0.1	9.1	0.22	5.4	3.7	2.04	0	5
Pulverized Clay	17～19	Mohr coulomb	29.5	18	26	11.6	0.35	12.9	4.3	1.88	5	0
Gravelous clay	19～34	Mohr coulomb	-	23	30	9.3	0.35	10.3	3.4	2.10	5	0

Tab. 4 - Parameters of Lining Concrete

Supporting structure	*γ*/(kN·m^{-3})	*E*/MPa	*v*	Thickness /m
Grouting layer	24	2	0.2	0.15
Lining segment	24	3.45E10^4	0.2	0.40

To gauge the impact of dual-tunnel excavation on surface settlement, observation points were established above the tunnel (illustrated in Figure 5), arranged across one lateral and three longitudinal axes.

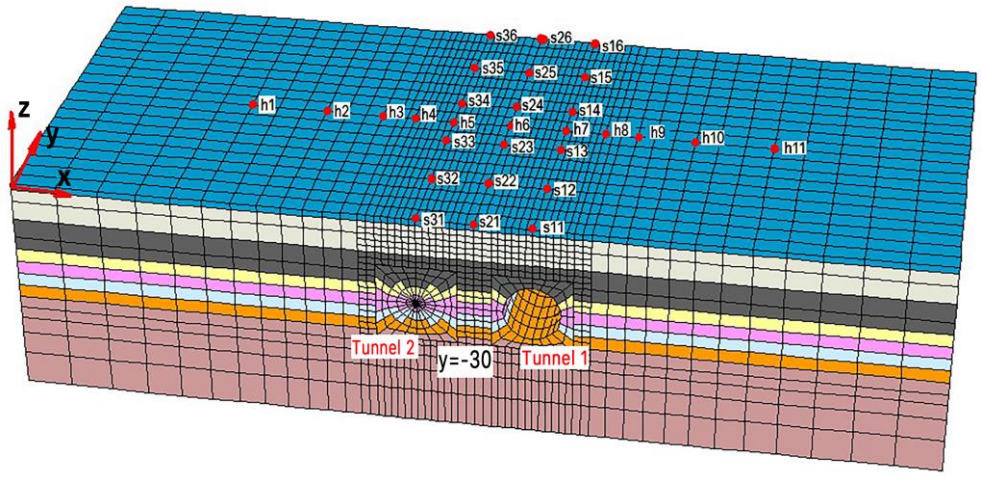

Fig.5 – Location diagram of observation points

(4) *Analysis on simulation results*

The surface settlement curves for three longitudinally distributed observation points during the Tunnel 1 shield tunneling are displayed in Figures 6, 7, and 8, respectively. Figure 6 indicates that the surface directly above Tunnel 1 exhibits a pattern of initial slight elevation, followed by settlement. When the shield machine passes directly below point S11, rapid settlement occurs, stabilizing at 2.2 cm once the shield advances 20 m further. As depicted in Figure 7, the ground subsidence pattern at the line's center mirrors that directly above Tunnel 1, characterized by an initial uplift followed by subsidence post-shield passage, with the subsidence not exceeding 1.0 cm. Moreover, the surface subsidence or uplift deformation stabilizes relatively swiftly after the shield's passage. Assuming a propulsion speed of 10 m/day, the ground surface deformation stabilizes within 2-3 days. Figure 8 illustrates that Tunnel 1's shield tunneling construction causes a maximum uplift of 0.4 cm on the surface directly above Tunnel 2, with this point horizontally aligned with the bottom arch depth of Tunnel 1.

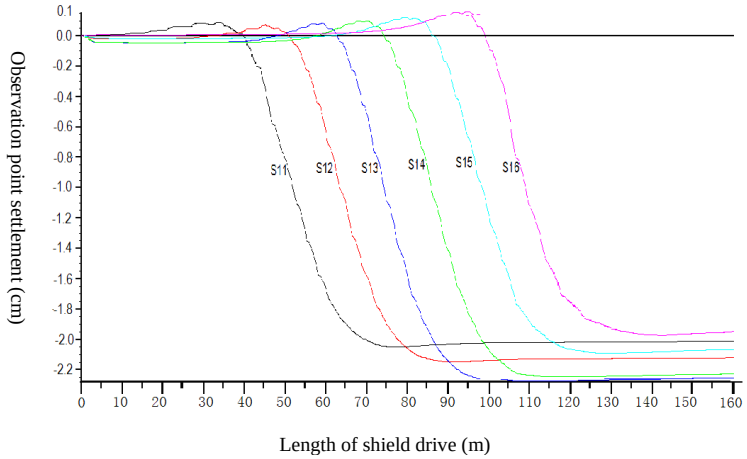

Fig.6 – Settlement of the surface observation point directly above tunnel 1

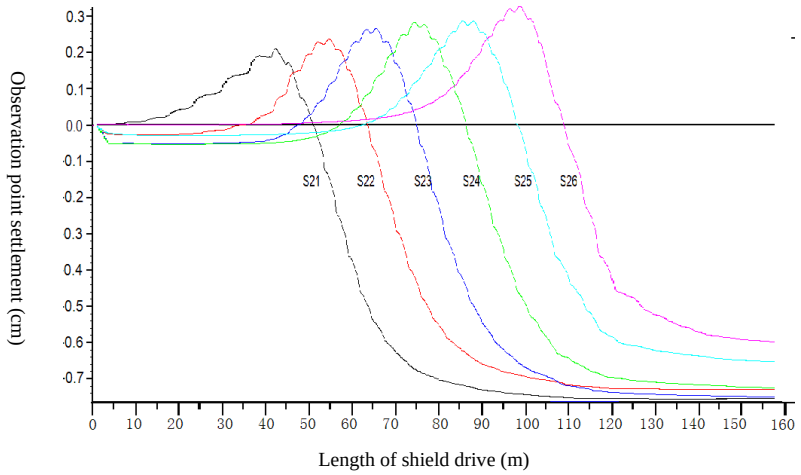

Fig.7 – Settlement of the surface observation point in the center of the line

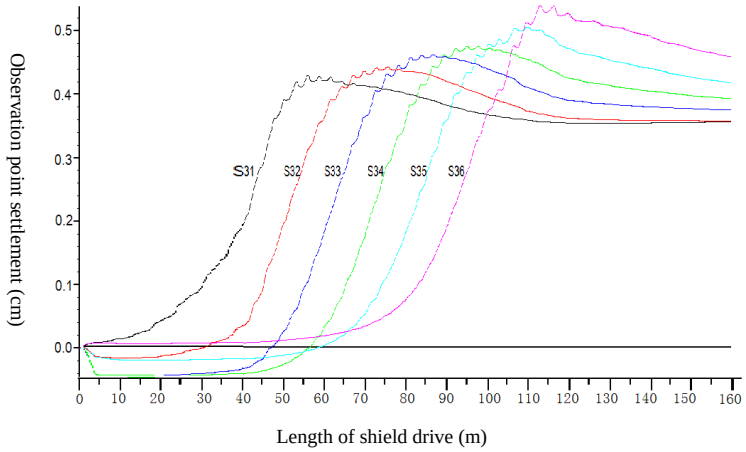

Fig.8 – Settlement of the surface observation point directly above tunnel 2

The surface settlement curves for laterally distributed observation points during Tunnel 1's shield excavation are presented in Figure 9. It shows that points h1 and h11, being distant from the tunnel, are minimally affected by the shield excavation; whereas, h4 and h5, located directly above Tunnel 2, experience an uplift following the shield's passage. Points h6, h7, and h8 undergo a degree of settlement after Tunnel 1's excavation. This suggests that during single-line shield construction, areas distanced more than 20m from the shield tunnel experience negligible impact. Based on the surface settlements at points h7 and h11 in Figure 9, the maximum settlement difference perpendicular to the tunnel's longitudinal direction is calculated at 2.8 cm, with a maximum differential settlement of 0.93‰, fulfilling the airport's requirement for differential settlement to be less than 1.5‰.

Figures 10, 11, and 12 display the surface settlement curves for three longitudinally distributed observation points during Tunnel 2's shield excavation. Figure 10 reveals that surface settlement directly above Tunnel 1 diminishes post-Tunnel 2 excavation due to the soil extrusion effects. Figure 11 illustrates a pattern of initial uplift followed by settlement at the two-line tunnel's center during Tunnel 2 excavation. Figure 12 shows a decrease in surface uplift directly above Tunnel 2 during its excavation, eventually transitioning to settlement, with a settlement value of about 1 cm. The soil body above Tunnel 2, having been pre-affected by tunnel excavation, experiences a smaller magnitude of surface settlement after Tunnel 2's excavation compared to that during Tunnel 1's excavation.

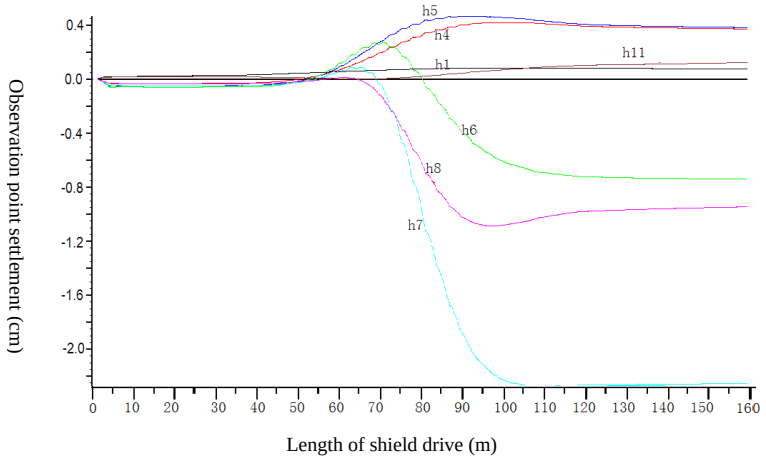

Fig.9 – Surface settlement of the transverse arrangement observation point of tunnel 1 during construction

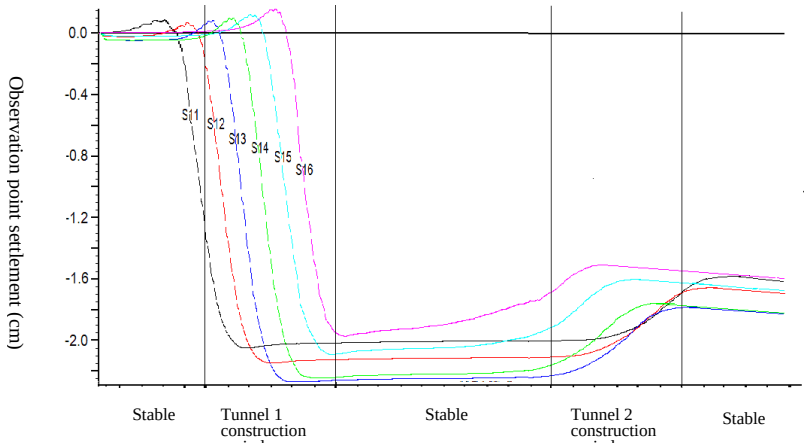

Fig.10 – Settlement of the surface observation point directly above tunnel 1 during construction of tunnel 2

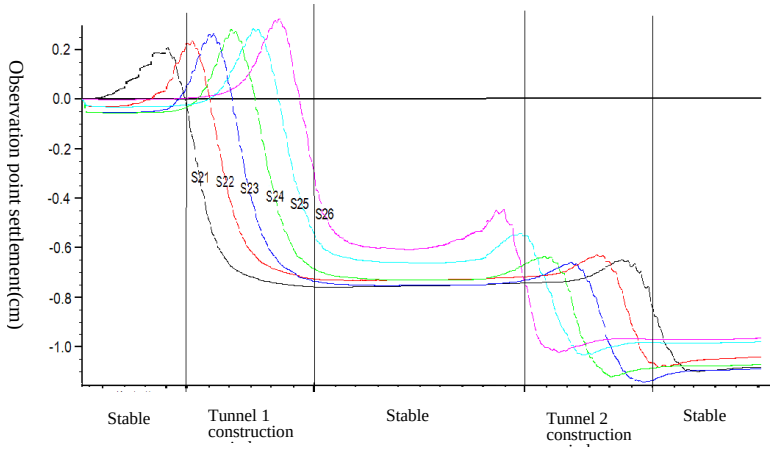

Fig.11 – Settlement of the surface observation point in the center of the line

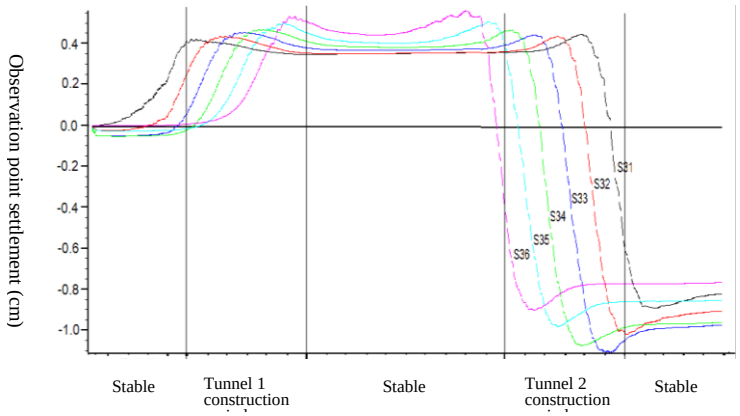

Fig.12 – Settlement of the surface observation point directly above tunnel 2

The lateral distribution of surface settlement observation points during the shield tunneling of Tunnel 2, as illustrated in Figure 13, reveals that the maximum settlement difference perpendicular to the tunnel's longitudinal direction—calculated between points h7 and h11—is 2.8 cm, with a maximum differential settlement rate of 0.93‰. This falls within the airport's stipulated differential settlement requirement of less than 1.5‰.

Analysing the surface settlement observations across all designated points, it's noted that once the tunnel shield progresses directly below S11 and continues for an additional 20 m, the peak ground settlement atop Tunnel 1 reaches 2.2 cm. This settlement is a direct consequence of the loosening and subsequent settling of strata surrounding the tunnel due to the shield tunnelling method, manifesting visibly as surface subsidence. Consequently, this affects the integrity of the airport's built pavement directly above the tunnel and the flat pavement at the west station of the T3 building, inducing approximately 2 cm of settlement. Such settlement results in damage and compromises the functional evenness of the pavement, thereby impacting traffic operations on the surface.

Moreover, during the shield tunnelling activities for Tunnels 1 and 2, varying degrees of surface settlement were observed at each point. The most significant settlement difference, standing at 2.8 cm perpendicular to the tunnel's longitudinal direction, and a maximum differential settlement rate of 0.93‰, could potentially induce cracks and damage to the airport pavement above the tunnel and the T3 building's west station flat pavement. This poses potential safety risks for the movement of aircraft and vehicles.

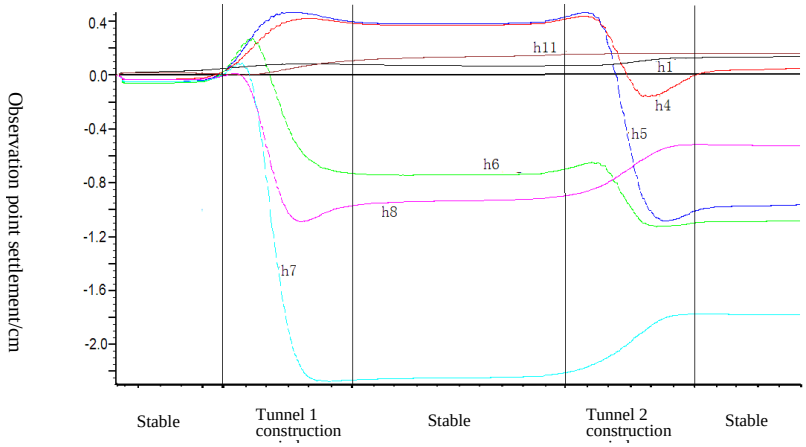

Fig.13 – Settlement of surface lateral arrangement observation point during tunnel 2 construction

Construction period

Drawing upon the shield construction experience from the Shenzhen metro, the advancement rate in the soft soil layers at the airport is observed to range between 5-7 loops daily,

translating to approximately 10 meters with each loop measuring 1.5 meters. Notably, the highest daily advancement recorded is 30 meters, with the domestic record standing at 40.5 meters. Given the necessity for maintenance and the integration of various processes, an average shield penetration rate of 8 meters per day is considered both reasonable and achievable. The design service life of a shield machine for subway projects is estimated at 10 kilometers, implying that the cost of the shield machine is amortized over a construction span of 10 km.

For this project, which spans an interval of 1800 meters, economic analysis suggests that employing a single shield machine, for designed interval turnaround use, is the most appropriate strategy. Should the construction timeline require acceleration, the deployment of two shield machines could effectively shorten the construction period by approximately 8 months. It is advisable to establish shield initiation and reception shafts on the north side of the vertical connecting road, integrating shield turning shafts in conjunction with the T3 building station. The construction strategy involves propelling the shield machine from north to south for the station turnaround, then reversing the direction back to the reception shaft. In scenarios where two shield machines are utilized, the starting well is positioned at the northern extremity, with the machines advancing from north to south in 15-20 day intervals, and emerging at the T3 building station. Reflecting on the shield construction experiences within the Shenzhen metro, the deployment of a single shield machine results in a total construction duration of 28 months; conversely, the use of two machines reduces this to 20 months.

Tab. 5 - Construction Period of One Shield Machine

No	Item	First year												Second year												Third year			
		1	2	3	4	5	6	7	8	9	10	11	12	1	2	3	4	5	6	7	8	9	10	11	12	1	2	3	4
1	Shield customization																												
2	Preparation for construction																												
3	Originating shaft																												
4	Originating																												
5	Turning shaft																												
6	Right line																												
7	Turning																												
8	Left line																												
9	Out of the shaft																												

Tab. 6 - Construction Period of Two Shield Machines

No	Item	First year												Second year							
		1	2	3	4	5	6	7	8	9	10	11	12	1	2	3	4	5	6	7	8
1	Shield customization																				
2	Preparation for construction																				
3	Originating shaft																				
4	Starting on the right line																				
5	Right line																				
6	Out of shaft on the right line																				
7	Starting on the left line																				
8	Left line																				
9	Out of shaft on the left line																				

Cost of the shield scheme

Considering similar subway shield tunnel projects in the region with analogous geological conditions, the cost for constructing a single tunnel is calculated at 70,000 RMB/m, and 140,000 RMB/m for a dual tunnel using one shield machine. Consequently, the expenditure for a 1800 m dual-line tunnel amounts to 252 million RMB. The introduction of two shield tunneling machines escalates the cost for a dual tunnel to 190,000 RMB/m, culminating in a total expense of 342 million RMB, marking a 90 million RMB increase.

Construction schemes comparison between open excavation method and shield method

A comparison of tunnel construction methodologies for the airport section, between the open excavation and shield methods, indicates a preference for the latter. The open excavation approach is considerably influenced by subsurface and groundwater conditions, presenting a higher risk in excavation and support. Moreover, constrained by the operational demands of the airport's second runway and the station on the west apron of the T3 building, this method is less favorable due to higher economic and technical requirements. Specifically, the unit price for a dual-line tunnel is roughly 183,000 RMB/m with a construction timeframe of 19 months, which is shorter than that of the dual-line tunnel utilizing the shield method. However, given the stratum conditions at the site, the shield method is deemed more suitable, offering minimal impact on the vertical connecting road and the west station apron, thereby ensuring negligible disruption to the opening of the second runway and the routine operations of the T3 building.

The ground settlement and differential settlement resulting from shield construction align with the airport's control index standards. Utilizing a single shield machine for turnaround construction positions the unit price of the dual-line tunnel at approximately 140,000 RMB/m, with a construction duration of about 28 months; employing two machines adjusts the unit cost to around 190,000 RMB/m, reducing the construction period to about 20 months. Upon conducting a comparative analysis of the technical, economic, and construction period indicators for tunnel construction in the airport section, the shield method emerges as the preferred choice. The decision to opt for one or two shield machines hinges on prioritizing cost savings versus a reduction in the construction timeline, respectively.

Tab. 7 - Comparison of Open Excavation Method and Shield Method

Construction scheme / Comparison aspects	Open excavation method	Shield method	
		One shield machine	Two shield machines
Unit cost of double-line tunnel / (Ten thousand RMB/m)	18.3	14	19
Total cost /(Hundred million RMB)	3.29	2.52	3.42
Duration /Month	19	28	20
Construction unfavorable or favorable factors and influence	**Unfavorable factor:** There are sand layers and muddy soil layers with a thickness of 5-6 m in this site, and the groundwater is rich and the risk of open excavation supporting is high. **Influence:** (a) If the construction of the connecting road does not affect the passage of the aircraft, a connecting road should be added on both sides. (b) During the open excavation construction, the west side of the T3 terminal was delayed by one year.	**Favorable factors:** (a) The bedrock is deeply buried, the pulverized clay and sandy clay layers are thick and shallow burial depth, and there is no boulder and waste building foundation, which is suitable for shield construction. (b) It can operate without stopping and does not affect the construction and operation of the west station pavement. **Influence:** (a) The maximum ground settlement at the top of the shield tunnel is 22 mm, not exceeding 30 mm, which meets the requirements of airport settlement less than 15 cm. (b) The maximum settlement difference perpendicular to the longitudinal direction of the tunnel caused by shield construction is 2.8 cm, and the maximum differential settlement is 0.93 ‰, which meets the requirement that the differential settlement of the airport is less than 1.5 ‰.	

MAIN PROBLEMS AND SUGGESTIONS FOR TUNNEL SHIELD CONSTRRUCTION

Considering the critical importance of the airport, alongside the inherent risks and uncertainties associated with underground engineering, an analysis of potential risks associated with shield construction is undertaken, tailored to this project's specific characteristics. To mitigate these risks, appropriate construction strategies and emergency response plans have been developed to ensure flawless execution.

(1) Settlement Control Issues: Shield construction has the potential to cause significant ground settlement, impacting the safe movement of aircraft on taxiways and the integrity of various pipelines across the station apron. To address these concerns, the following measures are proposed: 1) Select optimal construction parameters, such as propulsion speed and soil chamber pressure, and conduct trial section construction to validate the chosen parameters before commencing work on the vertical connecting road and tunnels beneath the station; 2) In line with geological assessments, increase the burial depth to circumvent strata prone to sand flow; 3) Enhance the implementation of synchronized and secondary grouting to effectively fill and compact any construction-induced voids.

(2) Ground Collapse: The risk of ground collapse in front of the shield machine poses a significant threat, potentially disrupting flight zone operations and, in severe cases, leading to catastrophic incidents. To mitigate this risk, the following precautions are recommended: 1) Avoid halting the shield machine beneath the vertical connecting road or flight station areas. Necessary

repairs or part replacements should be performed in zones where the shield machine's presence minimally impacts operations; 2) Establish a temporary 30×30m no-travel zone ahead of the shield machine's front to safeguard against collapses that could compromise aircraft safety.

(3) Construction Monitoring: With the second runway operational, access to the vertical connecting road and the station apron is strictly regulated, with construction personnel required to undergo thorough vetting and inspections prior to site entry. Consequently, airport boundary ground monitoring should be automated and require no manual oversight.

CONCLUSION

The impact of tunnel construction on airport infrastructure and the operational efficiency of rail transit access sections has been extensively analyzed, comparing open excavation and shield construction methodologies. This analysis considers various factors including navigability, technological aspects, construction timelines, costs, and overall construction impact, leading to the following conclusions:

(1) Given the susceptibility of tunnel excavation strata and groundwater conditions, the open excavation method, utilizing diaphragm walls or borehole pile steel supports, presents a higher risk. The shield method, in contrast, is more suitable given the ground conditions, exhibiting minimal impact on the vertical connecting road and the west station, ensuring negligible disruption to the operational readiness of the airport's second runway and the T3 Terminal.

(2) While the open excavation method boasts the shortest construction timeline, its unit cost falls between those of the shield method employing either one or two shield machines, closely aligning with the total cost of utilizing two shield machines.

(3) For extended tunnels in silt soil strata, the shield method emerges as the preferred option, praised for its maturity, safety, reliability, and minimal environmental footprint. This method also minimizes impacts on navigation, making it the favored choice. Cost considerations favor the deployment of a single shield machine, whereas timeline efficiencies advocate for the use of two.

(4) The anticipated maximum ground settlement resulting from shield construction is 20 mm, observed atop the tunnel. The greatest settlement variance perpendicular to the tunnel's longitudinal axis is 2.8 cm, with the maximum differential settlement recorded at 0.93‰. These figures comply with the airport's post-construction settlement and differential settlement control requirements, which are less than 15cm and 1.5‰, respectively. The shield construction's impact on ground deformation is minimal, extending to areas 24 m from the shield construction centerline.

These findings offer valuable insights for similar future projects. However, it's important to note the assumptions made regarding soil behavior, modeled on the Mohr-Coulomb elastic-plastic criterion, in the three-dimensional finite difference analysis. These assumptions may lead to overestimations of the maximum surface settlement and differential settlement compared to actual measurements. Additionally, estimations of the construction period and costs for subway tunnel projects, whether through open excavation or shield methods, carry certain inaccuracies, derived from extrapolating engineering experiences from similar geological conditions within the region.

ACKNOWLEDGEMENTS

The research is mainly supported by Henan Science and Technology Project (182102310003) in China. The authors thank all anonymous reviewers for reviewing the manuscript.

CONFLICTS OF INTEREST

The authors declare that they have no conflicts of interest.

REFERENCES

[1] TONG Jianjun, GUI Dengbin, WANG Li, et al (2020) Calculation Method of Additional Load of Metro

Tunnel Crossing underneath Existing Airstrip. Tunnel Construction 40(9): 1-8.
[2] DAI Xuan, XU Guanying, HUO Haifeng, et al (2019) Three-dimensional Finite Element Analysis of Impact of Utility Tunnel Construction on Overlying Deep Excavations. Chinese Journal of Geotechnical Engineering 41(S2): 21-24.
[3] TANG Zhao, TANG Xiongjun (2016) Structural Design and Safety Analysis of Enshi Under-passing Xujiaping Airport Tunnel. Highway Tunnel (4): 28-32.
[4] MA Dong, HUANG Lixin (2016) Settlement Repair Technique of Capital Airport Pavement Undercrossing Runway and Tunnel. Railway Construction Technology (8): 31-35,54.
[5] LUO Gang, PAN Shaokang, ZHANG Yulong, et al (2019) Settlement and Deformation Law of a Double-track Shield Tunnel Underpass Airport Expressway. Journal of Chang'an University (Natural Science Edition) 39(4):100-108.
[6] Zhang Yubin (2015) Study on the Ground Deformation Law of Large Cross-section Tunnel Construction under Airport Runway. Journal of Highway and Transportation Research and Development (Application Technology Edition) (10):163-164, 223.
[7] LU Xingbang, WANG Yuandong, QIAO Yafei, et al (2018) Investigation on Undercrossing Construction Methods Used in the Airfield Area under Non-suspending Condition. Modern Tunnelling Technology 55(S2): 375-385.
[8] JIANG Xiaorui (2017) Discussion on the Scheme of Intercity Railway Tunnel Passing under Airport Taxiway. Railway Standard Design 61(1): 71-75.
[9] LI Xinggao, YUAN Dajun, YU Jiao (2013) Study on Construction Method of Tunnels underneath Airport. Science and Technology Innovation Herald (31): 2-3.
[10] YUE Renhui (2021) Study on the Scheme of Large-span Municipal Highway Tunnel Under-passing Airport Runway. Shangxi Architecture 47(14):117-119.
[11] JIANG Xiaorui (2021) Research on the Influence and Countermeasures of Tunnel Crossing Airport Taxiway. Chengdu: Southwest Jiaotong University.
[12] MI Sixing, XIA Caichu, WANG Xiaohong, et al (2007) Comparative Reasearch on Construction Scheme of Tunnel under Runway. Chinese Journal of Underground Space and Engineering 3(2): 319-324.
[13] BOONYARAK T, PHISITKUL K, NG C.W.W. et al (2014) Effects of Construction Sequence and Cover Depth on Crossing-tunnel Interaction. Canadian Geotechnical Journal 52(7): 851-867.
[14] MIAO Linchang, WANG Fei, NG C.W.W. et al (2017) Centrifugal model tests on excavation of twin parallel tunnels. Chinese Journal of Geotechnical Engineerng 39(2): 373-379.
[15] LIU Xiaoguang, DU Shouji, LI Peng (2014) Centrifuge investigation into the effect of new shield tunneling on an existing underlying large-diameter tunnel. Tunnelling and Underground Space Technology, (42): 59-66.
[16] NG CWW, WANG R, BOONYARAK T (2016) A comparative study of the different responses of circular and horseshoe-shaped tunnels to an advancing tunnel underneath. Geotechnique Letters 6(2): 168-175. DOI: 10.1680/jgele.16.00001.
[17] JIAO Ning, SUN Shuai, LIU Jinyu. et al (2023) Analysis of existing railway deformation caused by double shield tunnel construction in soil–rock composite stratum. Energy Reports (9): 159-165.
[18] LIU Xiang, ZHANG Rui, FANG Qian. et al (2024). Subgrade settlements of existing railway lines and operational parameters of shield machine induced by twin shield tunnel excavations: A case study. J. Cent. South Univ. 31(1): 272-278.
[19] Boonyarak T, Ng CWW. (2016) Three-dimensional influence zone of new tunnel excavation crossing underneath existing tunnel. Japanese Geotech Soc Special Public 2(42):1512–1518.
[20] Jianshi Yao, Zifan Wang, Zichen Li. et al (2021) Research on Structural Deformation Law and Allowable Deformation of Shield Tunnel Underneath Passing High-Speed Railway Tunnel. Fifth International Conference on Traffic Engineering and Transportation System (ICTETS 2021), Proc. of SPIE, 1205832: 1-7.
[21] FEI Ruizhen, PENG Limin, ZHANG Chunlei. et al (2023) Mechanical characteristics of twin tunnel underneath construction on existing high-speed railway tunnel. Archives of Civil Engineering. (1): 403-420.
[22] WU Jingang, ZHAO Jinpeng, TAN Zhongsheng. et al (2022) Mechanical behavior of large-diameter adjacent shield tunnelling bridge piles: a case study of Chunfeng tunnel. Applied Sciences. (12):1-16.
[23] ZHAO Jinpeng, TAN Zhongsheng, LI Linfeng. et al (2024) Mechanism effect of umbrella arch supports in a shallow long‐span tunnel: a case study. Archives of Civil and Mechanical Engineering. (24): 1-17.
[24] YUAN Xinpeng (2015) Study on Settlement Control of Intercity Railway Tunnel under-passing Flight Area of Shenzhen Airport. High Speed Railway Technology 6(4):56-61.
[25] LI Zhijun, ZHANG Jianguo (2017). Influence Control of Subway Shield Driving through Airport Runway. Journal of Water Resource and Architectural Engineering 15(4): 153-156.

[26] XIAO Ming, LAI Ying (2011) 3D Numerical Analysis on Subsidence Control of Shield Tunnel Excavation under Airport Runways. Tunnel Construction 31(S1): 32-37.
[27] Civil Aviation Administration of China (2000). Regulations on the Administration of Non-stop Construction of Civil Airports.
[28] LI Guangxin (2004) Advanced soil mechanics. Beijing: Tsinghua University Press, 32-113.
[29] SIMA Jun, MA Xv, PAN Jian (2018) Experimental Study on Parameters of HS-Small Model for Natural Aged Clay in Wuhan. Journal of Water Resources and Architectural Engineering 16(3):93-97,112.
[30] GUAN Fei (2010) 3D numerical analysis for a ultra-large deep excavation in soft clay based on HSS constitutive model. Chinese Journal of Geotechnical Engineering 32(S1):177-180.
[31] Shenzhen Investigation & Research Institute (2004) Geotechnical Investigation Report for Preliminary design Stage of Site Reclamation and Soft Foundation Treatment for Shenzhen Airport Second Runway Project (Lot A).
[32] Shenzhen Construction Engineering Quality Testing Center (2009) Test Report of Cross Plate Shear and Drilling Test in Area II-1, II-4 and II-7 of Land Area Formation and Soft foundation Treatment Project of Shenzhen Airport Flight Area extension.

CIVIL ENGINEERING JOURNAL

Article no. 20

THE CIVIL ENGINEERING JOURNAL 2-2024

DIGITALIZATION OF IRRIGATION SYSTEMS FROM WATER MANAGEMENT MAPS

Adam Tejkl and Petr Kavka

Czech Technical University in Prague, Faculty of Civil Engineering, Thákurova 7/2077, 166 29 Praha 6 - Dejvice, Czech Republic, email: adam.tejkl@fsv.cvut.cz

ABSTRACT

With the increasing intensity of evapotranspiration caused by the changing climate, there is a growing need for water. This is especially true in locations where water-intensive vegetables are grown in intensive agriculture. Historically, irrigation systems were built in many intensive agriculture areas in Czechia, but they fell out of use, and evidence of their location was lost. However, Water Management Maps, which were only issued in paper form and have never been fully digitized, can provide evidence about the location of these large-scale irrigation systems. In this paper, we present a method for digitizing irrigation systems using the segmentation and classification of individual segments in the ArcGIS environment. The resulting raster is converted to polygons and is blended with the Land Parcel Identification System layer, resulting in a layer of irrigated land. Two statistical analyses were performed on this layer: statistics of the areas corresponding to the individual source watercourses, and statistics of the type of source.

KEYWORDS

Python, ArcGIS, Segmentation, Machine learning, Water Management Map, Climate change

INTRODUCTION

The social-economic changes following the end of the communist period in Eastern Europe led to the privatization of agriculture and to a decline in vegetable production, resulting in significant loss of data related to irrigation systems [1], [2]. The transfer of the irrigation agenda to various new authorities in the early 1990s and the abolition of the State Reclamation Administration resulted in the loss of entire archives containing project and operational documents for irrigation systems [3]. Moreover, the generational change of workers in agriculture and in government offices has further increased the unavailability of information sources [4], [5].

The extensive and planned construction of large-scale irrigation systems also came to an end in the early 1990s. The best remaining record of the irrigation systems at their greatest extent is preserved in the Water Management Maps, which were last updated in 1997 [6].

The prolonged drought between 2015 and 2017 highlighted the insufficient state of the information resources related to irrigation systems [7], [8]. Reanalysis of the irrigation systems from the Water Management Maps offers a way to obtain topographical, hydrological, and pedological data on implemented irrigation systems, even if they are no longer in operation [9].

Information on the location of the irrigation systems can help with planning, and with allocating resources when irrigation structures are restored or reconstructed. Large-scale irrigation systems were often implemented in areas with a historical need for irrigation, or in areas with a proven recurrence of dry years [10], [11]. Integrated irrigation solutions are more efficient than separate solutions for locations of limited size [12], [13], [14]. Large-scale irrigation systems also allow agricultural enterprises specializing in growing vegetables to rotate their crops without the need to build new irrigation systems [15], [16].

Information about the location of large-scale irrigation systems can be gathered from historical maps. These maps are in raster form, and automatic image classification is a valuable tool for speeding up the identification process.

Classification of images into groups with multiple labels is a fundamental but challenging task in computer vision. Remarkable progress has been made recently by predicting image labels with deep convolutional neural networks [17]. Traditional machine learning techniques have achieved good performance for terrain perception; however, most of the techniques require manually designed classifiers [18]. Many studies and research efforts follow the conventional pattern recognition paradigm, and some methods exploit a Convolutional Neural Network to conduct the classification task [19]. Data from RGB sensors classified using artificial, deep neural networks are often used in terrain recognition tasks. The results of this earlier work demonstrate the performance of artificial neural networks in terrain recognition tasks, and provide some hints on how to improve classification in the future [20].

Information extraction from historical maps using a Convolutional Neural Network for the recognition task was applied to extract human settlement symbols in the United States Geological Survey historical topographic maps [21]. Convolutional Neural Networks were used for digitizing historical maps to extract vector shapes of the objects of interest from raster images of maps. Convolutional Neural Networks provided efficient edge detection and filtering [22]. Techniques of deep learning were applicated for extraction of information from historical maps in an automated manner on the Early Twentieth Century Map series. These maps utilize standardized symbology and conventions, which greatly enhance the effectiveness of the method. The results obtained demonstrate that deep learning serves as an efficient tool for recovering georeferenced information represented in the form of conventional signs or lines. The method has consistently yielded excellent outcomes, particularly when sufficient training data is available. It performs optimally when applied to large map series that can furnish ample information for training. Deep learning approach offer the potential to map features across entire map series with significantly improved speed and coherence compared to other available methods [23].

The aim of our work is to find a way to usefully digitalize the irrigation systems depicted on the Water Management Maps. The irrigation system should be identified at the level of areas of agricultural land that receive water through these irrigation systems, such as irrigated fields. Furthermore, it should identify the source watercourses and the source types of these systems for example: river, reservoir or well [24]. Digitalized maps of irrigation pipes and pumping stations will later be used as a source for further analyses of systems, their position or irrigated soils.

METHODS

The 1:50,000 Water Management Map of the Czech Republic (hereafter referred to as ZVM) was published by the Czech Land Surveying and Cadastral Office. The map was processed and printed by the Land Surveying Office on 58x47 cm paper in a set of medium-scale basic map sheets. Around 20 map sheets were updated every year.

The map shows the network of watercourses, the distribution points and the hydrological division of the basin, structures in the state observation networks, structures and measures for the use of surface and underground water, protection zones of water structures, structures and equipment of the main water users (e.g., water pipes and sewers, use of water energy, water transport, industry) and other information [6].

Scans of ZVM sheets in tif format were imported into ArcGIS. These are rasters with a pixel size of 3.18 m. and a range of values in one pixel between 0 and 255.

For the purposes of the reanalysis, the most important lines were the lines symbolizing the underground irrigation pipes and the symbols of the irrigation pumping stations. These lines consist of a blue dashed line, with every 3 to 5 lines containing a bump. Due to the manual creation of these maps, the lengths of the spaces and dashes vary, there are different widths, and the shade of the

blue color used varies slightly (See Figure 1). However, the lines on any single map sheet are always very similar.

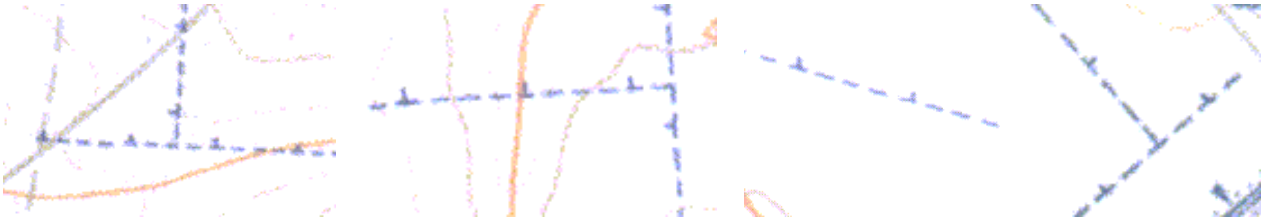

Fig. 1 – Examples of different variants of the irrigation piping symbol

Convolutional Neural Network method.

Our model is based on the winning model of the Kaggle machine learning competition [25] held in 2013, commonly known as Kaggle Cats vs. Dogs [26]. This model takes its name from the competition dataset that consists of photos of dogs and cats. The dataset was originally created as the Completely Automated Public Turing test to tell Computers and Humans Apart (CAPTCHA). Specifically, the task was known as Animal Species Image Recognition for Restricting Access (Asirra) [27].

The model was specifically designed to handle 25,000 labeled photos [28]. Due to its simplicity and the fact that it can be easily stored in memory, this model has become popular among beginners in the field of computer vision as a starting point for learning about convolutional neural networks. Additionally, this model's architecture is straightforward and adaptable, making it suitable for our purposes. While we considered other models, such as more complex deep learning architectures, the simplicity and robustness of the Kaggle Cats vs. Dogs model made it an ideal choice for the initial stages of our project. As we progress, we may explore more advanced models to further refine our approach.

Pipeline scheme

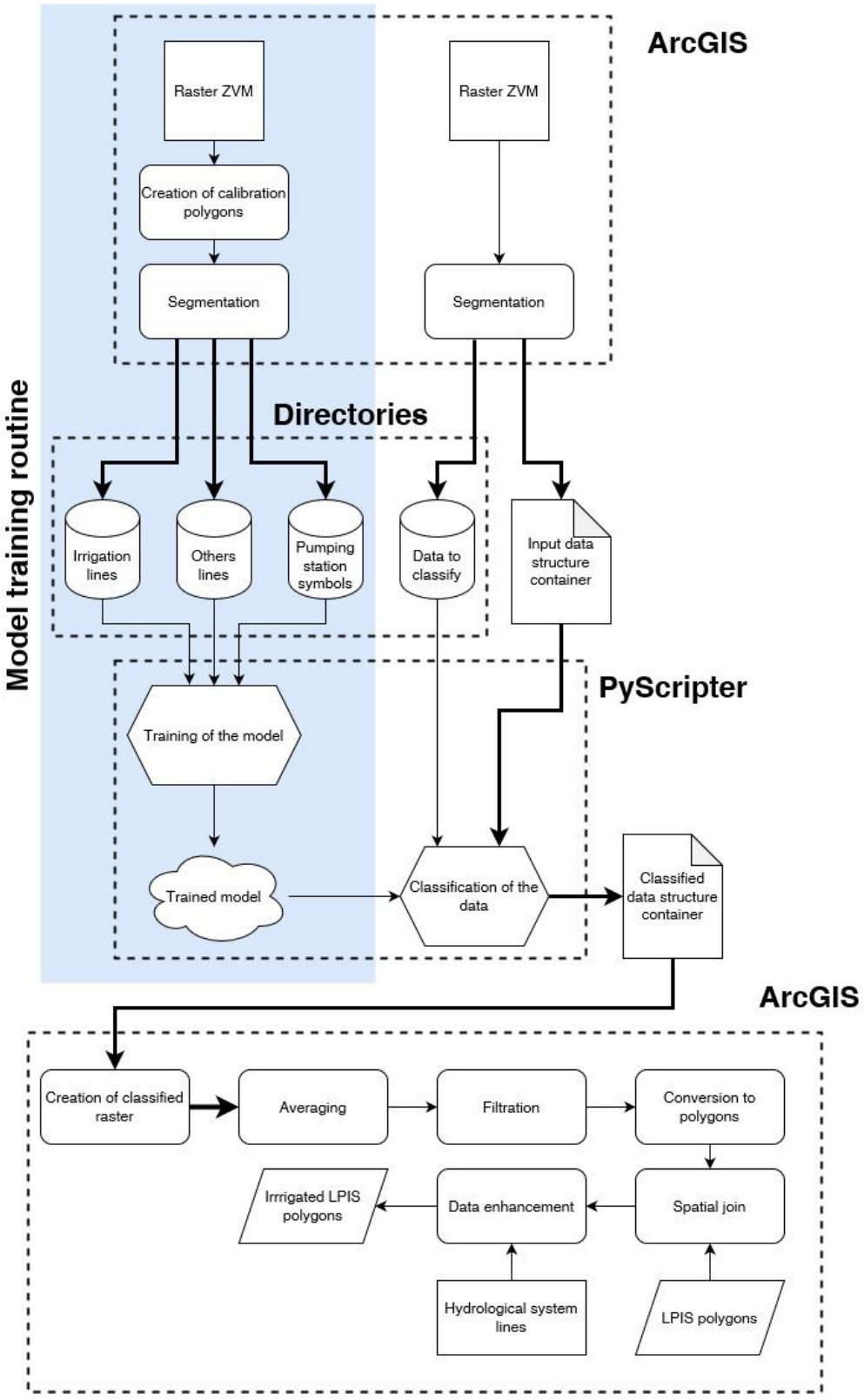

Fig. 2 – Analysis scheme

Input data treatment

Creation of training polygons

During the model training process, polygons were manually created on the georeferenced ZVM list of maps. Three distinct training categories were established: Irrigation, Other area, and Pumping station. The Irrigation Polygons closely replicated the line symbolizing the lines of irrigation pipes, with a slight offset (Figure 3). Creating these polygons proved to be a time-intensive task. Polygons belonging to the Other area class were predominantly rectangular in shape and encompassed areas where the irrigation lines were not visually identifiable. Pumping station polygons were delineated around the corresponding pumping station symbols, ensuring accurate representation within the dataset.

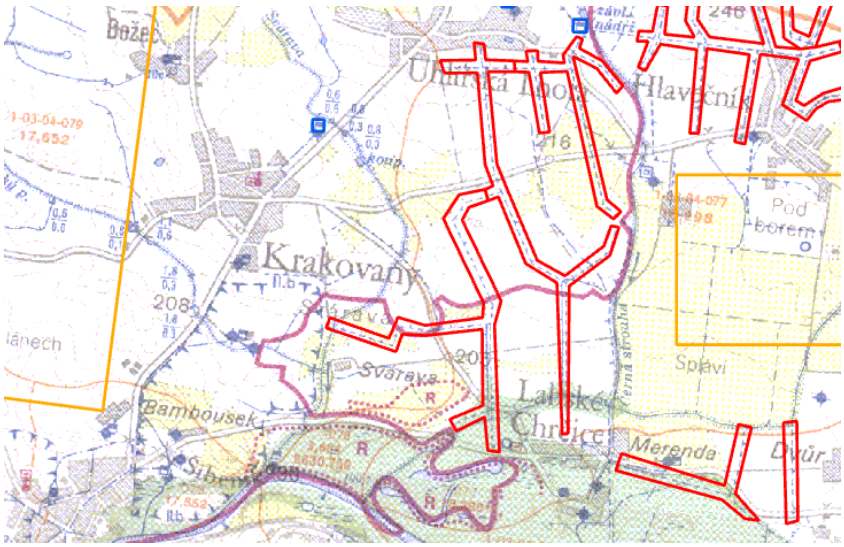

Fig. 3 – Example of training polygons at ZVM, red - Irrigation, orange - Other areas, blue - Pumping stations

Segmentation

Each map sheet is split into segments. The selected segment edge length was set to 31 pixels, equivalent to approximately 98.58 meters. By implementing the Segment shift technique, the resulting accuracy was effectively doubled, resulting in a segment size of 49.29 meters. This size was chosen to accommodate the dimensions of the pumping station symbol, ensuring that the entire symbol could be contained within a single segment. Opting for a larger segment size would have compromised the accuracy of the digitization process, increasing the risk of misclassifying non-irrigated fields as irrigated.

Next, the raster was systematically traversed in steps corresponding to the size of the edges of the individual segments. If training polygons were present within a segment, the segment was marked accordingly.

Segment shift

The shift was applied by half the length of the segment edge either in the horizontal direction, or in the vertical direction, or in both simultaneously (Figure 4). This adjustment generated additional mosaics that could be classified or utilized for model training purposes.

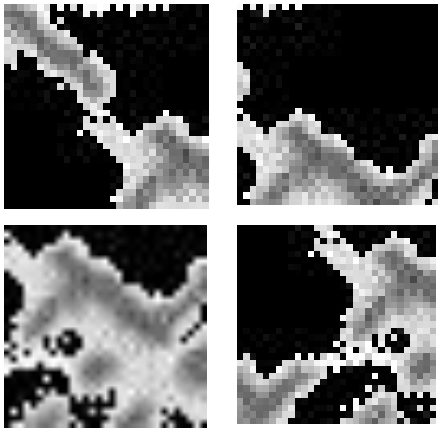

Fig. 4 – Example of segment shift. Segment side length is 31 pixels.

Building and training of the model

Model architecture is a Visual Geometry Group type and consists of blocks, where each block is composed of a 2D Convolution layer and a Max Pooling layer. As the number of layers increases in the Convolution Neural Network, the ability of the model to fit more complex functions also increases. Each layer will use the Rectified Linear Activation Function and He weight initialization, which are generally best practices. In a neural network, the activation function is responsible for transforming the summed weighted input from the node into the activation of the node or the output for that input.

Training the model

The original classification model categories were changed from Cats and Dogs to Irrigation, Other area and Pumping stations and model was trained on the relevant training data. The training data is loaded and split into a calibration part and a validation part for model calibration purposes. This split ratio was chosen to be 20%, which is a commonly used value.

Classification of the data

Individual map sheets not used for model training are classified by the trained model. The probability value with which the segments are classified as Irrigation, Pumping station or Other area is then saved as Classified Data. Training segments are omitted. The sum of these probabilities is equal to one. This process repeats for each classified segment, and for several thousands of segments per map sheet. This is the most time-consuming part.

Treatment of classified data

Averaging

By shifting the segments from each other, four classified rasters are created from a single map sheet. By calculating the arithmetic mean, a raster of average probabilities is created. During this step, the raster is also resampled. The edge length of the pixel of the new raster is 49.12 m, i.e., half the edge length of the classification segment.

Filtration

Filtering was done using Python script. This script first created a new raster with a value of 0. Subsequently, the filtered irrigation raster was scanned pixel by pixel, and the pixels or their immediate surroundings (a 3x3 pixel window) were analyzed. If the conditions for considering a pixel as a pixel containing irrigation were met, a value of 1 was written into the new raster.

The first filtering step was to zero out pixels with a value smaller than 0.5. Next, isolated pixels were zeroed. If a pixel had a value greater than 0.5 and was also in the neighbourhood of a

pixel with a value greater than 0.5, a value of 1 was written into the resulting raster. For pixels with a value greater than 0.75 and their immediate surroundings, the resulting raster value 1 was written to the filtered raster (Figure 5).

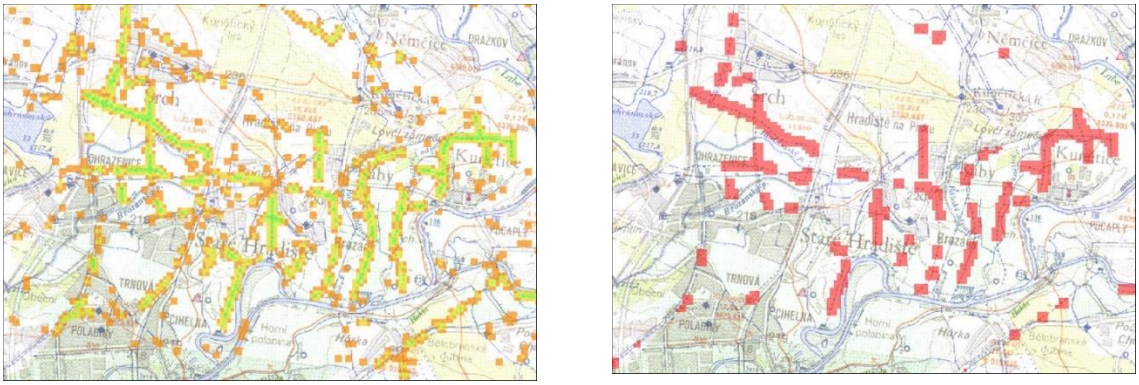

Fig. 5 – Example of filtration. The picture on the left shows pixels with high probability (green), and with lower probability (orange), and the picture on the right shows filtered data (red)

Creation of polygons

The filtered rasters were converted to a polygon. Subsequently, circular buffers with a radius of 1,000 m were created for all polygons with an area greater than 30,000 m2. Polygons with an area smaller than 30,000 m2 and not lying inside the buffers were deleted.

Manual cleaning

The resulting polygons were marked with the cadaster of the municipality where they were located and were subsequently combined into multipart polygons according to the cadaster designation. This was followed by going through this layer manually, from the smallest polygons according to size and erasing of them in cases when the polygon did not correctly mark the symbols of the irrigation pipe.

This is where the problem of the interchangeability of the irrigation pipes and the waste pipes became apparent. The waste pipe is symbolized by the same type of line, except that every fifth piece or so has the opposite orientation. In addition, the drinking water feeder from the Želivka water treatment plant was incorrectly marked, using the same symbology, only doubled (Figure 6).

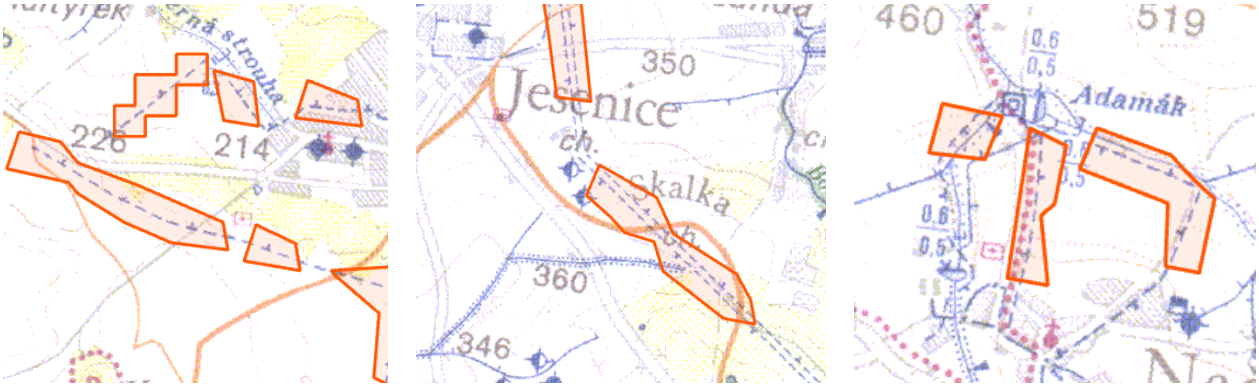

Fig. 6 – Example of resulting polygons, correctly classified irrigation on the left; part of the feeder from the Želivka water treatment plant in the middle; and waste pipe on the right

The result was a layer with more than 2200 polygons, which was converted to a single-part polygon layer and was further edited and refined. The result is 220 polygons.

Information enhancement

First, pumping stations were located and were signed with a point. These pumping stations were then given a name according to the particular irrigation system. The water source for these pumping stations was also found. The identified water sources are river, well, artificial channel, dam, storage tank, and others (Table 1).

Tab. 1. - Attribute table

Column name	Description
System_name	The unique identifier or name of the specific irrigation system polygon.
Source_type	The classification of the irrigation system based on a source type. River, lake, reservoir, well, or other.
Source_name	The name of the specific water source supplying the irrigation system. This could be the name of a river, artificial channel, dam, storage tank, and others.
River_name	The name of the river associated with the irrigation system, if applicable. This identifies the primary watercourse that supplies or is connected to the irrigation network.
Importance	The significance or priority level of the irrigation system.
RAD_III	Name of the third-class watershed in which is the system source located.

Referencing with LPIS data

The polygon layer is then merged with the LPIS layer, showing the agricultural land in use as of 2021. This layer was obtained from the Ministry of Agriculture website (https://eagri.cz). This creates a polygon layer of agricultural land that sits on top of the large-scale irrigation system. Final map is shown on Figure 9.

RESULTS

Efficiency of the model

During the run of the model, a total of 23 658 174 segments were generated, including the segment shift. 136 309 of these segments were used for training. The training dataset consisted of 106 942 Others class segments, 6 835 Pumping Station class segments and 22 532 Irrigation class segments (Fig. 7). This means less than 1% of the total number of segments was used for training the model. The trained model was then used to classify 23 521 865 segments.

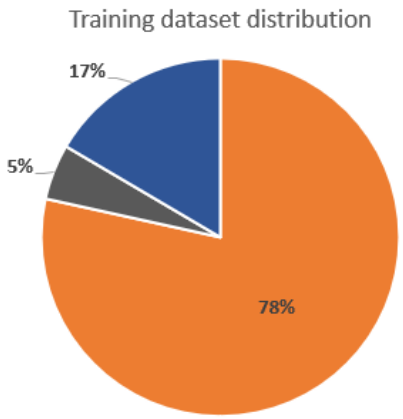

Fig. 7 – Graph showing statistics of the training dataset distribution classes. Class Others (Orange), class Irrigation (Blue) and class Pumping station (Grey).

After the creation and filtration of classified averaged rasters, a total of 344 615 irrigation pixels was reached. That amounts to 83 724,36 ha. These pixels were converted into polygons, and a total of 4783 polygons were created. Due to the Raster to Polygon tool, due to the use of the Simplify Polygon option, the area of these polygons is only 77 524,61 ha. Buffer filtration reduced the number of polygons to 1962, with an area of 58 617,46 ha. Subsequent manual go through and edit resulted in 238 polygons with an area of 69 082,97 ha (Figure 8). This sharp decrease in the number of polygons is created by joining the continuous nets polygons and merging them into the multipart feature.

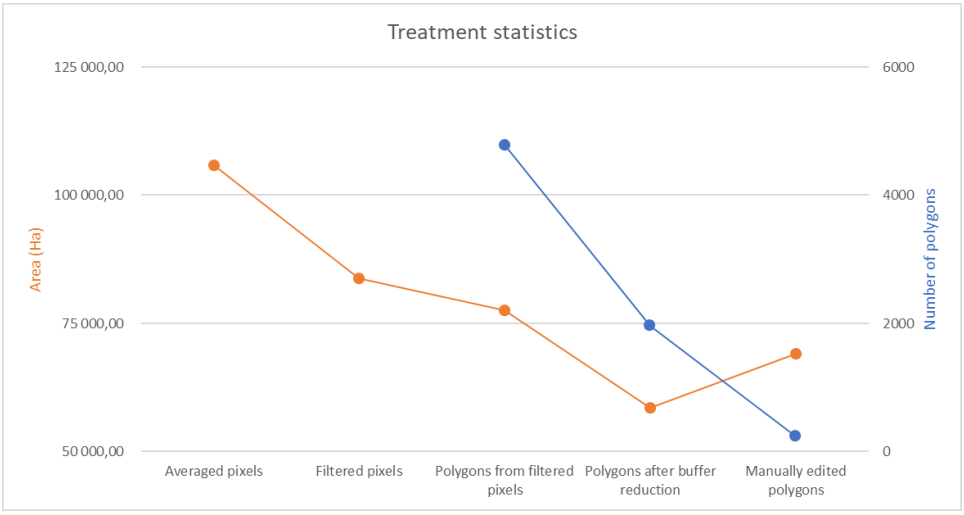

Fig. 8 – Graph showing the development of the number of pixels and hectares during the treatment of the data

Irrigated area and number of irrigation systems

Joining the manually edited polygons with the LPIS database resulted in 17 912 polygons belonging to 198 systems (Figure 9), covering an area of 189 743 ha. Most of the systems are in South Moravia. The rest of the systems follow the course of the Elbe River from East Bohemia to North Bohemia. There is one isolated irrigated region in Northwest Bohemia, in the rain shadow area. Several small systems are distributed all over the territory of Czechia. The only region without an irrigation system is West Bohemia. These results will be compared with further data sources (ISMS, SPÚ) in consecutive papers.

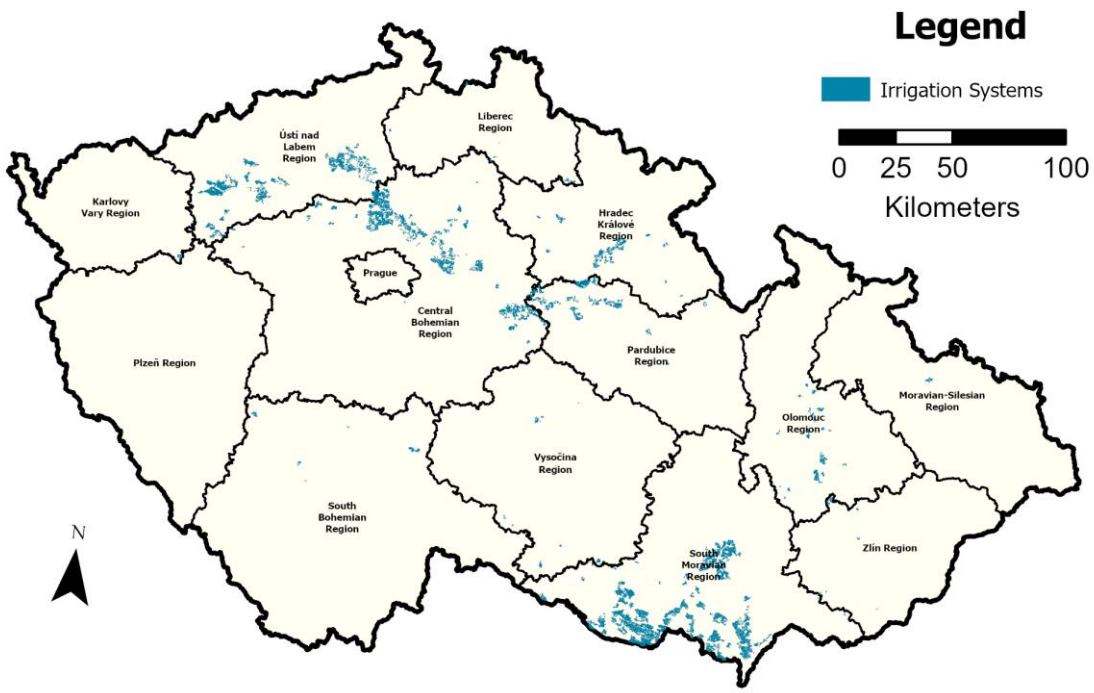

Fig. 9 – Distribution of identified irrigated fields across the territory of Czechia

The model for Digitalization of Irrigation systems is characterized by its high accuracy. This is a natural characteristic of neural networks. However, a lack of training data and the similarity between some symbols limited the use of the model for finding pumping stations. By segmenting the input data, the neural network processed smaller batches of data at a time. This allowed us to reduce the computational resources needed to train the model and enabled the use of ordinary computers instead of computational stations.

The main disadvantage of the model that we found is the need for a large, labeled dataset: Supervised neural networks require a large, labeled dataset for training. However, this was time-consuming and elaborate to create, especially for segmentation tasks that require precise labeling, e.g. pumping. Although the model provides the required results, it was overfitted in some locations.

Classification success level

The digitization success rate was rated as good. However, due to the time-consuming training and running of the model, the optimal segment size was not determined iteratively, and the required accuracy value was based on a value of approx. 50 m. A lower digitization success rate can also be tolerated because it was a one-time analysis, and the digitized polygons will not change. Digitized lines were subsequently used to mark fields specified in the LPIS database, thereby significantly reducing the influence of digitization errors on the result, as missing line elements will not prevent the marking of LPIS polygons.

A comparison between the model results and the Research Institute for Soil and Water Conservation database of irrigation systems (https://meliorace.vumop.cz) shows high agreement between the datasets. However, the database of irrigation systems also stores information about newly built systems. The Water Management Maps do not contain information about systems built after 1994, or about the current working status of the systems. Further comparison with newer data is planned in consecutive papers.

CONCLUSION

The application of segmentation in a supervised neural network model for digitalizing irrigation systems depicted on Water Management Maps has demonstrated significant potential. This method allows for the precise identification of irrigation fields, source watercourses, and source types. Compared to classical methods, our approach offers a more automated and scalable solution, addressing the current lack of information on irrigation infrastructure effectively.

However, there are certain limitations to consider. The accuracy of the model heavily relies on the quality of input data and labeling. Inadequate or inaccurate data can lead to less reliable results. Additionally, while our model has shown promise in initial tests, further validation with diverse datasets is necessary to confirm its robustness and generalizability.

The potential for practical applicability is substantial, particularly within the context of the Land Parcel Identification System (LPIS). The digitalized maps of irrigation pipes and pumping stations created by our model can serve as valuable resources for agricultural planning and resource allocation. This can lead to more efficient water management, especially in regions facing water scarcity and the impacts of climate change.

In summary, our solution offers a viable and innovative approach to addressing the information gap regarding irrigation systems. With further refinement and validation, it has the potential to significantly enhance the management and optimization of irrigation resources, contributing to more sustainable agricultural practices.

ACKNOWLEDGEMENTS

We would like to thank to T.G.Masaryk Water Research Institute for access to the scans of Water Management Maps on behalf of project The potential and risks of irrigation in the Czech Republic in a changing climate (SS01020052). The research is financed by the Technology Agency of the Czech Republic (research project TH02030428) and an internal student grant of CTU (SGS20/156/OHK1/3T/11).

REFERENCES

[1] Báčová M., Krása J., 2016. Application of historical and recent aerial imagery in monitoring water erosion occurrences in Czech highlands. Soil and Water Research, vol. 11, no. 4, 267–276. doi: 10.17221/178/2015-SWR.

[2] Buchtová I., Trnka Z., 2004. Situační a výhledová zpráva Zelenina. Prague: Ministerstvo zemědělství ČR (written in Czech).

[3] SPÚ, Historická souvislost - Meliorační stavby. Státní pozemkový úřad. Available: https://www.spucr.cz/stavby-k-vodohospodarskym-melioracim-pozemku/historicka-souvislost (written in Czech).

[4] Hosnedlová P., Zemědělci stárnou. Mladší generace nemají přístup k půdě a na zemědělství pohlížejí negativně. BusinessInfo.cz. Available: https://www.businessinfo.cz/clanky/zemedelci-starnou-mladsi-generace-nemaji-pristup-k-pude-a-na-zemedelstvi-pohlizeji-negativne/ (written in Czech).

[5] Vorlíček P., Gandalovič: Chceme stimulovat generační výměnu v zemědělství. KIS Středočeského kraje. Available: https://www.kis-stredocesky.cz/2008/01/gandalovic-chceme-stimulovat-generacni-vymenu-v-zemedelstvi/ (written in Czech).

[6] HEIS, HEIS VÚV - Informační stránky a data ke stažení. VÚV. Available: https://heis.vuv.cz/data/spusteni/pgstart.asp?pg=HTML_HEIS$ZVM50LN$stazeni&pgload=1&ico=icoopenid1.png&nadpis1=Z%25E1kladn%25ED vodohospod%25E1%25F8sk%25E1 mapa %25C8R 1:50 000: mapov%25E9 listy (archiv, 1986 - 1999)&nadpis2=Informa%25E8n%25ED str%25E1nky (written in Czech).

[7] MŽP, 2015. Národní akční plán adaptace na změnu klimatu. Prague (written in Czech).

[8] Fischer E. M., Sippel S., Knutti R., 2021. Increasing probability of record-shattering climate extremes. Nat Clim Chang, vol. 11, no. 8, 689–695. doi: 10.1038/s41558-021-01092-9.

[9] Daňhelka J., 2015. Vyhodnocení sucha na území České republiky v roce 2015. Český Hydrometeorologický ústav. Prague (written in Czech).

[10] Rozkošný M., Závlahy (VÚV TGM, v.v.i.). Accessed: Mar. 09, 2023. Available: https://heis.vuv.cz/data/webmap/datovesady/projekty/zavlahy/default.asp?lang=&tab=1&wmap= (written in Czech).
[11] Eslamian S., Eslamian F., 2023. Handbook of Irrigation Hydrology and Management. Boca Raton: CRC Press. doi: 10.1201/9780429290114.
[12] Kibret E. A., Abera A., Ayele W. T., Alemie N. A., 2021. Performance Evaluation of Surface Irrigation System in the Case of Dirma Small-Scale Irrigation Scheme at Kalu Woreda, Northern Ethiopia. Water Conservation Science and Engineering, vol. 6, no. 4, 263–274. doi: 10.1007/s41101-021-00119-8.
[13] Pardo M. Á., Riquelme A. J., Jodar-Abellan A., Melgarejo J., 2020. Water and Energy Demand Management in Pressurized Irrigation Networks. Water (Basel), vol. 12, no. 7, 1878. doi: 10.3390/w12071878.
[14] Trivedi A., Nandeha N., 2018. Small Scale Irrigation Development. Irrigation & Drainage Systems Engineering, vol. 07, no. 01. doi: 10.4172/2168-9768.1000206.
[15] Conrad C., Lamers J. P. A., Ibragimov N., Löw F., Martius C., 2016. Analysing irrigated crop rotation patterns in arid Uzbekistan by the means of remote sensing: A case study on post-Soviet agricultural land use. J Arid Environ, vol. 124, 150–159. doi: 10.1016/j.jaridenv.2015.08.008.
[16] Larney F. J., 2018. Irrigated Crop Rotations. Agriculture & Agri-Food Canada, Lethbridge.
[17] Chen T., Wang Z., Li G., Lin L., 2018. Recurrent Attentional Reinforcement Learning for Multi-label Image Recognition. 32nd AAAI Conference on Artificial Intelligence, AAAI 2018, 6730–6737. doi: 10.1609/aaai.v32i1.12281.
[18] Zhang W., Chen Q., Zhang W., He X., 2018. Long-range terrain perception using convolutional neural networks. Neurocomputing, vol. 275, 781–787. doi: 10.1016/j.neucom.2017.09.012.
[19] Makantasis K., Karantzalos K., Doulamis A., Doulamis N., 2015. Deep supervised learning for hyperspectral data classification through convolutional neural networks. 2015 IEEE International Geoscience and Remote Sensing Symposium (IGARSS), IEEE, 4959–4962. doi: 10.1109/IGARSS.2015.7326945.
[20] Kozlowski P., Walas K., 2018. Deep neural networks for terrain recognition task. 2018 Baltic URSI Symposium (URSI), IEEE, 283–286. doi: 10.23919/URSI.2018.8406736.
[21] Uhl J. H., Leyk S., Chiang Y. Y., Duan W., Knoblock C. A., 2020. Automated extraction of human settlement patterns from historical topographic map series using weakly supervised convolutional neural networks. IEEE Access, vol. 8, 6978–6996. doi: 10.1109/ACCESS.2019.2963213.
[22] Chen Y., Carlinet E., Chazalon J., Mallet C., Duménieu B., Perret J., 2021. Combining Deep Learning and Mathematical Morphology for Historical Map Segmentation. Lecture Notes in Computer Science, 79–92. doi: 10.1007/978-3-030-76657-3_5.
[23] Garcia-Molsosa A., Orengo H. A., Lawrence D., Philip G., Hopper K., Petrie C. A., 2021. Potential of deep learning segmentation for the extraction of archaeological features from historical map series. Archaeol Prospect, vol. 28, no. 2, 187–199. doi: 10.1002/ARP.1807.
[24] Kulhavý Z., Kulhavý F., 2008. Navrhování hydromelioračních staveb. Praha: Informační centrum ČKAIT.
[25] Jajodia T., Garg P., 2019. Image Classification-Cat and Dog Images. International Research Journal of Engineering and Technology. [Online]. Available: www.irjet.net
[26] Cukierski W., Dogs vs. Cats. Kaggle. [Online]. Available: https://www.kaggle.com/c/dogs-vs-cats
[27] Elson J., Douceur J. R., Howell J., Saul J., 2007. Asirra: A CAPTCHA that exploits interest-aligned manual image categorization. Proceedings of the ACM Conference on Computer and Communications Security, 366–374. doi: 10.1145/1315245.1315291.
[28] Sermanet P., Eigen D., Zhang X., Mathieu M., Fergus R., LeCun Y., 2013. OverFeat: Integrated Recognition, Localization and Detection using Convolutional Networks. 2nd International Conference on Learning Representations, ICLR 2014 - Conference Track Proceedings. doi: https://doi.org/10.48550/arXiv.1312.6229.